

CONTAMINANT FATE AND TRANSPORT IN
DOUBLE-POROSITY SOIL MEDIUM USING
LIGHT TRANSMISSION VISUALIZATION
TECHNIQUE



MOTASEM Y D ALAZAIZA

UMP

Doctor of Philosophy

UNIVERSITI MALAYSIA PAHANG

UNIVERSITI MALAYSIA PAHANG

DECLARATION OF THESIS AND COPYRIGHT

Author's Full Name : Motasem Y D Alazaiza

Date of Birth : 24/08/1986

Title : Contaminant fate and transport in double-porosity soil medium using light transmission visualization technique

Academic Session : ___2016/2017, Semester 2___

I declare that this thesis is classified as:

- CONFIDENTIAL (Contains confidential information under the Official Secret Act 1997)*
- RESTRICTED (Contains restricted information as specified by the organization where research was done)*
- OPEN ACCESS I agree that my thesis to be published as online open access (Full Text)

I acknowledge that Universiti Malaysia Pahang reserve the right as follows:

1. The Thesis is the Property of Universiti Malaysia Pahang
2. The Library of Universiti Malaysia Pahang has the right to make copies for the purpose of research only.
3. The Library has the right to make copies of the thesis for academic exchange.

Certified by:

(Student's Signature)

(Supervisor's Signature)

___3769064___
New IC/Passport Number

Date:

Name of Supervisor

Date:

NOTE : * If the thesis is CONFIDENTIAL or RESTRICTED, please attach with the letter page 2 from the organization with the period and reasons for confidentiality or restriction.

SUPERVISOR'S DECLARATION

I hereby declare that I have checked this thesis and in my opinion, this thesis is adequate in terms of scope and quality for the award of the degree of Doctor of Philosophy in Civil Engineering

(Supervisor's Signature)

Full Name : Dr. Ngien Su Kong

Position : Senior Lecturer

Date :



UMP

STUDENT'S DECLARATION

I hereby declare that the work in this thesis is based on my original work except for quotations and citations which have been duly acknowledged. I also declare that it has not been previously or concurrently submitted for any other degree at Universiti Malaysia Pahang or any other institutions.

(Student's Signature)

Full Name : MOTASEM Y D ALAZAIZA

ID Number : PKE15001

Date :



UMP

CONTAMINANT FATE AND TRANSPORT IN DOUBLE-POROSITY SOIL
MEDIUM USING LIGHT TRANSMISSION VISUALIZATION TECHNIQUE



MOTASEM Y D ALAZAIZA

Thesis submitted in fulfillment of the requirements
for the award of the degree of
Doctor of Philosophy

UMP

Faculty of Civil Engineering and Earth Resources

UNIVERSITI MALAYSIA PAHANG

OCT 2017

ACKNOWLEDGEMENT

First and foremost, all thanks and glory are due to “ALLAH” the Almighty, who gave me the power, the health and the patience to accomplish this research.

It is my great fortune to have Dr. Ngien Su Kong as the main supervisor during my research. I would like to express my warmest appreciation, gratitude and sincere thanks to him for his guidance, support, kind help and sound advice throughout the period of this research. Also, I would like to extend my thanks to my co-supervisor Assoc. Prof. Dr. Wan Mohd Faizal bin Wan Ishak, who gave me the opportunity to come to Universiti Malaysia Pahang (UMP) to conduct this research.

My appreciation extends to my field supervisor Dr. Samira Albati Kamaruddin from Universiti Teknologi Malaysia (UTM) for helpful suggestion and advice in performing the image acquisition and analysis.

A special thanks to Dr. Mustafa M. Bob from Taibah University, Kingdom of Saudi Arabia and Dr. Mohammed J K Bashir from Universiti Tunku Abdul Rahman (UTAR) for their help and support.

I would like to acknowledge the Faculty of Civil Engineering and Earth Resources, UMP for providing laboratory space and assistance to conduct the laboratory experiments. Also, I am very grateful to the Ministry of Higher Education of Malaysia (MOHE) for their financial support to this research through the Fundamental Research Grant Scheme (RDU 130139). Moreover, I wish to acknowledge the support of UMP to this research through the UMP Post Graduate Research Grant Scheme (PGRS 150393).

Also, I am very grateful to UMP financial support through the Graduate Research Scheme (GRS) to cover my living cost in Malaysia during my study.

My thanks go to all technicians in the Geotechnical laboratory and Environmental laboratory at UMP for their kind assistance and to all my friends at UMP.

On a personal note, I would like to thank my beloved friend Roshel for her support, prayers and friendship in Malaysia. Words are insufficient to express my appreciation for the unconditional love and support.

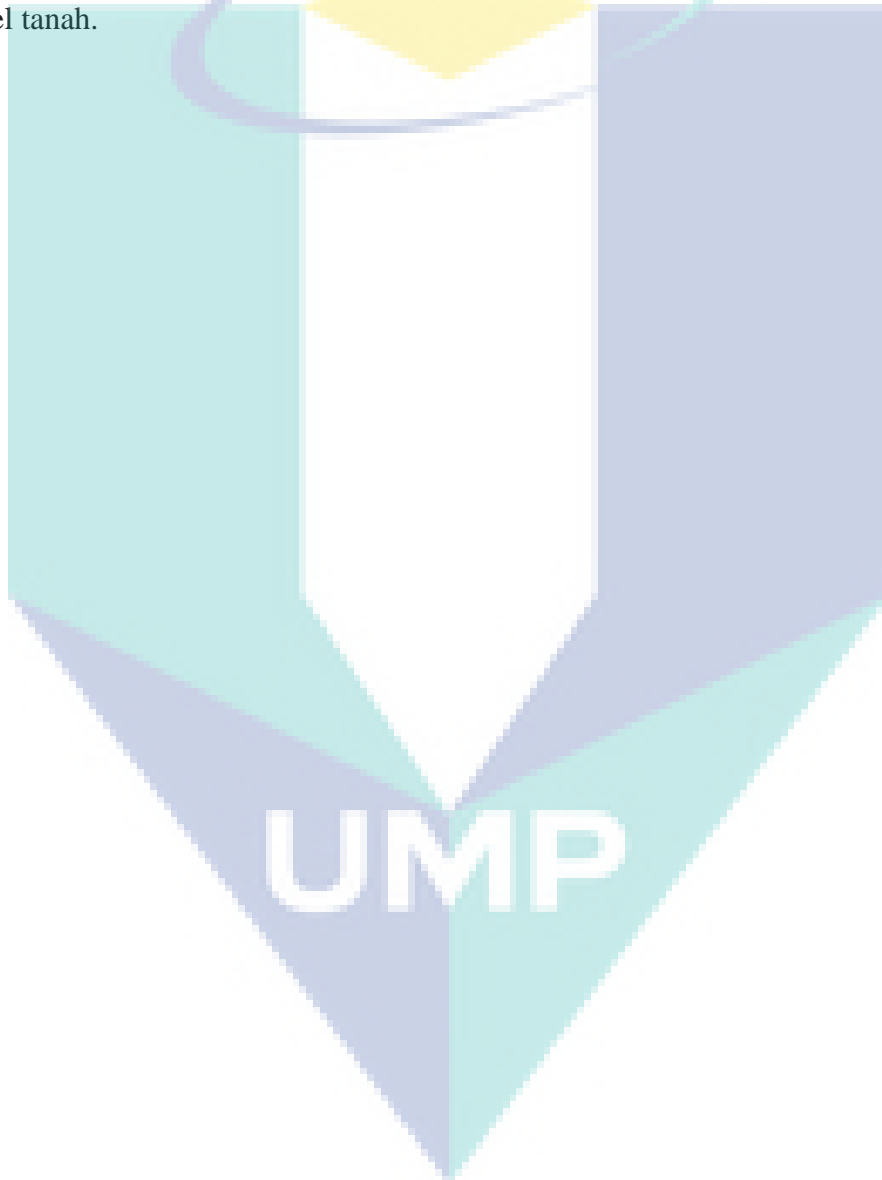
Lastly, this study is dedicated to my beloved parents and family for their unlimited love, inspiration, sacrifices and prayers.

ABSTRAK

Cecair fasa bukan akues adalah pencemaran air bumi dan tanah yang lazim. Produk petroleum, sebagai contoh cecair-cecair ini, berpotensi tinggi bocor ke dalam air bumi akibat aktiviti perindustrian dan pengangkutan. Keliangan berganda adalah fenomena semula jadi yang boleh dijumpai dalam banyak jenis tanah. Kehadirannya dalam sistem subpermukaan boleh menjejaskan kelakuan geobahan dan juga aliran bendalir berbilang fasa melaluinya akibat adanya dua jenis keliangan. Kajian ini dijalankan untuk mengkaji kelakuan satu jenis pencemar yang paling banyak tersebar iaitu penghijrahan cecair fasa bukan akues (NAPL) dalam tanah keliangan berganda di bawah keadaan yang berbeza menggunakan teknik transmisi visualisasi cahaya (LTV). NAPL yang dipertimbangkan dalam kajian ini adalah hasil daripada pelarut berklorin dan sebatian petroliam seperti tetrachloroethlene (PCE) dan toluena. Media keliangan berganda terdiri daripada campuran pasir silika tempatan (liang makro) dan bebola kaolin tanah liat tersinter (liang mikro) yang disusun secara berkala. Eksperimen makmal telah direka dan dijalankan dalam keadaan yang berbeza yang mewakili penghijrahan NAPL dalam sistem fasa dua bendalir, sistem fasa tiga cairan dan penghijrahan NAPL di bawah pengaruh hujan. Lima eksperimen telah diulang menggunakan media berkeliangan tunggal untuk menyiasat pengaruh liang-liang makro di antara pasir dan bebola kaolin ketika penghijrahan NAPL. Liang makro didapati berpengaruh dalam penghijrahan NAPL sejak jumlah liang makro sangat besar berbanding dengan liang-liang. Sebelum memulakan eksperimen makmal, persamaan diperolehi untuk mengira ketepatan NAPL tumpat (DNAPL) dalam keliangan berganda secara piksel ke piksel berdasarkan kaedah LTV. Penggunaan teknik LTV dengan serta-merta dapat menangkap imej penghijrahan DNAPL dalam media berliang. Imej-imej yang ditangkap telah dimasukkan melalui perisian pemprosesan imej, mengubah imej digital kepada nilai-nilai tahap kelabu yang kemudiannya digunakan dalam penciptaan semula dan plotan proses pengagihan DNAPL. Hasilnya menunjukkan bahawa teknik LTV dan analisis imej berjaya digabungkan untuk mendapatkan ketepatan NAPL dalam keliangan berganda. Kaedah ini telah disahkan menggunakan keseimbangan jisim di mana isipadu DNAPL disuntik dibandingkan dengan isipadu yang dikira menggunakan analisis imej. Selain itu, analisis statistik digunakan untuk mengesahkan ketepatan kaedah. Hubungan korelasi yang kukuh diperolehi antara isipadu DNAPL yang disuntik dan isipadu yang dikira dalam semua eksperimen ($R^2 > 0.90$). Keputusan menunjukkan sedikit perbezaan di antara cara eksperimen berulang yang menunjukkan bahawa kaedah ini dapat digunakan untuk pemantauan penghijrahan DNAPL dalam medium keliangan berganda. Tambahan pula, keputusan tersebut menunjukkan bahawa liang makro mempunyai kesan yang signifikan terhadap kedua-dua penghijrahan LNAPL dan DNAPL dalam tanah keliangan berganda di mana NAPL adalah lebih pantas dalam tanah keliangan berganda berbanding dengan tanah keliangan tunggal kerana jumlah liang makro. Kebolehasahan bendalir dan ciri-ciri tekanan kapilari yang wujud di dalam liang tanah didapati faktor yang berpengaruh dalam penghijrahan bendalir dalam media berliang. Kejadian kebolehasahan dalam sistem fasa tiga bendalir menyebabkan NAPL menjadi lebih perlahan berbanding penghijrahan dalam sistem fasa dua bendalir. Di samping itu, keputusan menunjukkan bahawa sifat kimia seperti faktor rencatan dan pekali pengagihan mempunyai pengaruh yang signifikan terhadap penghijrahan LNAPL

dan DNAPL dalam media berliang. Imbuan hujan didapati faktor yang berpengaruh pada penghijrahan cecair ringan fasa bukan akues (LNAPL) dalam tanah keliangan berganda. Aliran air hujan yang menyusup ke dalam tanah menyebabkan LNAPL yang terperangkap dalam media berliang ditolak ke bawah dalam semua eksperimen tidak kira isipadu LNAPL dan keamatan hujan. Tambahan pula, diperhatikan bahawa paras pinggiran kapilari tertekan di zon tepu disebabkan oleh pengaruh imbuan hujan pada kepulan LNAPL.

Secara keseluruhan, penerapan teknik LTV berjaya menyediakan kaedah yang tidak mengganggu dan tidak merosakkan untuk penyiasatan kelakuan NAPL dalam media tanah keliangan berganda dalam aliran bendalir berbilang fasa tanpa mengganggu sampel tanah.



ABSTRACT

Non-aqueous phase liquid is a common form of groundwater and soil contamination. Petroleum products, as an example of these liquids, have a high potential of leaking into groundwater due to industrial and transportation activities. Double-porosity is a natural phenomenon that can be found in many types of soil. Its presence in the subsurface system can significantly affect the behaviour of geomaterials as well as the multiphase fluid flow through it due to the presence of two types of porosities. This research was undertaken to study the behaviour of one type of the most wide spread contaminant which is the non-aqueous phase liquids (NAPLs) migration in double-porosity soil under different conditions using light transmission visualization (LTV) technique. The NAPLs considered in this study are the resulted from chlorinated solvents and petroleum compounds such as tetrachloroethylene (PCE) and toluene. The double-porosity media composed of a mixture of local silica sand (macro-pores) and sintered kaolin clay spheres (micro-pores) arranged in a periodic manner. The laboratory experiments were designed and carried out under different conditions which represent the NAPL migration in two-fluid phase systems, three-fluid phase systems and the NAPL migration under the influence of rainfall recharge. Five experiments were repeated using a single-porosity media to investigate the influence of the macro-pores between the sand and kaolin spheres on the NAPL migration. Macro-pores was found to be an influential in the NAPL migration since the volume of macro-pores is very large as compared to micro-pores. Prior of starting the laboratory experiments, equations were derived to calculate the Dense NAPL (DNAPL) saturation in double-porosity pixel by pixel based on LTV method. The usage of the LTV technique can instantaneously capture the DNAPL migration in the porous media. The captured images were fed through an image processing software, transforming the digital images into grey level values that were subsequently used in the re-creation and plotting of the DNAPL distribution process. The results demonstrated that the LTV technique and image analysis were successfully combined to obtain the DNAPL saturation in double-porosity. The method was validated using mass balance where the injected volumes of DNAPL were compared to the calculated volumes using image analysis. Moreover, statistical analysis was used to validate the accuracy of the method. Strong correlation was obtained between the injected DNAPL volumes and the calculated volumes in all of the experiments ($R^2 > 0.90$). The results show a slight difference between the means of the repeated experiments which indicates that the method is viable for monitoring DNAPL migration in double-porosity medium. Furthermore, the results show that the macro-pores have a significant effect on both LNAPL and DNAPL migration in double-porosity soil where the NAPL was much faster in double-porosity soil compared to single-porosity soil due to the volume of the macro-pores. Wettability of fluids and capillary pressure characteristics that exist in the soil pores were found to be influential factors in fluid migration within porous media. The occurrence of the wettability in the three-fluid phase system caused the NAPL to be more slower as compared to the migration in two-fluid phase system. In addition, the results show that chemical properties such as retardation factor and distribution coefficient have a significant influence on the LNAPL and DNAPL migration in porous media. Rainfall recharge was found to be an influential factor on the light non-aqueous phase liquid (LNAPL) migration in double-porosity soil. The flow of rainwater that seeped through the soil caused the LNAPL entrapped in the porous media to be pushed downward in all the experiments regardless of the LNAPL volume and rainfall intensity. Furthermore, it

was observed that the capillary fringe level was depressed in the saturated zone due to the influence of the rainfall on LNAPL plume.

Overall, the application of the LTV technique successfully provides a non-intrusive and non-destructive tool in investigating the NAPL behaviour in double-porosity soil media in multiphase fluid flow without disturbing the soil samples. In addition, the LTV method is a viable method in investigating and predicting the DNAPL migration in groundwater which can help the researchers in designing the remediation tools.

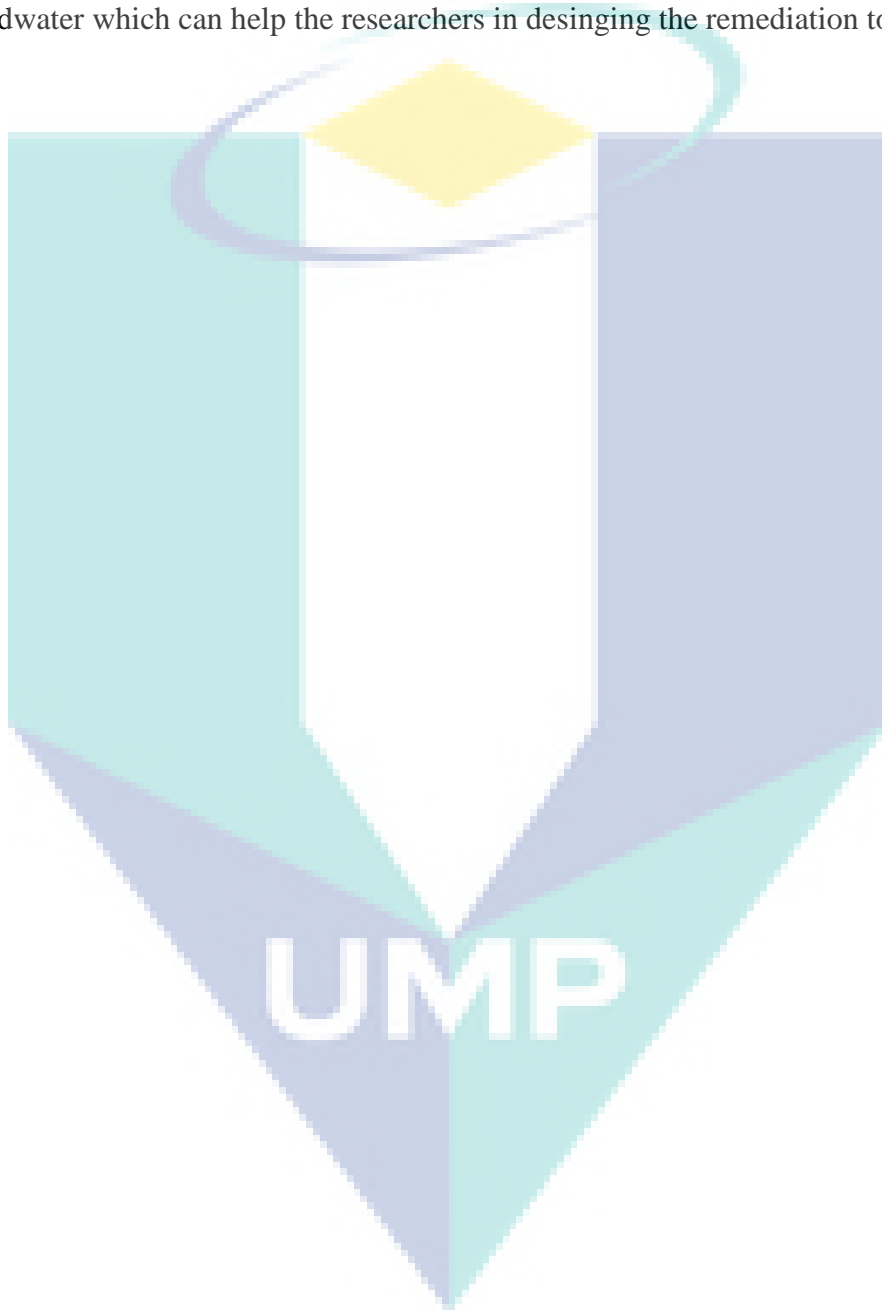


TABLE OF CONTENT

DECLARATION	
TITLE PAGE	i
ACKNOWLEDGEMENT	ii
ABSTRAK	iii
ABSTRACT	v
TABLE OF CONTENT	vii
LIST OF TABLES	xii
LIST OF FIGURES	xiii
LIST OF SYMBOLS	xv
LIST OF ABBREVIATIONS	xvii
CHAPTER 1 INTRODUCTION	1
1.1 Background	1
1.2 Problem Statement	3
1.3 Aim and Objectives of the Research	4
1.4 Scope of the Research	5
1.5 Significance of the Research	6
1.6 Outline of the Thesis	7
CHAPTER 2 LITERATURE REVIEW	8
2.1 Introduction	8
2.2 Groundwater Hydrology	8
2.3 Groundwater Contamination	11

2.4	Non-Aqueous Phase Liquids (NAPLs)	13
2.4.1	Movement of NAPL in the Vadose Zone	15
2.4.2	LNAPL Behaviour at the Groundwater Table	15
2.4.3	DNAPL Movement in the Saturated Zone	16
2.4.4	NAPL Pollution in Malaysia	17
2.4.5	Multiphase Flow in Porous Media	17
2.5	Soil Structure	19
2.5.1	The Double-Porosity History	20
2.5.2	Experimental Studies on Double-Porosity Soil	21
2.6	The Physics of Light	26
2.6.1	Wavelengths Regions	27
2.6.2	Optical Filters	30
2.7	Image Analysis Techniques	32
2.8	Photographic Methods	33
2.8.1	Light Reflection Method (LRM)	36
2.8.2	Light Transmission Visualization (LTV) Method	43
2.8.3	Multispectral Image Analysis Method	52
2.9	Summary	54
CHAPTER 3 MATERIALS AND METHODS		56
3.1	Introduction	56
3.2	Materials and Methods	56
3.2.1	DNAPL and LNAPL	56
3.2.2	Double-Porosity Materials	57
3.2.3	Physical Properties	58
3.2.4	Chemical Properties using Cation Exchange Capacity	59

3.2.5	Mineralogical Compositions	61
3.2.6	Creation of Double-porosity Media	61
3.3	Calculation of NAPL Saturation for Double-Porosity Soil	63
3.4	Laboratory Experiments	71
3.5	Design of Experiments	72
3.5.1	Group (1): PCE migration in two-fluid phase system in double and single-porosity soil	72
3.5.2	Image Analysis Procedures	77
3.5.3	Group (2) PCE and toluene migration in three-fluid phase system in double and single-porosity in	80
3.5.4	Group (3) Influence of rainfall recharge on toluene migration in double-porosity soil	82
3.5.5	Group (4) Correlation of the DNAPL migration to the macro-pores and micro-pores within double-porosity soil structure	88
3.6	Summary	89
CHAPTER 4 RESULTS AND DISCUSSION		90
4.1	Introduction	90
4.2	Soil Properties Results	90
4.2.1	Physical Properties	90
4.2.2	Chemical Properties	94
4.2.3	Mineralogical Properties	94
4.3	Results of The Experiments in Group (1)	96
4.3.1	PCE migration in double-porosity soil medium, Experiment (1)	96
4.3.2	PCE migration in single-porosity soil medium, Experiment (2)	103
4.4	Results of the Experiments in Group (2)	107
4.4.1	PCE migration in double-porosity, Experiment (3)	108

4.4.2	PCE migration in single-porosity, Experiment (4)	111
4.4.3	Toluene migration in double-porosity, Experiment (5)	113
4.4.4	Toluene migration in single-porosity, Experiment (6)	115
4.5	Results of the Experiments in Group (3)	117
4.5.1	LNAPL migration before rainfall recharge	117
4.5.2	LNAPL migration after rainfall recharge	118
4.5.3	Influence of LNAPL spillage volume	120
4.6	Results of the Experiments in Group (4)	124
4.6.1	PCE migration in Experiment (11)	124
4.6.2	PCE migration in Experiment (12)	128
CHAPTER 5 CONCLUSION & RECOMMENDATIONS		135
5.1	Introduction	135
5.2	Conclusion	135
5.3	Recommendations	138
REFERENCES		139
APPENDIX A	Properties of light shaping diffuser (LSD)	161
APPENDIX B	Properties of the band-pass filter	162
APPENDIX C	VBA script to convert matrix to XYZ format data	163
APPENDIX D	Particle size distribution results for materials	164
APPENDIX E	Hydrometer test results for raw kaolin	166
APPENDIX F	Specific gravity results for materials	164
APPENDIX G	Liquid limit test results for kaolin used in experiments	170
APPENDIX H	Plastic limit test results for raw kaolin used in experiments	168

APPENDIX I	Permeability test results	169
APPENDIX J	Example of calculation the CEC value	172
APPENDIX K	Calculation steps to determine the double-porosity value	173
APPENDIX L	Calculation steps to determine the number of pores (N_p)	175
APPENDIX M	Calculation of the average pore diameter (d_o)	177
APPENDIX N	Calculation of the PCE volume	178
APPENDIX O	Typical detailed calculation of PCE volumes	181
APPENDIX P	Repetition of Experiment (1)	200
APPENDIX Q	Repetition of Experiment (2)	201
APPENDIX R	Repetition of Experiment (3)	202
APPENDIX S	Repetition of Experiment (4)	203
APPENDIX T	Repetition of Experiment (5)	204
APPENDIX U	Repetition of Experiment (6)	205
APPENDIX V	Repetition of Experiment (11)	206
APPENDIX W	Repetition of Experiment (12)	207
APPENDIX X	Comparison between Experiment 1, 11 and 12	208
APPENDIX Y	Image Analysis Procedures	206
LIST OF PUBLICATIONS		222

LIST OF TABLES

Table 2.1	Types of groundwater pollution and their sources	12
Table 2.2	Comparison of current study with previous studies in double-porosity	25
Table 2.3	Wavelength regions	26
Table 2.4	Photographic methods usage in measurement of various fluid properties	34
Table 3.1	PCE and toluene properties*	57
Table 3.2	Frequency of image acquisition for Experiments 3, 4, 5, and 6	82
Table 4.1	Physical properties for raw kaolin, burned kaolin and sand	91
Table 4.2	Sieve analysis breakdown	93
Table 4.3	CEC values for materials used	94
Table 4.3	Important parameters calculated for Experiment 1 and Experiment 2	96
Table 4.4	Injected and calculated volumes of PCE for Experiment 1	99
Table 4.5	Injected and calculated volumes of PCE for Experiment 2	104
Table 4.6	Important parameters calculated for Experiment 11 and Experiment 12	124
Table 4.7	Injected and calculated volumes of PCE for Experiment 3	125
Table 4.8	Injected and calculated volumes of PCE for Experiment 4	128


UMP

LIST OF FIGURES

Figure 2.1	Content of the literature review	9
Figure 2.2	The hydrological cycle	10
Figure 2.3	Vertical groundwater distribution	11
Figure 2.4	Fate of NAPL in soil	14
Figure 2.5	Optical portion of the electromagnetic spectrum	27
Figure 2.6	Energy in electromagnetic spectrum	29
Figure 2.7	Wavelength region for Long-pass filter	31
Figure 2.8	Wavelength region for Band-pass filter	32
Figure 2.9	Light reflection experimental setup to determine LNAPL saturation in double-porosity aggregated kaolin	40
Figure 2.10	Light transmission visualization experimental setup to determine DNAPL saturation in silica sand	44
Figure 3.1	Kaolin sintered clay spheres obtained from burning the kaolin	62
Figure 3.2	Schematic diagram for double-porosity soil arrangement (The dark brown color is the kaolin spheres and the normal brown color is the sand)	63
Figure 3.3	Flow chart for laboratory experiments in the research	71
Figure 3.4	The dark room for conducting the laboratory experiments	72
Figure 3.5	Typical experimental setup for all experiments in the research	73
Figure 3.6	Schematic diagram for the main tool in the research (light box)	74
Figure 3.7	Image analysis procedures for extracting the NAPL light intensity	78
Figure 3.8	Correction zones at (a) The reference image when the flow chamber is fully saturated with water (b) The image after the increment of PCE	79
Figure 3.9	Schematic diagram for the experiments 3,4,5 and 6 (Group 2, PCE and toluene migration in three-fluid phase system)	81
Figure 3.10	Laboratory experiments in group (3) for the influence of rainfall intensity on LNAPL migration in double-porosity medium	83
Figure 3.11	Schematic diagram for the experimental setup in group 3 for LNAPL migration under the influence of rainfall recharge	85
Figure 3.31	Trial test for water drainage and LNAPL infiltration to determine the duration for stable conditions	88
Figure 4.1	Particle size distributions for sand and raw kaolin using sieve analysis and hydrometer tests	92
Figure 4.2	X-ray diffraction charts for (a) Raw kaolin (b) Burned kaolin (c) Silica sand to determine the mineralogical properties	95

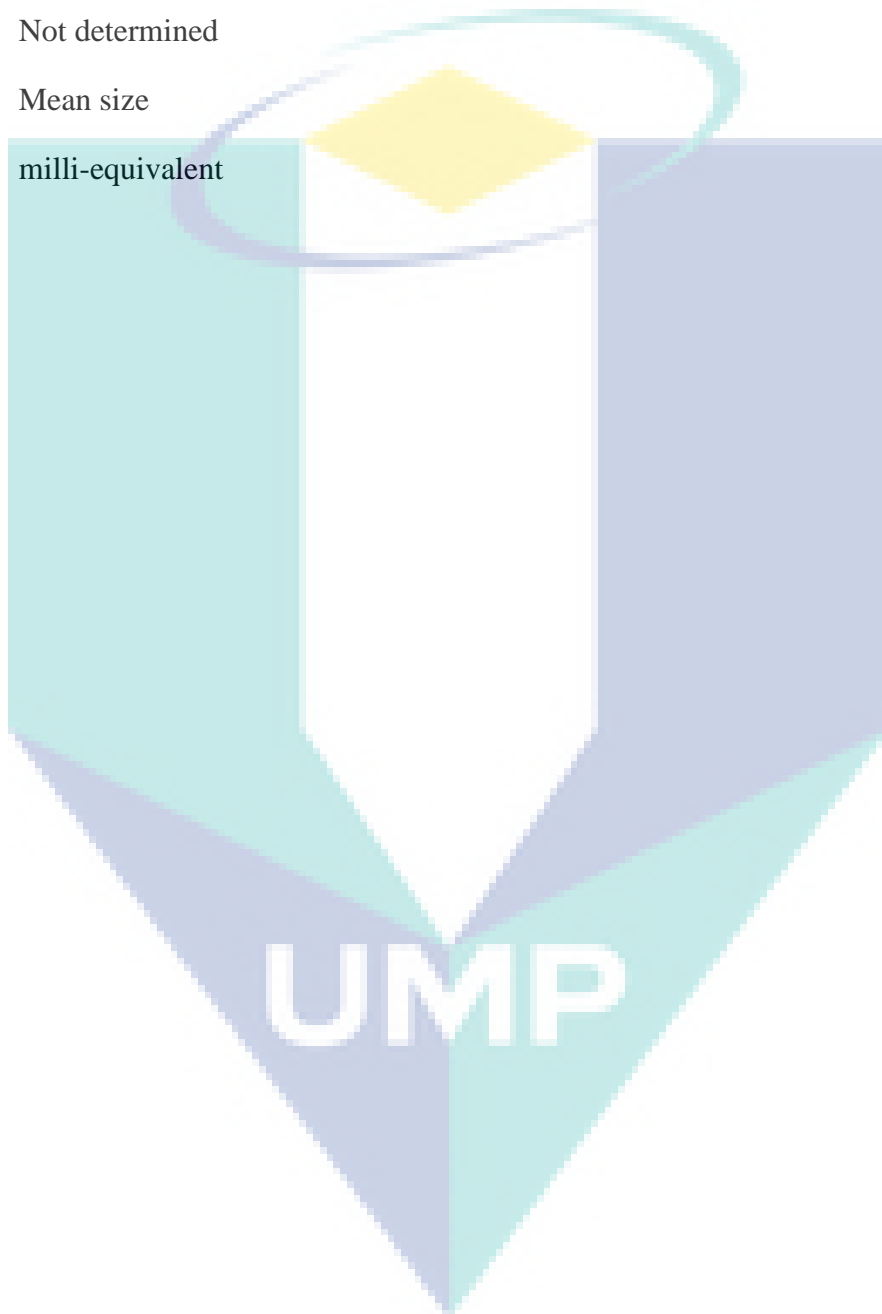
Figure 4.3	PCE volume calculated from image analysis vs. injected PCE volume into the flow chamber for Experiment 1.	97
Figure 4.4	PCE saturations in Experiment 1 after (a) 5 min. (b) 10 min. (c) 30 min. (d) 60 min.	102
Figure 4.5	PCE volume calculated from image analysis vs. injected PCE volume into the flow chamber for Experiment 2.	103
Figure 4.6	PCE saturations in Experiment 2 after (a) 10 min. (b) 60 min. (c) 120 min. (d) 180 min.	106
Figure 4.7	PCE migration in single and double-porosity soil mediums	107
Figure 4.8	PCE light intensity distribution in double-porosity soil media after (a) 10 min (b) 30 min (c) 76 min (d) 104 min	110
Figure 4.9	PCE light intensity distribution in single-porosity soil media after (a) 10 min (b) 30 min (c) 184 min (d) 228 min.	112
Figure 4.10	Toluene light intensity distribution in double-porosity soil media after (a) 10 min (b) 15 min (c) 30 min (d) 62 min	114
Figure 4.11	Toluene light intensity distribution in single-porosity soil media after (a) 10 min (b) 15 min (c) 60 min (d) 92 min	116
Figure 4.12	LNAPL migration depth for low and high LNAPL volume cases before rainfall recharge (Low LNAPL volume = 50 ml, High LNAPL volume = 100 ml)	118
Figure 4.13	Influence of rainfall on LNAPL migration for low and high volume cases (Low LNAPL volume = 50 ml, High LNAPL volume = 100 ml)	119
Figure 4.14	Influence of rainfall on LNAPL migration for the case of 100 ml LNAPL volume (a) before rainfall (b) after 30 min of rainfall (c) after 90 min of rainfall (d) after 120 min of rainfall	121
Figure 4.15	Light intensity of LNAPL migration (a) low LNAPL volume before rainfall (b) low LNAPL volume after rainfall (c) high LNAPL volume before rainfall (d) high LNAPL volume after rainfall	123
Figure 4.16	PCE volume calculated from image analysis vs. injected PCE volume into the flow chamber for Experiment 3.	125
Figure 4.17	PCE saturations in Experiment 11 after (a) 5 min. (b) 10 min. (c) 15 min. (d) 30 min.	127
Figure 4.18	PCE volume calculated from image analysis vs. injected PCE volume into the flow chamber for Experiment 12.	129
Figure 4.19	PCE saturations in Experiment 12 after (a) 5 min. (b) 10 min. (c) 15 min. (d) 30 min.	130
Figure 4.20	Cumulative PCE migration depth for the experiments in double-porosity medium	132
Figure 4.21	A correlation of the PCE migration to the volumetric fraction of the double-porosity	133

LIST OF SYMBOLS

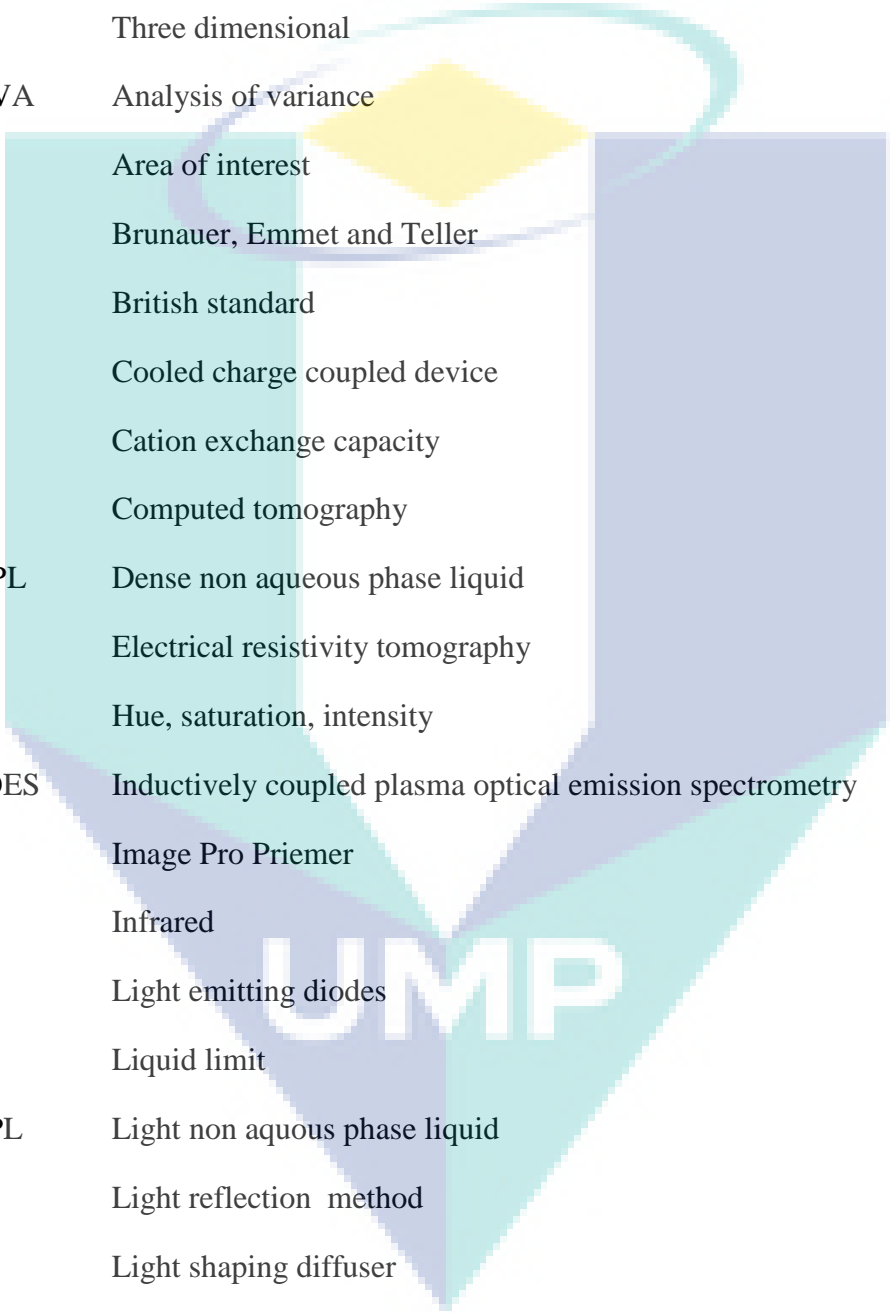


σ	Interfacial tension
θ	Contact angle (in degrees)
ϕ_T	Total porosity
ϕ_P	Primary porosity
ϕ_S	Secondary porosity
P_c	Capillary pressure
r	Radius of the pore
λ	Wavelength
τ	Transmission factor
n	Refractive index
R	Regression coefficient
R^2	Coefficient of determination
D	Optical density
D_i	Average optical density
ρ	Light reflectance
I_r	Reflected light intensity
I_o	Reflected light by an ideal surface
N	Number of objects
N_p	Number of pores
I	Emergent light intensity
C	Constant for correction
I_{in}	Incident light intensity
α	Absorption coefficient
d_o	Average pore diameter
S	Saturation

K_D Distribution coefficient
 rpm Revolution per minute
 C_u Coefficient of uniformity
 CO_2 Carbon dioxide
 ND Not determined
 D_{50} Mean size
 Meq milli-equivalent



LIST OF ABBREVIATIONS



1-D	One dimensional
2-D	Two dimensional
3-D	Three dimensional
ANOVA	Analysis of variance
AOI	Area of interest
BET	Brunauer, Emmet and Teller
BS	British standard
CCD	Cooled charge coupled device
CEC	Cation exchange capacity
CT	Computed tomography
DNAPL	Dense non aqueous phase liquid
ERT	Electrical resistivity tomography
HSI	Hue, saturation, intensity
ICP-OES	Inductively coupled plasma optical emission spectrometry
IPP	Image Pro Priemer
IR	Infrared
LED	Light emitting diodes
LL	Liquid limit
LNAPL	Light non aquous phase liquid
LRM	Light reflection method
LSD	Light shaping diffuser
LTV	Light transmission visualization
MIAM	Multi-spectral image analysis method
MOHE	Ministry of Higher Education
MW	Microwave

NAPL	Non aqueous phase liquid
PCE	Tetrachloroethylene
PL	Plastic limit
PSD	Particle size distribution
RGB	Red, green, blue
RMSE	Root mean squared error
SIAM	Simplified image analysis method
TCE	Trichloroethylene
UMP	Universiti Malaysia Pahang
UTAR	Universiti Tunku Abdul Rahman
UTM	Universiti Teknologi Malaysia
UV	Ultraviolet
VBA	Visual basic application
VOCs	Volatile organic compounds
XRD	X-ray diffraction



UMP

CHAPTER 1

INTRODUCTION

1.1 Background

Groundwater is considered as a major source of drinking water in many countries around the world. Over the last few decades, many incidents of groundwater pollution due to leakage of petroleum products from underground storage tanks and pipelines as well as spillage of hydrocarbon have been reported (Sreedharan and Sivapullaiah, 2017; Agaoglu et al. 2015). Contaminants from these sources affect the quality of groundwater and make it unsuitable for human as well as irrigation uses (Alias, 2003; Kamaruddin et al., 2011a). One of the most substantial contaminant types is non-aqueous phase liquids (NAPLs) (Soga et al., 2004).

Also known as immiscible hydrocarbons in the subsurface, non-aqueous phase liquid (NAPLs) are considered as among the top most widespread hazardous chemicals (Newell et al., 1995; Bedient et al., 1999). The understanding of the flow and transport through porous media in natural and engineered processes such as in groundwater and unsaturated zone flow is very important especially in multi-phase flow systems (Wildenschild and Sheppard, 2013). Transport of NAPL is very complex in the unsaturated zone because of the various phases involved (Ngien et al., 2012a).

Based on liquid density, NAPLs are classified into light non-aqueous phase liquid (LNAPL) which has density less than water and dense non-aqueous phase liquid (DNAPL) of which the density is higher than that of water. When the LNAPL is released into the subsurface, it will migrate downward under the influence of gravity until it reaches the water table. For DNAPL, it will behave similarly to LNAPL in the unsaturated zone after being released into the subsurface but while LNAPL tends to

pool on groundwater it encountered, DNAPL will continue to migrate downward vertically into the saturated zone (Ngien, 2012).

The main sources of LNAPL and DNAPL are the accidental surface release and inappropriate disposal of petroleum compounds such as refinery wastes, jet fuel, diesel, and others (EPA, 2009). In addition, volatile organic solvents are also considered as the main source of NAPL (Soga et al., 2004).

Several characteristics influence the migration of contaminants in the subsurface system such as fluid saturation, interfacial tension, wettability, capillary pressure and the soil structure (Mercer and Cohen, 1990). In natural case, several types of soils have two distinguished scales of porosity (Lewandowska et al., 2005) which known as double-porosity soil structure (Carminati et al., 2008). Double-porosity is considered a natural phenomenon (El-Zein et al., 2006) that usually found when two separate pore systems occurred simultaneously in structure of soil. Rock aquifers (Pao and Lewis, 2002) and agricultural top soil (El-Zein et al., 2006) are examples of geomaterials that potentially harbor double-porosity characteristics.

Lately, fluids migration in soil structure was found to be possibly investigated using image analysis techniques (Peng et al., 2015; Zhao et al., 2015; Bob et al., 2008). Over the last few decades, there was a quantum leap in the field of experimental technologies (Peng et al., 2015) especially in non-intrusive imaging techniques which means that characterization and understanding of the multiphase system can be more accurate (Agaoglu et al., 2015). A number of image analysis techniques have been reported by Oostrom et al. (2007) to investigate and measure multiphase fluid contents in laboratory experiments. These techniques include photon-attenuation methods and photographic methods. Light transmission visualization (LTV) method is one of the photographic methods that was used previously by many researchers to observe NAPL migration in subsurface systems. Hoa (1981) was the first to develop LTV to quantitatively calculate water saturation in a flow chamber filled with sand. After that, few researchers (Tidwell and Glass, 1994; Darnault et al., 1998; Niemet and Selker, 2001; Bob et al., 2008; Zheng et al., 2015) also used LTV in their NAPL migration observation.

In this research, LTV technique was used in order to study the migration of both LNAPL and DNAPL in double-porosity soil under different conditions is the problem that this research aims to deal with.

1.2 Problem Statement

Petroleum compounds are commonly used in many industries and applications around the world. Petroleum releases from a multitude of sources have occurred at thousands of sites around the world which are usually the results of gas and oil exploration, refining operation, leakages from pipelines and underground storage tanks (EPA, 2009). NAPLs are reported as one of the most wide spread petroleum-based contaminants which pose a risk to the environment and human health (Soga et al., 2004). Movement of NAPLs is influenced by several factors when they release into the subsurface system such as fluid properties and soil characteristics (Ngien, 2012).

Of late, the term double-porosity in soil has been gaining more attention from researchers around the world (Alaoui et al., 2003; Lewandowska et al., 2008; Li and Zhang, 2009; Peng et al. 2015). After the knowledge that double-porosity occurs naturally in soil (Jongmans et al., 2003; Ghezzehei and Or, 2003), some researchers started to investigate the behavior of fluid flow in double-porosity soil medium (Lewandowska et al., 2005; Szymkiewicz et al., 2008). Double-porosity soil structure contains two distinct porosities which are known as macro-pores and micro-pores. When NAPL is released into the double-porosity soil, it will infiltrate and nearly saturate all of the pores that are located around the area of the NAPL leakage or spillage regardless of whether the pores are micro-pores or macro-pores before it migrates further away from the source (Ngien et al., 2012b). Image analysis technique has enabled the qualitative and quantitative observation of LNAPL migration in double-porosity soil.

Ngien et al. (2012b) applied the light reflection method (LRM) to observe the migration of LNAPL in double-porosity soil structure. However, their method needs calibration curves to correlate the LNAPL saturation and optical saturation, which is a complicated

process and requires much effort. Bob et al. (2008) used LTV for DNAPL saturation measurement in single-porosity media without the need for saturation calibration curves. They took into account both absorption and refraction light theories and could directly measure DNAPL saturation in a two-phase (DNAPL-water) system. They explained that a one-step calibration is needed when dyed DNAPL is used. The research conducted in this thesis incorporated the method by Bob et al. (2008) to quantitatively and qualitatively observe both LNAPL and DNAPL migration in double-porosity soil system under different conditions. There is currently still a gap in the open literature with respect to the application of LTV in monitoring NAPL migration in double-porosity soil.

In this research, the migration of both LNAPL and DNAPL has been investigated in double-porosity soil medium under different conditions such as the migration of NAPL in double-porosity soil medium in two-fluid phase system, the influence of rainfall recharge on NAPL migration in double-porosity and the migration of NAPLs in three-fluid phase system. Equations have been developed to calculate the NAPL saturation in double-porosity soil media, pixel by pixel. A quantitative analysis was performed for DNAPL migration in saturated double-porosity. However, for other cases, a qualitative analysis was conducted.

Therefore, a study using LTV method to observe the migration of NAPLs in double-porosity soil is provided towards a better understanding of immiscible contaminants migration in double-porosity soil.

1.3 Aim and Objectives of the Research

The main aim of this research is to investigate the migration of NAPLs in double-porosity soil using LTV technique combined with image analysis under different conditions. In order to achieve the aim, the following objectives have been identified and they are:

- i. To propose a new image analysis method based on the LTV technique for DNAPL migration in double-porosity soil.

- ii. To assess the migration of LNAPL and DNAPL in double-porosity soil structure based on multiphase fluid saturation analysis such as two-fluid phase system (NAPL-water) and three-fluid phase system (NAPL-water-air).
- iii. To evaluate the influence of rainfall recharge on LNAPL migration in double-porosity soil structure.
- iv. To correlate the movement of the DNAPL to the volumetric fraction of the two distinct scales of porosity (macro-pores and micro-pores) within the double-porosity soil.

1.4 Scope of the Research

The scope of the first objective includes the development of equations for DNAPL saturation measurements to come up with a set of derivations suitable for double-porosity soil. The concept of these equations was derived from previous work reported by Bob et al. (2008) where the equations were derived for two-fluid phase system. These equations were used later to calculate the DNAPL saturation, pixel by pixel in 2-D laboratory experiments.

In the second objective, a set of 2-D laboratory experiments that made use of a rectangular acrylic model that is 45 cm height \times 30 cm wide \times 1 cm long were carried out and divided into two main parts. The first part comprises the quantitative analysis of DNAPL migration in single and double-porosity soil media in two-fluids phase system. Pre-determined amounts of DNAPL were injected into the 2-D models and these amounts were calculated using image analysis. A correlation was performed between the injected amounts and the calculated amounts of DNAPL from image analysis. The second part comprises the qualitative analysis for LNAPL and DNAPL migration in double-porosity in three-fluid phase system. Toluene represented the LNAPL whereas tetrachloroethylene (PCE) was used as the DNAPL. Both LNAPL and DNAPL were dyed with Oil-Red-O to facilitate visual observation before being injected into the test samples. Image Pro-Premier 9.1 was used to extract the light intensity grey levels of the captured images as well as to carry out the different image processes.

Surfer 8 software (Golden Software, Inc.) was used to convert the values of light intensity to contour lines.

The third objective comprises a qualitative analysis of the influence of rainfall recharge on the distribution of different volumes of LNAPL in saturated double-porosity soil media using different rainfall intensities in 2-D laboratory experiments. For this purpose, a special experimental setup was arranged to simulate the light and heavy intensities of a rainfall event.

In the fourth objective, a quantitative analysis was conducted for DNAPL migration in 2-D laboratory experiments in a two-fluid phase system that was filled with two different volumetric fractions making up the double-porosity soil in order to investigate the effect of the different fractions of porosities. Double-porosity soil structure was created from a mixture of sintered clay spheres made of kaolin mixed with fine sand. The double-porosity characteristic was embodied by the micro-pores and macro-pores produced by compacting layers of clay spheres and fine sand in a periodic manner.

1.5 Significance of the Research

Infiltration of NAPL spills and leakage into the subsurface caused a serious groundwater pollution. NAPLs behavior is influenced by different factors when they release into the subsurface system such as fluid properties and soil characteristics. Double-porosity structure is one factor that can possibly affect the behavior of NAPL in the subsurface. This study attempts to investigate the behavior of NAPLs in double-porosity soil structure using LTV technique. This includes different conditions of NAPL such as; NAPL behavior in two-fluid phase system and three-fluid phase system. In addition, the NAPL behavior was studied under the influence of rainfall recharge in double-porosity soil medium.

This study will contribute to improve the knowledge towards the NAPL behavior in subsurface system especially in double-porosity soil structure. Moreover, the development of the new image analysis method to measure the NAPL saturation in

double-porosity, pixel by pixel, will open the door towards more research investigation especially in the numerical simulation part.

1.6 Outline of the Thesis

This thesis consists of five chapters where Chapter 2 forms the literature review for this research that covers a general overview on groundwater and NAPLs contamination as well as its migration in porous media. In addition, the factors that influence contaminant migration have been introduced. Double-porosity structure and related studies on double-porosity have been also discussed. An overview of the physics of light, wavelength regions and types of optical filters is introduced. The methodology of laboratory experiments based on different photographic methods such as light reflection, light transmission, and multispectral image analysis are discussed in detail. The discussion highlights the efforts of previous laboratory experiments that were conducted to observe NAPLs migration in different types of porous media.

Chapter 3 describes the materials selection and their characteristics, the experimental setup and procedures, as well as the image analysis procedures. The experiments were divided into four groups based on the objectives of the thesis. The derivation of equations that were used to calculate NAPL saturation in double-porosity soil structure and their application was introduced.

Chapter 4 shows the results for the characteristics of the materials used as well as the results from the laboratory experiments.

Finally, Chapter 5 summarizes all the findings from the conducted experiments for LNAPL and DNAPL and includes some recommendations for the possible future researches.

CHAPTER 2

LITERATURE REVIEW

2.1 Introduction

This chapter generally summarizes the definition of NAPL and its types as well as the definition of the double-porosity term and the experimental studies on double-porosity. The main factors that influence the migration of contaminant are also introduced. Furthermore, the importance of the image analysis techniques and their uses are identified. In addition, a review of previous studies on double-porosity soil media as well as the application of different types of photographic methods such as light reflection, light transmission, and multispectral image analysis is presented in this chapter. Some basic information on groundwater hydrology, groundwater contaminants, porosity in soil, light physics and image analysis techniques is presented prior to entering the main theme in this chapter. Figure 2.1 shows a content of the structure of literature review.

2.2 Groundwater Hydrology

Groundwater hydrology is the science that studies the occurrence, movement, and distribution of water under the surface of the land (Vicaire, 2015). It also considers the quality and quantity aspect of this water (Charbeneau, 2006). Generally, the groundwater term is related to the water below the surface of a land. Groundwater is a main component of the hydrological cycle. The water circulation on land occurs in the context of the hydrological cycle as shown in Figure 2.2. Groundwater is an important natural resource that provides a drinkable water source in a reliable and economic way for rural and urban environments (Foster et al., 2004).

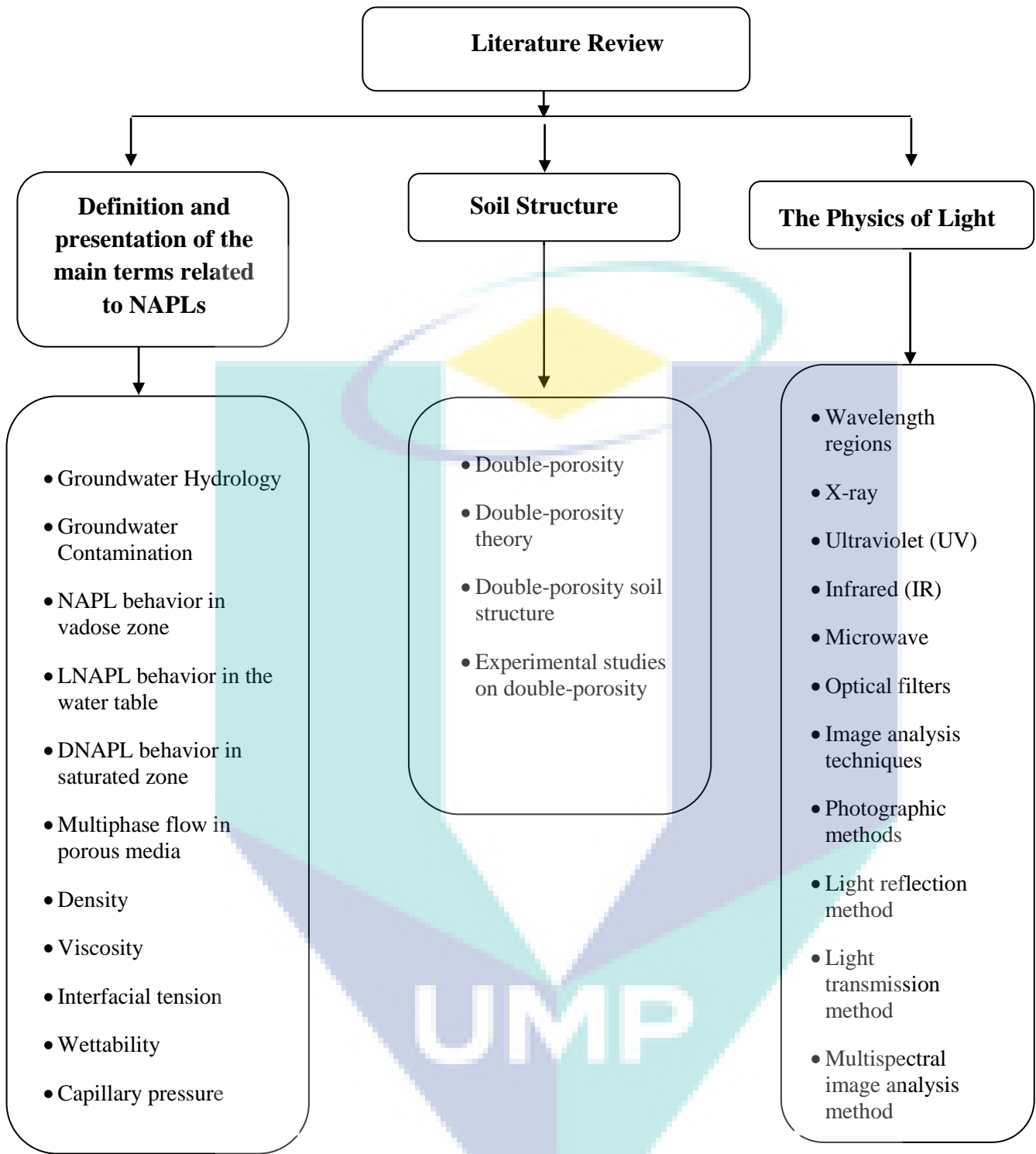
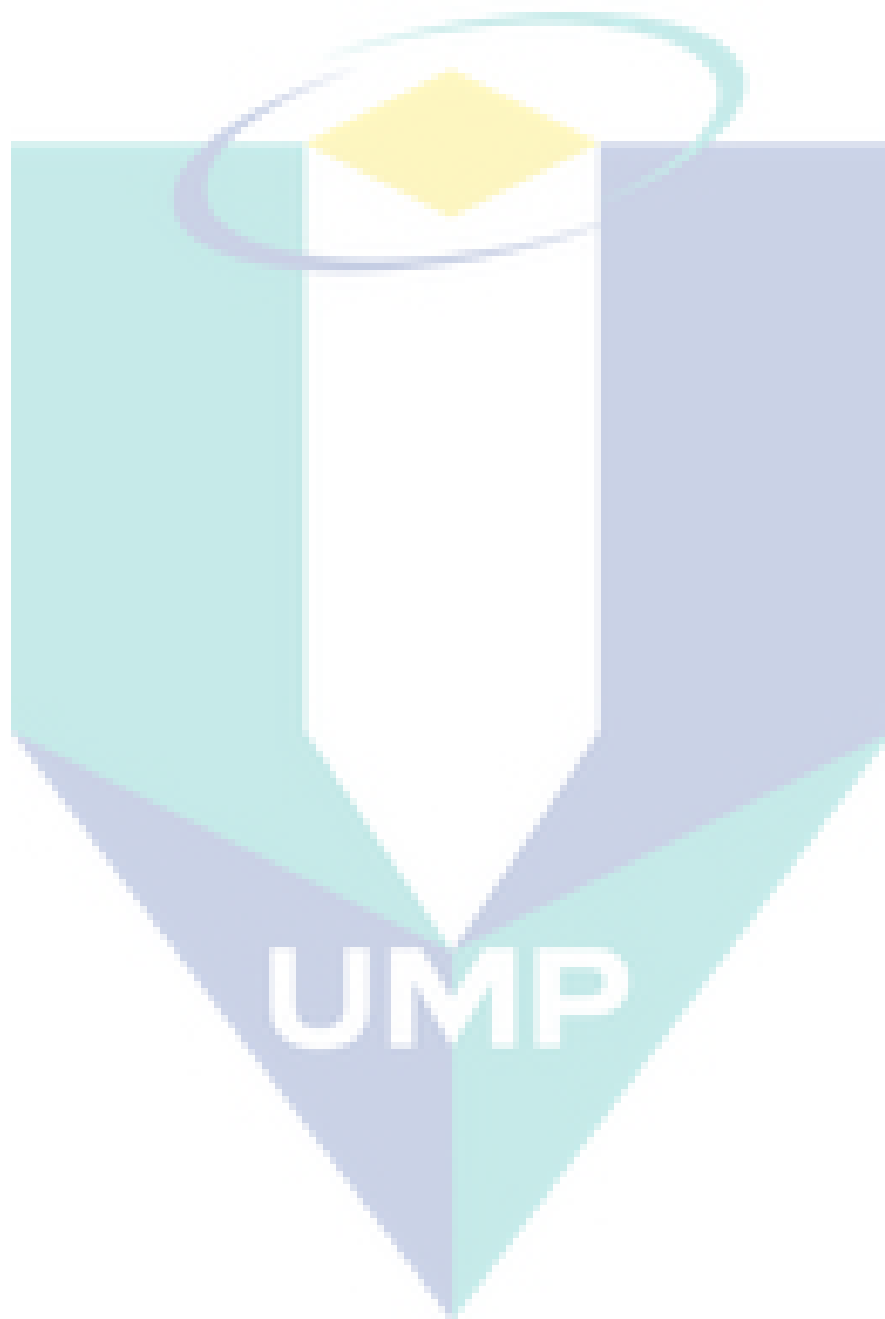


Figure 2.1 Content of the literature review

The largest portion of freshwater on earth is not found in lakes or rivers but is stored in aquifers (USGS, 2016). Groundwater occurs when a part of rain percolates downward through the soil while the remaining quantity evaporates or run off into surface water as rivers (Morris et al., 2003).



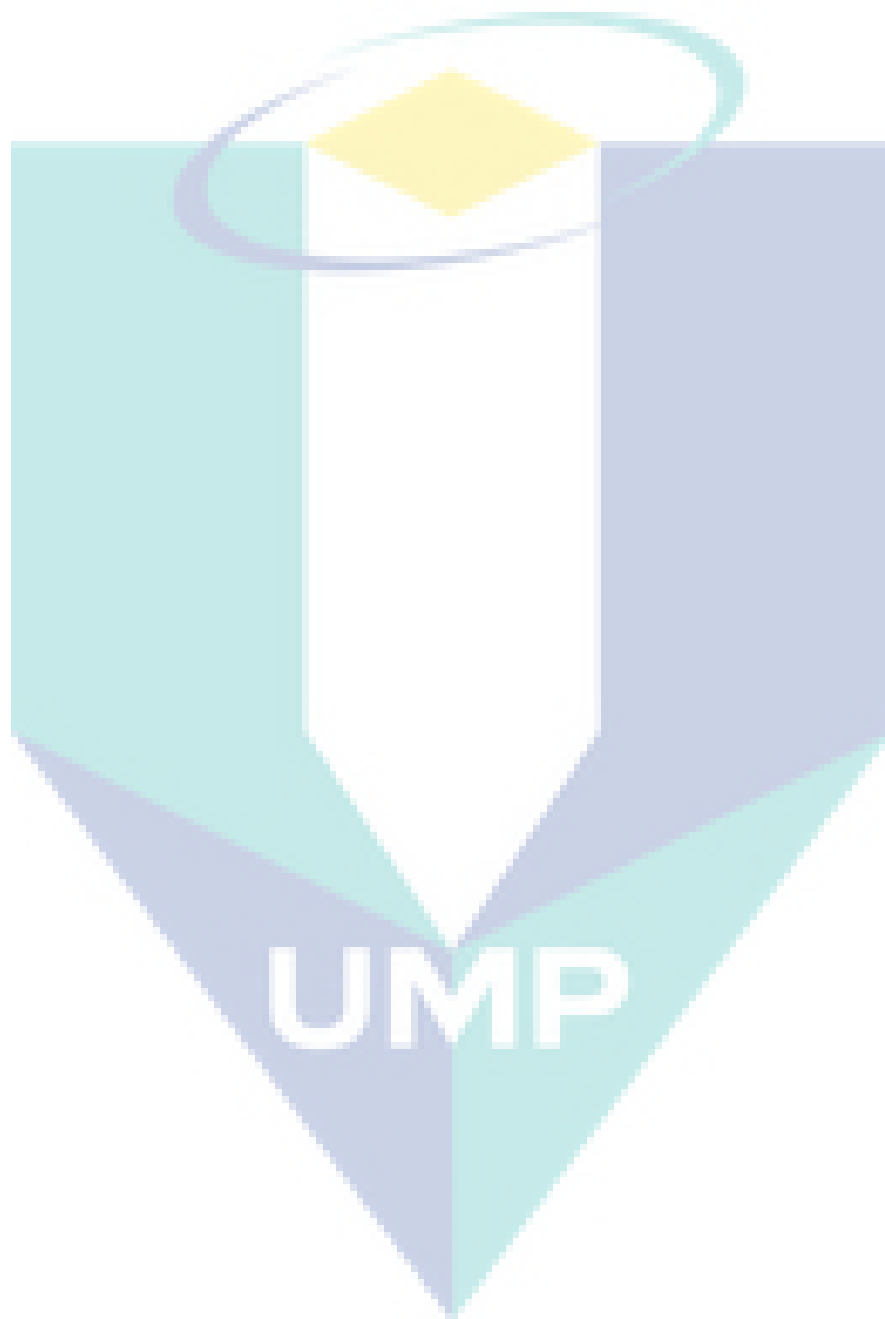


Table 2.1 Types of groundwater pollution and their sources

Source of pollution	Type of pollution
In-situ Sanitation	Nitrates; trace synthetic hydrocarbons; fecal organisms
Oil and Gas Exploration	Salinity (sodium chloride); aromatic hydrocarbons
Agricultural Works	Ammonium; nitrates; pesticides; fecal organisms
Sewage Sludge Disposal	Nitrates; various halogenated hydrocarbons; lead; zinc
Painting Works	Alkylbenzene; tetrachloroethylene; other halogenated hydrocarbons.
Pesticide Manufacture	Various halogenated hydrocarbons; phenols; arsenic
Dry Cleaning	Trichloroethylene; tetrachloroethylene
Disposal of Solid Waste	Salinity; ammonium; some halogenated hydrocarbons; heavy metals
Timber Industry	Pentachlorophenol; some aromatic hydrocarbons
Leather Tanneries	Chromium; various halogenated hydrocarbons; phenols
Gasoline Filling Stations	Benzene; phenols; other aromatic hydrocarbons

Source: Foster et al. (2004)

The sources of groundwater contaminants can be categorized based on three properties which are: their degree of localization, their loading history and the types of contaminants produced. The degree of localization depicts the type of source, whether it is a point source or a non-point source (Domenico and Schwartz, 1990). According to Deviny et al. (1990), the point sources include both direct and indirect disposal of hazardous material while the non-point sources include a wide range of definitions such as agricultural operation and mining activities. The loading history describes whether the source of contaminant is continuous or instantaneous. Example of an instantaneous source is the spillage from the accident of an oil tanker while the leakage from underground storage tanks is considered as a continuous source. Morris et al. (2003) grouped the types of contaminants produced into seven groups. These groups are radioactive, inorganic, pathogenic, trace metals, nutrients, organic and acidic contaminants.

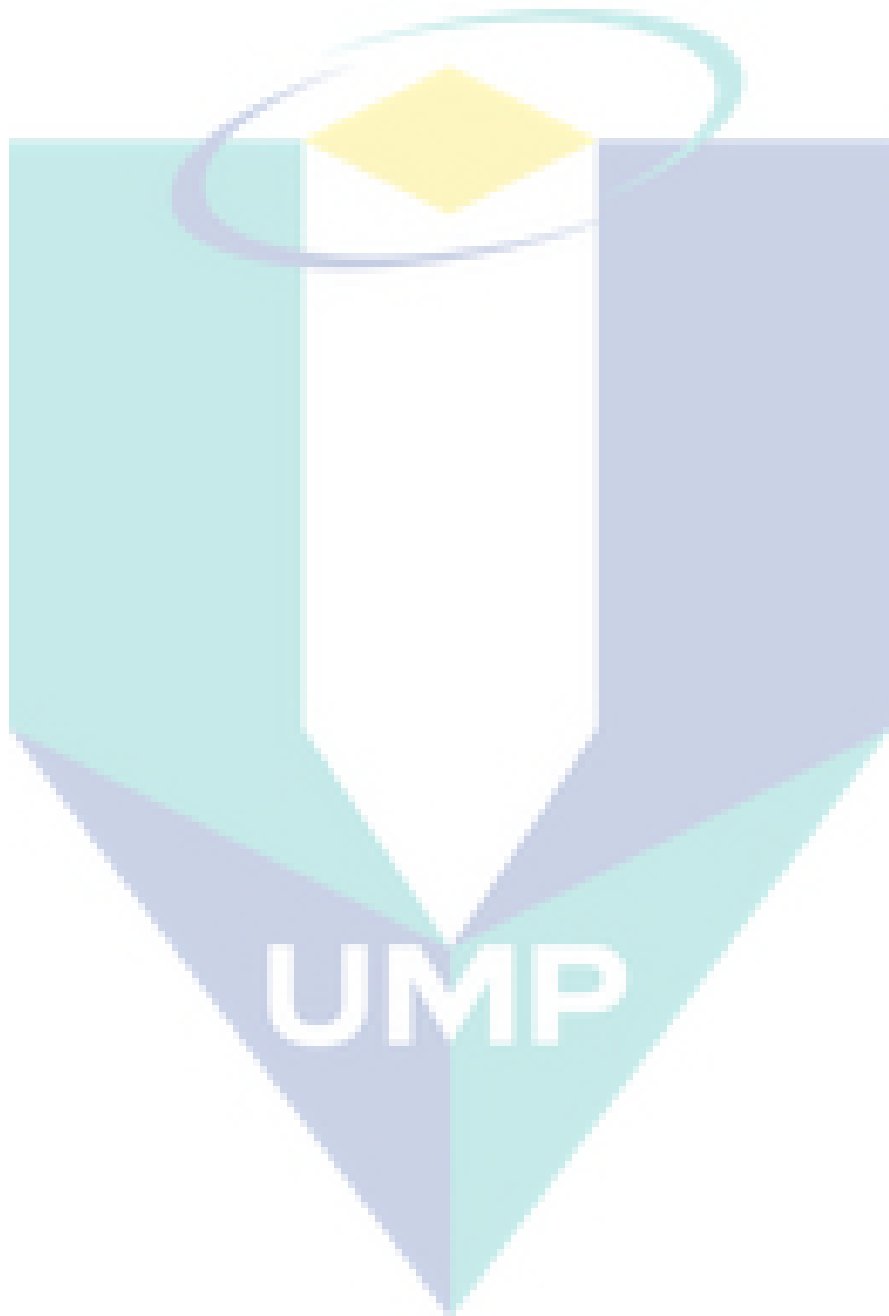
One of the major health risks to humans occurring in groundwater is posed by organic compounds (Bedient et al., 1999). These compounds may partition into four phases in the subsurface: the aqueous phase, gaseous phase, solid and NAPL (Newell et al., 1995). As the subject of this study focuses only on NAPL, it will be discussed in section 2.4 while the rest of the pollutant types will not be further elaborated.

2.4 Non-Aqueous Phase Liquids (NAPLs)

NAPLs are organic and immiscible compounds (Parker et al., 1994) with low solubility in water that are often found at contaminated sites and causes serious problems that are very difficult to remediate (Kechavarzi et al., 2005). The differences in the chemical and physical characteristics of NAPL and water result in the occurrence of a physical interface between these fluids which do not permit the two liquids from mixing (Newell et al., 1995). Different classes of NAPL and their fate in the subsurface are described in Figure 2.4. When a NAPL is released in the subsurface, the volatile part of the NAPL known as volatile organic compounds (VOCs) will evaporate into the vadose zone and into the atmosphere (Rivett et al., 2011). The VOCs may also contaminate the groundwater where billions of dollars have been spent to investigate their behavior as well as for remediation since the 1970s (Pankow and Cherry, 1996; Rivett et al., 2005; Rowe et al., 2007).

On the other hand, the liquid fraction of the NAPL will move either below or above the water table based on its density. LNAPL will enter the unsaturated zone and float on the top of the groundwater (Totsche et al., 2003), while the heavier DNAPL will penetrate the water table and continue its migration until it reaches the saturated zone and finally settle and collect on an impermeable stratum (Testa and Winegardner, 2000).

Surface spills and leakage of NAPLs associated with human activities are significant sources of groundwater contamination. Petroleum hydrocarbons are common LNAPLs that are introduced into the subsurface from leaking underground tanks and pipes (Illangasekare and Frippiat, 2012). Examples of LNAPLs are benzene, toluene, ethylbenzene, and xylene (BTEX), all with densities less than that of water. DNAPLs, including chlorinated hydrocarbons such as trichloroethylene (TCE) and tetrachloroethylene (PCE), have densities greater than that of water (Newell et al. 1995). The main sources of DNAPL are timber treating oils, coal tar and polychlorinated biphenyls (PCBs) (Kueper et al., 2003). These DNAPLs will act as a long-term pollution source which represents an unacceptable hazard to groundwater as well as human health (Yang et al., 2012).



2.4.1 Movement of NAPL in the Vadose Zone

When NAPL is released into the subsurface, it will first enter the vadose zone which is considered as the first line of defense for groundwater sources against the pollutants released from the ground surface (Li et al., 2000). In this zone, the NAPL acts as a source of vapor that intrudes into the structures of the subsurface (Illangasekare and Frippiat, 2012). NAPLs enter the unsaturated zone as a discrete liquid phase and move downward due to gravity and capillary forces (Pennell et al., 1993). Generally, in this zone, NAPLs are considered as the wetting fluid with respect to air (Bedient et al., 1999). Several properties such as viscosity, density, immiscibility, interfacial tension, saturation, wettability, residual saturation, capillary pressure, and gravity will affect the migration of NAPL in the unsaturated zone (Testa and Winegardner, 2000). These properties in addition to the non-linear soil properties result in the complex mechanisms of the flow and transport of NAPL in the vadose zone compared to the saturated zone (Bedient et al., 1999). Furthermore, the migration of NAPL in the subsurface is affected by other factors such as the volume of NAPL released, infiltration area, release time, properties of the media and the conditions of the subsurface flow (Mercer and Cohen, 1990).

For better understanding and modeling of multiphase fluid systems, it is crucial to identify the characteristics and the behavior of each phase. In a multiphase system, NAPL is released into the unsaturated zone and will enter the pore level when sufficient pressure occurs to push the NAPL into the throat of the pore and displace water, air or both which existed in the pore (Ngien, 2012).

2.4.2 LNAPL Behaviour at the Groundwater Table

Upon the release of LNAPL into the subsurface, it will migrate downward under the influence of gravity until it reaches the water table. LNAPL will migrate through the capillary fringe before it reaches the water table (Newell et al., 1995). The capillary fringe is a transition zone that separates two zones in the subsurface system (Lehmann et al., 1998). The first zone is the vadose zone where the NAPL is a partially wetting fluid, whereas the second system is the saturated zone where the NAPL is a non-wetting fluid (Bedient et al., 1999).

When the LNAPL enters the capillary fringe, the pores unoccupied by water will be filled with LNAPL but as a high proportion of the pores are already occupied by water, the LNAPL's relative permeability declines and a small proportion of LNAPL may start to spread laterally along the capillary fringe (Mercer and Cohen, 1990). When LNAPL penetrates the capillary fringe and reaches the water table, it will float on the surface of the groundwater because the density of the LNAPL is less than that of water (Corapcioglu et al., 1996). Fluctuations in the water table elevation such as the changes in the recharge or discharge in the coastal environment or tidal influence may cause LNAPL smearing at or near the water table (Newell et al., 1995). Moreover, LNAPL will redistribute itself in the subsurface due to the water table fluctuations (Sharma and Mohamed, 2003). In the case of a big volume of LNAPL or rapid release of the LNAPL, the capillary fringe at the contact point may collapse and the possibility of water table decreasing may be high (Domenico and Schwartz, 1990).

2.4.3 DNAPL Movement in the Saturated Zone

In such cases, a two-fluid phase system containing water and NAPL will occur in the saturated zone, while in the unsaturated zone it will be a three-fluid phase system containing water, air, and NAPL. When the DNAPL reaches the water table, it will float on the water table for a short while. DNAPL will penetrate the water table and displace the water from the fully saturated pores and continue its downward migration (Newell et al., 1995). This behavior is due to the combination of the pressure forces from the DNAPL volume and density which results in sufficient driving force that overcomes the entry pressure in the pores fully saturated with water (Bedient et al., 1999). The DNAPL will spread according to the topography of the lower impermeable layer. The spreading will stop when either the original source of DNAPL is exhausted (Domenico and Schwartz, 1990) or a low permeable formation stop it where it after that start to migrate laterally (Huling and Weaver, 1991).

2.4.4 NAPL Pollution in Malaysia

Malaysia has been experiencing rapid industrial development accompanied by greater pollution load especially from petroleum hydrocarbon due to its wide usage as an energy source (Sakari et al., 2008). NAPL pollution in Malaysia has been identified as one of the main factor causing the occurrence of brownfield sites as well as contaminated groundwater (Ong, 2006). Such contaminated lands are commonly found around motor workshops, petrol stations, but depots, landfills and industrial sites. (Rahman) 2008 has stated that in Malaysia, underground storage tanks as well as pipelines are prone to leakages due to aging and installation defects.

An example of groundwater pollution by NAPL that happened in Malaysia was highlighted by Tan (2004). The incident occurred in a village in Kelantan where people noticed the faint taste of oil in the water from the well which the people use for their daily water needs. The source of the oil was traced to a nearby petrol station with leaking underground storage tanks. Petrol from the leakage had seeped into groundwater bodies that fed the village wells. Another incident of NAPL pollution in Malaysia transpired in 2001 at Petaling Jaya where a leak in the underground piping of a petrol station caused petrol to seep 80 m into the drains and classroom floors of a nearby school (Tan,2004). These two examples of NAPL pollution are only a part of a few cases that were reported. Many contaminated sites remain hidded or unkown in Malaysia (Lee et al., 2011). Therefore, an understanding of the mechanisms of NAPL pollutant transport in the subsurface is very important in the effort to grasp and tackle NAPL pollution.

2.4.5 Multiphase Flow in Porous Media

During the past few decades, several studies have been conducted on the different aspects of multiphase flow systems (Bob et al., 2008; Ngien e al., 2012; Zheng et al., 2015). A detailed review study on NAPL behavior in the subsurface has been presented by Mercer and Cohen (1990). The authors reported that the NAPL's behavior is different compared to the dissolved solutes in the subsurface system. This difference is due to fluid properties such as density, viscosity, interfacial tension, wettability and capillary pressure (Ngien et al. 2012). The next subsections present the definition for each of these terms.

2.4.5.1 Fluid density

Density is defined as the mass per volume of a substance. The NAPL density has an important impact on gravity flow forces where it determines whether the NAPL will float or sink when it reaches the water table (Mercer and Cohen, 1990). NAPLs that have a density lighter than water (LNAPLs) can usually float on the water table. However, NAPLs with a density higher than water (DNAPLs) sink in the saturated zone.

2.4.5.2 Viscosity

Viscosity is defined as the internal friction of fluid to resist a flow. The viscosity of fluid is influenced by temperature where the viscosity reduces for most fluids as temperature increases (Franco and Nguyen, 2011). It is known that fluids with lower viscosities move more rapidly into porous media than fluids with high viscosity (Wang et al., 2014).

2.4.5.3 Interfacial tension

When two different immiscible fluids exist in a porous media, at the boundary between these fluids there exists a type of skin emerging due to the adhesion influences between the different phases as well as the difference in the molecular cohesion within a phase (Schlumberger, 2017). Interfacial tension is considered as a measure of this difference and affects the multiphase flow due to its direct influence on the capillary pressure within the immiscible fluid interface (Al-Gharbi, 2004).

2.4.5.4 Wettability

Wettability is a property that depends on the interfacial tension and defined as a description of the preferential spreading of a fluid (liquid or gas) onto a solid surface (Abdallah et al., 2007). The wetting fluid is usually spread over the grains of the porous media in preference to the non-wetting fluid. The smaller voids of the porous media will be occupied by the wetting fluid, while the larger pores will be occupied by the non-wetting fluid (Mercer and Cohen, 1990). The contact angle at a fluid-solid interface is a measure of wettability. Young's equation (Yuan and Lee, 2013) is used to describe the contact angle of the interface for two fluids such as NAPL and water as follow:

$$\cos \phi = \frac{\sigma_{NS} - \sigma_{WS}}{\sigma_{NW}} \quad 2.1$$

where σ_{NS} is the interfacial tension between NAPL (N) and solid (S), σ_{WS} is the interfacial tension between water (W) and solid and σ_{NW} is the interfacial tension between the NAPL and water while ϕ is the contact angle (in degrees) measured into the water.

2.4.5.5 Capillary pressure

Capillary pressure is defined as the difference in the internal pressure between the interface of the wetting fluid and non-wetting fluid phases in porous media (Falode and Manuel, 2014). Capillary pressure is an important factor in multiphase flow since it causes the porous media to draw in the wetting fluid and push out the non-wetting fluid from the smaller pore spaces and in turn influences the shape of the NAPL spillage in the saturated and unsaturated zone (Mercer and Cohen, 1990). Capillary pressure depends on many factors such as wettability, interfacial tension and the pore size distribution of the porous media:

$$P_{CNW} = \frac{2\sigma_{NW} \cos \phi}{r} \quad 2.2$$

where P_{CNW} is the capillary pressure between NAPL and water, σ_{NW} is the interfacial tension between the NAPL and water while ϕ is the contact angle and r is the radius of the pore that non-wetting fluid enters.

2.5 Soil Structure

Soil structure is an important factor in ecological systems, as it controls the storage and transport of different fluids such as gas, air, solutions and nutrients (Chun et al., 2011). The porosity of soil characterizes its pore space which presents the unoccupied volume by solid material. The basic property of the pore space influences and is influenced by critical aspects of everything that occurs in the soil such as movement of fluids including water, gas and air, transport of chemicals and residence

of roots (Chun et al., 2011). In the natural state, many types of soils have two distinct scales of porosity which explains the term of double-porosity soil structure (Carminati et al., 2008) which is one of the main elements in this research. The following subsections present an overview of the definition of double-porosity and the occurrence of double-porosity in soil as well as the most recent experimental studies on double-porosity soil structure.

2.5.1 The Double-Porosity History

Double-porosity is a natural phenomenon that can be found in many types of subsurface media due to different factors such as the aggregated nature of soil, the presence of fissures, root channels and worm holes (Russell, 2010). It is considered as the most substantial characteristic of micro-structure in a wide range of geomaterials (Tran Ngoc et al., 2014). The concept of double-porosity surfaced soon after the rise of petroleum industry in 1859 after the drilling of the first oil well named the Drake Discovery Well in Pennsylvania, North America (Black, 1998). The idea of fractured porosity was first introduced by Andrews (1861). He assumed that there is a direct relation between the amount of the extracted oil and the number of fissures in rock oil aquifers. A century later, Barenblatt et al. (1960) enunciated the concept of double-porosity based on the technique of overlapping continuum. They applied the continuum approach to conduct flow equations formulation for a rigid, double-porosity fractured reservoir. They used blocks separated from each other by a special system of fissures to establish the model and the two continuums were considered as overlapping.

Subsequently, the concept was adopted by Warren and Root (1963) when they applied it in the field of petroleum engineering. After the works of Barenblatt et al. (1960) and Warren and Root (1963), several researchers have attempted to further develop the concept of double-porosity and come up with different models to simulate the production and recovery of oil in fractured reservoir (Bai et al., 1996; Tran Ngoc et al., 2011) .

Two types of porosity form the double-porosity structure. The first one is the macropores (inter-aggregate, fractures or fissures) which are associated with high permeability and high hydraulic conductivity, and the other one with low hydraulic

conductivity is the micro-pores (intra-aggregate, porous matrix) (Lewandowska et al., 2008). This fracture porosity is the result of fissures, cracks, joints and faults that may be present in the formation (Berkowitz, 2002). Fractures present the paths of least resistance for contaminant transport (Bai et al., 1996). The total of the macro-pores and micro-pores is equal to the double-porosity (Tran Ngoc et al., 2014).

2.5.2 Experimental Studies on Double-Porosity Soil

In this section, a list of experimental studies on double-porosity soil is reviewed and summarized to investigate the influence of double-porosity on fluid migration. These studies are summarized to provide interesting insights on double-porosity in soil.

An experimental study was carried out by Coppola (2000) to investigate the water retention data for aggregated clay and examine the capacities of different approaches to conduct prediction for water retention curves. His results showed that in soils that consist of two pore systems, a bimodal approach that allowed for porous medium partitioning into macro-pores and micro-pores gave a better depiction of the retention data as compared to unimodal approaches that were investigated.

Šimůnek et al. (2001) conducted experiments to investigate the infiltration and evaporation for undisturbed aggregated soil samples to explain the presence of non-equilibrium water flow. They found that a redistribution of fluid occurred where the fluid slowly migrated from the larger macro-pores to the smaller micro-pores.

A significant research by Lewandowska et al. (2005) showed that the creation of double-porosity structure is possible in laboratory. Therefore, researches in the field of double-porosity soil structures have gained more attention after this discovery. Lewandowska et al. (2005) conducted a series of 1-D infiltration experiments in double-porosity soil medium. To create the double-porosity soil structure, a mixture of sintered clay spheres with small pore size and uniformly distributed sand which has larger pore sizes was arranged in a periodic manner. The difference in pore sizes produced marked differences in hydraulic characteristics, hence the double-porosity

feature. The double-porosity medium was unsaturated and under constant pressure head. The observation showed that a very reasonable quantitative and qualitative agreement between simulations and experimental results was obtained.

Subsequently, a set of drainage experiments for the double-porosity structure was performed by Lewandowska et al. (2008) using the same materials to create the double-porosity. The same set of drainage tests were conducted for homogeneous sand. They compared the results between the two media and found that there is a contribution from the micro-porosity in the sintered clay spheres to water retention as well as flux retardation in the soil.

The works of Lewandowska et al. (2005, 2008) was further developed by Szymkiewicz et al. (2008) using the same materials for double-porosity creation but in a two-dimensional acrylic box instead of columns. The procedure of the experiment was the same as described by Lewandowska et al. (2005). The main goal of the experiment was to conduct a numerical model validation produced by the same authors. The results showed a good agreement between the data observed and the infiltration data produced from the numerical model.

Bagherieh et al. (2009) carried out a series of one-dimensional drying and consolidation experiments on double-porosity structure represented by aggregated kaolin samples. They created the double-porosity structure by mixing dried powdered kaolin with a sufficient amount of water to achieve a water content of 25 % before placing the mixture in a sealed plastic bag for 24 hours. After that, the kaolin mixture was broken by hand and passed through a 2.36 mm sieve to get kaolin granules. After that, a prescribed amount of granules was placed in a stainless steel mold and compressed to 19 mm height and dry unit weight of 12 kN/m^3 . From findings, they found that the response of aggregated soil can approach that of a non-aggregated soil in terms of water retention and compressibility when a certain vertical effective stress is applied. Furthermore, it was found that the changes in aggregated material volume can be predicted using the effective stress principle. In addition, the experiments showed that suction hardening may not be occurring in all unsaturated soils.

In the same year, a research by Li and Zhang (2009) studied the formation of double-porosity in compacted granitic, decomposed soil samples, and also the development of the micro-porosity structure in the samples during the wetting-drying process. They used dry soil samples with various void ratios to study the composition of micro-porosity structure as a result of sample compaction. Also, saturated soil samples were used to assess the micro-porosity structure variation after sample saturation and during the drying process. The formation of macro-pores and micro-pores occurred when the soil samples were under compaction. It was found that under applied stress, the macro-pores were very compressible. During compaction, changes in macro-pores were dominant, while during saturation and drying, changes in micro-pores were dominant. They also reported that it is easy to predict the pore size distribution at any void ratio.

Tran Ngoc et al. (2011) modeled the fluid migration in double-porosity soil medium using the same method as Lewandowska et al. (2008, 2005). The fluid was a salt solution and the experimental setup was identical to that used by Lewandowska et al. (2005, 2008). The sole difference in their study was dividing the columns into two steps. The first step was imposing a constant flow from the bottom of the column to establish unsaturated water flow. The other step was using the salt to displace the water. The results from the series of 1-D laboratory experiments were used for calibration and validation of a theoretical model that was also developed by Tran Ngoc et al. (2011).

All the previous studies mentioned in this section presented insightful knowledge on the behavior of double-porosity, but the common issue is that the fluid used in the experiments was limited to water.

A significant study by Ngien et al. (2012b) was conducted as the first study to investigate the behavior of LNAPL in double-porosity soil in 1-D circular columns using image analysis technique based on the light reflection method. In their study, two experiments were carried out using acrylic circular columns, and the sole difference between the two experiments was the size of the soil columns. The columns were made of an acrylic material to provide an obvious view of the soil within. From the observation, they found that during the first 10 seconds of the experiment, the migration of the LNAPL was very fast, and then after 10 seconds, the downward migration was

gradually slowing. This behavior could be due to the pressure exerted by the collection of the LNAPL above the aggregated sample which had to percolate into the sample surface. The authors compared these results with results obtained by another study conducted by Alias (2003), who investigated the migration of LNAPL in a poorly graded sand. One liter of LNAPL was poured into a soil column made from the same material and with the same diameter as the one used in Ngien et al. (2012). From the Alias (2003) results, the average speed was much lower than the average speed of LNAPL migration obtained from the Ngien et al. (2012) experiments. The authors reported that the type of medium is the major difference between their study and the Alias (2003) study. Hence, it can be summarized that the main reason for the difference in LNAPL flow speed and depth is the type of the soil medium.

Tran Ngoc et al. (2014) conducted a series of NaCl dispersion experiments in two water flow conditions, saturated and unsaturated steady state, in the double-porosity physical model. They conducted the same experiments for single-porosity soil for comparison purpose. To create double-porosity soil, they used the same materials by Lewandowska et al. (2005, 2008) and Tran Ngoc et al. (2011). In the double-porosity soil experiments, the results can be used for validation purposes for different theoretical models on double-porosity media that were proposed in the literature or for new media.

After one year, a study by Sa'ari et al. (2015) was carried out to investigate the LNAPL migration in double-porosity using different moisture contents and followed the method used by Ngien et al. (2012b) to create the double-porosity. Two experiments with two different moisture contents were conducted. The water content of 25% and 33% were used for kaolin in Experiments 1 and 2, respectively. The LNAPL pouring technique was different in both experiments. This difference influenced the behavior of the LNAPL as shown in the results. The observation showed that the speed of LNAPL migration in the second experiment was faster than that of the first experiment. The authors explained that this behavior was because of the higher water content and uneven compaction for the soil sample in the second experiment. In addition, it was observed that the maximum water content in double-porosity kaolin was 35%. The kaolin will be crushed after this percentage.

Subsequently, Peng et al. (2015) conducted three-dimensional (3-D) experiments for water flow in a double-porosity medium consisting of sand and sintered clay spheres using computed tomography (CT). The findings showed that water infiltration into the clay spheres was negligible at the observed time scale. They measured and found that the time required for water transfer into the clay spheres was larger than the infiltration experiment time. The authors managed to monitor the water front displacement using CT imaging via a new image analysis method and they measured water distribution in two and three dimensions. They concluded that their experimental setup still needed more enhancements for reasons such as the insufficiency of spatial resolution to investigate processes at the pore scale between sand particles and inside clay spheres.

Table 2.2 summarizes several experimental studies that were conducted on double-porosity soil media and shows the difference between the previous studies and the current study.

Table 2.2 Comparison of current study with previous studies in double-porosity

Author	Medium	Measurements	Dimensions
Coppola (2000)	Aggregated clay	Water retention	1 D
Simunek et al. (2001)	Aggregated clay	Water infiltration and evaporation	1 D
Alaoui et al. (2003)	Silty sand	Water infiltration	1 D
Lewandowska et al. (2005)	Clay and sand	Water infiltration	1 D
Lewandowska et al. (2008)	Clay and sand	Water drainage	1 D
Szymkiewicz et al. (2008)	Clay and sand	Water drainage	2 D
Bagherieh et al. (2009)	Aggregated clay	Water drainage	1 D
Li and Zhang (2009)	Granitic soil	Double-porosity formation	-
Tran Ngoc et al. (2011)	Clay and sand	Salt solution	1 D
Ngien et al. (2012b)	Aggregated clay	LNAPL migration	1D
Tran Ngoc et al. (2014)	Clay and sand	NaCl dispersion	1 D
Sa'ari et al. (2015)	Aggregated clay	LNAPL migration	1 D
Peng et al. (2015)	Clay and sand	Water flow	3 D
Present study	Sintered kaolin spheres and silica sand	LNAPL and DNAPL migration	2 D

In 1-D, fluid flow is parallel to some straight line and the characteristics of flow do not change in moving perpendicular to this line. However, in 2-D, the fluid flow velocity at

every point is parallel to a fixed plane. The velocity at any point should be constant (Horritt and Bates, 2002).

2.6 The Physics of Light

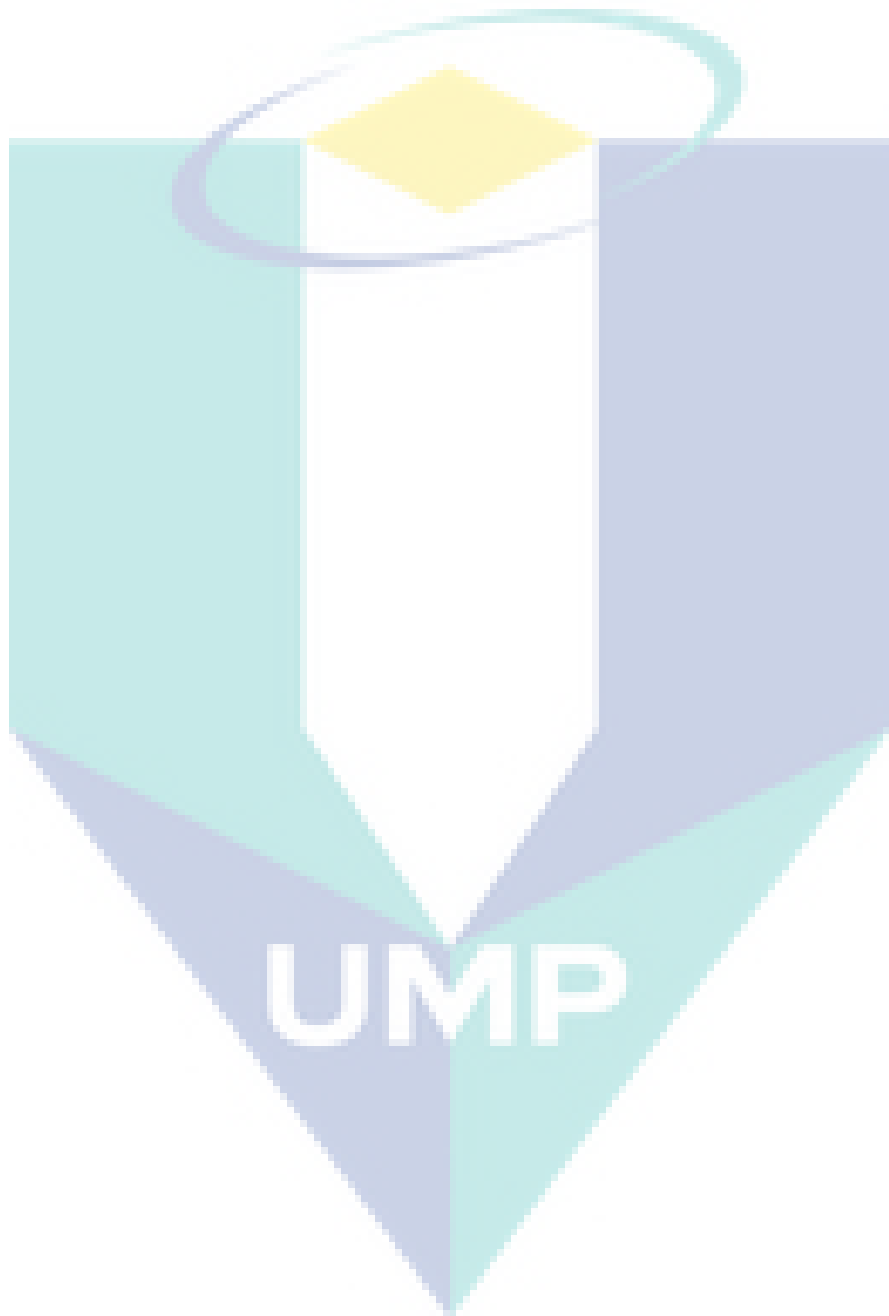
Electromagnetic radiation spread in space as electrical and magnetic energy. Light is one portion of the different electromagnetic waves existing in space. The electromagnetic spectrum covers a wide range of wavelengths, from radio waves with large wavelengths of a meter or more to x-rays with small wavelengths of less than a billion of a meter. Optical radiation exists between radio waves and x-ray waves, displaying a mix of waves, rays and quantum properties (Ryer, 1998). Figure 2.5 depicts the optical portion of the electromagnetic spectrum.

Table 2.3 Wavelength regions

Wavelength Region		Wavelength	Frequency	
Gamma Rays		$< 1 \times 10^{-11}$ (m)	$< 3 \times 10^9$ (Hz)	
X-Rays		$1 \times 10^{-11} - 1 \times 10^{-8}$ (m)	$3 \times 10^{16} - 3 \times 10^{19}$ (Hz)	
Ultraviolet		100 ~ 400 (nm)	750 ~ 3000 (THz)	
UVA		315 ~ 400 (nm)	750 ~ 3000 (THz)	
UVB		280 ~ 315 (nm)	750 ~ 3000 (THz)	
UVC		100 ~ 280 (nm)	750 ~ 3000 (THz)	
Visible		0.4 ~ 0.7 (μm)	430 ~ 750 (THz)	
Near Infrared		0.7 ~ 1.3 (μm)	240 ~ 430 (THz)	
Infrared	Reflected IR	Shortwave Infrared	1.3 ~ 3.0 (μm)	100 ~ 230 (THz)
		Intermediate Infrared	3 ~ 8 (μm)	38 ~ 100 (THz)
	Thermal IR	Thermal Infrared	8 ~ 14 (μm)	22 ~ 38 (THz)
		Far Infrared	14 μm ~ 1 mm	0.3 ~ 22 (THz)
Radio Wave	Micro-wave	Millimetre	1 ~ 10 (mm)	30 ~ 300 (GHz)
		Centimetre	1 ~ 10 (cm)	3 ~ 30 (GHz)
		Decimetre	0.1 ~ 1 (m)	0.3 ~ 3 (GHz)
	Very Short Wave	1 ~ 10 (m)	30 ~ 300 (MHz)	

Source: Wade (2012)

In the case of short wavelengths (i.e x-ray and gamma-ray), the electromagnetic radiation tends to be quite particle-like in its behavior. However, in the case of a long wavelength, its behavior is mostly wave-like. The visible light portion occupies an intermediate position, presenting both particle and wave characteristics in varying



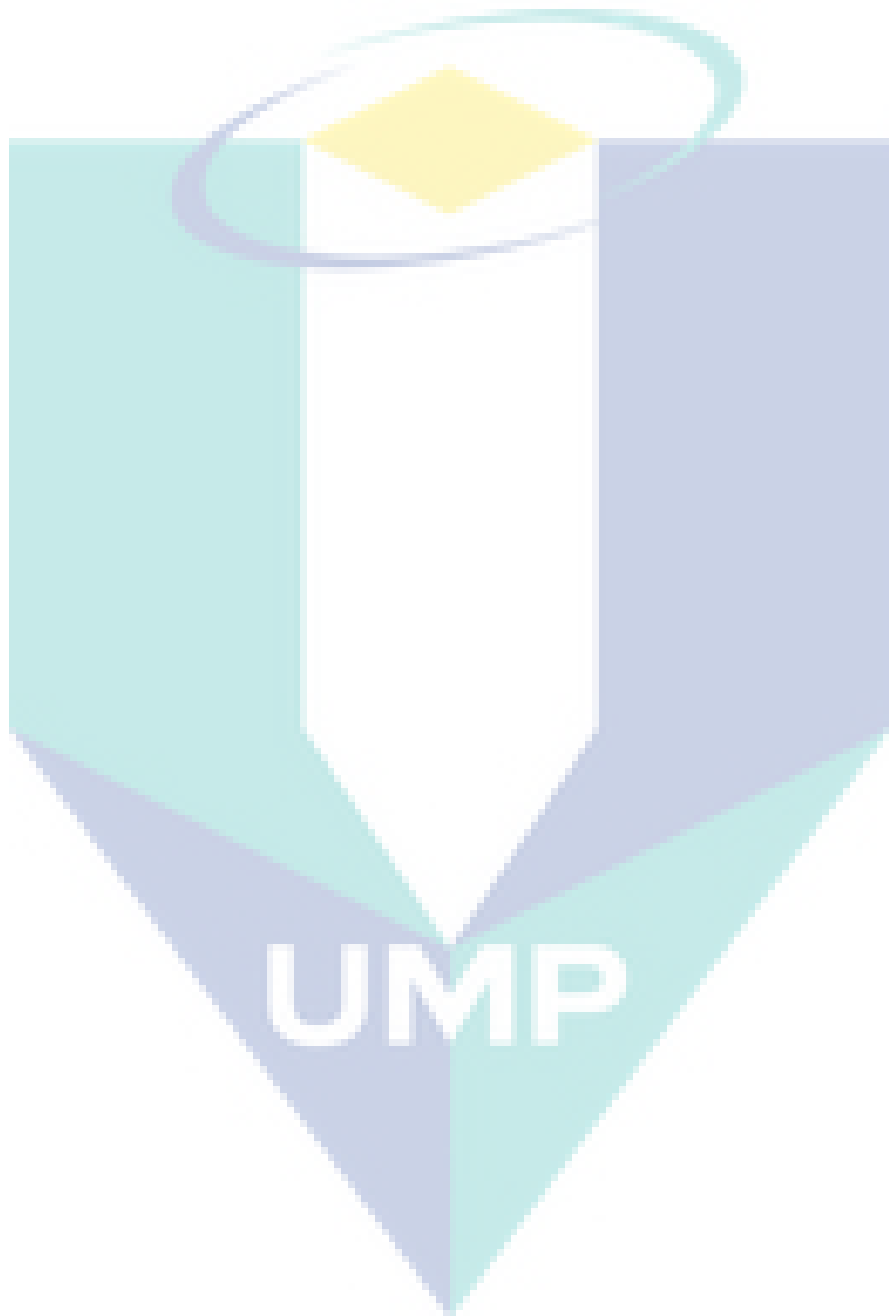
refraction can be negligible due to its velocity which varies much less in the different materials compared to visible light. It can be generated using an X-ray tube which consists of two electrodes, the first being negative (cathode) and the other positive (anode) (Carlsoon and Carlsoon, 1996).

2.6.1.2 Ultraviolet light (UV)

Ultraviolet radiation (UV) is similar to visible light in all physical aspects. However, it is unable to be seen by human eyes (CCOHS, 2016). Its radiation covers the wavelength region from 100 nm to 400 nm and it is subdivided into three regions (CCOHS, 2016). The division of UV radiation into different spectrums was put forward at the Second International Congress on Light in 1932 (Diffey, 2002). The congress recommended that the three spectral regions can be defined as UVA 400-315 nm, UVB 315-280 nm, and UVC 280-100 nm. Another subdivision was recommended by environmental and dermatological photo-biologists as (Diffey, 2002): UVA 400-320 nm, UVB 320-290 nm, and UVC 290-200 nm. UV radiation can be produced using two methods; the first method is heating a body to a high temperature like the case of solar UV, whereas the second method is passing an electric current through a gas (usually vaporized mercury) (Diffey, 2002). UVA has the least energy which leads to the least harm compared to the other two divisions. It is often called black light and is used due to its relative harmlessness. Most tanning booths and phototherapy use UVA lamps in their applications. On the other hand, UVB has more energy that can damage biological tissues and is considered as the most destructive form of UV light. UVB is dangerous and is known to cause skin cancer. The case of UVC is different since UVC is completely absorbed in the air, so it is invisible in nature (Ryer, 1998).

2.6.1.3 Visible Light

Visible light is a portion of light that with wavelengths that are visible to human eyes. It is located between the infrared (IR) regions and UV regions (Live Science, 2017). The wavelength range of the visible light is located between 400 - 700 (nm) and the color range from violet through red. The human eyes cannot see any other radiation with wavelengths that are located outside the visible range (Wade, 2012). Different visible colors are located in the visible light region and they can be defined based on the



2.6.1.5 Microwaves

Microwaves (MW) are considered as a non-ionizing radiation that has not enough energy for ions and molecules ionization under normal conditions (Yakymenko et al., 2011). MW cover a part of the radio-frequency range and have a range of frequency from 300 MHz to 300 GHz. As shown in Figure 2.7, MW have long wavelengths and less energy compared to UV, visible, and IR regions. Recently, it was reported that long-term exposure to low-intensity MW is carcinogenic (Yakymenko et al., 2011).

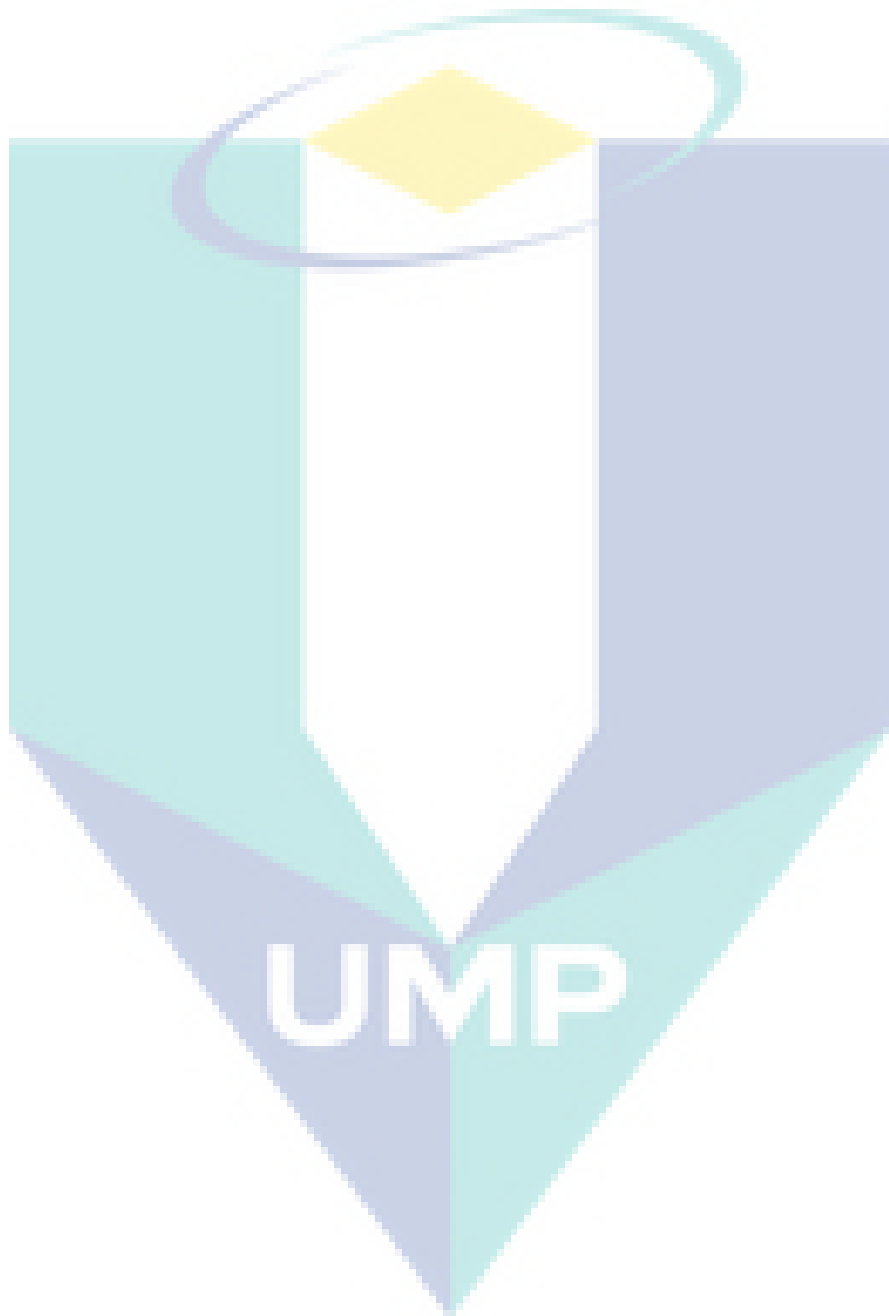
As illustrated before, the frequency of the MW region is located between the frequency of radio region and infrared region. Frequency represents the number of wave cycles that pass from a certain point within one second. The measurement unit of frequency is Hz, where 1 Hz = 1 cycle/sec (University of Colorado, 2002). Also, it is known that light can interface with each other. This characteristic leads to that the fact the light can be filtered using wavelengths (Ryer, 1998). For this purpose, optical filters are used to filter the wavelengths interface. The next subsections provide an overview of the different types of optical filters.

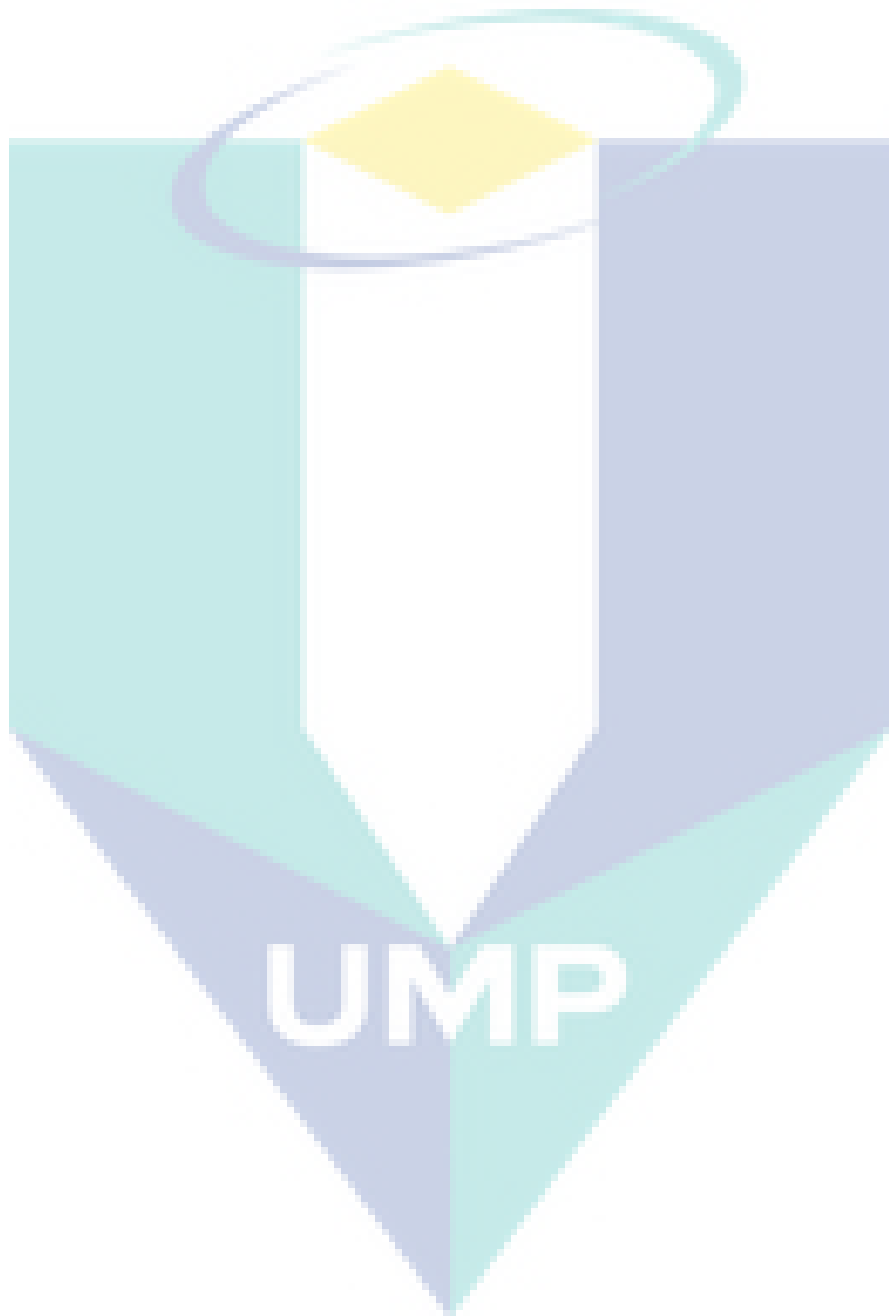
2.6.2 Optical Filters

Optical filters are devices used to transmit or reject a desired wavelength or a range of wavelengths. They are used in a wide field of applications such as spectroscopy, fluorescence microscopy, or clinical chemistry (Edmund Optics, 2016). Based on spectral properties, optical filters can be divided into several groups. The most important types are defined and explained in the following subsections.

2.6.2.1 Long-pass filters

This type of filters allows the passing of long wavelengths while blocking the short wavelengths. It is characterized by the fact that the short wavelength region is joined to the area of high transmission in the long wavelength region as shown in Figure 2.7 (Stasinopoulos and Hangarter, 1990).





method (MIAM) (Kechavarzi et al., 2000; 2005). In general, the non-intrusive or non-destructive methods used to measure fluid saturation, such as gamma ray or conventional X-ray attenuation techniques, do not allow the acquisition of dynamic fluid saturation distribution in the entire flow domain at one time (Oostrom et al., 2003). Because of practical limitations in source intensity, long counting times are needed and only one point can be measured at one time (Darnault et al., 1998) in the conventional X-ray, synchrotron X-ray measurements have proven to be a reliable method to measure phase saturation during multiphase transient flow (DiCarlo et al., 1997; Rimmer et al., 1998). Synchrotron X-ray allows measurements with short counting times in the order of seconds but only regions less than 0.5 cm^2 can be characterized at a given time (Darnault et al., 1998). These limitations lead to more attention being given to photographic methods which are considered cheaper and easier to use. As this research focuses on the LTV technique, only photographic methods will be discussed in detailed as presented in the next sections.

2.8 Photographic Methods

As mentioned previously, photographic methods are considered as one of the most effective techniques in monitoring the migration of NAPLs. All photographic techniques require image acquisition using either a digital camera or video camera depending on the image specification for later processing (Kamaruddin et al., 2011b). The main advantages of photographic methods are images of larger domains can be obtained instantaneously and no radiation risk is involved. However, the main drawbacks of these methods are that they require thin flow cells and sometimes require complicated calibration procedures (Oostrom et al., 2007). Table 2.4 shows selected studies that used photographic methods for different measurements.

Table 2.4 Photographic methods usage in measurement of various fluid properties

Authors	Measurement	Method	Size of Tank (cm ³)	Digital Camera Model	Image Analysis Software
(Deng et al., 2017)	Migration of TCE	LTV	60×45×2.5	CCD digital camera	Not mentioned
(Pan et al., 2016)	Migration of Diesel and PCE	LTV	60×65×6	CCD digital camera	Origin 8
(Sa'ari et al., 2015)	Migration of dyed toluene	LRM	Column : D = 9.4 H = 30	Nikon D90 DSLR	REIVAL, a MATLAB routine
(Ngien et al., 2012b)	Migration of dyed toluene	LRM	Two columns: D = 13.8 ,9.3, H = 30	Nikon D40	REIVAL, a MATLAB routine
(Kamaruddin et al., 2011b)	Infiltration and redistribution of dyed toluene and benzene	LRM	37×117×10 81×56×5	-	MATLAB
(Luciano et al., 2010)	Saturation of dyed hydrofluoroether (HFE-7100)	LRM	70×100×12	Digital camera	Not mentioned
(Simantiraki et al., 2009)	Infiltration of dyed Soltrol 220 and Diesel	LRM	120×100×2	-	Not mentioned
(Wang et al., 2008)	PCE mass and mass reduction	LTV	30×20×1.7	CCD digital camera	MATLAB
(Bob et al., 2008)	Saturation of undyed PCE	LTV	15.24×15.24×1.40 48.26×48.26×1.40	CCD camera (Model Number 7486-0002)	Image-Pro Plus software
(Konz et al., 2008)	Concentration of salt dye concentration	LRM	60×158×4	Nikon D7	Not mentioned
(Flores et al., 2007)	Water and LNAPL saturation	LRM	50×3.5×3.5	Nikon D70s	MATLAB R2006a
(Kechavarzi et al., 2005)	Distribution of fluid saturation	MIAM	180×120×8	Kodak Professional DCS 420IR	Image-Pro Plus software
(O'Carroll et al., 2004)	Saturation of dyed PCE	LRM	1-D: D = 5, H = 4.8 2-D: 38.4×30.6×1.7	Digital camera	Not mentioned
(Weisbrod et al., 2003)	Colloids concentration	LTV	60×50×1.27	CCD camera	Transform 3.4

Table 2.4 Continued

Authors	Measurement	Method	Size of Tank (cm ³)	Digital Camera	Image Analysis Software
(Ye et al. 2009)	Effect of biofilm growth	LTV	50×45×1.28	CCD camera	-
(Parker et al. 2006)	CO ₂ flow	LTV	50×50×1	CCD camera	Transform 3.4 (Fortner Software LLC)
(Yarwood et al., 2002)	Effect of biofilm growth	LTV	45×56×1	CCD camera	Transform 3.4 (Fortner Software LLC)
(Gerhard and Kueper 2003)	Saturation of dyed hydrofluoroether HFE 7200	LTV	103×5×1	Three TMC-7DPS color CCD cameras (Pulnix)	WIT software
(Darnault et al. 2001)	Water content and Soltrol 220 content	LTV	55×45×1	Sony color video camera	IPLab Spectrum V3.00 software
(Niemet and Selker 2001)	Liquid Saturation	LTV	60×50×1.27	CCD camera	Transform 3.4 (Fortner Software LLC)
(Conrad et al. 2002)	Saturation of TCE	LTV	60×60.5×1	CCD camera	Not mentioned
(Glass et al. 2000)	Saturation of dyed TCE	LTV	60×26×1	CCD camera	Not mentioned
(Darnault et al., 1998)	Water content and Soltrol 220 content	LTV	32.5×26×1	Cohu Color Camera	SP0228 V1.00 Color Tutorial software
(Tidwell and Glass 1994)	Water saturation	LTV	60×25×1	CCD camera	Not mentioned
(Van Geel and Sykes 1994)	Saturation of n-heptane	LRM	120×150×6	-	EASI, P.C.I., Inc. (Toronto, Ontario, Canada- V. 5.0)

2.8.1 Light Reflection Method (LRM)

Light reflection method (LRM) was used previously in several studies to investigate the infiltration of NAPL under controlled lighting conditions such as using two tungsten light source to light the flume front wall in a dark room (Van Geel and Sykes, 1994; Kechavarzi et al., 2000). The following sections illustrate the application of LRM in measuring different fluid properties.

2.8.1.1 *Liquid saturation*

LRM was used by Van Geel and Sykes (1994) to quantify LNAPL concentration. N-heptane was used as LNAPL and colored with red dye (Sudan III) to give clear visualization. Two 1000-W tungsten filament flood lights were used in addition to a set of color slides to record the movement of the spills. The slides were initially digitized as both RGB and black-and-white images. No additional information was provided from RGB images beyond that contained in the black-and-white images. The images that were taken before the starting of LNAPL infiltration were subtracted from the images taken during the multifluid flow experiment resulting in the creation of images containing only the changes in the grey level values because of the occurrence of the LNAPL or compression of the capillary fringe. Calibration for the normalized images was conducted to the known volume of LNAPL in the flow chamber to specify the saturation distribution. During the analysis, the distribution of LNAPL was assumed to be uniform across the depth of the box and the images on the front side really represented the internal saturations away from the wall. The authors reported that the main disadvantage of LRM is that the change in the LNAPL saturation could only be measured when the water saturation remain constant over time.

Similarly, O'Carroll et al. (2004) used LRM but to estimate DNAPL saturation in a flow chamber. They used PCE as the DNAPL and correlated the hue from the dyed PCE light reflection to known saturations in a small glass cell. The authors noted that these observations represent only the PCE occurrence in the first few millimeters of sand adjacent to the glass. Hence, they assumed that the observation of the behavior was representative of the entire cell thickness. A linear relationship was obtained between the hue and PCE saturation with an R^2 value of 0.91. The variance in lighting as well as

differences in glass thickness between the flow cell and calibration cells led to the normalization of the sum of PCE hue to known PCE volume. The estimation method was confirmed using linear trend between the sum of the organic phase hue over all the pixels and the known total volume of PCE that gave an R^2 value of 0.94.

Several years later, Flores et al. (2007) studied the suitability of using LRM to measure water and LNAPL saturation distributions. In their study, they took into account the influence of groundwater fluctuations on LNAPL migration in the groundwater. They used 50 various types of Toyoura sand. The difference here was dyeing the water with blue dye and mixing it with the sands. A 1-D column with dimensions of 3.5 cm × 3.5 cm × 50 cm made of transparent glass wall was filled with fully saturated Toyoura sand. A digital camera was used and pictures were taken every 30 minutes to monitor the migration of LNAPL. Two 500 W lights were used and turned on / off 30 seconds before and after each image was taken to avoid temperature changes in the column. For different soil samples, there was a logarithmic relationship between saturation and average optical density when saturation values as low as 2% were included in the analysis. This relation allowed the authors to measure the distribution of water saturation over time in a one-dimensional columnar porous medium in LNAPL-water phase. They reported that the image analysis method used in their study provided good information about the distribution of water saturation over time in an entire column domain for LNAPL-water two-phase systems.

Luciano et al. (2010) used LRM to measure DNAPL saturation distribution during the infiltration process in a 2-D laboratory scale chamber. The porous media used in the experiment was two types of glass beads in order to simulate two different media permeability, and the DNAPL applied was hydrofluoroether (HFE-7100), colored with Sudan (III) dye. Three floodlights were used in a dark room to get a uniform and constant light conditions. The authors mentioned that the pixel size is near to the grain dimensions; hence the information returned by the pixel size represented the presence of DNAPL with zero value grey level or its absence with 255 grey level or intensity. However, the saturation was calculated from the ratio of the volume occupied by DNAPL to the pore volume in the space. Mass balance calculation was used to validate the accuracy of LRM. The injected DNAPL amount was compared to the calculated

volume from the acquired pictures. The DNAPL volume was calculated by multiplying the calculated saturation with the average porosity. The estimated error between the actual injected volume of DNAPL and the estimated volume from image analysis was 6% which affirms the validity of the technique for measuring saturation.

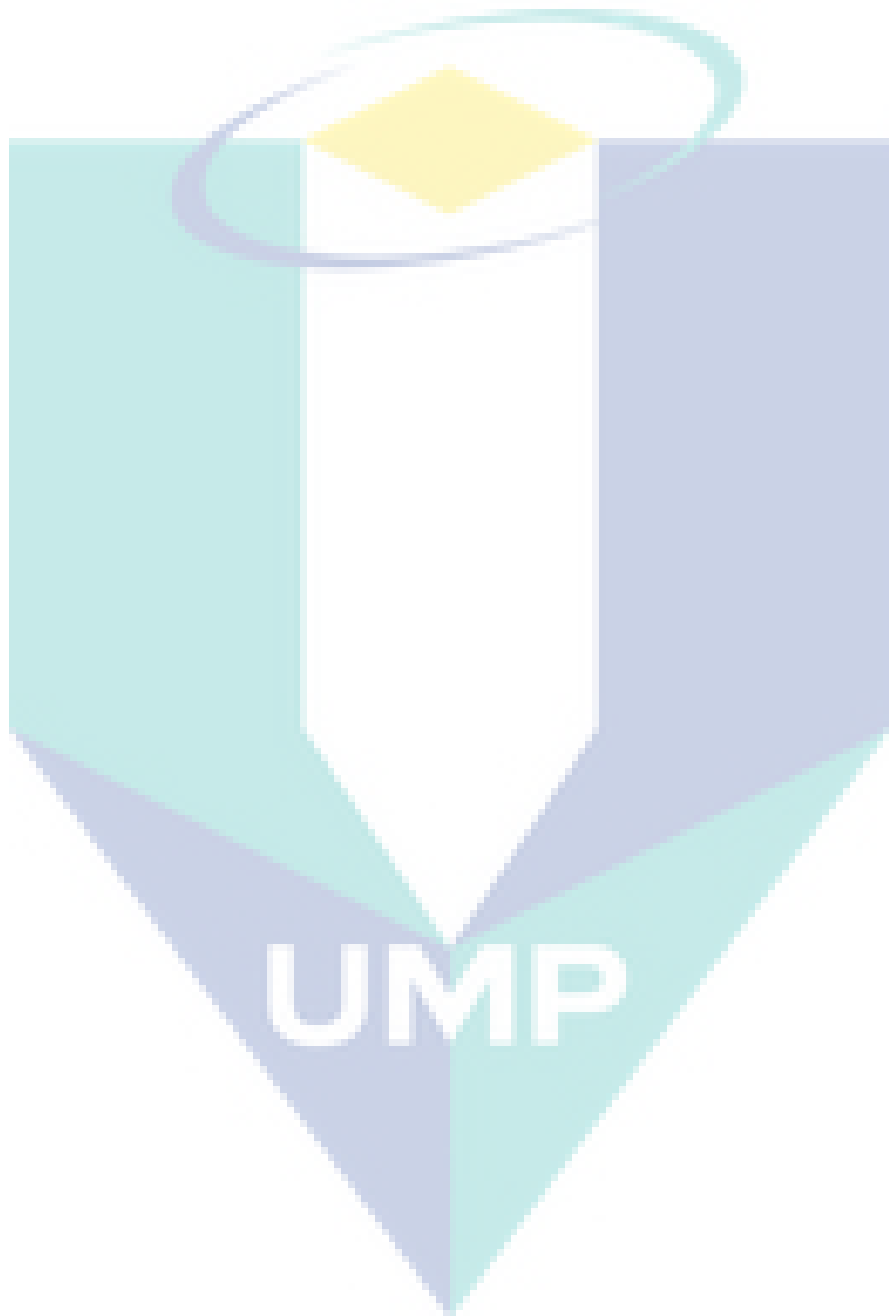
2.8.1.2 Liquid migration and distribution

Simantiraki et al. (2009) investigated the infiltration and distribution of LNAPL in the subsurface using LRM. Two types of LNAPL (Soltrol 220 and Diesel) were used in two types of different unsaturated sand. The LNAPLs were colored using 0.003% Sudan (III) dye. Four experiments were conducted using different layers of fine and coarse sand. A calibration curve had to be created for each type of sand and LNAPL which is considered the main drawback similar to the Darnault et al. (1998) study. A specific volume of each LNAPL type was added into the cells to achieve different values of LNAPL saturation. This resulted in every percentage of LNAPL saturation corresponding to a certain value of mean intensity. Calibration curves were generated from data of coarse and fine sands for both types of LNAPL. From the calibration data, it was concluded that the relation between intensity (represented by LNAPL presence) and saturation is linear. However, Darnault et al. (1998) proved that hue of the light transmission had a direct relationship with water content within the porous media. The authors reported that adding a similar amount of LNAPL resulted in different contamination plume size and shape in the same unsaturated porous media. Moreover, a comparison between spread velocities was studied and it was noted that the spread of Diesel was faster than Soltrol 220 due to the higher viscosity and density of Diesel. In all experiments, the flow was slower in the fine sand compared to the coarse sand due to the smaller porosity in the fine sand. Furthermore, the properties and configuration of sand layers play an important role in LNAPL retention.

Similarly, Kamaruddin et al. (2011b) accentuated the value of LRM technique in the investigation of the infiltration and redistribution of LNAPL in the vadose zone. Two different 2-D models were used for this purpose and similar to the Simantiraki et al. (2009) study, two types of sand and LNAPL were used. The two models A and B were packed with fine sand and silica sand, respectively. The LNAPL types used were toluene and benzene that were colored with Oil-Red-O. A digital camera was used to

record the images. From the recorded images, it was noted that clear changes of the shape and intensity of red toluene color in the first day of the experiment were observed, whereas in the following days no great changes were observed. However, migration at a slow rate still occurred in the porous media. Based on hue, saturation, and intensity (HSI) values that were generated from the image analysis program written in MATLAB, the images represent the contour of LNAPL migration. The main advantage of using HSI format is that the color is treated approximately the same way as humans perceive and interpret the color (Darnault et al., 1998). It was observed that at the first injection time for toluene, the depth of migration was only 8 cm and then the spot of toluene was broken into two parts. The range of HSI values was from 0.25 to 0.6. After 0.208 days of the toluene injection, the circular shape of toluene looked better and the HSI values were between 0.25 and 0.7 while the depth of migration was observed to reach 12 cm. After one day of injection, the downward migration of toluene was slower and the depth of migration reached only 13.2 cm. The HSI values rose to 0.8. After two days of injection, no significant changes were noted for the toluene. The authors compared the migration depth between toluene and benzene. They reported that the migration depths for toluene and benzene were 13.2 cm and 37 cm respectively. It is obvious that the migration depth for benzene is approximately three times the depth for toluene. This big difference may be due to the difference in the chemical properties for both LNAPL types.

A significant improvement to the LRM technique was achieved by Ngien et al. (2012b) when they used LRM to investigate the migration of LNAPL in 1-D circular columns. The significant difference in their study compared to the previous studies is the soil medium. Double porosity aggregated kaolin was used as the soil media. Kaolin is considered as a clay consisting essentially of minerals from the kaolinite group (Ribeiro et al., 2007). This study proved that LRM is viable when using kaolin as a soil medium. The study of Ngien et al. (2012b) refuted the argument of Oostrom et al. (2007) that photographic methods are typically limited to silica sand. In Ngien et al. (2012b) study, two experiments were conducted using circular columns, and the main difference between the two experiments was the size of the soil columns. The acrylic columns provided an obvious view of the medium within. The column in the first experiment had an inner diameter and outer diameter of 138 mm and 150 mm, respectively while in



The average calculated speed for LNAPL migration in Experiment 1 and Experiment 2 was 0.278 mm/s and 0.417 mm/s respectively. The authors compared these results with the results obtained by Alias (2003) who investigated the migration of LNAPL in a poorly graded sand with a permeability of 3.39×10^{-2} mm/s. One liter of LNAPL was poured into a soil column with the same type and diameter as the one used in Experiment 1. From the Alias (2003) results, the average speed was 7.5×10^{-2} mm/s, which indicated that this value was much lower than the average speed of LNAPL migration obtained from the Ngien et al. (2012b) experiments. The authors reported that the type of medium is the major difference between their study and Alias (2003)'s study. The authors concluded that the amount of LNAPL did not affect the migration speed. Hence, it can be said that the main reason for the difference in migration speed and depth is the type of the soil medium. The authors conducted another comparison between their study and a study by Pokrajac and Deletic (2006). Pokrajac and Deletic (2006) investigated the migration of LNAPL in a 1-D column packed with builder's sand as the single porosity medium. The average speed of LNAPL was 0.292 mm/s which was around the range reported in Ngien et al. (2012b). Ngien et al. (2012b) explained that this may be due to the presence of slots along the column wall that resulted in a reduction of the air resistance and hence accelerating the migration speed of LNAPL. Thus the LNAPL migration speed in the two studies was approximately the same. From the previous comparisons, it can be concluded that the LNAPL migration in double-porosity soil is much faster compared to single-porosity soil due to the presence of secondary porosity features in the double-porosity soil. Furthermore, other factors such as capillary pressure and wettability of the fluids existing in the soil pores also contributed to the results of the experiments.

The most recent study in the field of NAPL migration measurement using LRM was conducted by Sa'ari et al. (2015). Using the same method, Sa'ari et al. (2015)'s study reaffirmed the findings of Ngien et al. (2012b) that LRM is a valuable tool in monitoring and visualizing the migration of LNAPL in double-porosity soil media. Sa'ari et al. (2015) improved the study of Ngien et al. (2012b) by distinguishing the behavior of LNAPL migration in double-porosity using various moisture content in the soil. The diameter of the soil column was 94 mm and the height was 300 mm similar to the height used by Ngien et al. (2012b). Two experiments with two different moisture

contents were conducted. The water content of 25% and 33% were used with dry kaolin in Experiments 1 and 2, respectively. The same procedure in Ngien et al. (2012b) was followed by the authors. The pouring technique of LNAPL was different between the two experiments. In Experiment 1, the pouring was uniform on the top surface of the soil column whereas, in Experiment 2, the pouring technique was changed to be instantaneous which resulted in non-uniform coverage of the surface by the LNAPL before penetrating the sample. It was found that LNAPL required approximately 38 minutes to reach the bottom of the sample in Experiment 1. However, in Experiment 2, the overall migration duration was 15 seconds. The authors stated that the major reason for the difference in the speed of LNAPL migration is due to the technique of pouring. The average LNAPL migration speeds were 0.04 mm/s and 1.668 mm/s for Experiments 1 and 2, respectively. This was due to the higher percentage of water content and uneven compaction for the soil sample in Experiment 2. From the previous results, it can be summarized that the migration rate for Experiment 2 is faster than Experiment 1. Several factors affected the LNAPL migration in double-porosity soil such as the technique of pouring, compaction consistency, and water content. The authors compared the results of Experiments 1 and 2 with the results obtained by Ngien (2012) who used a different moisture content which was 30% but in a similar laboratory setting. The LNAPL migration required about 6 minutes to reach the bottom of the soil sample and the average calculated speed for LNAPL migration was 0.278 mm/s. The behavior of LNAPL migration in 30% moisture content of soil sample in Ngien et al. (2012b) work was akin to the behavior in the sample with 25% water content. However, they required different duration to reach the bottom of the sample. Furthermore, it was observed that the soil sample with 33% moisture content had macro-pores larger than the macro-pores in the soil sample with 25% water content. The observation is that the speed of LNAPL migration was influenced when the soil has more moisture content because the capillary pressure influences the movement of the LNAPL. Ngien et al. (2012b) explained that “pores with larger size reduce the capillary pressure that LNAPL has to overcome to enter those pores and thus move through the soil”. However, results showed that the limit for water content in double porosity kaolin is 35%. After this percentage, kaolin will start to disintegrate.

Other studies used LRM for other purposes such as Konz et al. (2008). In their study, they observed the solute concentration using LRM. However, this research only focused on observing water and LNAPL behavior.

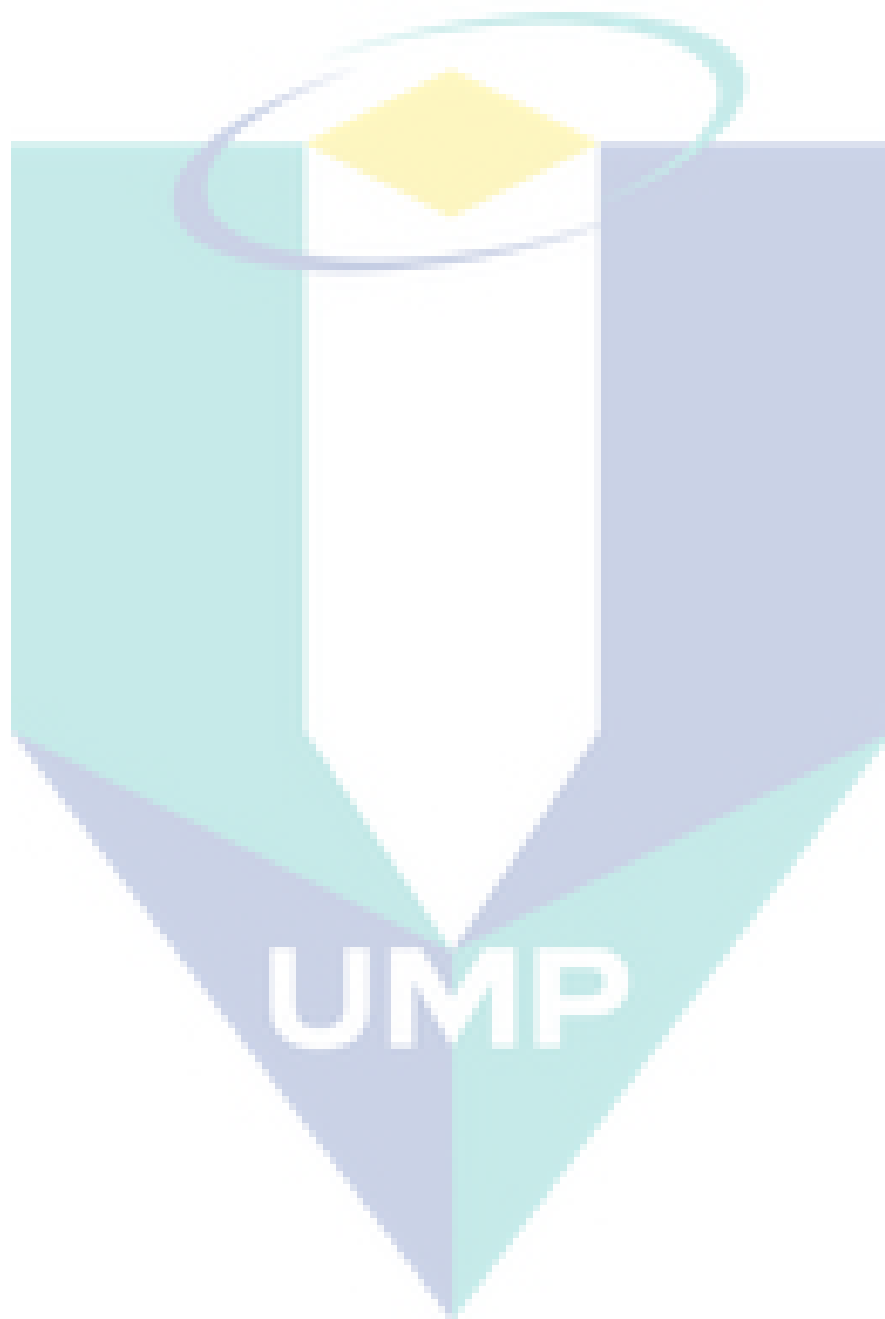
From the previous studies, it can be concluded that LRM is still a promising and influential technology, particularly in NAPL migration. According to the literature, LRM technique can measure the liquid saturation and content within the whole domain of the sample and do not require much time compared to photon attenuation method. Furthermore, the most significant concern with this method was using it in observing the NAPL migration within double-porosity soil (clay) which is considered a major development for this technique. On the other hand, the drawbacks of this technique are the reflection of light and the need for calibration curves which usually need a long time and a lot of efforts. Most studies used LNAPL as the contaminant. Further studies are required on DNAPL migration using LRM.

2.8.2 Light Transmission Visualization (LTV) Method

The theory behind the light transmission technique (LTV) is the passing of electromagnetic energy into the test media where the distribution of liquid saturation is measured as the variation in the light intensity field (Tidwell and Glass, 1994). There is a linear relationship between saturation and light intensity due to closer matching between the refraction index of the porous media and water relative to the porous media and air (Glass et al., 1989). The light transmission factor τ is calculated by Fresnel's Law in equation 2.3 (Tidwell and Glass, 1994).

$$\tau = \frac{4n_1n_2}{(n_1 + n_2)^2} \quad 2.3$$

where n is the refractive indices ratio of the two phases. For example, the refractive indices of water, sand, and air are 1.33, 1.6 and 1.0 respectively. When light is passing through phases that have different refractive indices, a portion of the light will be absorbed based on Fresnel's law due to many factors such as relative indices of



and they argued that this relation was due to the closer matching of the refraction indices of solid and water relative to solid and air. The image that showed only water content was obtained by subtracting the images of the dry porous medium from flow cell images. It was easy to obtain and record the behavior of water movement especially during fingering due to this technique's ability to take pictures in a fraction of a second (approximately 1/30 s).

Thereafter, Darnault et al. (1998) improved the methods of Glass et al. (1989) and Tidwell and Glass (1994) by using the LTV method to investigate the relationship between hue and water content through the full field in a two-fluid phase system (water – NAPL) using HSI format. The authors discussed that the reason for using hue as the best variable to measure water content was based on the method used for color specification. There are two common ways to specify the color for video cameras, computer graphics, and color monitors. The first way is the definition in term of a vector with three components of RGB. The other way to identify the color vector involves HSI. Hue depicts the pure color. Saturation depicts the degree to which the color is diluted with water. Intensity corresponds to the grey level (black and white). They found that the major problem in measuring water and NAPL saturation in the system was due to the similar refraction indices of these liquids. For that, they used 0.005 % FD&C blue dye to color water in a 2-D flow chamber packed with 12/20 coarse sand. They found that both saturation and intensity have no considerable correlation to water content. However, a linear relationship was found between hue and water content with an R^2 of 0.97. Also, they evaluated the method using mass balance and synchrotron X-ray technique. They injected 20 ml of blue water into an oil saturated chamber. The mass balance calculation showed that the total amount of water was 19.85 ml which was within 1% of the applied amount of water. The main advantage of LTV that is reported in Darnault et al. (1998) study is that the fluid content can be recorded in less than 0.05 seconds throughout the whole flow field. Furthermore, it was proven that the LTV method is viable to measure moisture content in 2-D chambers compared to synchrotron X-rays. However, the drawback of LTV is that translucent media such as silica sand has to be used as the porous media. Moreover, it is necessary to develop calibration curves for each type of sand and each camera used.

After a few years, Darnault et al. (2001) developed a method to measure fluid content in a three-fluid phase system (NAPL –water – air). The idea was generated from previous studies which indicated that in two-fluid phase (air-water) systems, the intensity is related to water content (Hoa, 1981; Glass et al., 1989) and another study where hue was related to water content in NAPL-water systems (Darnault et al., 1998). From these two findings, Darnault et al. (2001) hypothesized that hue and intensity of blue water colored by copper sulphate can be used in characterizing the water content and total liquid content in three-fluid phase systems (NAPL –water – air). Then the air content can be determined by subtracting water and NAPL content from the porosity. A 2-D calibration chamber was used to obtain a calibration curve between intensity and total liquid content as well as between hue and water content. For correlating hue to water content, different equations had to be used to correlate above and below the point of 0.076 water content. This point controls the correlation since above this point, hue and water content are uniquely correlated, whilst below this value, hue depends on NAPL and air content in the cell. Furthermore, total liquid content is a function of light intensity and hue. Results obtained from synchrotron X-ray were used to compare with the results from LTV for both static and transient experiments. In the static experiment, the regression coefficient for water and NAPL contents obtained from the two methods were 0.97 and 0.92, respectively. For the transient experiment, the two methods compared favorably based on measured finger widths in the air-dried and NAPL saturated sand. LTV can be developed to validate 1-D and 2-D computer codes for the transient flow of water, NAPL, and air in three phase flow phenomena. It was proven that LTV is an effective measurement tool in rapidly changing and in three-fluid phase systems. The advantages and disadvantages reported by the authors are the same as those in the Darnault et al. (1998) study.

The Tidwell and Glass (1994) study presented a major improvement to the Glass et al. (1989) method by deriving equations to relate the saturation to light intensity and light transmission factors at the sand-water and sand-air interfaces. These equations calculate the number of pores filled with water (P) by multiplying water saturation (S) with the total number of pores across the model thickness (K). They also calculated saturation from measured light intensity by assuming an individual drainage conceptual model and

assuming that each pore is either full or empty of water. Their method did not need calibration curve and K can be calculated empirically for each experiment.

Subsequently, Glass et al. (2000) modified the technique presented by Tidwell and Glass (1994) to compute TCE saturation using LTV. Three different translucent silica sand were packed in flow chambers to model the heterogenic structure. A 12-bit digital camera resulting in 4096 gray levels with 1317×1035 pixels and a resolution of 0.25 mm^2 per pixel was used. 0.9 g/l of Oil-Red-O dye was used to color the TCE instead of coloring the water with blue dye as Darnault et al. (1998) and Darnault et al. (2001) had done in their study. TCE saturations can be calculated from energy absorption by the dye, analogous to X-ray transmission equations shown by Tidwell and Glass (1994). The comparison conducted by Oostrom et al. (2007) showed that the calibration procedure used by Glass et al. (2000) is easier than the procedures described by Darnault et al. (1998) in two phase systems. For the estimation of TCE saturations in pools, the LTV method used by Glass et al. (2000) requires a scaling approach on the basis of expected maximum value of TCE saturation. They noted that the saturation was different from the front to the back of the chamber and the regions with high TCE saturations were close to the regions that were completely water saturated which presented problems in conducting the LTV method. They reported that the overall error in TCE volume was around 12% and this error can be reduced using more calibration. However, some errors cannot be avoided and still remained. From the previous observations, LTV seems to be a valuable tool in multifluid flow chamber experiments.

The technique described by Glass et al. (2000) was later improved by Conrad et al. (2002) to obtain TCE saturation in a heterogeneous flow cell packed with four types of silica sands. A digital camera with 1024×1024 pixels, a resolution of 0.36 mm^2 per pixel and 4096 grey levels was used. The same dye that was used by Glass et al. (2000) was used in the experiment. It was noted that the light transmission was influenced by the change in TCE saturation. However, this was not the only reason. It was reported that several confounding factors resulted in the failure to apply LTV. The first of these factors is the influence of surfactant and permanganate remedial solution on light transmission. For instance, salt occurrence in the surfactant solutions leads to a rise in the transmission, whereas purple potassium permanganate caused a decrease in

transmission. Second, the solubilization process of TCE is faster than the dye. Finally, the problems of exposure were taken into account in the finest sand and at the textural interface because of the rather large disparity in light transmission. The previous factors have a negative influence on the process of quantifying TCE saturations. The authors stated that the digital pictures can only be used to display qualitative spatial and temporal differences during the course of the experiments.

A study by Niemet and Selker (2001) was conducted to measure liquid saturation using LTV. The dimensions of the flow chamber used were 50 cm wide \times 60 cm high \times 1.27 cm thick and the light source consisted of 10 fluorescent tubes. Five models containing translucent porous media were used in their study. The first four models were packed with (Accusand silica) sand of uniform pore size while in the fifth model, they used the same type of sand but with distributed pore sizes. They reported that there was no need for calibration or to measure the empirical parameters in the determination of saturation. Their method was easy to apply since the number of pores (k) can be calculated mathematically, pixel by pixel from dry and saturated light intensities. They found that the model with distributed pore sizes was the best model to measure the liquid saturation from the light transmission.

Gerhard and Kueper (2003) measured DNAPL saturation using LTV method in water – dyed DNAPL system. Sand mixtures consisting of two types with different grain size distribution were used. HFE 7200 represented the DNAPL which was colored with blue dye for better visualization. Three connected computer controlled CCD video cameras were used to produce a time series of color images. Calibration of water content to the saturation component of the HSI system was used. They noted that saturation distribution profiles were conducted successfully using LTV. Furthermore, the relationship between light transmission calibration curves and physical distribution of DNAPL as well as DNAPL saturation was very sensitive which led the authors to conclude that during the development of these calibration curves, saturation hysteresis must be taken into consideration. The main drawback of their method was using three cameras in the experiments which accrued high cost and the need for more efforts to connect cameras and correlate the images.

A major contribution to LTV method was achieved by Bob et al. (2008), who studied the quantification of PCE saturation in 2-D, two-fluid phase system. The porous media used was silica sand. For the first time and different from the previous studies, this method was applied to measure undyed PCE saturations in a two-fluid phase, water-DNAPL system. Their method did not require calibration curve in the case of undyed PCE. However, it was necessary to use a single point calibration step when dyed PCE is used to calculate the change in the transmission factor at the dyed PCE-water interface. A comparison between known injected amounts of PCE and calculated amounts result from image analysis was reported. They found a very high correlation with an R^2 value of 0.993 between the known amounts of PCE and image analysis results obtained from LTV. In the case of dyed PCE, a stronger correlation ($R^2 = 0.999$) was obtained between the amount of dyed PCE and the results from image analysis. An inverse relationship was found between the volumes of PCE and the errors in mass balance. GS/MS and carbon column extraction were used to compare the mass balance results obtained from LTV. Similar mass balance results were reported from these independent techniques.

An improved LTV method was conducted by Zhao et al. (2015) to measure the LNAPL saturation in a simulated vadose zone inside a 2-D flow cell filled with glass beads. They used diesel as a model for LNAPL. 100 ml of diesel was injected into the flow cell with a rate of 1.492 ml/min. The observation of the experiments was up to 24 hr from the start of the experiment. The results showed that three areas were contained in the vadose zone starting from top to bottom as follows: dry area, transition zone, and capillary zone. When the LNAPL penetrated the dry area, transition zone, and capillary zone, a fan-shaped plume was created near the wet interface where the LNAPL saturation inside the plume gradually decreased from the center to the boundaries. On the other hand, high saturation of LNAPL was observed near the wet interface. From the results, the authors verified their method with mass balance and they found that the relative error was 4.38% which represented a viable method to observe NAPL migration and distribution.

In the same year, Zheng et al. (2015) applied the LTV method to investigate the influence of both flow velocity and spatial heterogeneity on DNAPL migration in

Accusand silica sand. For this purpose, six experiments were carried out in 2-D two-fluid phase systems. PCE was the DNAPL injected into the flow chamber from an injection point located at the middle of the top side of the flow chamber. Water was injected through three inlet ports fixed on the left side of the flow chamber. The results showed that large flow velocity increases the vertical and lateral DNAPL migration when the DNAPL is in the low viscosity case when there are no lenses in the porous media. However, when lenses exist in the porous media, the infiltration rate of the DNAPL decreased and the horizontal spread increased because the lenses retarded the migration of low viscosity DNAPL. The authors compared the results of their experiments with results from the numerical simulation where the results of experiments were consistent with the results obtained from simulation. The authors noted that the results of their work suggested that the combination of the high geological heterogeneity and groundwater flow velocity may significantly warn against the position of the source zone as well as its migration paths.

After one year, Pan et al. (2016) used LTV to investigate the migration of both LNAPL and DNAPL in four types of porous media under the influencing factors of NAPL migration including the type of NAPL, low permeability lens, initial soil water content, lithological sharp interface and leak location. Diesel and PCE were used as a representative for LNAPL and DNAPL. From the results, they reported that the LNAPL does not always stay on the top of the groundwater after penetrating through the vadose zone but partially pervade into the saturated zone where the degree of invasion is controlled by both capillary pressure and buoyancy force. For DNAPL, it moved deeply through the unsaturated zone and saturated zone until it reached water resisting layers where it will stop its movement.

The most recent study involving the LTV method was performed by Deng et al. (2017). They used the LTV method to evaluate the ability of electrical resistivity tomography (ERT) in monitoring the migration of DNAPL in porous media with different permeability conditions. The ERT method was used to capture the changes in the resistivity while the LTV method was used to visualize the DNAPL migration and provide high resolution saturation data. The results show that the ERT was successful in monitoring the DNAPL migration in heterogeneous porous media with different permeabilities.

LTV have been used by other researchers to investigate the behavior of items other than NAPL as discussed in the following studies:

A study by Yarwood et al. (2002) was carried out to measure the bacterial growth in porous media using LTV method. For this purpose, the authors investigated the bacterial strain and growth conditions inside a 2-D flow chamber with dimensions of 51 cm wide \times 61 cm height \times 1.3 cm thick using a 14 bit digital CCD camera. The investigation of the bacterial growth was mapped daily over a 7 days period. The results obtained showed that the LTV method is an effective tool to study microbial-hydrologic interactions in porous media.

Gas phase transport was studied using LTV as reported by Parker et al (2006). CO₂ transport in the unsaturated sand was investigated inside a 2-D flow chamber following the method of Niemet and Selker (2001). A pH indicator dye was used to measure CO₂ concentration based on soluble CO₂ alteration of pH. A total of 120 images of gas phase and dissolved phase CO₂ plumes were produced. The authors used a 14 bit digital CCD camera to acquire the changes in CO₂ behavior. The results showed that the LTV has many appealing features for the observation of CO₂ flow in porous media. The spatial resolution obtained at the millimeter scale provides temporal resolution of seconds which allows simultaneous observation of the key parameters such as liquid saturation and solute distribution.

The work of Wang et al. (2008) used locally calibrated LTV method to measure PCE mass and mass reduction in porous media. They demonstrated five models; four of these models were developed from previous studies of light transmission models in porous media, while the fifth model was a novel multiple wavelength model. The authors colored the water with dye, unlike the most common methods which dyed the NAPL phase. For this purpose, a 16 bit CCD digital camera with 1396 \times 1096 pixel array and 65,536 gray levels was used in addition to two 10 nm bandpass filters with a center wavelength of 630 nm and 650 nm. Their method did not require external calibration chambers. The results showed that the distribution of PCE was characterized using the spatial center of mass in horizontal and vertical dimensions. During remediation process, the center of mass was mobile in down-gradient and downward

directions. This LTV method with new dual wavelength is viable for advanced studies of multiphase flow and transport in permeable media since this dual wavelength depends on the assumption that the refractive indices are equivalent when using two wavelengths that are not significantly different (e.g 630 nm, 650 nm).

The LTV method was used by Ye et al. (2009) to study the influence of methane gas generation and biofilm growth on water flow in porous media. A 2-D anaerobic flow chamber with dimensions of 55 cm wide \times 45 cm height \times 1.28 cm thick was filled with silica sand for this purpose. The distribution of biofilm in the sand was monitored by confocal laser scanning microscopy. Protein analysis was used to measure the biomass distribution in the water and on the sand in the flow chamber. The results showed that both gas generation and biofilm growth were influential factors on the fluid transport.

2.8.3 Multispectral Image Analysis Method

Kechavarzi et al. (2000) developed a multispectral image analysis technique (MIAM) for the determination of the dynamic distribution of NAPL, air, and water saturation in 2-D three-fluid phase laboratory experiments. Images of sand samples with different saturation degree of NAPL, air, and water were captured using a digital near-infrared camera under constant light conditions using three narrow spectral bands of visible and near-infrared spectrum. The authors defined a relationship between the reflectance of NAPL and water saturation of sand samples and the optical density in two or three fluid phase systems within three 10 nm spectral bands with centers at 500, 760, and 970 nm. To record the intensity of reflected light, interference filters were placed on the digital near-infrared camera and used within three narrow spectral bands. The optical density, D , was defined by Kechavarzi et al. (2000) in equation 2.4 in terms of the reflectance.

$$D = -\log_{10}(\rho) \tag{2.4}$$

The reflectance is defined in equation 2.5 as

$$\rho = \frac{I_r}{I_o} \quad 2.5$$

where I_r is the reflected light intensity and I_o is the light that would be reflected by an ideal white surface. The system used in Kechavarzi et al. (2000) consisted of NaCl solution as the aqueous phase, Soltrol 220 dyed red representing LNAPL, and air. Unconsolidated uniform silica sand was used as the porous medium. Seventy-four sand samples with different NAPL and water contents were used in the experiments for calibration purposes. The samples were divided as follows: 18 samples for air-water two fluid phase system, 17 samples for air-NAPL two fluid phase system, and 39 samples for air, NAPL, and water three phase system. After preparing the samples, digital images were captured within the three spectral bands that were obtained by fitting the band-pass filters in the front of the camera lens. Each sample was placed next to a grey scale to correct the variations of spatial and temporal lighting condition between images. The intensity of light was divided into 4096 grey levels. A fixed area (constant number of pixels on the image) of interest (AOI) was determined for each image to measure the average optical density D_i of pixels in the AOI. Equation 2.6 can give D_i as shown in the following:

$$D_i = \frac{1}{N} \sum_{j=1}^N d_{ji} \quad 2.6$$

where N represents the number of pixels in the AOI for the determined spectral band i , and d_{ji} is the individual pixel optical density. An inverse relationship was found between the mean of the optical density and the water content. However, linear relationships were observed between D and aqueous phase (water) saturation, as well as LNAPL saturation. Furthermore, in the case of three-fluid phase systems and constant water saturation, a linear function was found between average optical density and both NAPL and water saturation. To assess the overall error related to the image analysis method, a mass balance test was conducted between the injected NAPL in the experiment and the calculated volume from the image analysis. The errors varied from

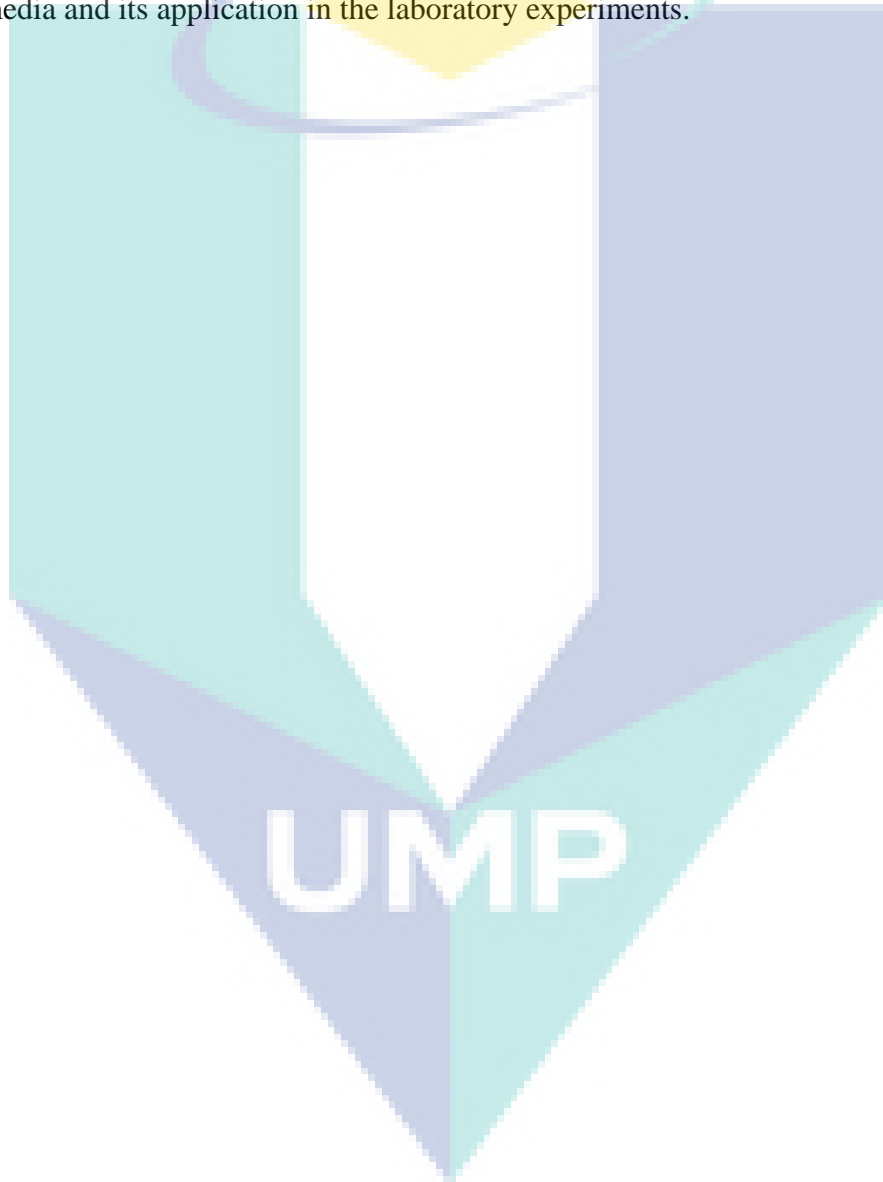
2.8% to 10.5% according to the experiment. The authors mentioned a number of reasons for the observed errors, including porosity variations, the effects of the wall, and flow cell bulging. MIAM provides a non-intrusive and non-destructive tool to capture images of multifluid flow in systems with rapid changes, similar to LTV and LRM.

Using the same method as Kechavarzi et al. (2000), Kechavarzi et al. (2005) measured the saturation distribution of LNAPL, air, and water. Fine and uniform silica sand was used in the experiments while Soltrol 220 was used as the LNAPL and it was dyed using Oil-Red-O. Kechavarzi et al. (2005) decreased the number of spectral bands used from three to two narrow spectral bands of 10nm centered at 500 nm and 960 nm. The average saturation of LNAPL, water, and air was measured using the calibration equations for each element. Mass balance calculation was conducted and the average relative error was 8.5% between the injected volume of LNAPL and the calculated volume from the image analysis. In addition to image analysis technique, reduced sensitivity investigations were done to observe the variations in vertical water saturation. Therefore, the water saturation could be observed from the calculated resistivity of the three-fluid phase system by using calibration equation that was developed separately for the two-phase system. The amount of LNAPL injected was 3 liters over a duration of 0.14 days. At the beginning of the infiltration process, it was noted that the gravity effect on the total potential gradient was small compared to the forces from the injection pressure and capillary pressure, which resulted in the spread of LNAPL in the form of a quasi-circular plume. The LNAPL reached the top of the capillary fringe after 1 day. The results showed that the maximum saturation value of LNAPL was 0.66 at 0.14 days. However, LNAPL saturation decreased over the rest of the experiment period (0.54 at 0.19 days, 0.42 at 1 days, and 0.39 at 3 days).

2.9 Summary

This chapter summarized the main concepts and definitions related to the study as well as the related studies in the field of NAPL migration, double-porosity, and image analysis techniques. An overview of the last studied that conducted on double-porosity soil media has been presented. In addition, a review of the last studies on the

different photographic methods including LRM, LTV, and MIAM has been illustrated. This chapter summarized the usage of the different three photographic methods as well as their advantages and disadvantage. Obvious gaps in research include the application of LTV method in monitoring the NAPL migration in double-porosity soil have been reported. Therefore, this study addresses this problem as will be discussed in the following chapters. The next chapter will present the materials and methods used to carry out this research as well as the calculation of NAPL saturation in double-porosity soil media and its application in the laboratory experiments.



CHAPTER 3

MATERIALS AND METHODS

3.1 Introduction

In this chapter, the work described is divided into two main parts. The first part describes the development of the equations that were used for NAPL saturation measurement in the double-porosity soil. The second part of this chapter covers the methodology used in the laboratory experiments. Prior to starting the laboratory experiments, a general characterization of the materials used was performed which included, physical, chemical and mineralogical properties. Moreover, experimental setup, experimental procedures and image analysis procedures based on LTV method are also presented. Only the research methodology will be described in this chapter. The results from the laboratory experiments will be presented in Chapter 4.

3.2 Materials and Methods

Before starting the experimental setup and experimental procedures, an overview of the materials used in the research and their characteristics are presented.

3.2.1 DNAPL and LNAPL

Tetrachloroethylene (PCE) (System, ChemAR) which is known as a major cause of groundwater contaminant due to its extensive use in industry (Zheng et al., 2015) was chosen as the DNAPL in all experiments due to the combined factors of cost and ease of procurement. PCE is extensively used and nominated as one of the

appropriated DNAPL by several researchers (O'Carroll et al., 2004; Bob et al., 2008; Zheng et al., 2015).

Toluene (System, ChemAR) was used as the LNAPL in all the experiments due to its cost and ease of procurement. Toluene is classified as BTEX which is considered as one of the main contaminants that have attached wide due to their high solubility in water (Cheng et al., 2016). The chemical properties of both materials are presented in Table 3.1. Prior to the start of the experiments, the amount of PCE and toluene needed for each experiment was dyed with Oil-Red-O dye powder at a concentration of 0.01 %. Oil-Red-O was used by several researcher (Bob et al., 2008, Ngien et al., 2012b). This concentration was found to be sufficient to facilitate a good visual observation of the PCE migration through the acrylic wall of the flow chamber. Using a small amount of dye is enough as reported by Kechavarzi et al. (2000). For each single experiment, the amount of PCE/toluene was prepared separately in prior of starting each experiment. For example, 12 ml of PCE was used in the first group of experiments. The 12 ml of PCE was prepared and put in a beaker, then 0.01% from the weight of the 12 ml of PCE, Oil-Red-O was added to the PCE and mixed using spatula. After PCE/toluene preparation, it was stored in a beaker covered by a parafilm.

Table 3.1 PCE and toluene properties*

NAPL	Chemical Formula	Density [g/cm ³]	Viscosity [mPa]	Molar Mass [g/mole]	Boiling Point [°C]	Solubility in water [g/l]
PCE	C ₂ Cl ₄	1.63	0.89	165.82	121	200
Toluene	CH ₃ C ₆ H ₅	0.867	0.59	92.14	110.6	520

*These properties were provided by the supplier (System, ChemAR)

3.2.2 Double-Porosity Materials

The double-porosity structure was created using a mixture of spheres made of sintered clay (micro-pores) and silica sand (macro-pores) (Peng et al., 2015) following a method described by Lewandowska et al. (2005). The sand used was local silica sand

(Kaolin, Malaysia, Sdn, Bhd) and the sintered clay spheres were made from commercially available kaolin S300 (Kaolin, Malaysia, Sdn, Bhd). The kaolin was originally from Perak, Malaysia. This type of kaolin possesses a platy structure which is hydrophilic and easy to be mixed with water to form a slurry in order to produce homogeneous soft clay (Marto et al., 2014). Kaolin is clay consisting of minerals from the kaolinite group (Ribeiro et al., 2007) with the chemical composition $Al_2Si_2O_5(OH)_4$ (Mohiuddin et al., 2016). The basic mineral structure of kaolin is a 1:1 layers of single octahedral sheet combined with layers of a single tetrahedral sheet (Murray, 1999). The kaolinite contains a high percentage of aluminum oxide, and almost complete absence of alkalis (Venturelli and Paganelli, 2007). No information about the sand and kaolin properties was provided by the supplier. Hence, the soil properties have to be determined in the laboratory. A general characterization for the sand and kaolin was done which include physical, chemical and mineralogical properties. It is worth mentioning that for kaolin, the properties were determined under two conditions; the first condition was for the raw kaolin and the second condition was for the kaolin after burning, since the kaolin has to be burned to create the double-porosity as will be discussed in Section 3.4.6. It is believed that the characteristics of clay can be changed due to the thermal effect (Yilmaz, 2011). During clay firing, some transformations may occur such as dehydroxylation (losses in crystalline water) and sintering (Venturelli and Paganelli, 2007). Dehydroxylation is the loss of the so-called "structural water" which takes place as an endothermic reaction from kaolin clays at temperatures around 450 - 600 °C (Venturelli and Paganelli, 2007). Therefore, the same physical, chemical and mineralogical tests were carried out again for the kaolin after burning to investigate the thermal effect on kaolin.

3.2.3 Physical Properties

3.2.3.1 Particle size distribution

The most common technique for the determination of particle size distribution is using the sieve analysis based on a method stated in the British Standard BS:1377 (British Standard Institution, 2012). For fine grained soils and clay fraction, hydrometer test is usually used to determine the particle size distribution (Faroughi and Huber, 2016). In this research, sieve analysis test was used for both sand and kaolin and

hydrometer test based on BS:1377 (British Standard Institution, 2012) was used for the fine portion of the kaolin which passed sieve size (0.063 mm).

3.2.3.2 Particle density

The particle density is determined by using the most common geotechnical approach which is the pycnometer method (British Standard Institution, 2012).

3.2.3.3 Permeability

The soil permeability is a characteristic of the soil that indicates its capacity to allow fluids to infiltrate through it (Geotechdata, 2008). There are two tests to determine the coefficient of permeability in the laboratory; the first test is the falling head permeability test which is more suitable for fine materials such as clay whereas the second test is the constant head permeability test which is suitable for grainy material such as sand, as mentioned in British Standard Institution (2012). Both tests were used in this study to determine the permeability coefficient of sand and kaolin.

3.2.3.4 Liquid limit and plastic limit

The liquid and plastic limits are usually conducted to measure the moisture content of the soil when it changes from a major physical condition to another. The liquid limit was measured using a cone penetrometer BS:1377 (British Standard Institution, 2012). The plasticity index was calculated from both liquid limit and plastic limit.

3.2.3.5 Surface area

Brunauer-Emmett-Teller (BET) method is a major method to determine the surface area for dry soil (ShamsiJazeyi and Kaghazchi, 2010). In this research, the surface area of the raw kaolin and the burned kaolin was acquired using the ASAP 2020 from Micrometrics.

3.2.4 Chemical Properties using Cation Exchange Capacity

The cation exchange capacity (CEC) is an intrinsic characteristic of soil that defines the concentration of the negatively charged soil colloids that can adsorb exchangeable cations (Sikora et al., 2014). CEC is a good indicator of soil productivity

(Sikora et al., 2014). On the other hand, it is a measure of exchangeable acids and soil bases at a specific soil pH. The CEC is usually expressed in milliequivalent per 100 g of dry soil. In this research, the CEC values for raw kaolin and burned kaolin were measured using ammonium acetate method at pH 7 following a method reported by (Tadza, 2011). The method can be summarized as follow:

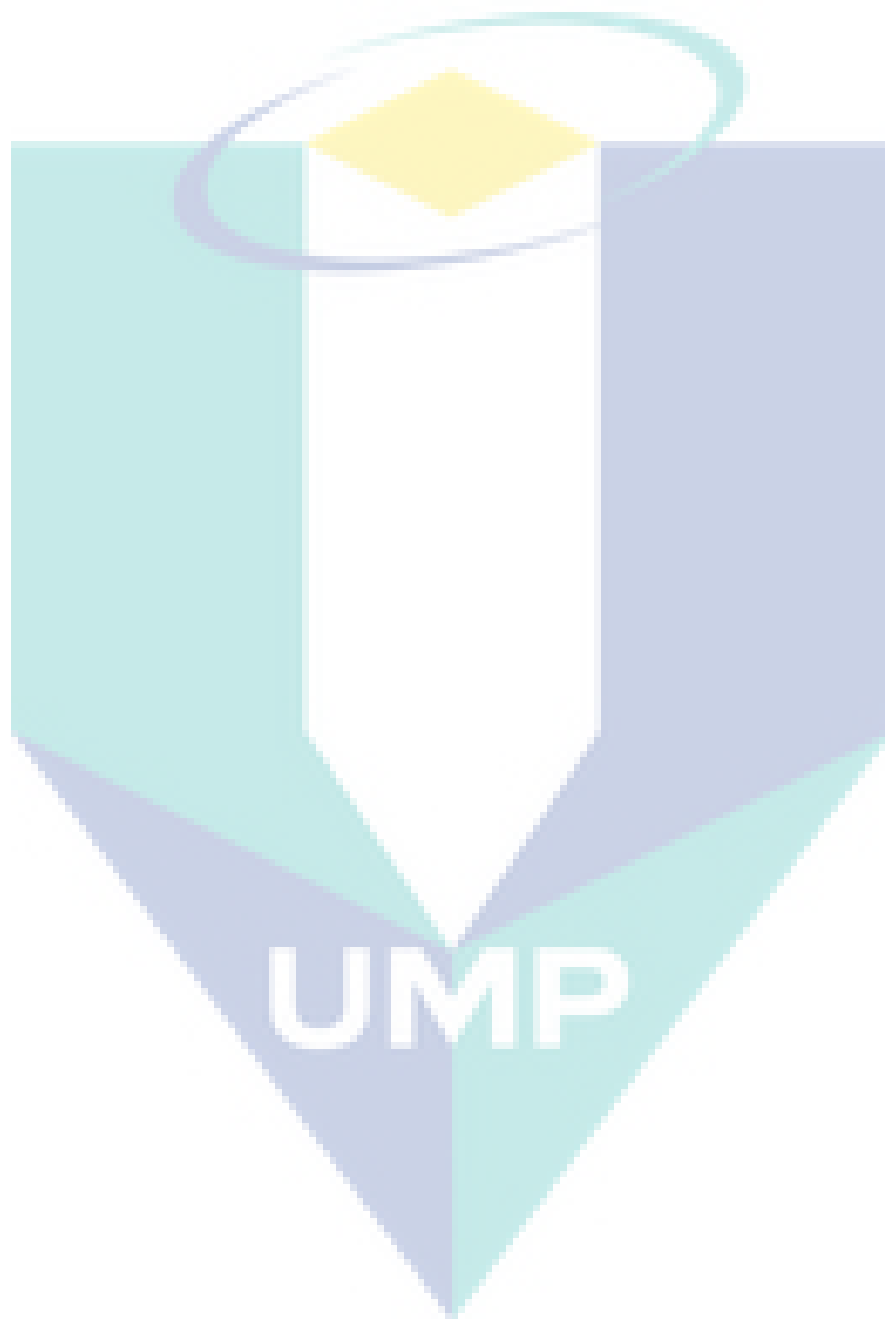
- One mole (1M) of ammonium acetate was prepared by dissolving 77.08 g of NH_4OAc with distilled water and then moved to volume in a 1 L volumetric flask.
- After that, 5 g of dry soil was mixed with 40 ml of ammonium acetate solution in a 50 ml centrifuge tube. It is very important to adjust the pH to 7 using ammonium hydroxide to raise the pH or acetic acid to lower it before placing the samples into the centrifuge located at the Environmental laboratory, Faculty of Civil Engineering and Earth Resources, UMP to and using a pH conductivity meter to adjust the pH.
- The samples were then placed into a 2420 centrifuge from KEBOTA and subjected to a rotation of 115 rpm for 15 minutes.
- After agitation in the centrifuge, the mixture was left to stand overnight. On the second day, the samples were shaken again for 15 minutes before filtration of the solution using Whatman filter paper with the assistance of a vacuum pump to accelerate the extraction process.
- Thereafter, a 30 ml of 1M ammonium acetate was poured four times (the total was 120 ml for every sample) by letting each portion to be filtered completely before pouring the next portion to rinse the sample by taking care not to allow the sample to become dry during the extraction (Pansu and Gautheyrou, 2007).
- After that, the extracted liquid from each sample was collected and sent to the Central Laboratory at UMP to be analyzed using Inductively Coupled Plasma Optical Emission Spectrometry (ICP-OES). The detailed calculation of CEC is shown in Appendix J.

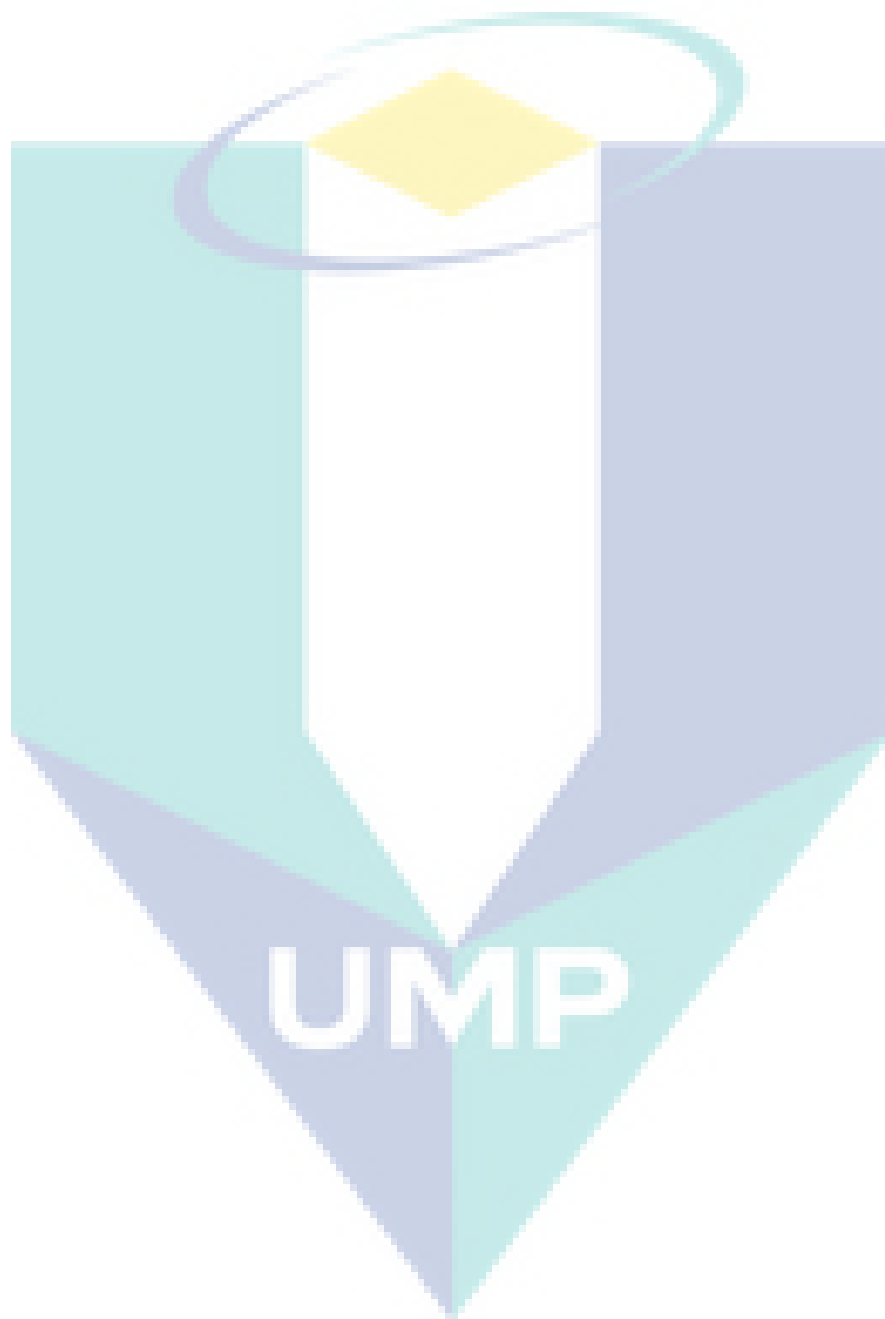
3.2.5 Mineralogical Compositions

The mineral compositions of the soil are usually determined using X-ray diffraction (XRD) instrument (Wang and Lu, 2014). In this research, a Rigaku Miniflex 2, was used for the mineralogical test where the clay powders were scanned at angle range from 30,000 to 80,000 degree.

3.2.6 Creation of Double-porosity Media

Double-porosity media was created following an approach proposed by Lewandowska et al. (2005) and Tran Ngoc et al. (2014) using a mixture of fine sand and sintered clay spheres. They used Hostun sand (HN38) that was very fine and the clay comes from La Bisbal, North-East Spain (Tran Ngoc et al., 2014). A discussion with the corresponding author of the Tran Ngoc et al. (2014) paper was conducted. The author mentioned that the double-porosity characteristic can be built from any material and it is not necessary to use the same materials. In this research, the double-porosity structure consists of a mixture of fine sand and sintered clay spheres made of kaolin. Sintering of kaolin is a densification process which implies a shrinkage (i.e reduction in volume) (Venturelli and Paganelli, 2007). Local silica sand was used as the filler. Prior to use the sand, a cleaning process was conducted. Following Niemet and Selker (2001), the sand was washed with distilled water and oven-dried at 45 °C for 48 hours to ensure that it is clean from any fine residual. To further ensure that the sand was clean, the absorption of the waste distilled water that was used to wash the sand was monitored using a spectrophotometer (Hach DR 5000). The washing process was continued until the absorption of the used distilled water for cleaning was similar to the absorption of the clean distilled water using the same wavelength. Meanwhile, to create the sintered clay spheres, a method by Lewandowska et al. (2005) was followed. The kaolin powder was mixed with sufficient water and formed into spheres by hand before being fired at 1000° C for 1 hour (Lewandowska et al., 2005). The clay spheres were put inside the furnace and the temperature was increased gradually until it reached 1000 °C (Lewandowska et al., 2005). This process was to make the kaolin hard as well as to increase its ability to withstand the disintegration during the saturated phase. When clay is exposed to a high temperature of 1000 °C, the clay particle will pass through several processes starting





calculate the DNAPL saturation in the flow chamber. Thereafter, the calculated DNAPL will be compared with the real amounts of DNAPL that was injected into the flow chamber in order to assess the errors from mass balance.

Niemet and Selker (2001) proposed that Beer's law (Ryer, 1998) and Fresnel's law (Griffiths, 1989) can be applied to quantify the absorptive and interfacial light losses when the light is transmitted from phase to phase for the total thickness of the porous media as follows:

$$I = C I_{in} \tau_i \exp(-\sum d_i \alpha_i) \quad 3.1$$

where I is the emergent light intensity, C is the constant for correcting the difference between light observation and light emission (in this research, it can be omitted since the camera is approximately the same distance from each light source and the soil media inside the flow chamber), I_{in} is the incident light intensity, τ_j is the transmittance of the interface between the two phases i and $i+1$, α_i is the absorption coefficient of i phase, and d_i is the thickness of the phase i .

Equation 3.1 can be applied to the experimental flow chamber used in this research following the assumption of Bob et al. (2008) that porous media is a water wetting media as well as the assumption that each pore is either full or empty of water as stated by Tidwell and Glass (1994). By applying equation 3.1 and following Bob et al. (2008) to neglect the visible light absorption by air and water, equation 3.2 is presented assuming that all three phases (air, water, NAPL) are present in the flow chamber:

$$I = I_{in} \tau_{pw}^{2N_p} \tau_{wa}^{2N_p X} \tau_{wn}^{2N_p(1-X-S)} \exp(-\alpha_p d_p N_p - \alpha_n d_o N_n) \quad 3.2$$

where τ_{pw} is the transmission factor at the porous media particles-water interface, τ_{wa} is the transmission factor at the water-air interface, τ_{wn} is the transmission factor at water-NAPL interface, N_p is the number of pores across the flow chamber thickness, X is the fraction of pores that are filled with air (air saturation), S is the fraction of pores that

are filled with water (water saturation), α_p is the absorption coefficient of the porous particles, d_p is the diameter of the porous particles, N_{pp} is the number of porous particles across the thickness of the flow chamber, α_n is the absorption coefficient of the dyed NAPL, d_o is the average pore diameter, and N_{pn} is the number of the pores that are filled with NAPL.

Equation 3.2 presents the case of a three- fluid phase system. However, in the case of two-phases, equation 3.2 can be rewritten with $X = 0$ (i.e only water and NAPL occurs). So, equation 3.2 will become:

$$I = I_{in} \tau_{pw}^{2N_p} \tau_{wn}^{2N_p(1-S)} \exp(-\alpha_p d_p N_{pp} - \alpha_n d_o N_{pn}) \quad 3.3$$

Equation 3.3 is valid only in cases where the soil is of single porosity. However, in this research double-porosity soil is the media that was studied as stated in the previous sections. Therefore, modifying these equations is necessary for them to be valid and suitable in the case of double-porosity. The main difference is in the transmission of the light for double-porosity media. In the case of single-porosity, the light is transmitted through only one type of soil with a certain porosity. However, in the case of double-porosity, there are two types of soil with two distinct scales of porosity known as macro-pores and micro-pores.

The double-porosity soil in this research is made up of kaolin spheres and fine sand. In this case, the light will be transmitted through three different interfaces: sand-water interface, clay-water interface, and water-NAPL interface. In this case, equation 3.3 can be rewritten as:

$$I = I_{in} \tau_{sw}^{2N_{ps}} \tau_{cw}^{2N_{pc}} \tau_{wn}^{2(N_{ps}+N_{pc})(1-S)} \exp(-\alpha_s d_s N_{ps} - \alpha_c d_c N_{pc} - \alpha_n d_o N_{pn}) \quad 3.4$$

where τ_{sw} is the transmission factor at the sand particles-water interface, τ_{cw} is the transmission factor at the clay particles-water interface, k_s and k_c are the numbers of sand particles and clay particles across the thickness of the flow chamber, respectively,

α_s is the absorption coefficient for sand particles, d_s is the diameter of sand-particle, d_c is the diameter of clay particle and α_c is the absorption coefficient for clay particles.

In the case where the flow chamber is fully saturated with water, substituting $S = 1$ in equation 3.4 will result in Equation 3.5 where I_s represents the light intensity for each pixel at fully water saturated condition.

$$I_s = I_{in} \tau_{sw}^{2N_{ps}} \tau_{cw}^{2N_{pc}} \exp(-\alpha_s d_s N_{ps} - \alpha_c d_c N_{pc}) \quad 3.5$$

In the case where the flow chamber is fully saturated with NAPL, substituting $S = 0$ in equation 3.4 will result in producing I_N which stands for the light intensity at each pixel under full NAPL saturation as shown in equation 3.6.

$$I_N = I_{in} \tau_{sw}^{2N_{ps}} \tau_{cw}^{2N_{pc}} \tau_{wn}^{2(N_{ps}+N_{pc})} \exp(-\alpha_s d_s N_{ps} - \alpha_c d_c N_{pc} - \alpha_n d_o N_p) \quad 3.6$$

To get an expression for I_N as a function of I_s , equation 3.5 can be divided by equation 3.6.

$$\frac{I_s}{I_N} = \tau_{wn}^{-2(N_{ps}+N_{pc})} \exp(\alpha_n d_o N_p)$$

Arranging the equation to get I_N and I_s on different sides:

$$I_N = I_s \tau_{wn}^{2(N_{ps}+N_{pc})} \exp(-\alpha_n d_o N_p) \quad 3.7$$

Equation 3.7 was used to calculate the I_N theoretically since it is too arduous and not practical to fully saturate the flow chamber with NAPL each time the model is packed. To eliminate I_{in} , from equation 3.4, divided it with equation 3.6 which will result in equation 3.8

$$\frac{I}{I_N} = \tau_{wn}^{2(N_{ps}+N_{pc})(1-S-1)} \exp(-\alpha_n d_o N_{pn} + \alpha_n d_o N_p) \quad 3.8$$

Arranging equation 3.8 to get I_N and I on different sides result in equation 3.9.

$$I = I_N \tau_{wn}^{-2S(N_{ps}+N_{pc})} \exp(-\alpha_n d_o N_{pn} + \alpha_n d_o N_p) \quad 3.9$$

It is known that K is the total number of the pores across the thickness of the flow chamber. The flow chamber contains clay pores (k_c) and sand pores (k_s). Therefore, it can be considered that K is the sum of k_s and k_c as shown in equation 3.10.

$$N_p = N_{ps} + N_{pc} \quad 3.10$$

Substituting the term N_p instead of $N_{ps} + N_{pc}$ into equation 3.9 will result in equation 3.11:

$$I = I_N \tau_{wn}^{-2SN_p} \exp(-\alpha_n d_o N_{pn} + \alpha_n d_o N_p) \quad 3.11$$

To eliminate I_N , substitute equation 3.7 into equation 3.11 and rearrange to get equation 3.12:

$$I = I_s \tau_{wn}^{2N_p(1-S)} \exp(-\alpha_n d_o N_{pn}) \quad 3.12$$

Applying (ln) for both sides will give:

$$\ln \frac{I}{I_s} = 2N_p \ln \tau_{wn} - 2N_p S \ln \tau_{wn} - \alpha_n d_o N_{pn} \quad 3.13$$

As mentioned earlier, S is the fraction of pores that are filled with water (water saturation), so S_n is assumed to be the fraction of pores that are filled with NAPL. Therefore, it can be considered that the total saturation is equal to the two saturations as shown in equation 3.14.

$$S + S_n = 1 \quad 3.14$$

Moreover, S_n represents the pores that are filled with NAPL across the thickness of the flow chamber. Hence, it can be considered that equation 3.15 is true:

$$S_n = \frac{N_{pn}}{N_p} \quad 3.15$$

Substituting equation 3.14 and equation 3.15 into equation 3.13 and rearranging will give equation 3.16:

$$\ln \frac{I}{I_s} = 2N_p \ln \tau_{wn} - 2N_p (1 - S_n) \ln \tau_{wn} - \alpha_n d_o S_n N_p$$

Then, by arranging the right side:

$$\ln \frac{I}{I_s} = 2N_p \ln \tau_{wn} - 2N_p \ln \tau_{wn} + 2N_p S_n \ln \tau_{wn} - \alpha_n d_o S_n N_p$$

Then,

$$\ln \frac{I}{I_s} = S_n [2N_p \ln \tau_{wn} - \alpha_n d_o N_p] \quad 3.16$$

For equation 3.7, applying (ln) to both sides of the equation will give equation 3.17:

$$\ln \frac{I_N}{I_s} = 2N_p \ln \tau_{wn} - \alpha_n d_o N_p \quad 3.17$$

Substituting equation 3.17 into equation 3.16 will give equation 3.18:

$$\ln \frac{I}{I_s} = S_n \left[\ln \frac{I_N}{I_s} \right] \quad 3.18$$

Equation 3.18 can be rearranged to get an expression for S_N (NAPL saturation) at each pixel as shown in equation 3.19:

$$S_n = \frac{\ln I_s - \ln I}{\ln I_s - \ln I_n} \quad 3.19$$

Equation 3.19 can be used directly to calculate the NAPL saturation pixel by pixel in a two-phase system (NAPL, water) in double-porosity soil media without the need to use a calibration curve which achieves the first objective of the research.

The total number of pores across the thickness of the whole flow chamber (N_p) can be determined as proposed by Niemet and Selker (2001), shown in equation 3.20:

$$N_p = \frac{\ln \left(\frac{I_s}{I_d} \right)}{2 \ln \left(\frac{\tau_{pw}}{\tau_{pa}} \right)} \quad 3.20$$

where τ_{pa} is the transmission factor at the porous media particles-air interface, and I_d is the light transmission at each pixel when the flow chamber is dry. In the case of double-porosity, there are two types of soil as stated before. In this case, N_p consists of N_{ps} and N_{pc} which can be determined separately as shown in equation 3.21 and equation 3.22:

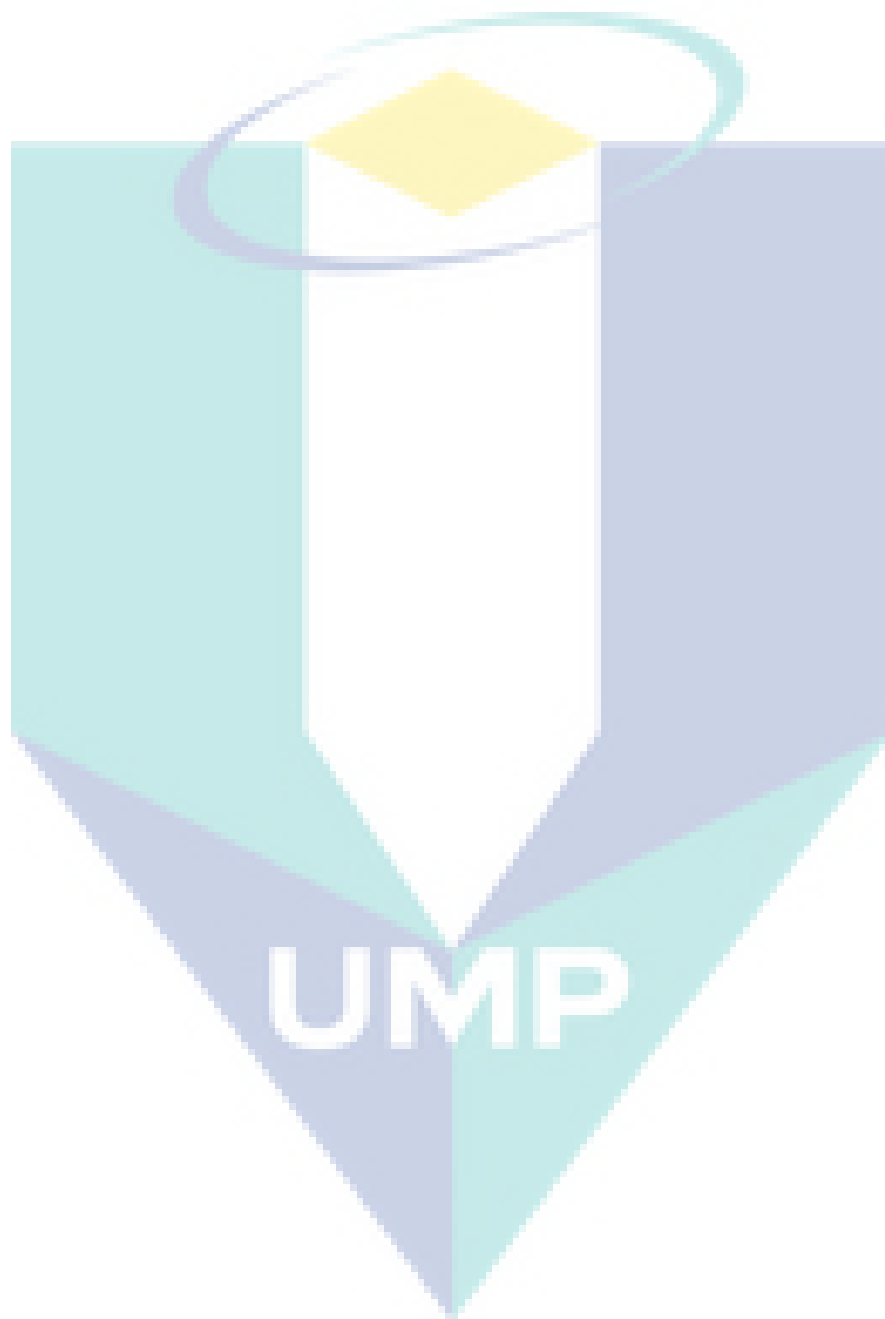
$$N_{ps} = \frac{\ln\left(\frac{I_s}{I_d}\right)}{2 \ln\left(\frac{\tau_{sw}}{\tau_{sa}}\right)} \quad 3.21$$

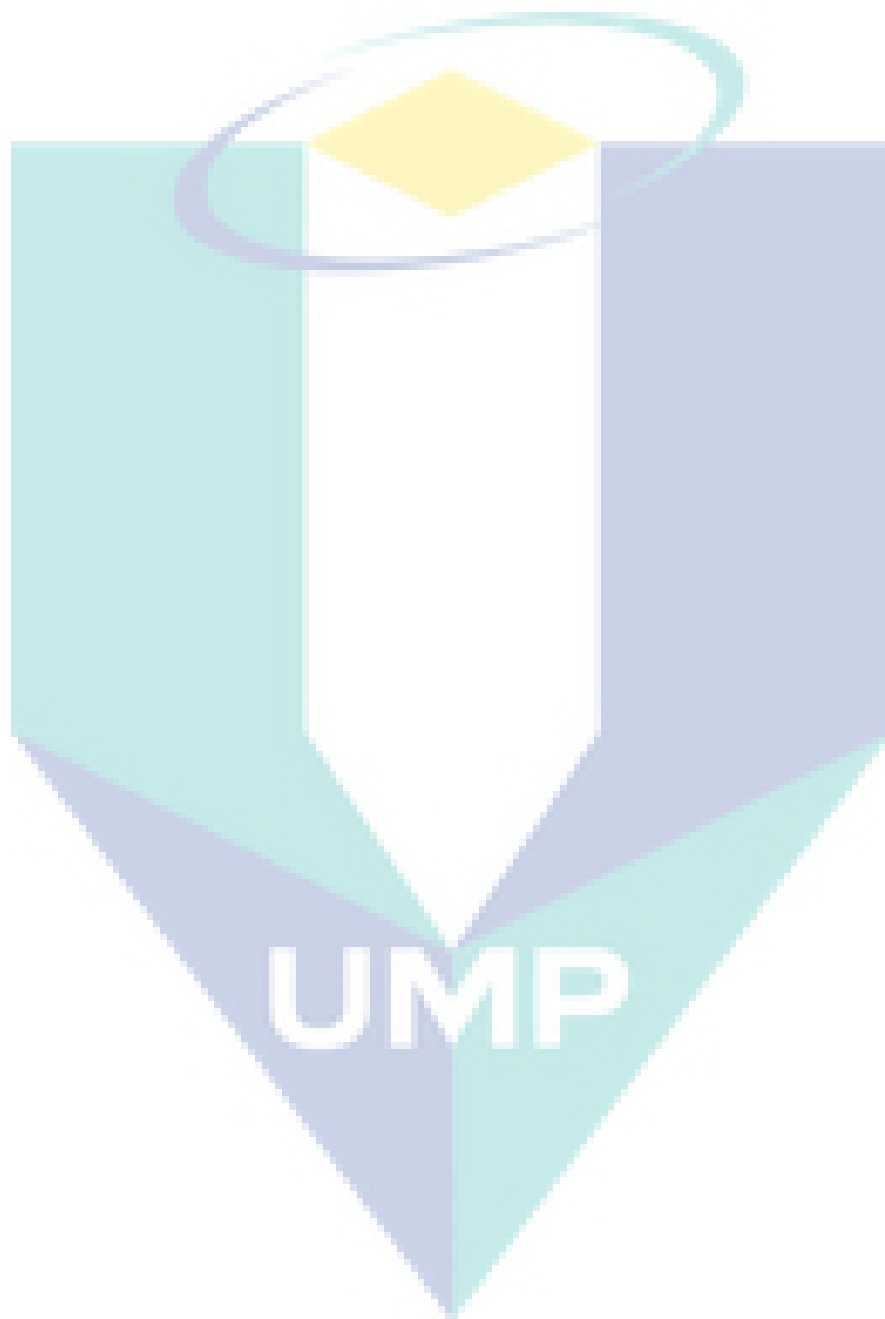
$$N_{pc} = \frac{\ln\left(\frac{I_s}{I_d}\right)}{2 \ln\left(\frac{\tau_{cw}}{\tau_{ca}}\right)} \quad 3.22$$

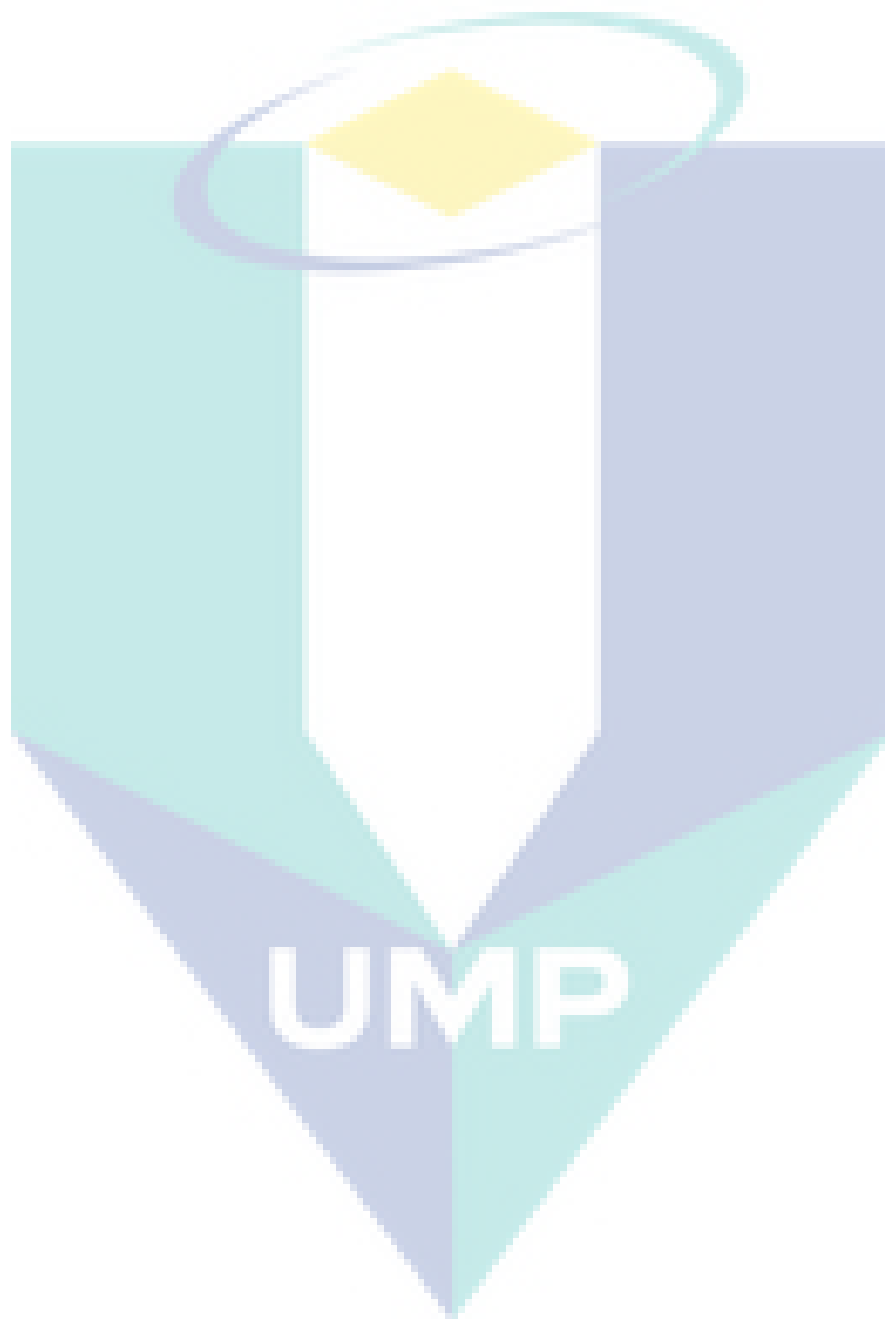
By using Fresnel's law (Ryer, 1998), the transmission factor τ can be calculated between any two phases by measuring the refractive index (n) of these two phases using equation 2.3.

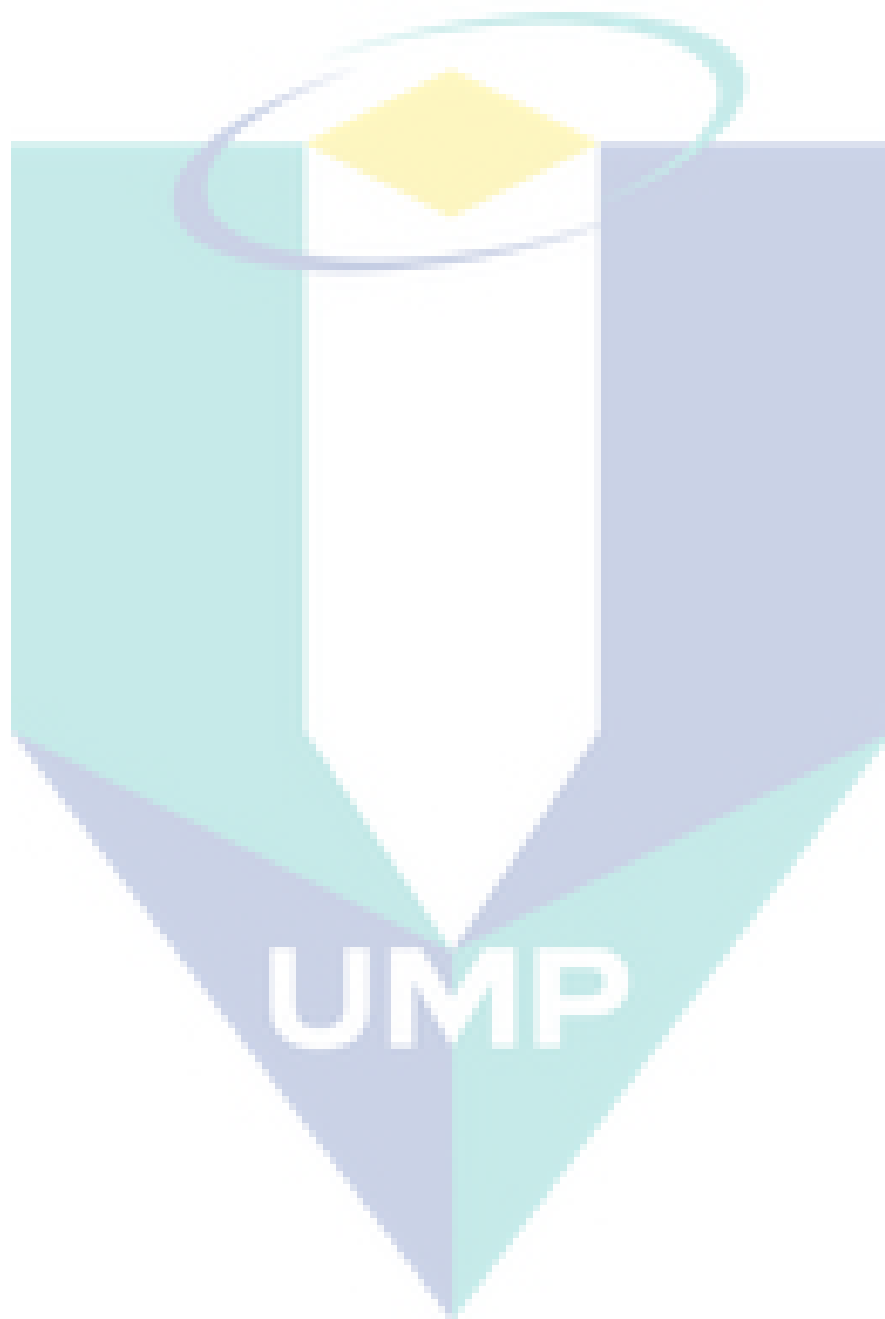
The refractive index value is 1 for air, 1.6 for sand, 1.33 for water (Tidwell and Glass, 1994; Niemet and Selker, 2001) and 1.56 for kaolin (Ghosh et al., 1990). These values can be used to calculate the transmission factors for the different interphases. Also, the transmission coefficient for water-NAPL (τ_{wn}) can be calculated similarly to the sand/clay – water/air interfaces, using PCE refractive index of 1.501 (Bob et al., 2008).

For equation 3.7, it is also needed to measure the absorption coefficient for dyed PCE (α_n), which can be measured using a spectrophotometer. Furthermore, the pixel averaged pore diameter (d_o) can be calculated by dividing the total length of the voids by N_p . The total length of voids across the thickness of the model can be calculated by multiplying the thickness of the model by porosity (Bob et al., 2008).









The flow chamber was kept in a fixed position inside a steel frame in front of the light source. A holographic light shaping diffuser (LSD) (Luminit, USA) was placed behind the flow chamber and in front of the light source to homogenize the light and provide a uniform pattern of light in the flow chamber. The properties of the LSD are shown in Appendix A. Two drainage steel ports were attached to the bottom of the model. These ports were connected by a plastic tube to a water tank and CO₂ cylinder. A steel valve located between the flow chamber and water tank/CO₂ cylinder regulated the flow of water/CO₂ into the flow chamber. An inspection was conducted visually to verify that no leakage occurred during the inflow and outflow of water.

Image analysis was the method to observe the PCE migration in the flow chamber as this method has been used to quantitatively and qualitatively analyze NAPL migration in soil (Ngien et al., 2012b; Bob et al., 2008; Niemet and Selker, 2001). Advances in the current imaging technology have made visualization of the NAPL saturation possible with more accuracy and efficiency. The main equipment in this technique is the digital camera used for measuring and capturing the NAPL migration at predetermined time intervals.

Digital images were captured using a Nikon digital camera (Nikon D7100, Malaysia) which was kept at a constant distance of 1.5 meters from the light box. The camera has 24 megapixels (6000 × 4000 pixels) that result in a very high spatial resolution (i.e. each pixel represented approximately 0.07 mm² of the chamber surface area) and has two systems for the dynamic range. The first system is the 14-bit dynamic range that results in 16,384 (i.e. 2¹⁴) grey levels while the second system is the 12-bit range that results in 4,096 grey levels. The second system was used in order to be compatible with the monochrome system in the image analysis software used. All images were processed using Image-Pro Premier 9.1 (IPP) (Media Cybernetics Inc.). This powerful scientific software has been used by several researchers and provides a convenient direct image processing solution compared to the additional efforts required by other software and programs such as MATLAB routines (Kamaruddin et al., 2011a).

Images were collected using a 600 nm center wavelength 10 nm band-pass filter (Orientir Inc, China) which was attached to a 67 mm lens (Nikkor 18-105mm f/3.5-5.6 GED VR). The purpose of using this filter is to permit transmission for a light with a

defined wavelength range and block all others. Kechavarzi et al. (2000) reported that the light is absorbed by the dyed NAPL in blue and green regions (400-600 nm) but most of its transmission is located in the red region (600-700 nm). This was the reason for choosing a band-pass filter with 600 nm center wavelength. The properties of the band-pass filter are shown in Appendix B. The camera was connected to a laptop and the image acquisition was controlled by the Nikon camera Control-Pro software. The aperture setting of the lens was adjusted in order to fully utilize the dynamic range of the camera using exposure times of a few seconds. The aperture of the lens which describes the lens speed was fixed at focal length (f 5.6) for all images and the exposure time or shutter speed (which is the time for the camera shutter to be open during the capture of the image) was 1 second.

3.5.1.2 Experimental procedures

After packing the flow chamber with the double-porosity media in the case of Experiment 1 and with silica sand in the case of Experiment 2, the top frame of the flow chamber was closed carefully and sealed with silicon to prevent evaporative losses. The light source was switched on, and after 30 minutes the light transmission image for the dry media condition (I_d) was collected. After that, the flow chamber was saturated with distilled water with constant head boundary conditions from the bottom to the top of the model. The left-hand and right-hand sides of the flow chamber were considered as zero-flux boundary condition. Prior to saturation with water, the packed flow chamber was slowly purged with CO_2 gas through the bottom ports for around 40 min to displace air from the porous media and to minimize the risk of trapped air bubbles in the porous media when the flow chamber was saturated with water. The duration of the CO_2 injection (i.e 40 min) was determined after many trials in order to make sure that the flow chamber is empty from air based on the value of the light intensity as compared to the case of the dry flow chamber. The average light intensity for the case of saturated flow chamber should be greater than that of the dry flow chamber. CO_2 is very effective in displacing air and dissolves relatively well in water (Bob et al., 2008) since its solubility in water is greater than that of air (Yarwood et al., 2002). This step is very important to make sure that the model was under two-fluid phase system (NAPL-water). The saturation process continued until the water level was above the surface of

the porous media. Following Niemet and Selker (2001), about 1 hour after saturating the flow chamber with water, the saturated transmission image (I_s) was acquired.

The next step was injecting pre-determined amounts of PCE into the water-saturated flow chamber through the top of the model using an injection needle (syringe). The needle was penetrated into the soil to about 2 cm below the top of the model before the PCE was released. Injection of the PCE was done in seven consecutive amounts (1.0 ml, 1.0 ml, 2.0 ml, 2.0 ml, 2.0 ml, 2.0 ml and 2.0 ml). After each PCE injected stopped of movement, the image was captured using the remote control software. It is worth mentioning that the first and second increments were 1 ml which are smaller than the other increments because the first increment was used for PCE light transmission calibration as will be discussed later. Using of small amounts of PCE is easier to get good calibration (Bob et al. 2008). The total amount of PCE in each experiment was 12 ml. These intermittent injections with increments are necessary for mass balance calculation where the usage of seven increments will result in seven different points which are better for correlating between the injected PCE amounts and calculated PCE amounts.

A spectrophotometer was used to quantify the absorption of the dyed PCE at 600 nm. After images acquisition, the amounts of injected PCE in the flow chamber were calculated based on image analysis and the results compared to the actual injected amounts. Mass balance check was then performed to investigate the difference between the calculated amount of PCE based on image analysis and the actual amounts added into the flow chamber. For PCE saturation calculation in double-porosity, equations derived in Section 3.3 were used for Experiment 1. However, for Experiment 2 that represented the case of single-porosity, the equations reported by Bob et al. (2008) were used.

3.5.2 Image Analysis Procedures

For each captured image, image analysis procedures were conducted to extract the light intensity values for images as shown in Figure 3.7. Prior of conducting the image analysis, all images have to be corrected for the temporal variation in the light intensity as stated by Bob et al. (2008). Temporal variation is a random noise that

usually resulted in image sensors which deteriorates imaging performance (Nakamura, 2016).

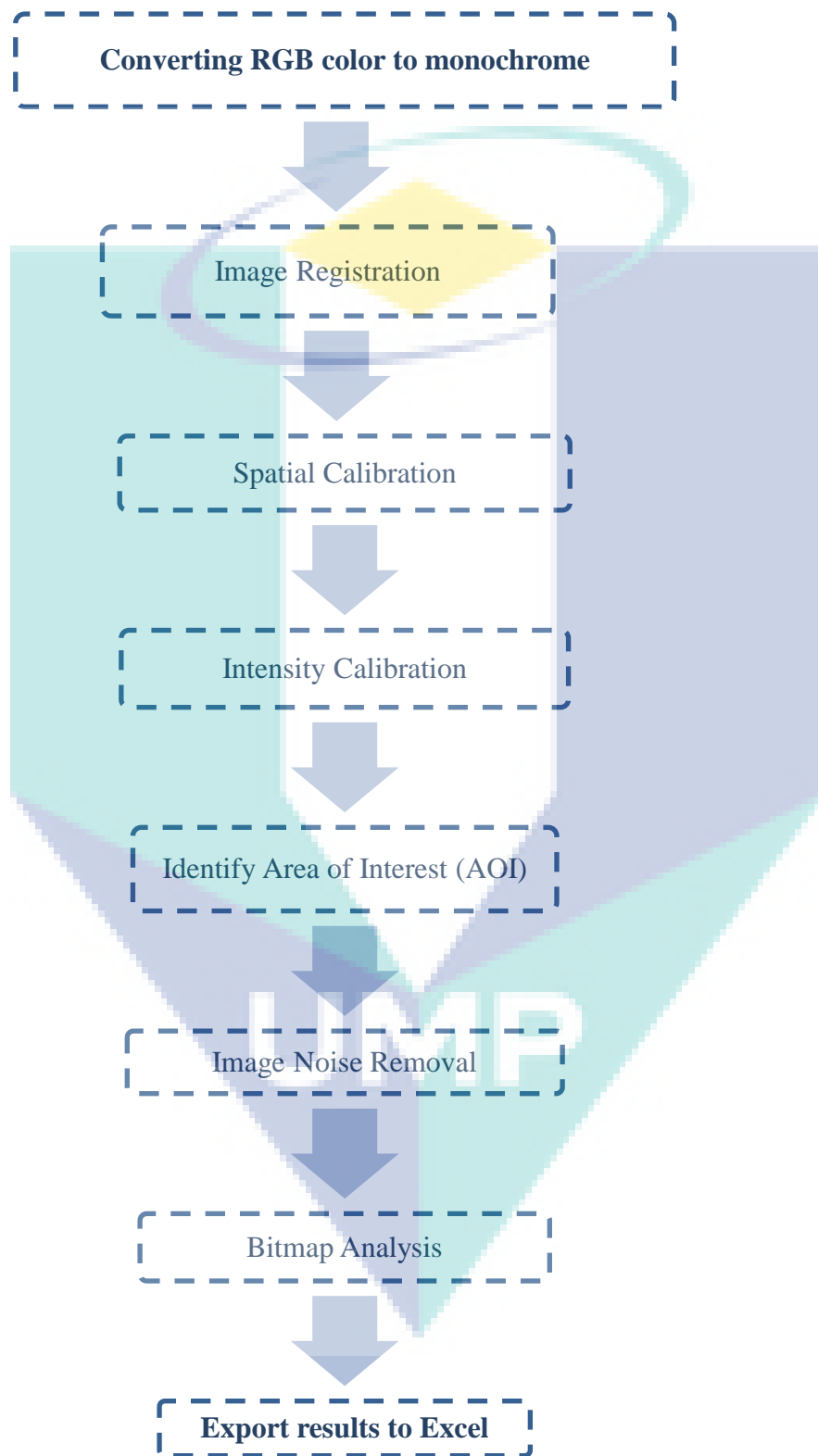


Figure 3.7 Image analysis procedures for extracting the NAPL light intensity

To carry out a correction on the temporal variation in light intensity, a reference image, usually the image captured when the flow chamber is fully saturated with water, was chosen.

Two small zones (5 cm × 5 cm) on the reference image were identified and referred to as “correction zones”. Once the correction zones have been determined, it is very important to ensure that for all other images, these two zones are always fully saturated with water and remain under the same conditions so that any change in light intensity in the correction zones is due to the change in light intensity from the light source.

A “correction coefficient” was identified and calculated from the ratio of the average light intensity of the correction zones for the reference image to the average light intensity of the correction zones of the image that need to be corrected. To correct a specific image, the correction coefficient of the image to be corrected was multiplied by the light intensities of each pixel in the image. For each image collected, it is important to capture three frames consecutively and then take the average value of the light intensities of these three images for calculations. Figure 3.8 shows a schematic diagram for images correction.

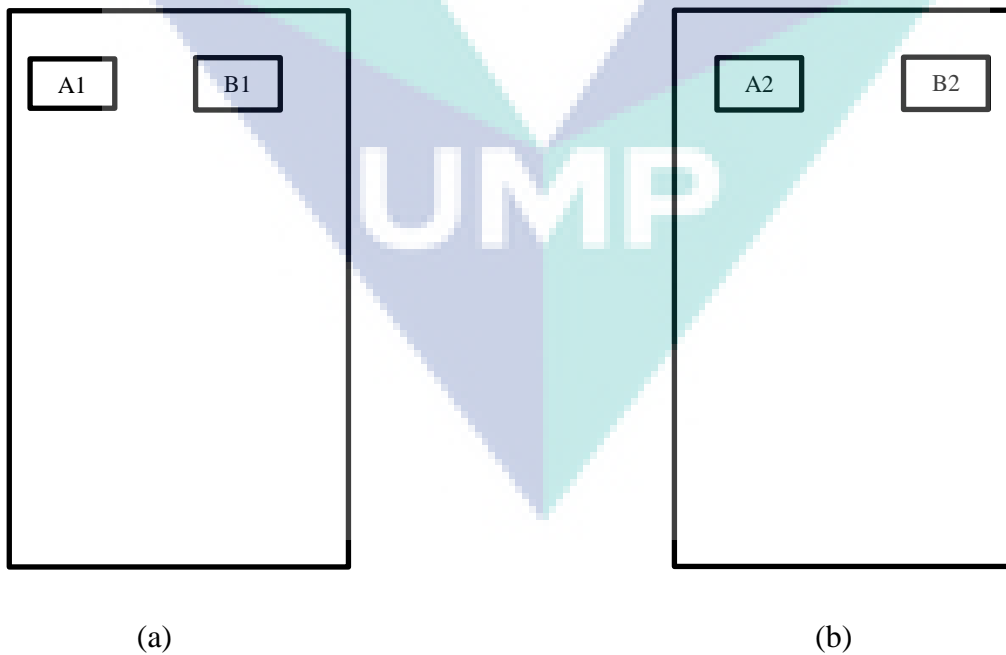


Figure 3.8 Correction zones at (a) The reference image when the flow chamber is fully saturated with water (b) The image after the increment of PCE

For example, to correct the image (b), the correction coefficient can be calculated as follow: Correction Coefficient = Average light intensity between (A1 & B1) / Average light intensity between (A2 & B2). After that, the correction coefficient has to be multiplied to each pixel for the image (b). Thereafter, steps described in (Appendix Y) have to be followed to extract the light intensities for the images.

3.5.3 Group (2) PCE and toluene migration in three-fluid phase system in double and single-porosity in

In this group, four 2-D laboratory experiments were carried out to qualitatively analyze the migration of PCE and toluene in double and single-porosity in three-fluid phase system in order to achieve the second part of the second objective of this research. The experimental setup for the laboratory experiments for this group is somehow similar to the previous experiments in group 1. However, the experimental procedures were different. In this group, the experimental program was divided into four experimental runs which were designated as Experiment 3, 4, 5, and 6, respectively. The methodology for all the experiments is basically the same; the sole difference is the porous medium and the type of NAPL. In Experiment 3 and 4, PCE migration was investigated in double-porosity and single-porosity, respectively in three-fluid phase system. In Experiment 5 and 6, toluene migration was investigated in double-porosity and single-porosity, respectively in three-fluid phase systems.

In each of the experiments, the flow chamber was packed dry with either double-porosity or single-porosity media. After the chamber was fully packed with the porous media according to the packing procedure in section 3.2.6, the top frame of the flow chamber was attached and silicon was used to seal all gaps. After that, the packed chamber was purged of air by CO₂ gas injection through the ports at the bottom of the flow chamber and then distilled water was slowly introduced into the flow chamber from the bottom ports under a positive pressure. After 1 hour of saturating the flow chamber with water, the valve was opened and the water was allowed to drain, creating two zones where the upper zone represents the three-fluid phase while the lower zone represents the two-fluid phase zone as shown in Figure 3.28.

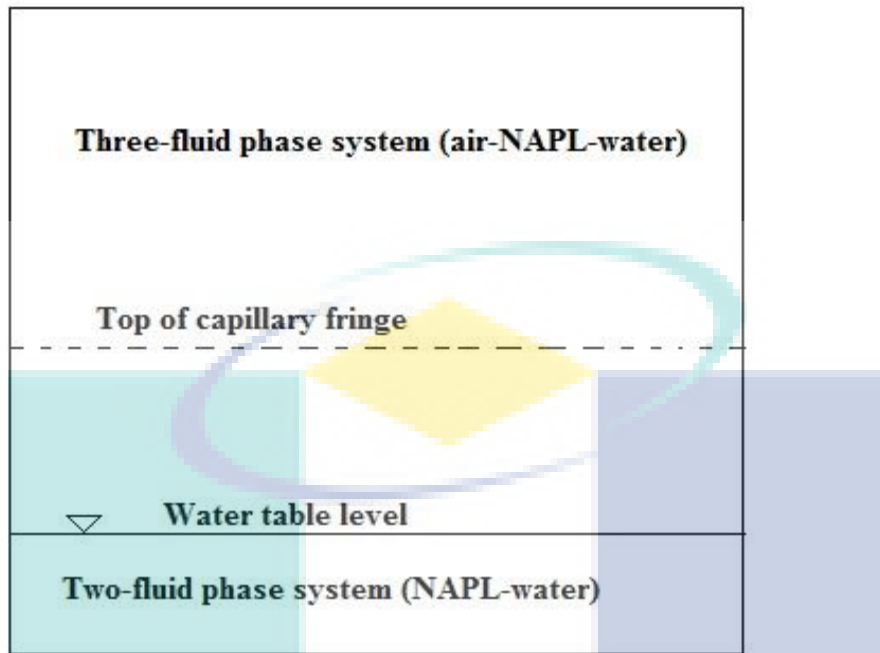


Figure 3.9 Schematic diagram for the experiments 3,4,5 and 6 (Group 2, PCE and toluene migration in three-fluid phase system)

Following Schroth et al. (1998), the period of water drainage was 12 hours prior to the release of the NAPL. Before releasing the NAPL into the flow chamber, the camera captured an image of the flow chamber, and this image was used as a reference image for the system. This image was used later for image subtraction where images with the NAPL increments were then subtracted from the reference image. Thereafter, in every experiment, 20 ml of the NAPL was injected into the flow chamber using a syringe. Image acquisition was carried out based on the change of the NAPL movement and the frequency of image capturing was shown in Table 3.2. After that, the same procedures presented in (Appendix Y) were followed in order to extract the light intensity of PCE and toluene.

Table 3.2 Frequency of image acquisition for Experiments 3, 4, 5, and 6

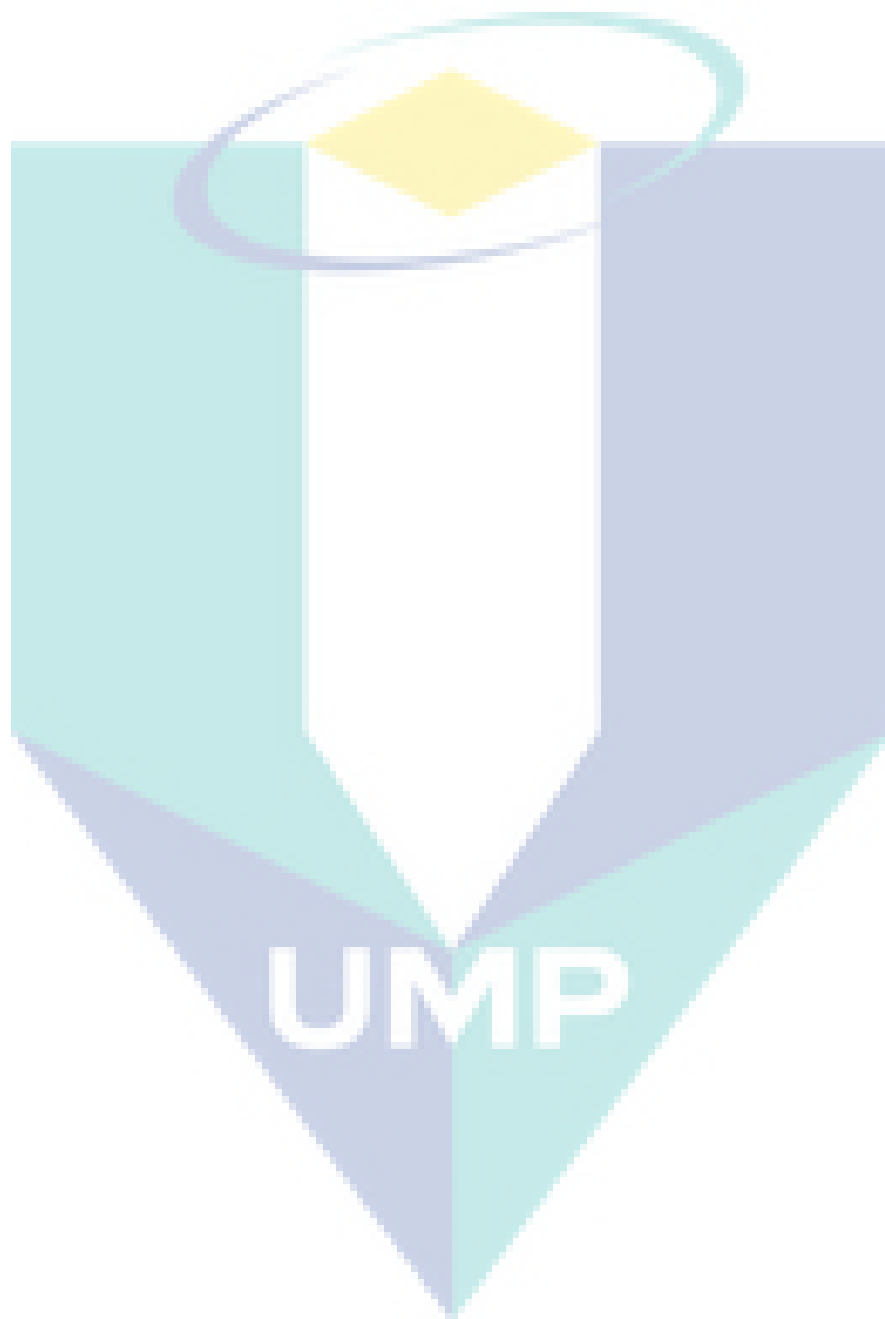
Duration (min)	Experiment 3	Experiment 4	Experiment 5	Experiment 6
0-3	5 sec	10 sec	5 sec	10 sec
3-10	20 sec	30 sec	20 sec	30 sec
10 -15	1 min	1 min	1 min	1 min
15 - 30	2 min	2 min	2 min	2 min
30 - 60	3 min	3 min	3 min	3 min
60 - 120	5 min	5 min	5 min	5 min
120 - 180	10 min	10 min	-	10 min
180 - 260	15 min	15 min	-	-

The duration of image capturing was determined based on the changes in DNAPL shape. The differences in the time period of image capturing was according to the type of soil medium applied in the experiments. For example, in experiments 3 and 5, the soil medium was double-porosity. Based on the literature, the DNAPL velocity in double-porosity is faster than that in single-porosity. Therefore, the time period for image capturing in double-porosity was less than that in single-porosity since the change in DNAPL shape will be faster in double-porosity.

3.5.4 Group (3) Influence of rainfall recharge on toluene migration in double-porosity soil

When rain is introduced to the subsurface, the water phase portion will increase which in turn affects the vertical NAPL migration. As water percolates through the porous media, it takes the place of NAPL held in smaller pores by capillary forces and increases the pore water pressure (Kamaruddin, 2012).

In a previous study, Kamaruddin (2012) carried out an experimental study to investigate the influence of rainfall on the migration of LNAPL in silica sand. The author reported that the LNAPL was easily moved downward by the rainfall recharge. In addition, her results showed that the rainfall recharge can significantly reduce the residual LNAPL saturation at the upper part of the capillary interface. Subsequently, another study was conducted by Flores et al. (2013) to investigate the LNAPL behavior under precipitation effect using simplified image analysis method (SIAM). In their study, they observed the LNAPL migration under the influence of two different types of rainfall intensity in (1-D) column filled with Toyoura sand. The authors noted that both



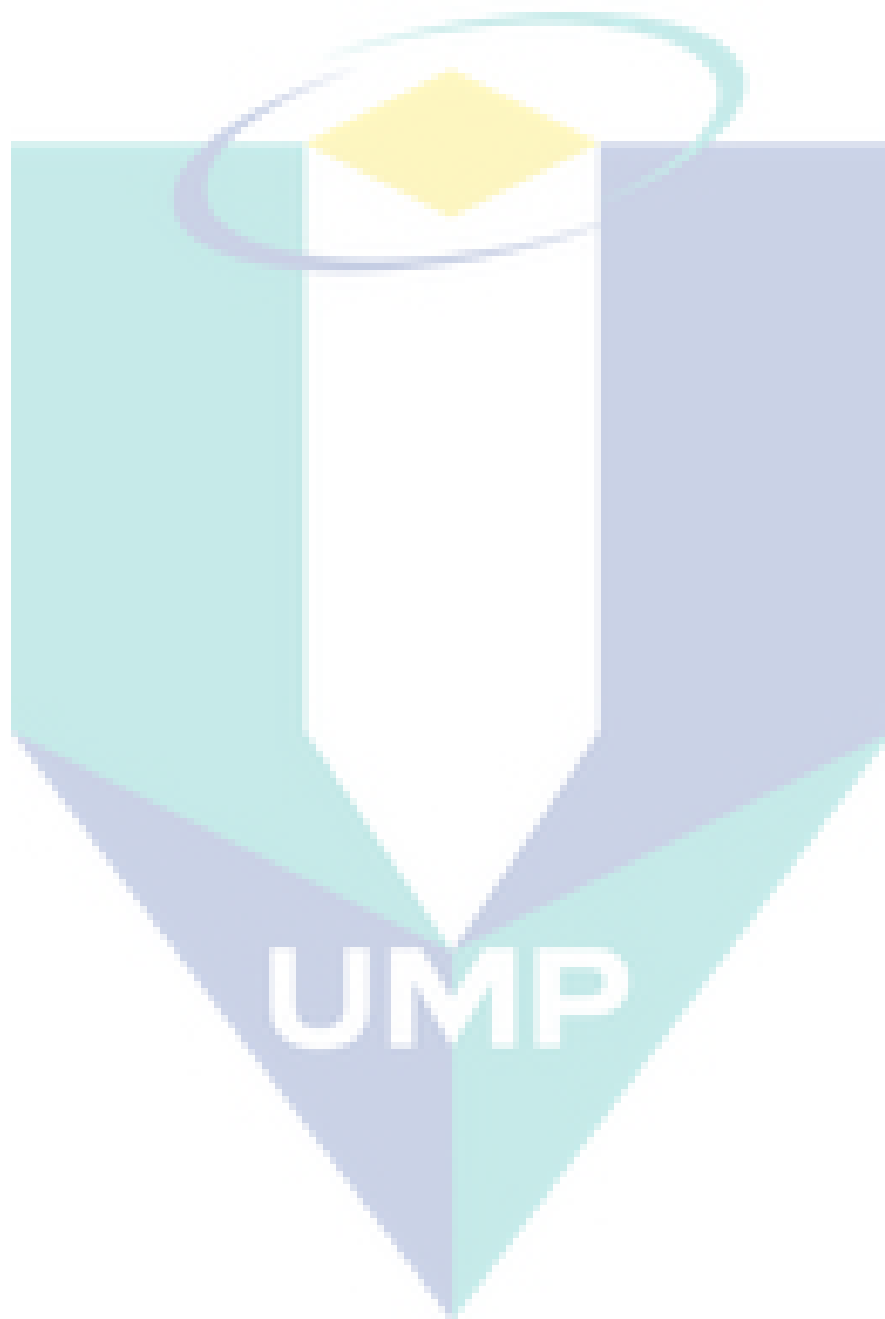
combinations were conducted to achieve the third objective of this research as shown in Figure 3.29.

3.5.4.1 Experimental setup

The set of the experiments in this group was carried out inside the same 2-D flow chambers with the same dimensions. The LTV system was also the same. However, the main difference in the experimental setup in this group was establishing the rainfall simulation as will be discussed in the next subsection.

3.5.4.2 Rainfall simulation

Rainwater was required to observe the influence of rainfall recharge to the LNAPL migration. For a typical rainfall simulation, the characteristics that should be considered are drop size, intensity, and kinetic energy (Dunkerley, 2008). In this study, a dripping method was used to simulate the rainfall event due to the ease of installation and its economic advantage (Kamaruddin, 2012). Dropping method needs least tools which is considered relatively cheap as compared with other methods which need more complicated tools (Kamaruddin, 2012). Since the dripping method was used, uniform rainfall and drop size do not resemble natural raindrops (Kamaruddin, 2012). Simulation of rainfall by dripping method purposely allows the water infiltration to occur as a recharge. Therefore, the influence of kinetic energy on the model surface has been neglected. The simulation of rainfall was designed to produce no ponding at the surface of the soil sample. Water was released from an adjacent tank to flow to a horizontal pipe above the top of the flow chamber. A manual valve was used to control the water flow to produce a constant flow rate. For all experiments, small holes were drilled along the horizontal pipe at every 4 cm-distance to produce the artificial rain. The system was pre-tested by releasing water drips into a pan to estimate the water flow rate. Lee et al. (2011) reported that the rainfall intensity is equal to the flow rate when the rain event occurs over a certain area.



3.5.4.3 *Experimental Procedures*

The flow chamber was initially packed with the double-porosity media as discussed in chapter 3. After packing, the model was fully saturated with distilled water from the bottom ports. Thereafter, each experiment was divided into three stages as laid out in the following subsections.

a. Water drainage

After fully saturating the flow chamber with water, the drainage valve connected to the bottom ports was opened to allow for water drainage. The top of the flow chamber was opened to avoid producing of vacuum state. This stage was pre-tested to determine the standard duration before the experiments were conducted.

b. LNAPL injection

In this stage, either one of two volumes of toluene was released from the top of the flow chamber through the double-porosity soil sample using a syringe. The low volume was 50 ml (1.67 ml/cm²) whereas the high volume was 100 ml (3.33 ml/cm²). These LNAPL volumes were determined based on a previous study conducted by Ramli (2014). In his study, he observed the influence of rainfall on LNAPL migration in 1-D column filled with silica sand. He used 25 and 50 ml of NAPL in his study. Based on the difference in the size of the column used in his study and the flow chamber used in the current study, double volume was chosen for the low and high LNAPL. After the LNAPL was released, the camera started automatically to capture images for LNAPL distribution.

c. Rainfall event

Using the upper valve connected to the water tank, the flow rate was controlled to simulate the light and heavy rainfall. Specifically, prior to starting each experiment, the valve was opened for about 5 minutes to release the water and the volume of the released water was measured using a beaker in order to get the required rainfall intensity. After the rainfall was stopped, the model was left to stabilize and the observation of the LNAPL behavior was continued until it reached the stable state. All images were processed using IPP software to extract the light intensity values. The light intensity was then visualized using Surfer software.

Before starting the experiments, a trial experiment was conducted to determine the ideal time for water drainage and LNAPL infiltration in the double-porosity soil. Specifically, prior to LNAPL migration stage, the system was water drained until the sample reached equilibrium in the vadose zone and capillary zone. The equilibrium phase was tested based on the changes in the light intensity for the captured images during the pre-test. The duration taken at this stage was used later as a standard duration for the drainage stage for all the rest of the experiments. The trial experiment was carried out in the same flow chamber that was used for all the subsequent experiments. The sample preparation, as well as the experimental procedure, are also similar to all experiments. The sole difference in the trial experiment is the time duration where it is much longer compared to the real experiments. The trial test was carried out over one day where the first 6 hours was dedicated to water drainage while the rest of the time was for LNAPL migration. The test was conducted using the high LNAPL volume which was considered as the critical case. The observation was based on the changes in the average light intensity for the captured images during the water drainage phase as well as LNAPL infiltration phase. From observation, the water drained very fast from the flow chamber because the double-porosity samples have a high permeability. This fact is due to the presence of macro-pores in double-porosity which contribute to the increase in the velocity of fluids through it (Ngien et al., 2012b). The drainage process reached a stable level in less than 3 hours (i.e 2 hours 47 minutes). Therefore, the duration of the water drainage stage for all experiments was set at 3 hours which represents the stable state for the vadose zone and capillary zone as in the natural state.

After 6 hours, the LNAPL was injected into the flow chamber and the movement of the LNAPL was observed until it reached a stable depth. The duration for the tested LNAPL to reach a stable depth was used later for all experiments as a standard duration for LNAPL injection stage. From the observation, it can be seen that as time increases, the light intensity of the LNAPL changed in the double-porosity which means a variation in LNAPL saturation. The light intensity of the LNAPL varied in the vadose zone as well as in the capillary zone with the increase of time. This variation in light intensity was due to the LNAPL movement from the point of release in the upper zone to the capillary zone. The LNAPL continued its migration until it reached the capillary zone, and then it took some time to reach the stable state. The required time for the

LNAPL to reach a stable state was approximately 6 hours. Figure 3.31 shows the water drainage and LNAPL infiltration to determine the duration for the stable condition in the trial experiment. After that, the same procedures discussed in sections 3.5.2 and 3.5.3 were followed in order to extract the light intensity of toluene.

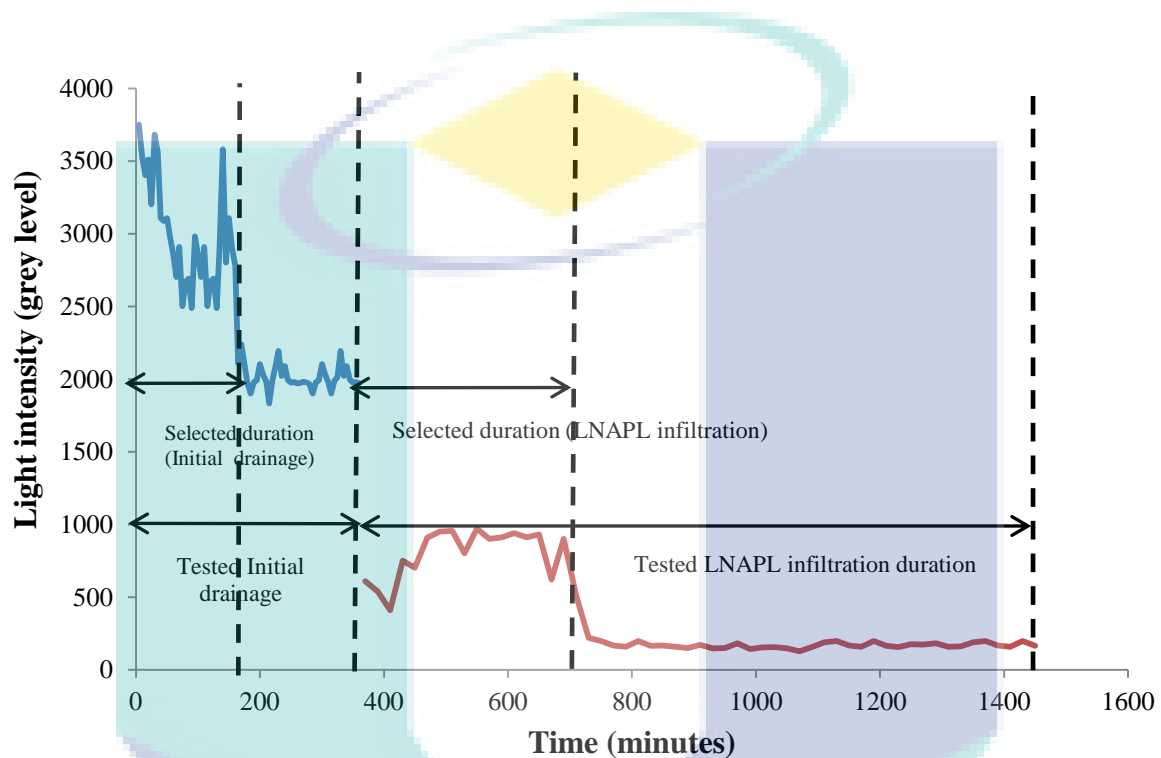


Figure 3.12 Trial test for water drainage and LNAPL infiltration to determine the duration for stable conditions

3.5.5 Group (4) Correlation of the DNAPL migration to the macro-pores and micro-pores within double-porosity soil structure

Understanding fluid flow transport in porous media is important to natural soil science (Ghanbarian et al., 2015). Fluid flow in subsurface systems is influenced by several factors. One of these factors is the soil structure. As presented earlier in this study, the double-porosity soil is a significant micro-structure property that has two distinct scales of porosity. It is believed that the difference in the volume of the materials that used to build the double-porosity medium may affect the migration of the NAPL through it. Therefore, this group of experiments aims to achieve the last objective of this thesis which is correlating the DNAPL migration to the macro-pores

and micro-pores by using a different volumetric fraction of kaolin spheres and silica sand to build the double-porosity medium. The same equations that derived in Section 3.3 were used to calculate the DNAPL saturation in the double-porosity soil. The DNAPL migration behavior was investigated in two experiments having two different volumetric fractions of kaolin spheres and silica sand. These two experiments were combined to Experiment 1 from group 1 in order to find the relation between the constitution of the double-porosity using different volumetric fractions of macro-pores and micro-pores, and the DNAPL migration velocity through it.

The experimental setup in this group of experiments is the same as in the group 1. However, the sole difference is the volumetric fractions of macro-pores and micro-pores in each experiment. The same procedures were used to build the double-porosity using the same materials. PCE was used as the DNAPL as in the previous experiments.

Two experiments refer to Experiment 11 and 12 were carried out in this group. For Experiment 11, the volumetric fraction of the (sand) macro-pores was 55 % whereas the (clay spheres) micro-pores fraction was 45 %. For Experiment 12, the macro-pores were increased 5 % to be 60 % macro-pores and 40 % micro-pores. These differences resulted in different weights of silica sand and kaolin clay fractions which in turn differ in sand layers thickness. The thickness of sand layers was 1.12 and 1.10 cm for experiments 11 and 12, respectively. It is believed that this difference in the thickness of sand layers (macro-pores) may affect the DNAPL migration in double-porosity. After packing the flow chambers with the double-porosity mediums, the same procedures were followed as in group 1. IPP, as well as Surfer software, were used to analyze the PCE migration.

3.6 Summary

This chapter presented the materials used to carry out the laboratory experiments in order to achieve the aim of this study. In addition, the methodology of all experiments was discussed. Moreover, the image analysis procedures were illustrated. The next chapter will present the results of the conducted experiments as well as the materials properties.

CHAPTER 4

RESULTS AND DISCUSSION

4.1 Introduction

This chapter presents the results obtained from the laboratory experiments described in the previous chapter. The results of the soil characteristics tests performed on the sand and kaolin used in the experiments are presented in Section 4.2. Section 4.3 presents the results from the Group 1 while Section 4.4 expound on the results from Group 2. Sections 4.5 and 4.6 present the results of Group 3 and Group 4.

4.2 Soil Properties Results

4.2.1 Physical Properties

The results of the physical properties of the materials used in this research are presented in this section. Table 4.1 summarizes the physical properties of sand, raw kaolin and kaolin after burning. Detailed calculations of the physical properties can be accessed from Appendices D to I. The particle size distribution (PSD) of the sand and the raw kaolin obtained from sieve analysis are shown in Figure 4.1.

Based on the PSD curves as well as the coefficient of uniformity (C_u), the kaolin S300 can be classified as clayey soil, well graded while the silica sand can be classified as sandy soil poorly graded according to the BS:1377 standard.

Table 4.1 Physical properties for raw kaolin, burned kaolin and sand

Material	Test	Parameter	Value
Raw kaolin	Liquid limit	Liquid limit	37.20 %
	Plastic limit	Plastic limit	25.61 %
		Plasticity index	11.59 %
	Falling head permeability	Coefficient of Permeability	8.54×10^{-12} m/s
	Small pyknometer	Specific gravity	2.63
	Sieve analysis	Mean size, D_{50}	0.062 mm
		Coefficient of uniformity, C_U	1.01
	BET test	Surface area	2.016 m ² /g
Burned kaolin	Liquid limit	Liquid limit	ND*
	Plastic limit	Plastic limit	ND
		Plasticity index	ND
	Falling head permeability	Coefficient of Permeability	6.8679×10^{-12} m/s
	Small pyknometer	Specific gravity	2.65
	BET test	Surface area	1.37 m ² /g
Silica sand	Sieve analysis	Mean size, D_{50}	0.32 mm
		Coefficient of uniformity, C_U	2.37
	Constant head permeability	Coefficient of Permeability	2.78×10^{-5} m/s
	Small pyknometer	Specific gravity	2.69

*ND: not determined

From the previous table, it is worth mentioning that for the burned kaolin, some parameters are not possible to determine such as liquid limit and plastic limit due to the thermal effect on kaolin. Yilmaz (2011) reported that the exposure of kaolinite to a temperature above than 400 °C make it non-plastic. Therefore, in his study, he could only measure the Atterberg limits for the kaolinite under 20 °C, 100 °C and 200 °C. In addition, another study conducted by Zihms et al. (2013) reported that the liquid limit for kaolin exposed to 1000 °C cannot be determined because the clay not mixing properly with water and its behavior is somehow non-plastic. This means that the mixing motion ceased the sample liquefied and it was difficult to create a testable sample (Zihms et al., 2013). This behavior can be explained due to the high temperature 1000 °C that caused a dehydroxylation of kaolin followed by aggregation of particles and ended with sintering (Fabbri et al., 2013). Therefore, the kaolin particles become

hydrophobic where the hydrophobicity influences the dynamic properties of the clay such as grain-water and grain-grain interactions (Zihms et al., 2013).

The specific gravity of kaolin slightly increased after burning from 2.63 to 2.65. This increasing is because of the formation of larger particles due to the collapse of aggregates (Wang et al., 1990). This is in agreement with the study of Yilmaz (2011). The author did not observe a change in kaolin specific gravity under 600 °C. The small change in kaolin specific gravity in this research can be explained due to the high temperature 1000 °C as compared to the 600 °C that used in Yilmaz (2011)'s study.

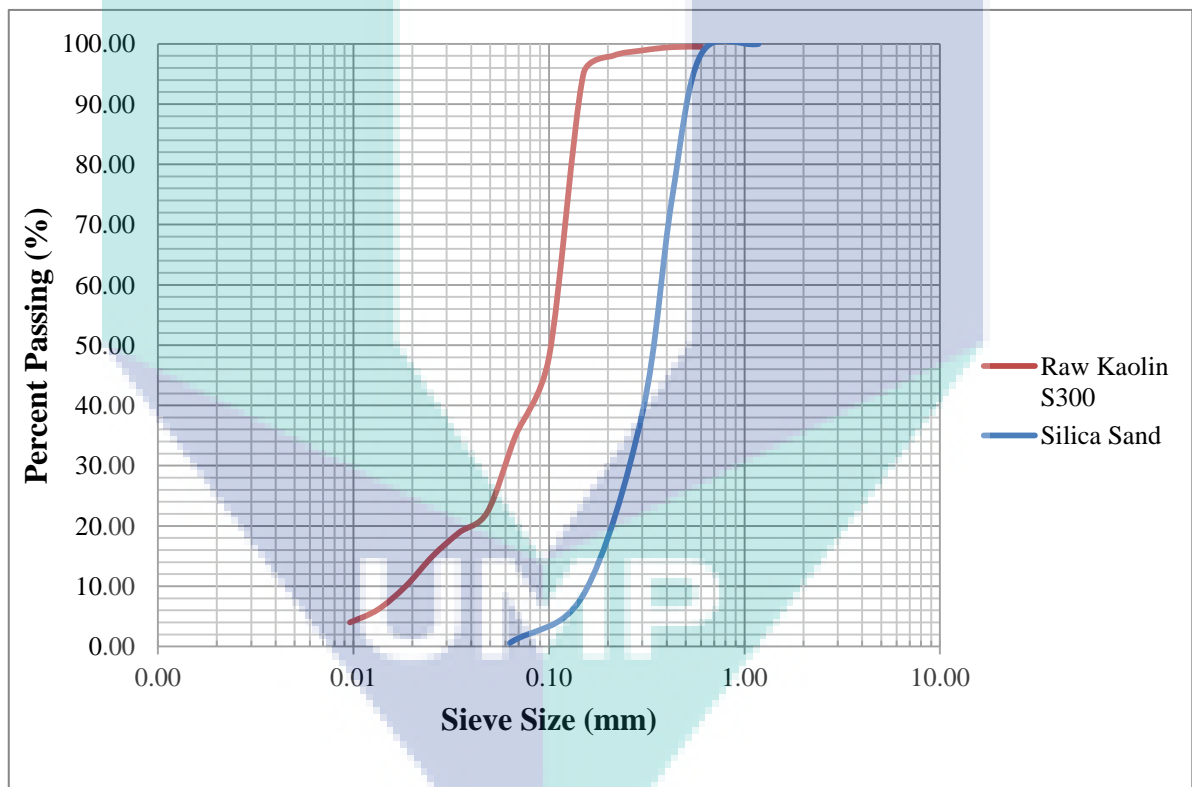


Figure 4.1 Particle size distributions for sand and raw kaolin using sieve analysis and hydrometer tests

Table 4.2 Sieve analysis breakdown

Sieve Size (mm)	1.18	0.6	0.425	0.3	0.15	0.063	Pan
% Passing (Silica sand)	99.97	98.27	74.14	38.66	8.61	0.58	0.00
% Passing (Raw Kaolin)	100	99.51	99.45	98.90	95.00	41.70	0.00

The surface area of kaolin decreased after burning from 2.016 m²/g to 1.37 m²/g. This change was occurred because the exposure of kaolin for high temperature lead to change the crystal structure of kaolin which in turn decrease its surface area (Edomwonyi-Otu et al., 2013). When kaolin is exposed to high temperature, the particle size will decrease due to the shrinkage and disintegration of clay particles that resulted from the removal of absorbed water (Yilmaz, 2011). The space between the 1:1 layers in the structure of kaolin is decreased which in turns decreased the available surface area of kaolin (Sarikaya et al., 2000). This result is linked to the specific gravity result where the temperature caused to increase the specific gravity of kaolin due to the collapse of aggregates and clogging of voids which in turn decreasing the surface area of kaolin.

The permeability of kaolin decreased after burning. This change is expected since several researchers reported that the temperature reduces the clay permeability due to different factors such as thermal expansion (Somerton, 1992), mineral dissolution (Tenthorey et al., 1998) or particle mobilization due to variations in the surface charges of the minerals (Schembre and Kovscek, 2005). A study by Rosenbrand et al. (2014), investigated the influence of hot water injection on the permeability of different types of sandstone, observed that the sandstones that contain kaolinite, the temperature reduced the permeability due to the kaolinite mobilization. Wong (1979) explained the reduction in permeability with increasing temperature is due to the particulate plugging due to the thermal expansion of mineral grains at pore throats. This result is linked to the change in kaolin specific gravity which was increased after burning due to the collapse of aggregates and clogging of voids by the dispersed clay minerals which in turns reduce the permeability.

4.2.2 Chemical Properties

The results from ICP-OES are usually obtained in (ppm) which in turn needs to be converted to meq/100g. Table 4.3 summarizes the CEC values for the raw kaolin and burned kaolin. Detailed calculation of the CECs is shown in Appendix J.

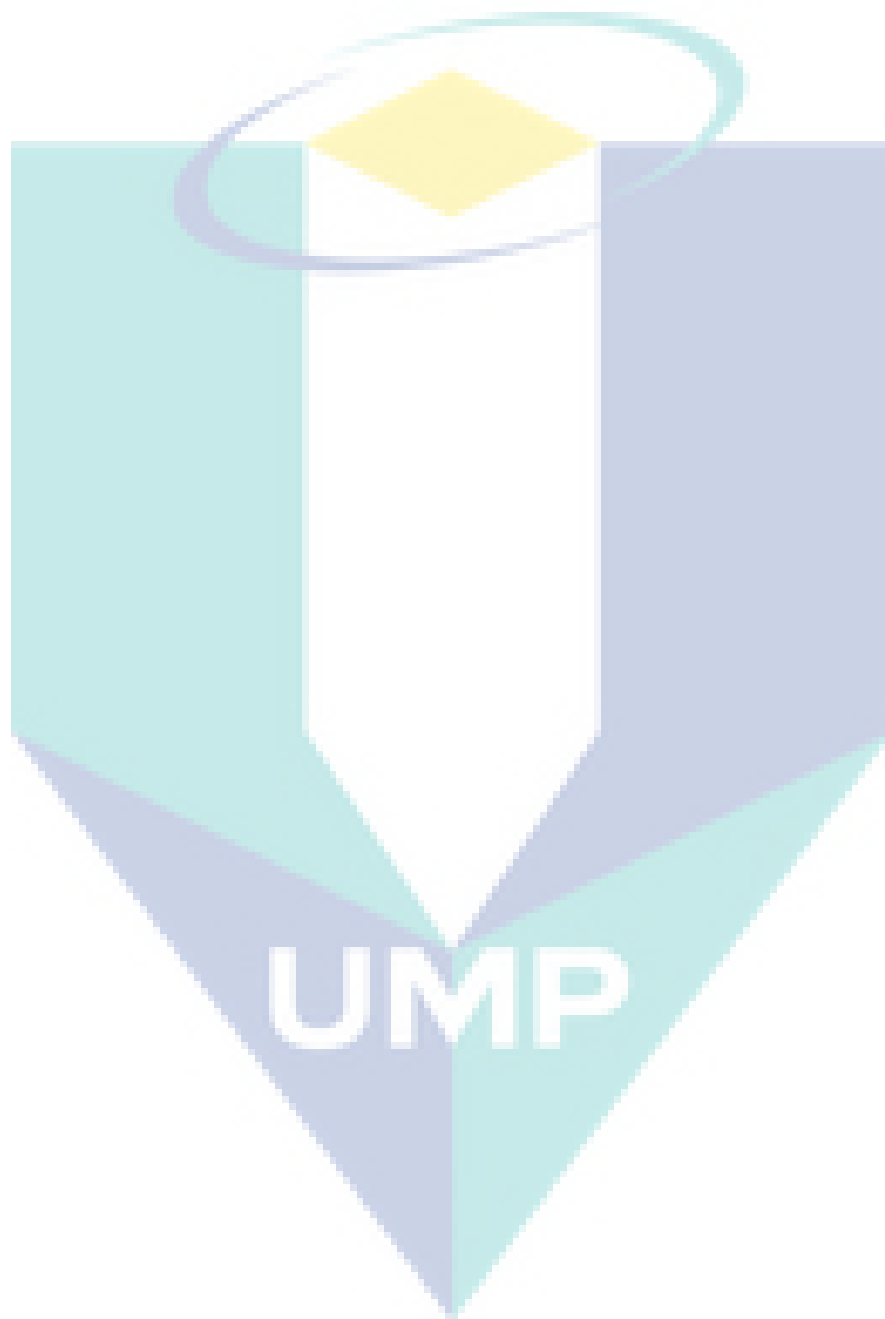
Table 4.3 CEC values for materials used

Element	Value (meq/100g)	
	Raw Kaolin	Burned Kaolin
Na ⁺	0.115	0.109
Ca ²⁺	0.207	0.205
Mg ²⁺	0.034	0.033
K ⁺	1.437	1.323
Total CEC	1.793	1.680

From Table 4.2, the CEC values for the raw kaolin and burned kaolin were found to be 1.793 meq/100g and 1.680 meq/100g, respectively. This result shows that the CEC value for kaolin was slightly decreased by the influence of temperature. There is an inverse relationship between the temperature and CEC value. As the temperature increases, the CEC decreases due to the reversible dehydration. The space between the 1:1 layers in the structure of kaolin is decreased which in turns decreased the available surface area of kaolin (Sarıkaya et al., 2000). Since the number of available cations depends on the available surface area, the CEC reduced by reducing surface area which emphasizes the surface area result. This result is in agreement with a previous study reported by Hedges and McLellan (1976). In their study, they tested four different types of clay where their composition was mainly kaolinite. They observed that the CEC values fluctuated under different temperature values, but all clays CEC were decreased at 1000 °C.

4.2.3 Mineralogical Properties

The XRD charts are presented in Figure 4.2. The XDR results indicated that the main mineral of the raw kaolin was kaolinite. Similarly, kaolinite was the main mineral of the burned kaolin. For silica sand, it was mainly composed of quartz as shown in Figure 4.2.



4.3 Results of The Experiments in Group (1)

4.3.1 PCE migration in double-porosity soil medium, Experiment (1)

Experiment 1 focused on the quantification of PCE saturations in 2-D, two-fluid phase systems in a double-porosity soil sample. Different amounts of PCE were injected into the flow chamber (i.e 1.0 ml, 2.0 ml, 4.0 ml, 6.0 ml, 8.0 ml, 10.0 ml, 12.0 ml). These PCE increments were cumulative (i.e every time adding 2 ml except the first increment). These increments were necessary to establish good mass balance. Since the PCE was dyed using Oil-Red-O, the absorption process and the light refraction have a significant effect in the determination of PCE saturations. When the PCE is dyed, it results in a reduction of the light transmission in the flow chamber. For PCE saturation calculation, important parameters were calculated and shown in Table 4.4.

Table 4.4 Important parameters calculated for Experiment 1 and Experiment 2

Term	Experiment 1	Experiment 2
Porosity	0.395	0.33
N_p (number)	51.27	36.2
Absorption coefficient (α_n)	0.260	0.172
Average pore diameter (d_o)	0.0079	0.0065
Transmission factor (τ_{wn})	0.993	0.9965

From Table 4.4, the porosity was calculated from the compaction of the two materials (sand and clay spheres) as shown in Appendix K. The total number of pores across the thickness of the acrylic model (K) was calculated from equations 3.20 and 3.21 for both materials as shown in Appendix L. The absorption coefficient (α_n) was measured in the laboratory using a spectrophotometer at wavelength 600 nm. The average pore diameter (d_o) was calculated as mentioned earlier in Section 3.3 (see Appendix M) and the transmission factor (τ_{wn}) was calculated from the calibration of the first increment of the PCE (see Appendix N). All these terms are important in calculating the DNAPL saturation.

As mentioned earlier, the transmission factor for the colored PCE-water interface (τ_{wn}) was unknown because the influence of the dye on the light refraction at the PCE-water interface was unknown. Therefore, a one step of mass balance calibration was used to

determine the transmission factor for the colored PCE-water interface (τ_{wn}). For this purpose, in the first image that was captured after the initial increment of PCE (1.0 ml of PCE), τ_{wn} was calibrated when I_N was calculated to give the exact amount of the injected volume of PCE (i.e. equal to 1.0 ml). Then, the resulted value of τ_{wn} was used in all subsequent calculations. The value of τ_{wn} obtained for PCE-water interface was 0.993 as shown in Appendix N. It is worth mentioning that all previous values were calculated pixel by pixel for all images. The detailed calculations of the first PCE increment were shown in Appendix O.

After calculating all PCE volumes as shown in Table 4.4, the injected volume of PCE was plotted against the calculated volume of PCE from image analysis as shown in Figure 4.3.

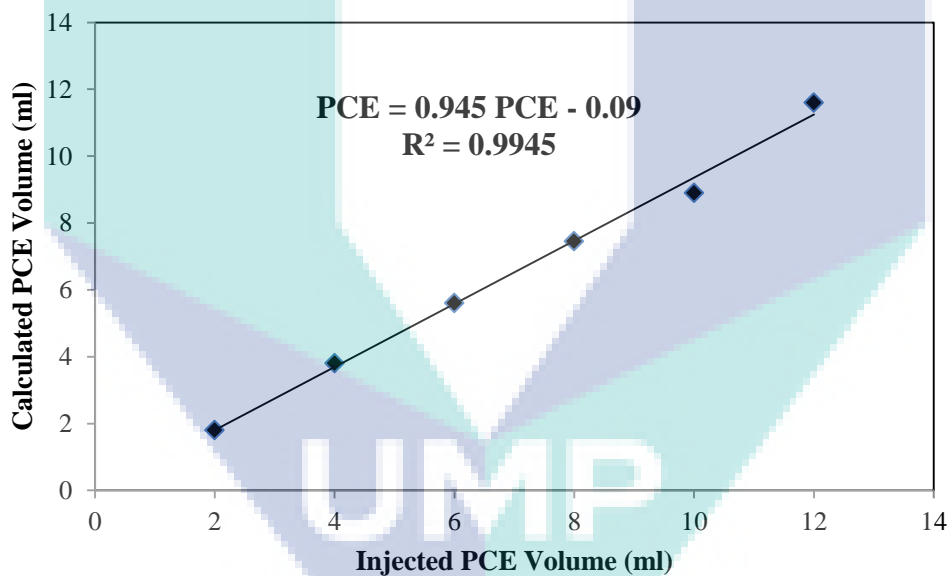


Figure 4.3 PCE volume calculated from image analysis vs. injected PCE volume into the flow chamber for Experiment 1.

Good correlation was found between the injected and calculated volumes of PCE ($R^2 = 0.994$). To calculate the overall deviation of the calculated PCE volumes from the injected volumes, the root mean squared error (RMSE) as given in Equation 4.1 was used.

$$RMSE = \sqrt{\frac{1}{N} \sum (V_{cal} - V_{inj})^2} \quad 4.1$$

where N is the number of PCE increments, V_{cal} is the calculated PCE volume from image analysis and V_{inj} is the injected PCE volume. V_{cal} was calculated following Niemet and Selker (2001) as follow:

$$V_{cal} = S_N \times \emptyset \times V_{pixel} \quad 4.2$$

where S_N is the saturation of the PCE, \emptyset is the porosity and V_{pixel} is the volume of one pixel. The V_{pixel} can be calculated by dividing the true dimensions of the flow chamber in (cm) by its dimensions in pixels from the IPP (Peng et al. 2015).

From the calculation, an RMSE value of 0.56 ml was found for the calculated data. The maximum error was 11 % where the minimum error was 3.33 %. This error in the calculation of PCE volume can be due to several factors as will be discussed in the next subsection. Another factor which can possibly results in this error is the volatilization of PCE. The PCE volatilization depends on different factors such as the area/volume ration, the concentration of PCE, and the organic carbon content (Zytner et al., 1989).

As shown in Figure 4.3, the image of the initial PCE increment (1.0 ml) was excluded from the graph since it was used to calibrate the transmission factor for the colored PCE-water interface.

Table 4.5 Injected and calculated volumes of PCE for Experiment 1

Injected volume of PCE (ml)	Calculated volume of PCE (ml)	$(V_{cal} - V_{inj})^2$	Error (%)
2.00	1.80	0.0400	10.0
4.00	3.80	0.0400	5.00
6.00	5.60	0.1600	6.66
8.00	7.45	0.3025	6.87
10.0	8.90	1.2100	11.0
12.0	11.6	0.1600	3.33
Total		1.9125	

$$RMSE = \sqrt{\frac{1}{6} \sum (1.9125)^2}$$

$$= 0.48$$

4.3.1.1 Errors in mass balance calculation

Many types of errors that influence the light intensity measurements have been reported by several researchers such as (Tidwell and Glass, 1994; Bob et al., 2008) as follows:

- Errors in the measurements of light intensity are usually the results of the non-uniform variations in light source intensity as well as noise in the camera signal. Improving the stability of the light source can reduce the errors resulting from the variations in light source intensity. As suggested by Tidwell and Glass (1994), it is possible to improve the stability of the light source by minimizing the number of times the light source turned on and off. In this research, the variation in light intensity was minimized by switching on the light source approximately 30 minutes before the start of the image acquisition and leaving it turned on during the whole duration of the experiments. Light emitting diodes (LEDs) can be also used as a more stable light source (Bob et al., 2008). Since noise in the camera signal existed in every pixel, it is believed that its influence does not affect the mass balance calculation since it averages out in the summation of all the pixels (Niemet and Selker, 2001).

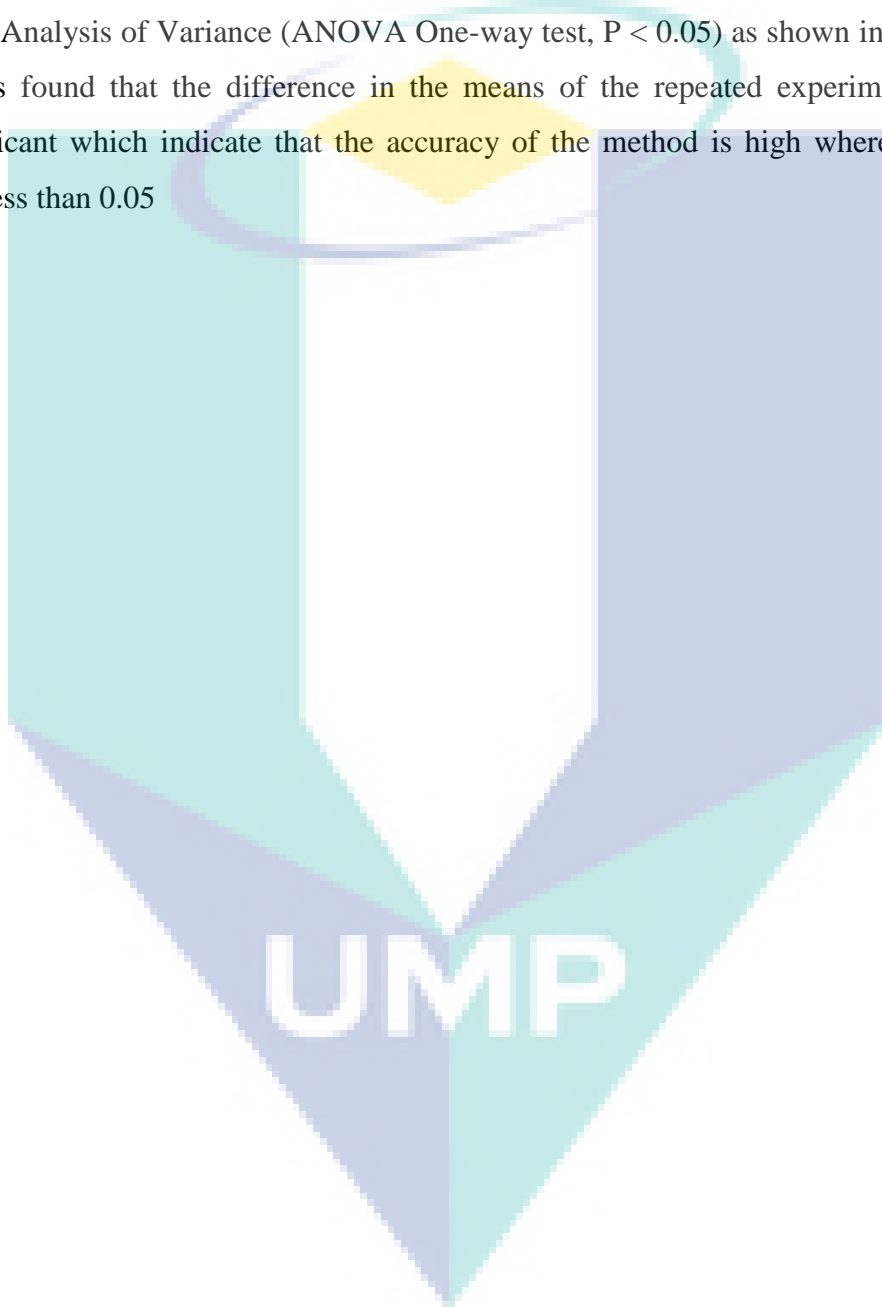
- On the top of the two factors aforementioned, there are other factors that may contribute to the error in mass balance calculation in these experiments. The conceptual model that was used to calculate the PCE saturation is one possibility. In the conceptual model, it was assumed that each pore was either full or empty of PCE and this may not necessarily be the case. In reality, it is possible that only a small fraction of the pore volume was filled with PCE which in turn resulted in an underestimation of PCE volumes by image analysis.
- Moreover, the conceptual model supposes that inside the flow chamber, the average pore diameter is the same whereas in reality the pore diameters are varied especially in clay spheres. All previous factors mentioned may contribute to errors in the mass balance calculation.

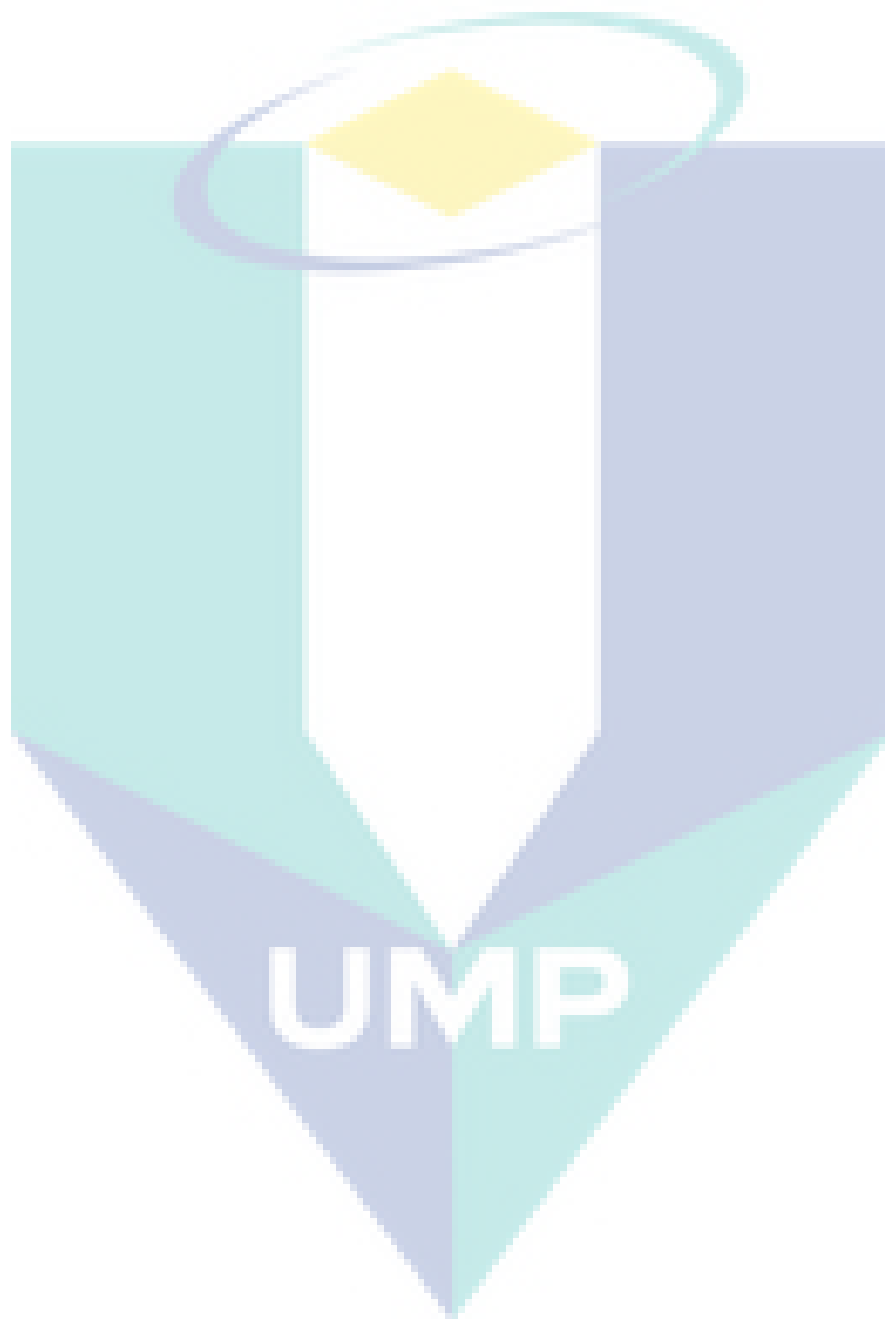
After calculating the PCE saturations, Surfer software was used to visualize the contour map of the PCE migration. Figure 4.4 portrays the PCE saturation distribution after 5 min, 10 min, 30 min and 60 min.

In the first 5 minutes, the PCE migration was very fast and it reached nearly halfway through the double-porosity sample as can be seen in Figure 4.4(a). After 5 minutes, PCE velocity slowed down significantly and reached the bottom of the flow chamber after 34 minutes before migrating horizontally across the bottom of the flow chamber. It is believed that the PCE flow would occur preferentially through the macro-pores since the size of the macro-pores were many times larger than the size of the micro-pores. This means that for pores that contain water, the PCE have to overcome a relatively lower capillary pressure to enter the macro-pores compared to micro-pores. Upon reaching the bottom of the flow chamber, the PCE migrated horizontally across the bottom side of the flow chamber. It is believed that in the top layers of the flow chamber, there were more macro-pores compared to the bottom layers. This situation is most likely due to an uneven compression in the top layers. This result is in agreement with Sa'ari et al. (2015). In their study, they observed the migration of LNAPL in double-porosity soil represented by aggregated kaolin. They noted that the downward

migration of the LNAPL was very fast during the first 100 seconds but the migration velocity gradually declined.

This experiment was conducted three times, and statistical analysis was used to validate the accuracy of the method as well as to compare the means and standard deviation using Analysis of Variance (ANOVA One-way test, $P < 0.05$) as shown in Appendix P. It was found that the difference in the means of the repeated experiments was not significant which indicate that the accuracy of the method is high where the P-value was less than 0.05





4.3.2 PCE migration in single-porosity soil medium, Experiment (2)

Experiment 2 was conducted following the same procedures as in the previous experiment. The sole difference was that the flow chamber was filled with only silica sand as a single-porosity medium to investigate the influence of the double-porosity characteristics found in Experiment 1 on the migration of PCE. In this experiment, the equations derived by Bob et al. (2008) was used for the PCE saturation calculation since the porous medium is single-porosity. For mass balance calculation, the findings were in agreement with the previous experiment where a good correlation was found between the injected volume of PCE and the calculated amount of PCE from image analysis ($R^2 = 0.989$) as shown in Figure 4.5.

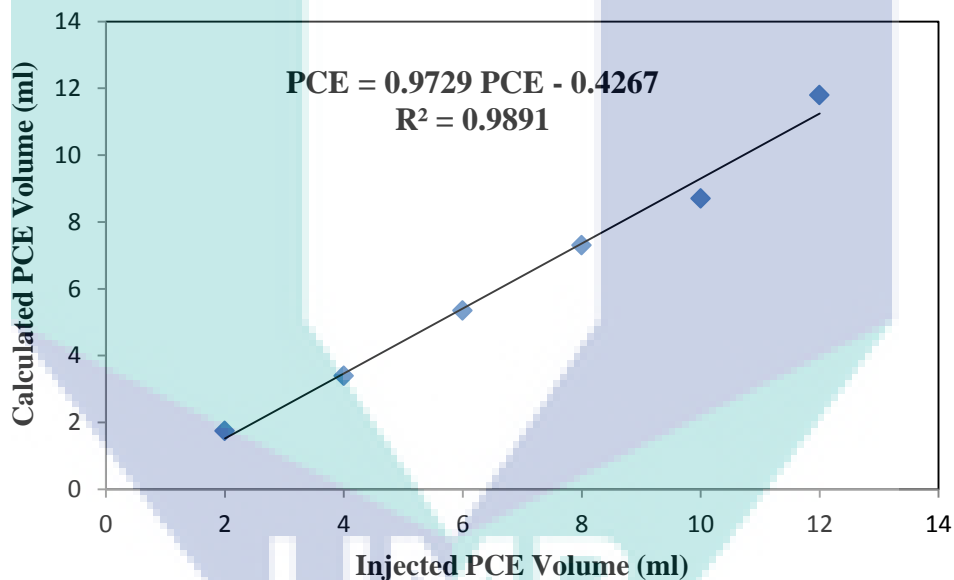


Figure 4.5 PCE volume calculated from image analysis vs. injected PCE volume into the flow chamber for Experiment 2.

The overall deviation of the calculated PCE volumes from the injected ones was also calculated as shown in Table 4.6, and the RMSE value was found to be 0.58 ml in this experiment where the maximum error was 12.5 % and the minimum error was 1.66 %. The range of the allowable error for RMSE is between 0.3 and 0.6 (Veerasingam et al., 2011).

Table 4.6 Injected and calculated volumes of PCE for Experiment 2

Injected volume of PCE (ml)	Calculated volume of PCE (ml)	$(V_{cal} - V_{inj})^2$	Error (%)
2	1.75	0.0625	12.5
4	3.65	0.1225	8.75
6	5.35	0.4225	10.83
8	7.55	0.2025	5.625
10	8.9	1.21	11
12	11.8	0.04	1.66
Total		2.06	

$$\begin{aligned}
 \text{RMSE} &= \sqrt{\frac{1}{6} \sum (2.06)^2} \\
 &= 0.58
 \end{aligned}$$

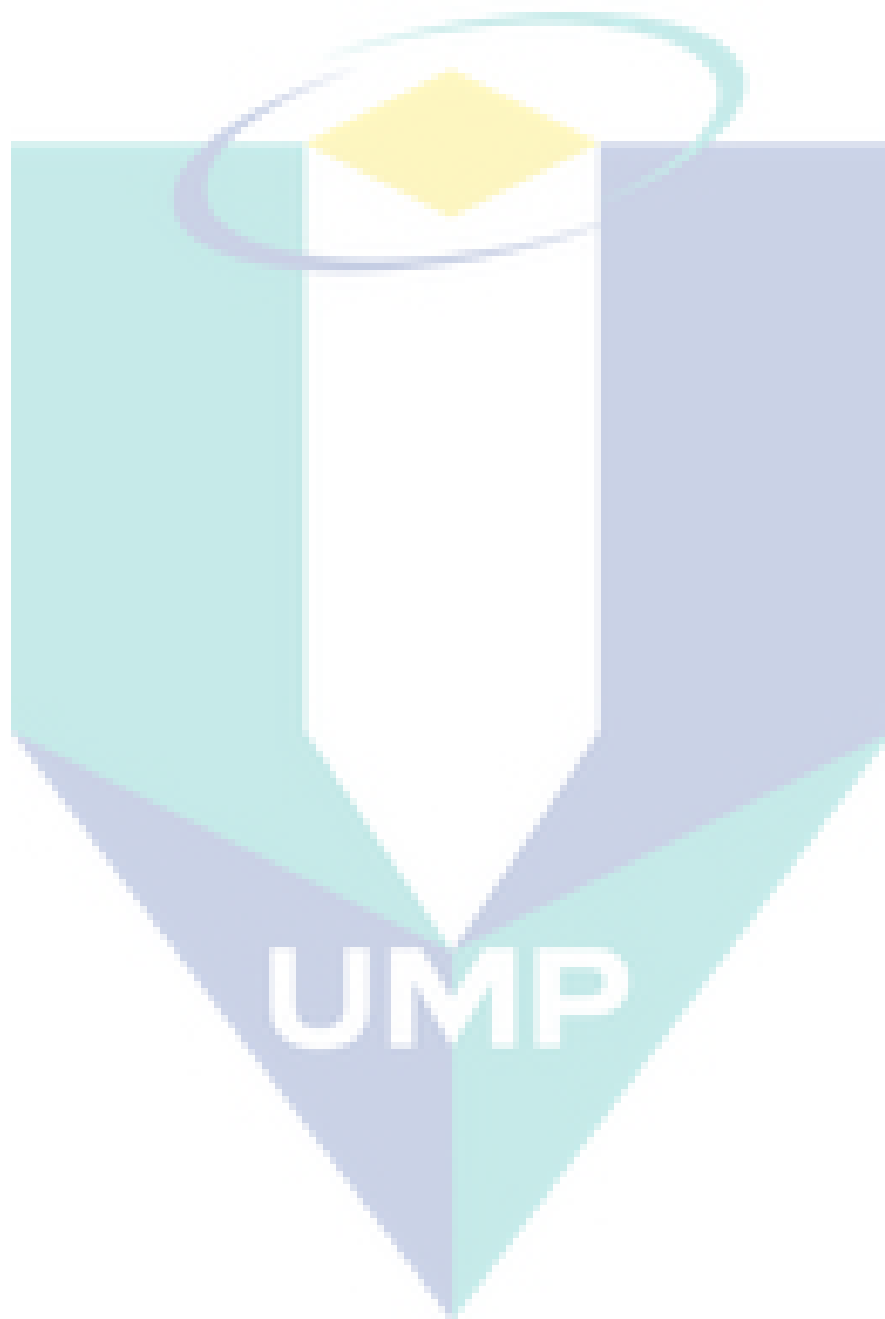
The transmission factor τ_{wn} was calculated following the same procedures as in Experiment 1. The transmission factor τ_{wn} obtained for PCE-water interface was 0.996 which is higher than that from the double-porosity case. As mentioned earlier, the absorption process has a significant effect in PCE saturation calculations with many factors influencing the absorption process. One of these factors is the average pore diameter (d_o) which is different for single and double-porosity mediums. It is believed that the light intensity through the flow chamber was reduced due to the different interfaces that resulted from the composition of double-porosity soil which in turn caused a decrease in transmission factor in double-porosity as compared to single-porosity.

For PCE behavior in single-porosity as shown in Figure 4.6, it is different from that found in double-porosity. It was clear that the velocity of the PCE in the sand is very small as compared to the velocity in double-porosity. The PCE migrated roughly 7 cm during 10 minutes of injection whereas, within the same duration in the double-porosity soil, it traveled more than half of the height of the flow chamber for the experiment in double-porosity medium. Basically, the two experiments were conducted under the same conditions, same PCE volumes and same flow chamber dimensions with the only difference being the type of medium used. It is believed that the main factor that influenced the PCE velocity is the porous media. Macro-pores in the double-porosity

soil, which constitute the main difference in the composition of single and double-porosity, have a substantial effect on the migration of PCE. The porosity in the double-porosity sample was higher than that in the single-porosity sample which means that the permeability in the double-porosity sample is higher than that of the single-porosity sample. This fact resulted in the higher PCE velocity in the double-porosity sample. This observation is in agreement with the findings of Ngien et al. (2012b). They conducted an experimental study for LNAPL migration in a 1-D column filled with double-porosity aggregated kaolin and compared their results with a study by Alias (2003) who conducted the same experiment using single-porosity, poorly graded sand. Ngien et al. (2012b) reported that LNAPL migrated much faster in double-porosity media as compared to those with single-porosity and this is due to the occurrence of macro-pores. Figure 4.6 shows the PCE migration in single and double-porosity soil mediums.

An interesting phenomenon of PCE flow behavior in the single-porosity was observed after 1 hour of migration. Some PCE portions appeared in the two corners at the bottom of the flow chamber. This behavior could be due to uneven compaction of the sand layers and it might also be that some PCE fractions were migrated faster at the back of the flow chamber and then appeared at the bottom. Another unexpected but interesting phenomenon in the single-porosity experiment was that when the PCE reached the bottom of the flow chamber; it climbed up the sides of the flow chamber against gravity as can be seen in Figure 4.6 (d). A similar occurrence was also observed by Bob et al. (2008) study which was explained due to the wall effect on the PCE migration. The wall effect is common in 2-D flow chambers and results in looser packing along the walls of the flow chamber than the rest of the chamber (Bob et al. 2008).

The experiment was carried out three times and the same analysis as in Experiment 1 was carried out as shown in Appendix Q. The PCE migration velocity within Experiment 1 and 2 is shown in Figure 4.7.



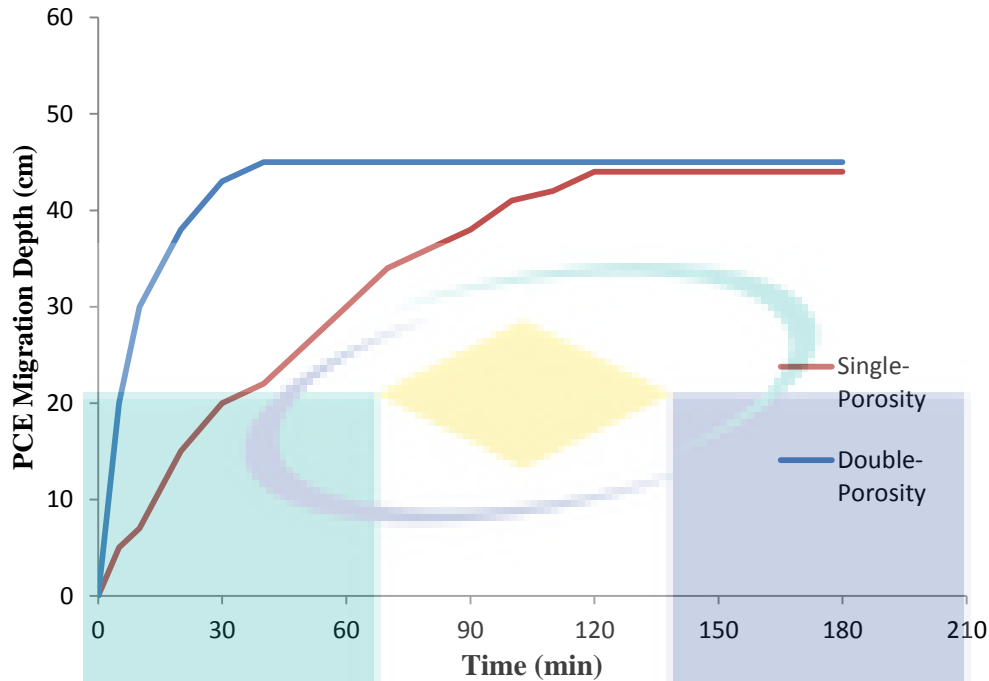


Figure 4.7 PCE migration in single and double-porosity soil mediums

Based on Figure 4.7, the PCE migrated fastest within the first few minutes in Experiment 1 as the gradient of the graph line was steepest within that duration. The same behavior is somehow similar to Experiment 2 but with less PCE velocity. In the experiment with double-porosity medium, the PCE reached the bottom of the flow chamber after 35 minutes as shown in the figure. After that, the movement of the PCE was stopped. However, in the case of single-porosity, the PCE continued its migration and reached the bottom of flow chamber after approximately 2 hours. After that, some parts of PCE moved up and climbed the sides of the flow chamber. As discussed earlier in this section, the main difference between the two experiments was the macro-pores that occur in double-porosity medium which caused the PCE to be more faster as compared to single-porosity.

4.4 Results of the Experiments in Group (2)

As mentioned earlier, the set of experiments in this group aims to achieve the second objective in this research which is the qualitative analysis of PCE and toluene migration in single and double-porosity in three-fluid phase system. The following subsections present the results of the experiments.

4.4.1 PCE migration in double-porosity, Experiment (3)

After opening the valve, a visual observation for the inclination of the water table during draining of the flow chamber was noted. From the differences in the transmitted light, the areas that have higher water saturation within the porous media can be easily delineated from the areas that have lower water saturation. The capillary fringe was clearly distinguished as a dry-wet boundary.

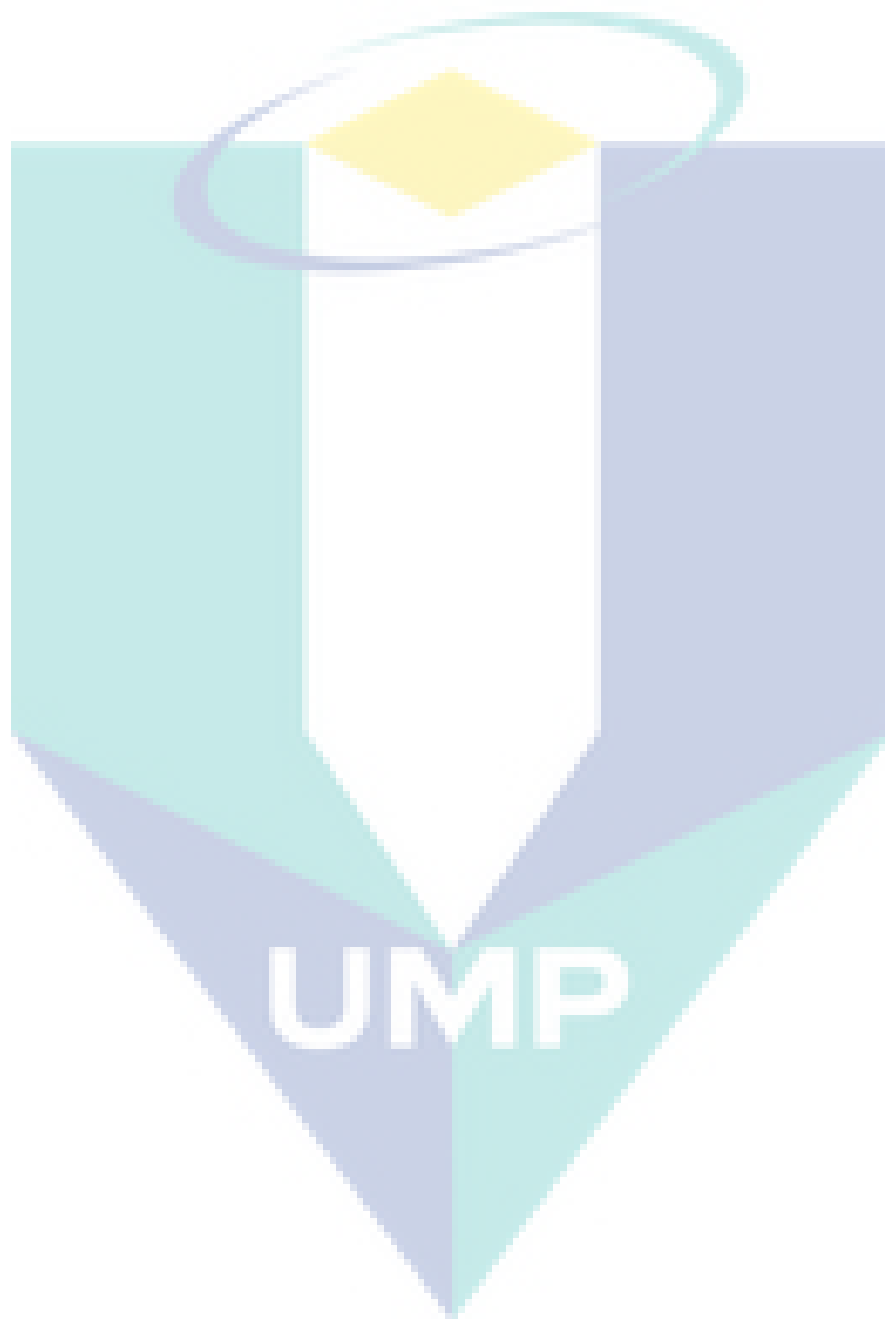
The water continued draining until it reached approximately 35 cm from the top of the flow chamber. The upper part is a simulation for three-fluid phase system (air- NAPL- water) whereas the lower part is still two fluid phase system (NAPL-water).

After releasing the PCE into the flow chamber, it started to move horizontally during the first three minutes before migrating vertically downward. It was observed that the PCE migration was slow in the three-fluid phase system zone as compared to its migration velocity in the two-fluid phase system zone. The PCE downward migration took about 76 minutes to reach the water table which translates to an average velocity of 7.6×10^{-2} mm/s as shown in Figure 4.8. However, when the PCE entered the two-fluid phase system zone, its migration rate increased substantially as compared to the velocity in the previous zone. This observation was most likely due to the existence of air in the three-fluid phase zone. When three fluids are present in a subsurface system, the largest pores are usually filled with air, whereas the smallest pores are occupied by water. NAPLs fill the intermediate pores (Schroth et al., 1998). In this experiment, the PCE migration was very slow in the three-fluid phase zone because PCE migrated through the intermediate pores and took more time to overcome the capillary pressure to enter the smallest and largest pores. In addition, another factor that probably influenced the PCE migration between the two zones is the wettability of the fluids present in the physical model. In the vadose zone, simulated by the upper zone in this experiment, water is usually a wetting fluid with respect to NAPL whereas NAPL is a wetting fluid with respect to air (Mitchell and Soga, 2005). At the pore level, the capillary pressure forces the wetting fluid to enter the pore and displace the existing fluid inside the pore while the non-wetting fluid will be repelled (Bear, 1972). Therefore, when the PCE was released into the flow chamber, it would have migrated and infiltrated initially through the air-filled pores since the PCE is the wetting fluid

with respect to air. This explanation was validated by observations during the experiment. It was noted that some air bubbles were observed at the surface of the flow chamber in the three-fluid phase zone which verified the explanation. This finding is in agreement with Ngien et al. (2012b). In their study, they observed the migration of LNAPL in 1-D columns filled with unsaturated double-porosity soil media using light reflection method. They noted that the wettability has a major influence on the migration of LNAPL in the double-porosity soil. Moreover, they noted the occurrence of air bubbles at the surface of the column that proves the influence of the wettability of fluids.

On the other hand, when the PCE entered the two-fluid phase zone, it continued its migration until it reached the bottom of the flow chamber. PCE migration took roughly 28 minutes from the water table until it reached the bottom of the flow chamber with an average velocity of 5.9×10^{-2} mm/s. This observation emphasized the wettability influence on the migration of PCE between the three-fluid phase system and two fluid phase system zones.

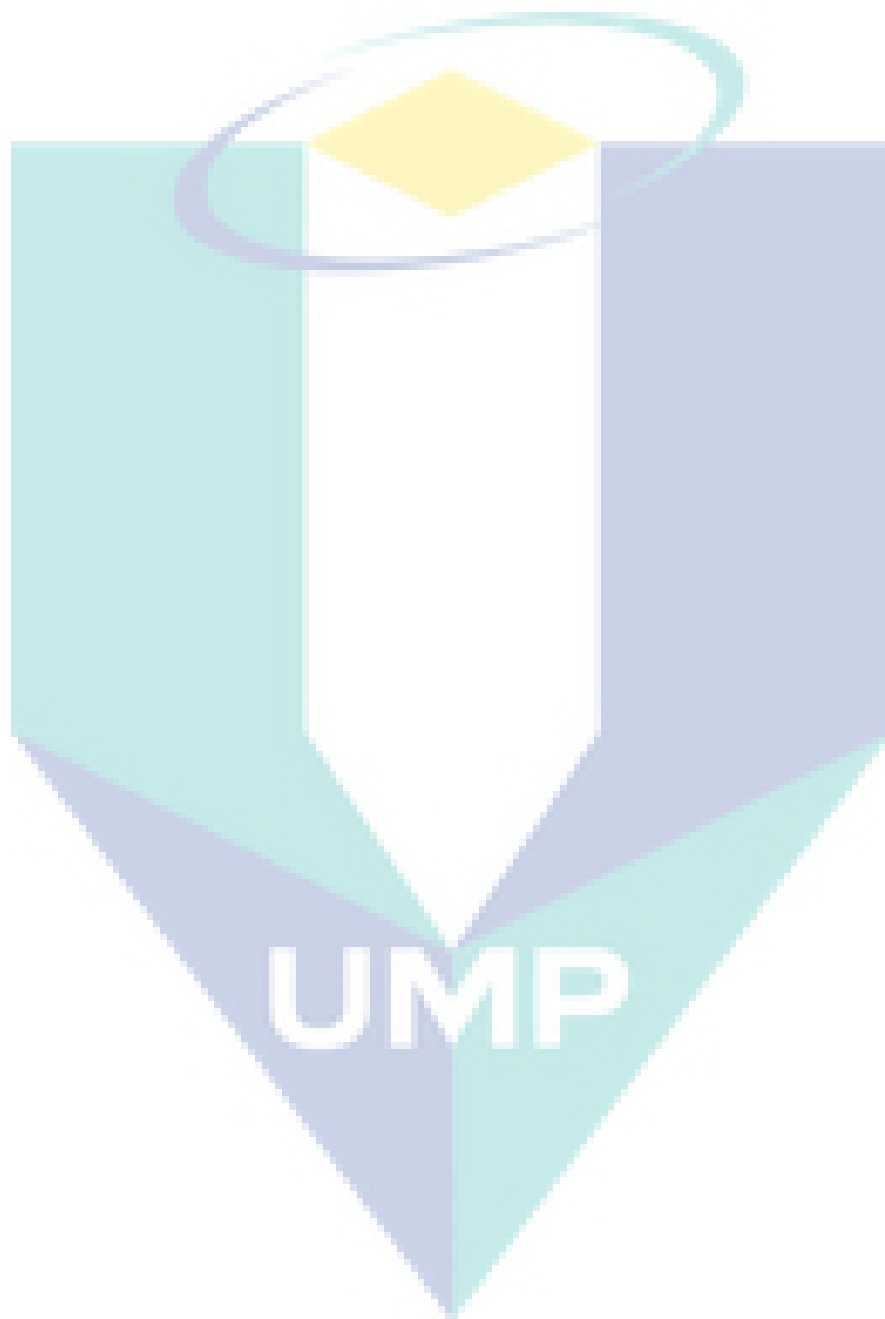
The behavior of PCE migration is shown in Figure 4.8. Comparison of repeated measurements showed similar results for the precision of the technique as shown in Appendix R.



4.4.2 PCE migration in single-porosity, Experiment (4)

A similar experiment with the same conditions as in the previous experiment was conducted but using only silica sand as the single-porosity media for comparison purpose. Similarly, 20 ml of PCE was injected into the flow chamber under the same flow rate. When the valve was opened for water drainage following the same procedures, the water level reached 13 cm from the bottom of the flow chamber, which is approximately one-third of the height of the flow chamber. The behavior of the PCE in Experiment 4 was almost similar to the behavior of the PCE in Experiment 3. Upon its release into the flow chamber, the PCE started to migrate horizontally along the top surface of the flow chamber before migrating vertically downward. It was noted that the PCE migration was very slow in the upper zone as compared to Experiment 3 at the same zone. The time taken by the PCE to reach the water table was 184 minutes, which translates to an average speed of 2.8×10^{-2} mm/s as compared to 3.3×10^{-2} mm/s in Experiment 3. This observation was most likely due to the occurrence of macro-pores in the double-porosity soil media in Experiment 1 that played a role in increasing the velocity of fluid through the soil media. The presence of macro-pores in double-porosity media means that a larger pore volume was present. It is known that the large pores contribute to reducing the capillary pressure that the NAPL need to overcome to go through these pores and thus migrate through the soil. Therefore, the velocity of fluid in double-porosity is much faster compared to single-porosity. This observation is in agreement with Ngien et al. (2012b). In their study, they compared the velocity of LNAPL migration between single and double-porosity soils and reported the same findings. They reported that the average speed of LNAPL was 0.417 mm/s in double-porosity soil compared to 7.5×10^{-4} mm/s in single-porosity.

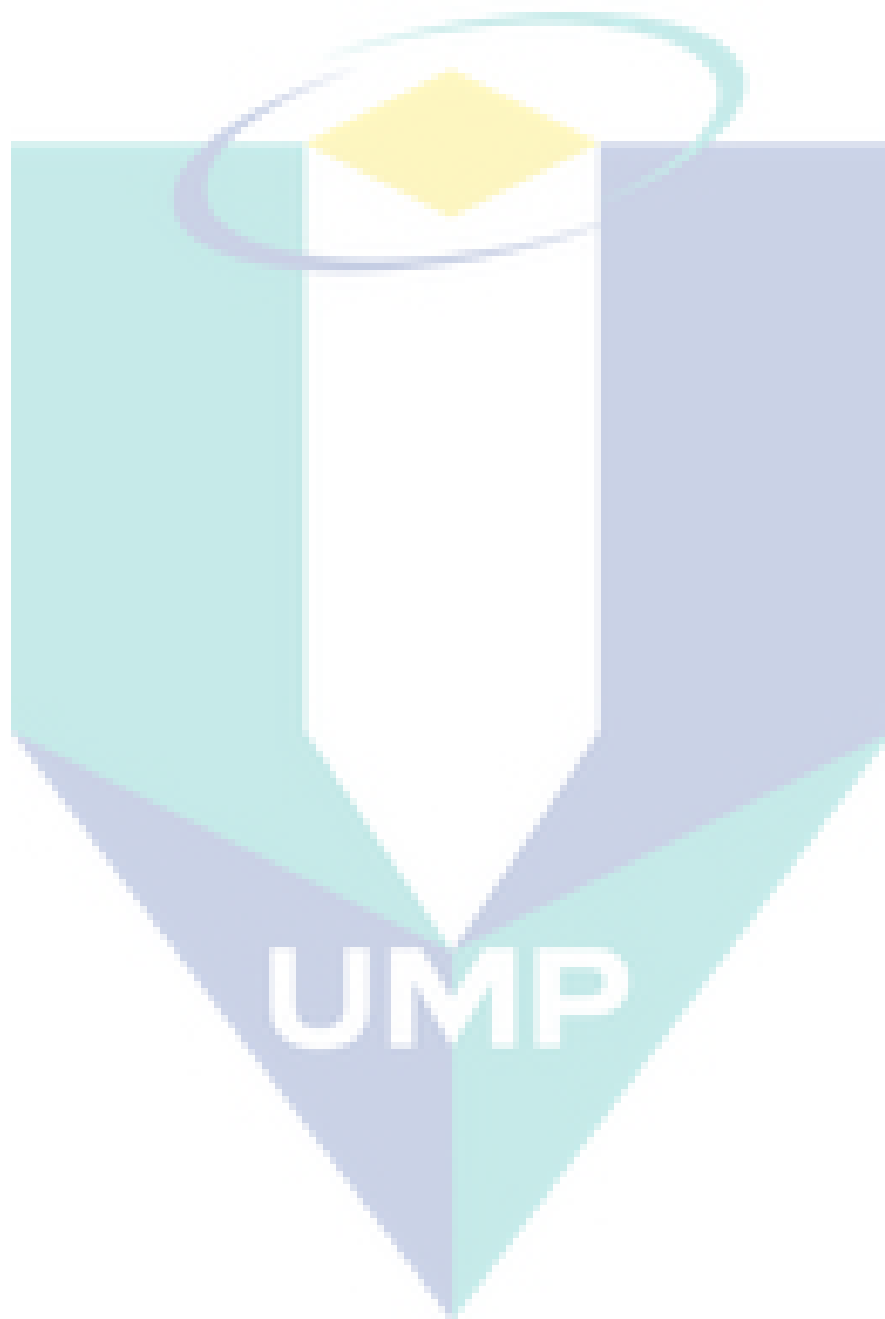
In addition, the PCE exhibited the same behavior in the two-fluid phase zone as the PCE migration was much faster in the two-fluid phase zone compared to the three-fluid phase zone in Experiment 4. The duration of PCE migration from the water table to the bottom of the flow chamber was 44 minutes which translates to an average speed of 4.9×10^{-2} mm/s compared to 5.9×10^{-2} mm/s in Experiment 3. The explanation for this occurrence is basically the same as that given for Experiment 3. Figure 4.9 shows the distribution of PCE migration during Experiment 4. The repetition of Experiment 4 is shown in Appendix S.



4.4.3 Toluene migration in double-porosity, Experiment (5)

Following the same procedures as in the previous experiments, 20 ml of toluene was injected into the flow chamber to investigate the behavior of the LNAPL migration in double-porosity media in three fluid-phase system. After opening the valve for water drainage, the water level gradually lowered until it reached 12 cm from the bottom of the flow chamber. Upon its release into the flow chamber, the toluene moved horizontally during the first two minutes and then migrated vertically downward until it reached the water table. The velocity of toluene migration was much faster compared to the PCE migration velocity in the three-fluid phase zone. Toluene took around 62 minutes to reach the water table compared to 76 minutes for PCE. This observation can be explained by the difference in the chemical characteristics of the two materials. The significant factor influences the fluid transportation underground is the distribution coefficient (K_D) of substances (Ruffino and Zanetti, 2009). The distribution coefficient of toluene and PCE reported by Ruffino and Zanetti (2009) were 0.521 L/kg and 0.963 L/Kg, respectively. This means that the retardation factor of toluene due to adsorption is lower than that for PCE in the same porous media. In addition, the material solubility in the water likely plays a significant role in contaminant migration. For the case of existing soil moisture, toluene will move faster as expected because it has higher water solubility compared to PCE. This result emphasizes the fact that chemical properties of the NAPL have considerable influence on their migration through porous media. This result is in agreement with Kamaruddin (2012) study. In her study, she observed that the benzene infiltrated deeper into the porous media as compared to toluene. This is most likely due to the difference in the distribution coefficient between benzene and toluene, where the distribution coefficient of benzene is 0.142 L/kg.

Consequently, after toluene reached the water table, it floated on the surface of the water table and the downward migration of the toluene ceased as expected. Figure 4.10 shows the distribution of toluene in the double-porosity soil during Experiment 5. This experiment was repeated, and the result is shown in Appendix T.



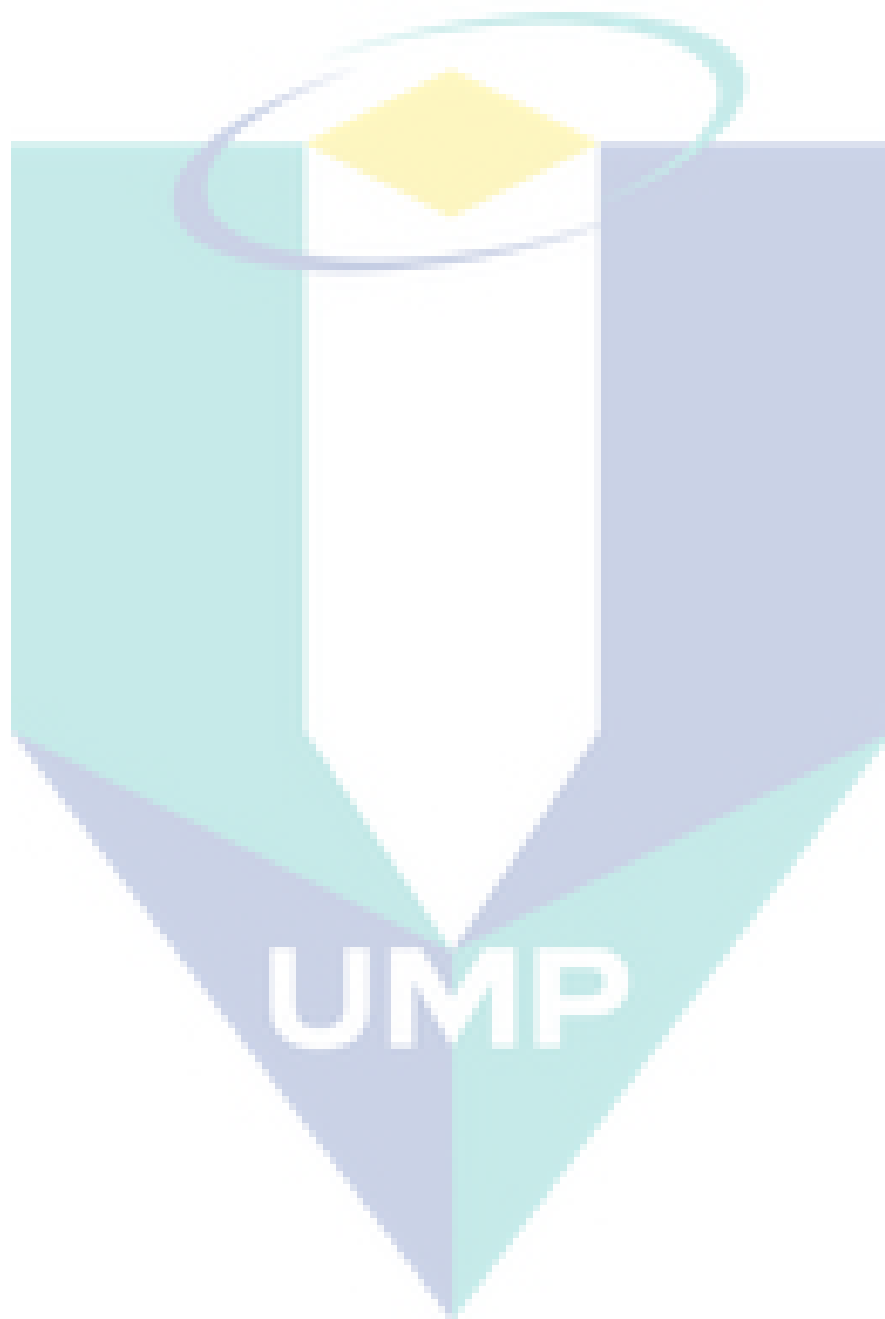
4.4.4 Toluene migration in single-porosity, Experiment (6)

In Experiment 6, toluene was applied to investigate its migration in silica sand as a type of single-porosity media. The same procedures were followed as mentioned in the previous experiments. Toluene exhibited the same behavior as in Experiment 5 but the major difference was in the migration velocity when compared to the case of double-porosity. Toluene took more time to reach the bottom of the flow chamber as compared to the behavior in Experiment 5. Toluene took approximately 92 minutes to reach the water table. The explanation of this behavior is the same as mentioned in section 4.4.4. This proves that the macro-pores have a significant influence on the fluid migration in porous media through three-fluid phase system. The distribution of toluene during the experiment is shown in Figure 4.11.

From the results of all the experiments, it can be summarized that several factors influenced the movement of NAPL in subsurface systems when three-fluid phase existed include the chemical properties of the NAPLs. The repetition of this experiment is shown in Appendix U.

The logo for UIMP (Universitas Islam Malang) is a large, downward-pointing arrow shape. It is composed of four triangular sections meeting at a central point. The top-left and bottom-right sections are light blue, while the top-right and bottom-left sections are a darker blue. The letters 'UIMP' are written in white, bold, sans-serif font across the center of the arrow.

UIMP



4.5 Results of the Experiments in Group (3)

As discussed in Chapter 3, the laboratory experiments in Group 3 aim to achieve the third objective in this research which is studying the influence of rainfall recharge on LNAPL migration in double-porosity soil medium. The following subsections illustrate the results of the experiments.

4.5.1 LNAPL migration before rainfall recharge

In all the experiments, when the bottom valve was opened, the water drained from the fully saturated double-porosity samples due to the gravitational force. The occurrence of two types of porosity (i.e macro-pores and micro-pores) caused the water drainage process to be relatively fast and the capillary zone was observed after less than 3 hours. When LNAPL was released into the flow chamber, it migrated deeper into the double-porosity soil due to the gravitational force until it reached the capillary zone. The capillary zone was measured up to 32 cm of the flow chamber height, which left around 13 cm for the vadose zone. Based on the captured images, an obvious change in the shape and intensity of the red color of the toluene plume was observed during the experiment. All images were calibrated by converting the images from RGB system to gray level system ranging from 0 to 4096 for black to white pixels, respectively using IPP software. The normalized image has a brighter plume and a darker background which contrasts with the original gray image that has a darker plume of LNAPL and a brighter background. The background of the normalized image is darker because the background of the plume image was subtracted from the background of the initial image. Any changes due to increasing LNAPL volume resulted in brighter pixels containing higher intensity value.

From the observations, the LNAPL migrated deeper during the first hour of migration and become slower for the next few hours. The migration depth of the LNAPL depends on the volume released where the LNAPL migrated deeper in the case of the high LNAPL volume. Visually, the LNAPL migrated 21 cm and 27 cm deep for the cases of 50 ml and 100 ml of spilled LNAPL, respectively. The LNAPL continued before ceasing when it reached the equilibrium at interfacial tension. Figure 4.12 shows the

migration rate of LNAPL for the low volume and high volume cases. From Figure 4.12, it can be seen that the LNAPL migration rate was much faster in the case of high volume compared to the case of low volume. This occurrence is most likely due to the higher weight of 100 ml which provided more pressure that pushed the LNAPL at a faster rate. Moreover, the higher volume of LNAPL provides a higher pressure to overcome the capillary forces in order to move into the finer pores saturated with water. High LNAPL volume took about 2 hours to reach the stable depth whereas the low LNAPL volume reached the stable depth after approximately 6 hours.

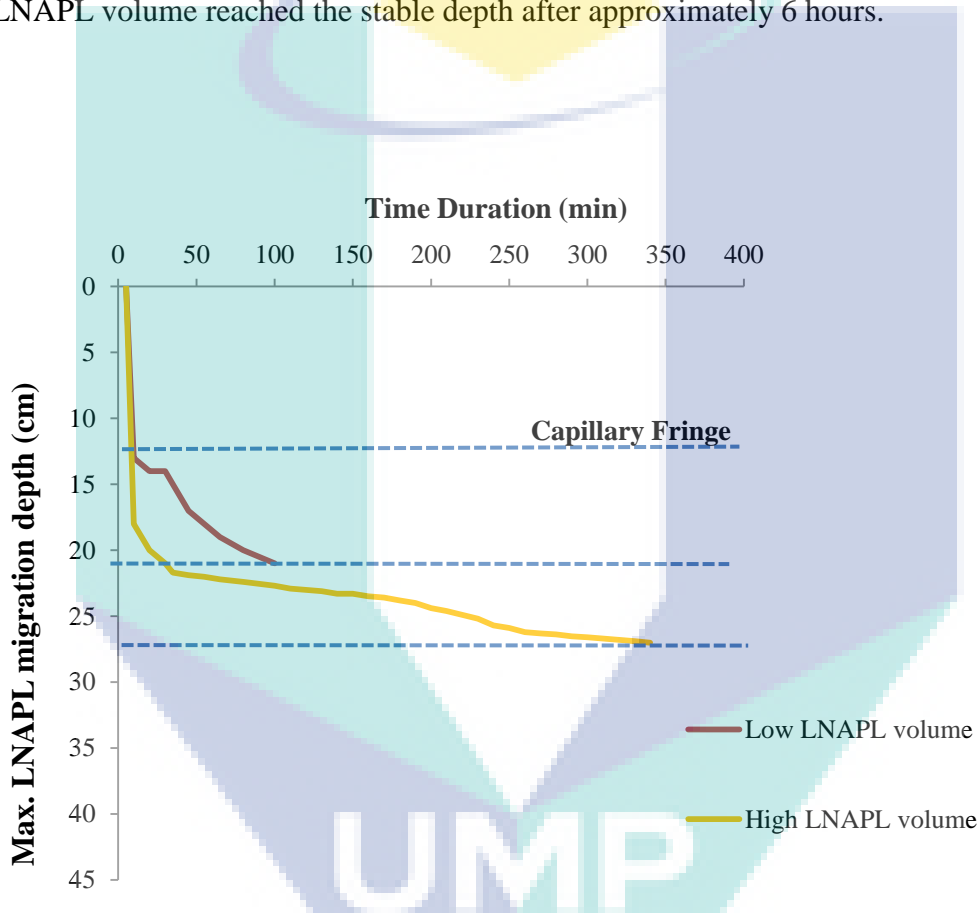


Figure 4.12 LNAPL migration depth for low and high LNAPL volume cases before rainfall recharge (Low LNAPL volume = 50 ml, High LNAPL volume = 100 ml)

4.5.2 LNAPL migration after rainfall recharge

The LNAPL ceased to migrate deeper upon it reached a stable depth because both LNAPL and water have reached the interfacial tension equilibrium. This status changes as soon as rainfall infiltrates the contaminated double-porosity soil. The

contaminated flow chamber was exposed to a rainfall event for 2 hours after being observed for 2 hours for the high LNAPL volume case and 6 hours for the low LNAPL volume case. The influence of the rainfall recharge on the LNAPL migration can be easily studied using the differences in light intensity of the LNAPL migration images. After the LNAPL reached the stable depth, its migration ceased because both the LNAPL and water had reached the interfacial tension equilibrium. This status started to change as soon as the rainfall recharge began to infiltrate the contaminated double-porosity layers. The rainfall recharge was subjected to a gravitational force which in turn flowed towards the groundwater table. In general, it can be said that the rainfall recharge caused the LNAPL entrapped in the porous media to be pushed downward in all the experiments regardless of the LNAPL volume or rainfall intensity as shown in Figure 4.13. However, the rate of the LNAPL downward movement was different. The LNAPL migrated downward until it became entrapped in the capillary zone. The LNAPL reached a depth of 25 cm and 36 cm for low and high LNAPL spillage volumes, respectively.

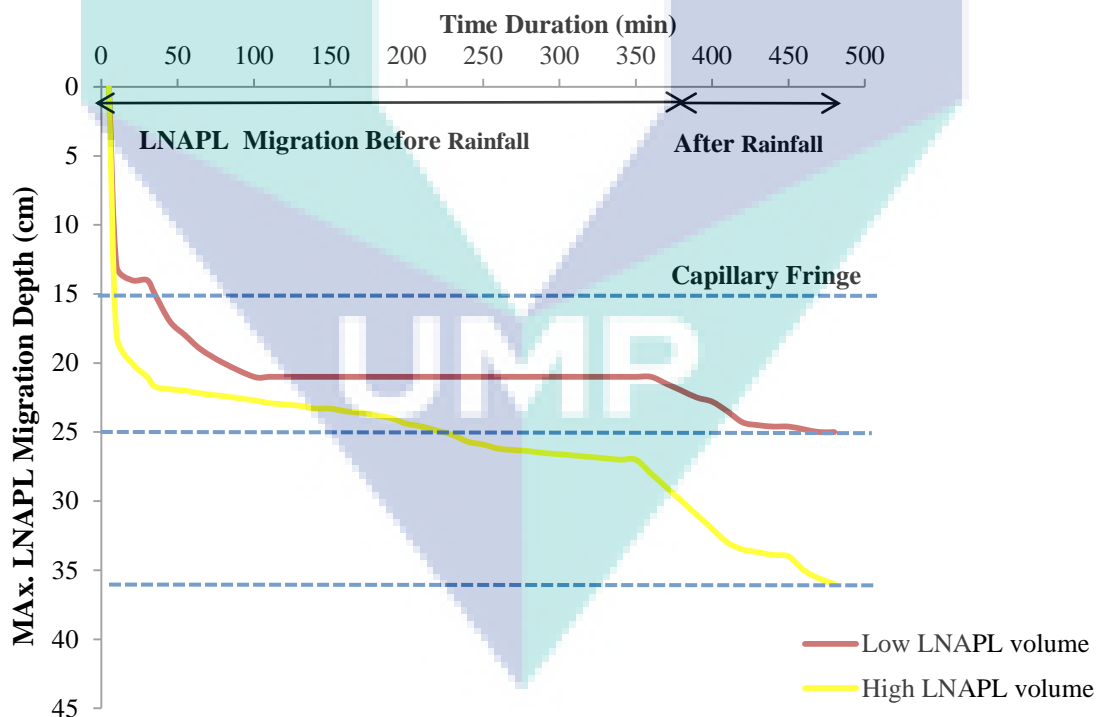


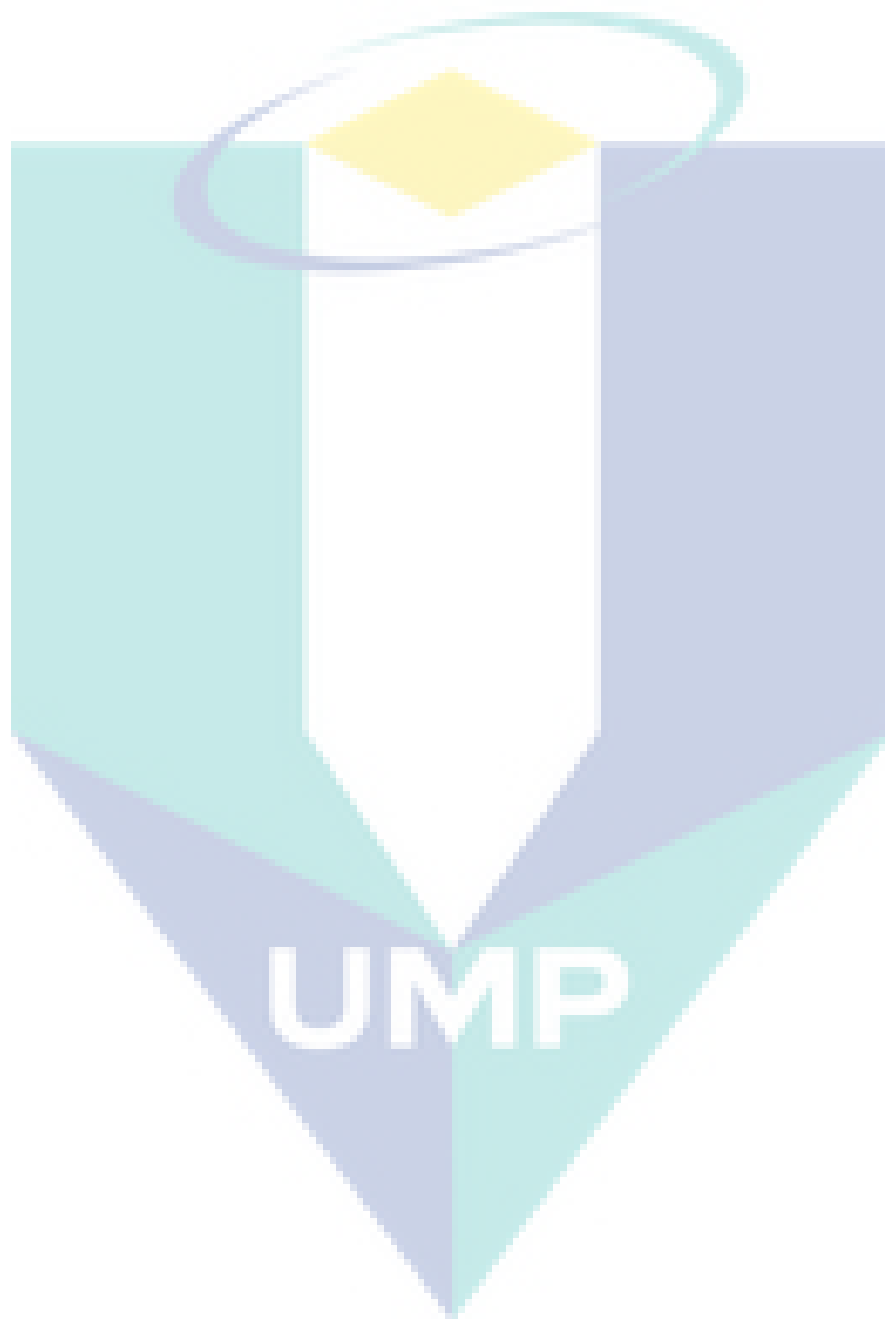
Figure 4.13 Influence of rainfall on LNAPL migration for low and high volume cases (Low LNAPL volume = 50 ml, High LNAPL volume = 100 ml)

Figure 4.14 reveals the influence of rainfall recharge on the LNAPL migration in double-porosity soil media. Furthermore, it was observed that the capillary fringe level was lowered in the saturated zone due to the influence of the rainfall recharge on the LNAPL plume. This observation is in agreement with a study conducted by Henry and Smith (2002). In their study, they reported that upon the surfactant solution reaching the capillary fringe, a depression of the capillary fringe was observed. Therefore, a new capillary fringe height was established which means that the contaminant can migrate deeper through the saturated capillary zone and pollute the groundwater. It is believed that the surfactant solution has a relatively similar effect compared to the LNAPL since both materials have a density less than that of water. The density of solution surfactant in Henry and Smith (2002) study is 0.99.

4.5.3 Influence of LNAPL spillage volume

Since the LNAPL density is lighter than that of water, once the LNAPL migrates downward due to the effect of the gravitational force, it will occupy the available pores. When the rainfall recharge infiltrates the contaminated double-porosity media, it will encounter the pores that are filled with LNAPL. Due to the fact that the water and the LNAPL are immiscible liquids, the rainfall recharge will push the LNAPL down until the LNAPL become entrapped in deeper soil pores or stop due to capillary influence. By comparing the two LNAPL spillage volume (low and high), it was found that in the case of low LNAPL spillage volume, more mobile LNAPL was spread through the LNAPL plume when the LNAPL was exposed to a rainfall event.

However, in the case of high LNAPL spillage volume, the LNAPL continued to migrate vertically downward as shown in Figure 4.15. Two factors influence the LNAPL migration in high and low LNAPL volumes as reported by Wipfler and Van Der Zee (2001). The first factor is related to the LNAPL occupancy state in the soil pores while the second factor is related to the distribution of LNAPL saturation within the LNAPL plume during its infiltration. With regards to the first factor, the presence of the pollutant inter-connecting bridge within soil pores influences the effect of rainfall recharge on the contamination movement. The inter-connecting bridge of the non-wetting (LNAPL) liquid is most likely to develop when the liquid volume is sufficient.

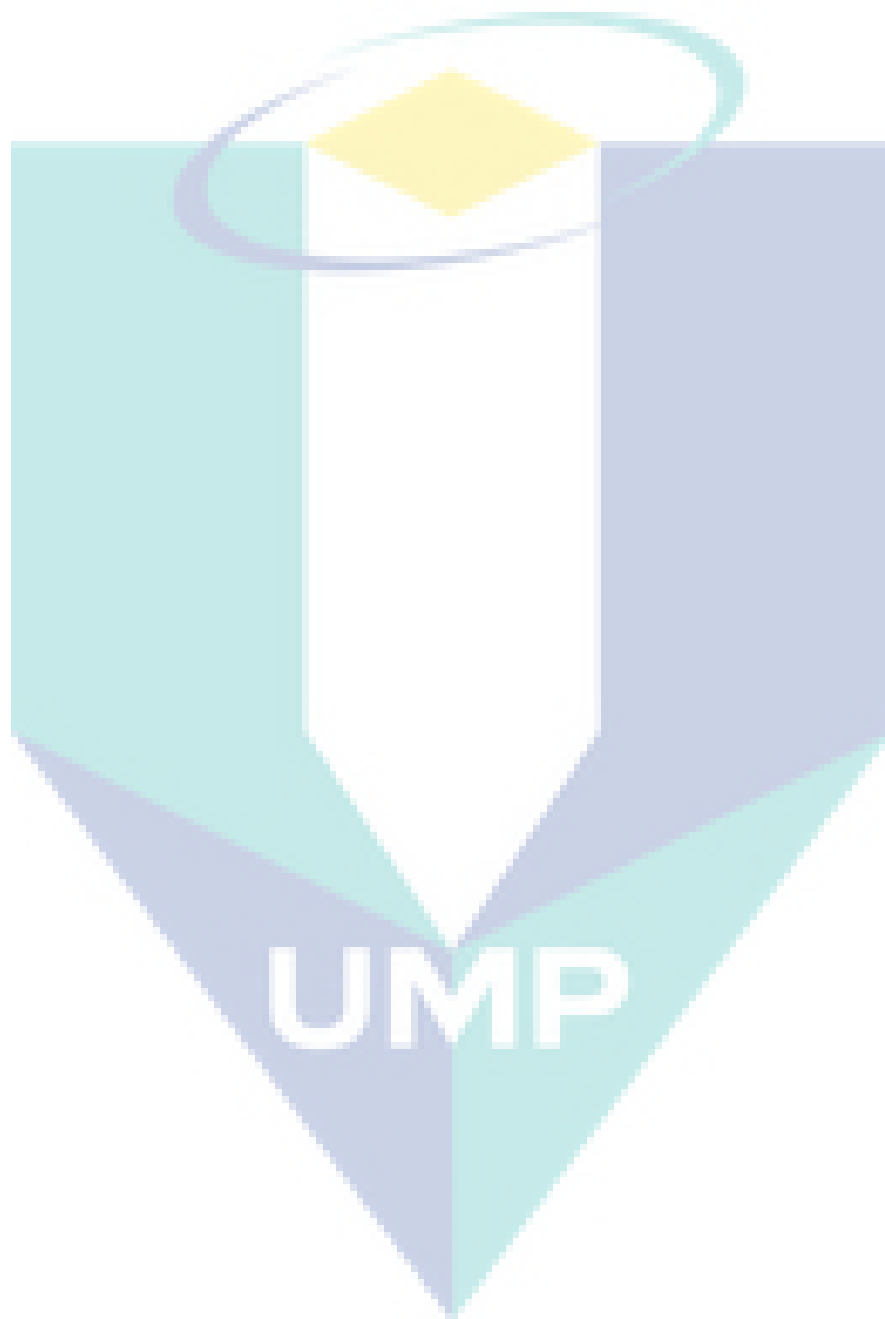


This behavior means that the greater volume of LNAPL, the more occupation of voids within the soil pores. In turn, a bridge inside the soil pores within the water surface is created because the LNAPL and water are immiscible liquids. For the second factor influencing the LNAPL migration, the initial distribution of LNAPL saturation influences how the rainfall recharge affects the contaminant movement. When the spillage volume of LNAPL is high, it will migrate deeper more rapidly due to the high weight of the LNAPL spillage which pushes the LNAPL downward. Some of the LNAPL will occupy the soil pores due to the capillarity feature during its downward migration. However, for the case of low LNAPL spillage volume, the LNAPL migration was shallow. Thus, the LNAPL saturation was spread within the area of the LNAPL plume.

Thus, when the contaminated porous media was subjected to rainfall event, it is very easy for rainfall recharge to accumulate when the volume of the available pores are high. This accumulation of rainfall recharge resulted in the LNAPL being pushed downward.



UMP



4.6 Results of the Experiments in Group (4)

4.6.1 PCE migration in Experiment (11)

In Experiment 11, the volumetric fraction was 45 % and 55 % for clay spheres and sand, respectively. After packing the model with double-porosity media, the same PCE amounts similar to those in group 1 were injected into the flow chamber. The PCE saturation was calculated following the same procedures discussed in Section 3.5.1. Important parameters for PCE saturation calculation were shown in Table 4.7 was calculated as discussed in the previous chapter. Figure 4.16 shows the injected volume of PCE plotted against the calculated volume of PCE from image analysis.

Table 4.7 Important parameters calculated for Experiment 11 and Experiment 12

Term	Experiment 11	Experiment 12
Porosity	0.388	0.382
N_p (number)	49.35	50.70
Absorption coefficient (α_n)	0.217	0.248
Average pore diameter (d_o)	0.0073	0.0075
Transmission factor (τ_{wn})	0.989	0.990

A strong correlation was found between the injected and calculated volumes of PCE ($R^2 = 0.998$) where the maximum error was 10 % whereas the minimum error was 3.75 % as shown in Table 4.8. An RMSE value of 0.44 ml was found for the calculated data.

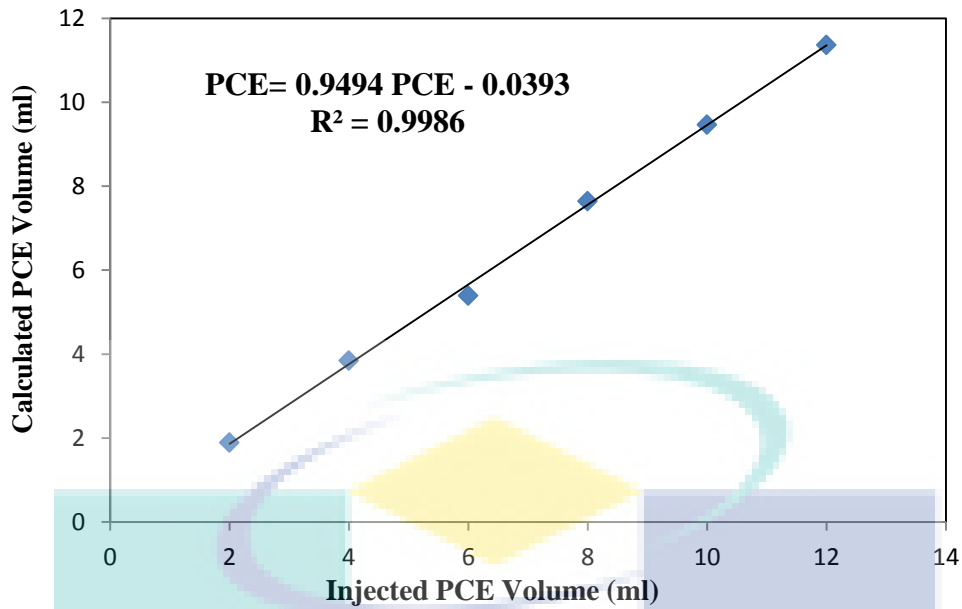


Figure 4.16 PCE volume calculated from image analysis vs. injected PCE volume into the flow chamber for Experiment 3.

Table 4.8 Injected and calculated volumes of PCE for Experiment 11

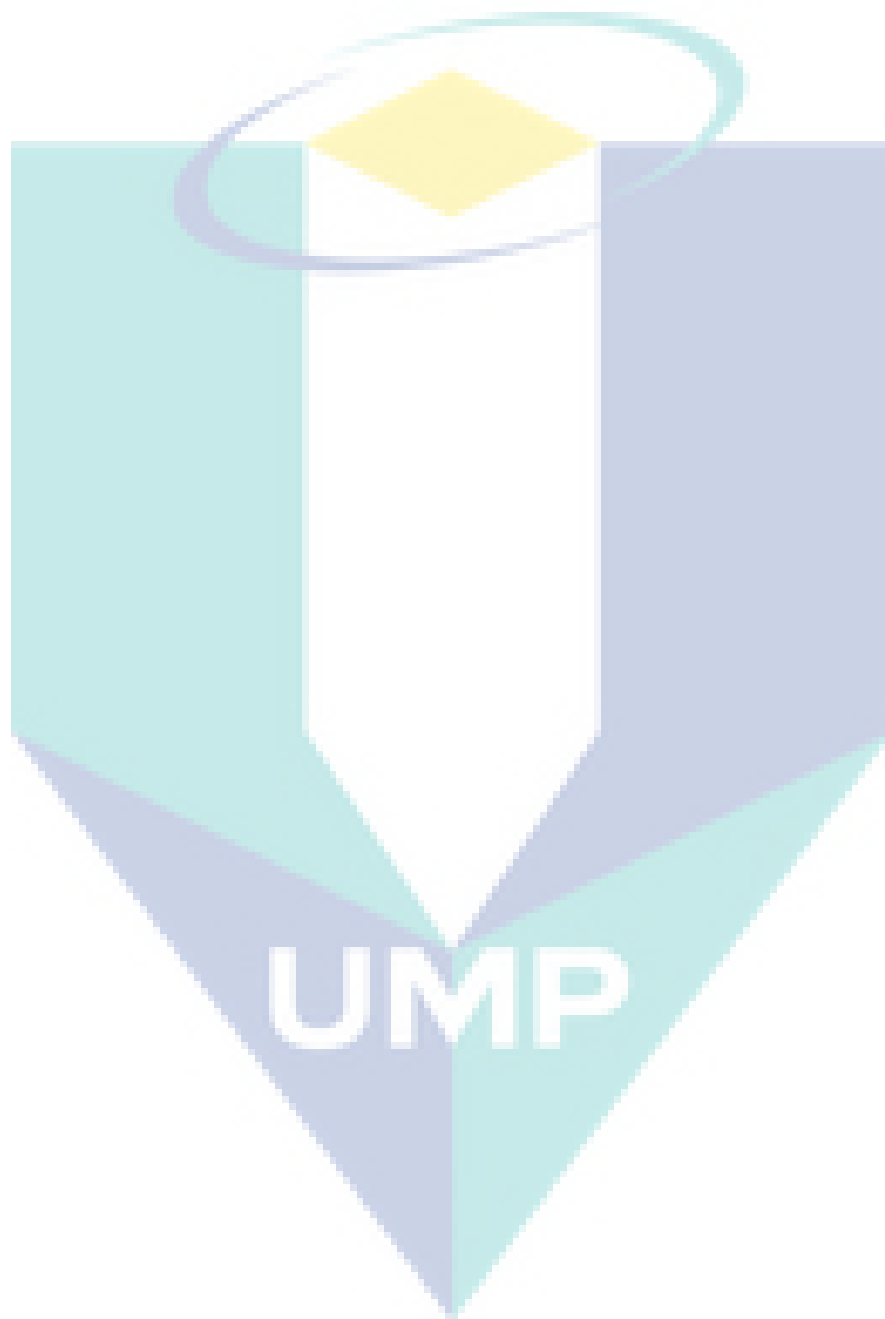
Injected volume of PCE (ml)	Calculated volume of PCE (ml)	$(V_{cal} - V_{inj})^2$	Error (%)
2	1.9	0.01	5
4	3.85	0.0225	3.75
6	5.4	0.36	10
8	7.65	0.1225	4.375
10	9.47	0.2809	5.3
12	11.37	0.3969	5.25
Total		1.1928	

$$RMSE = \sqrt{\frac{1}{6} \sum (1.1928)^2} = 0.44$$

The behavior of PCE was different in Experiment 11 as compared to the behavior in Experiment 1 in which the velocity of PCE migration was much faster in Experiment 11. In the first five minutes of migration, the PCE penetrated more than half the length

of the flow chamber and it reached the bottom of the flow chamber after 23 min. In Experiment 11, during the first five minutes, five of the seven increments were injected into the flow chamber where the velocity of the PCE increments was almost similar for all observations. The velocity of the PCE during the first five minutes was 4.8 cm/min and then it decreased to an average velocity of 1.27 cm/min until it reaches the bottom of the flow chamber. This could be because of the higher pressure of the PCE due to high amount of PCE injected during the first five minutes which in turn reflected on its migration velocity. The same behavior was observed in Experiment 1 but with a difference in the PCE migration velocity. During the first five minutes of the PCE migration, five PCE increments were injected and they migrated with an average velocity of 4.3 cm/min. After the sixth minute, the velocity decreased to an average velocity of 0.79 cm/min until it reached the bottom of the flow chamber. Figure 4.17 shows the PCE behavior in Experiment 11. This result is most likely due to more macro-pores existing in Experiment 11 as compared to Experiment 1. It is known that the size of macro-pores are many times bigger than the size of micro-pores (Ngien et al., 2012b). This means that for the pores that contain water, the PCE needs to overcome a lower capillary pressure to enter the macro-pores as compared to the micro-pores. Therefore, the PCE will move preferentially through the macro-pores. When the double-porosity has more macro-pores, this means that the capillary pressure is smaller which in turn less PCE resistance to migrate through the soil medium. Therefore, the PCE migration velocity is faster in the double-porosity with higher macro-pores volume fraction. Furthermore, the volume fraction of sand in Experiment 11 is higher than that in Experiment 1 which results in more sand layers in Experiment 11. Therefore, the equivalent permeability for the double-porosity in Experiment 11 was higher than that of Experiment 1. The equivalent permeability is the vertical permeability for the fluid in the layers of the double-porosity and it was measured by compiling the permeability for all sand and clay spheres layers.

This experiment was conducted three times, and statistical analysis was used to validate the accuracy of the method as well as to compare the means and standard deviation using ANOVA (One-way test, $P < 0.05$) as shown in Appendix V.



4.6.2 PCE migration in Experiment (12)

In Experiment 12, the macro-pores were increased where the volumetric fraction used was 60 % of sand and 40 % of clay spheres. The same packing procedure was followed similar to the previous experiment. The value of τ_{wn} calculated for the PCE-water interface in Experiment 12 is shown in Table 4.8. In addition, the correlation between the PCE volume injected into the flow chamber and the calculated PCE volume from image analysis was plotted ($R^2 = 0.995$) as shown in Figure 4.18. The maximum error was 12.5% while the minimum error was 2.5 % as shown in Table 4.9. The RMSE was calculated and a value of 0.53 ml was obtained.

Table 4.9 Injected and calculated volumes of PCE for Experiment 12

Injected volume of PCE (ml)	Calculated volume of PCE (ml)	$(V_{cal} - V_{inj})^2$	Error (%)
2	1.75	0.0625	12.5
4	3.6	0.16	10
6	5.72	0.0784	4.66
8	7.3	0.49	8.75
10	9.1	0.81	9
12	11.7	0.09	2.5
Total		1.6909	

$$\begin{aligned} \text{RMSE} &= \sqrt{\frac{1}{6} \sum (1.6909)^2} \\ &= 0.53. \end{aligned}$$

The observation of PCE migration is shown in Figure 4.19. As can be seen, in the first five minutes of migration, the behavior of PCE was totally different as compared to Experiment 1 and 11. The PCE migrated horizontally during the first several minutes of injection. Specifically, after the second increment of PCE (i.e 2 ml), it started to move to the right side of the flow chamber, after which it moved downward as shown in Figure 4.19(a). During the first 5 minutes, the PCE migrated nearly halfway vertically through the soil sample which is less than the distance traveled in Experiment 11 and this result was not expected. It is believed that the PCE slowed down due to horizontal

migration during the first five minutes. This behavior can be due to more compaction for the double-porosity medium in the top of the flow chamber.

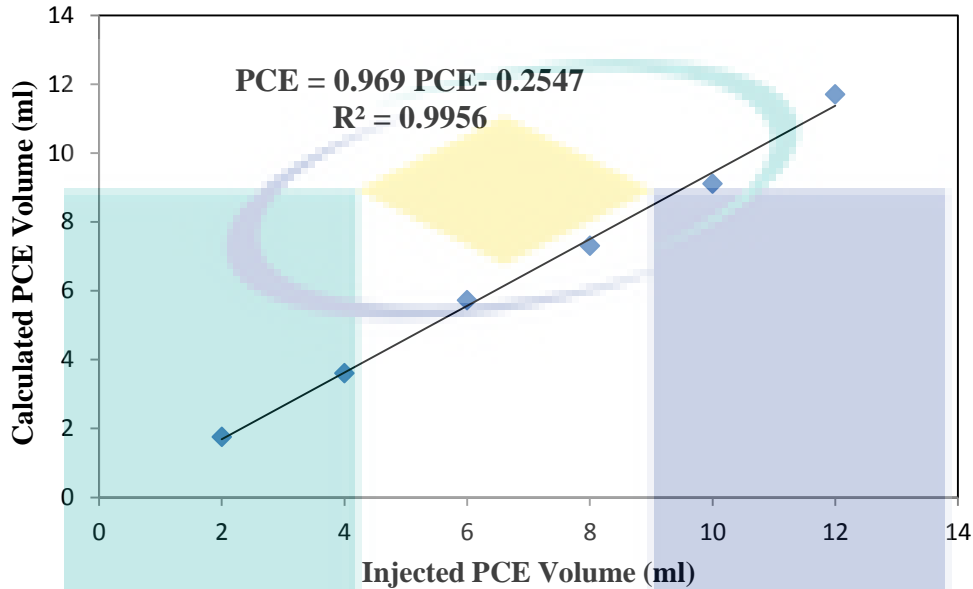
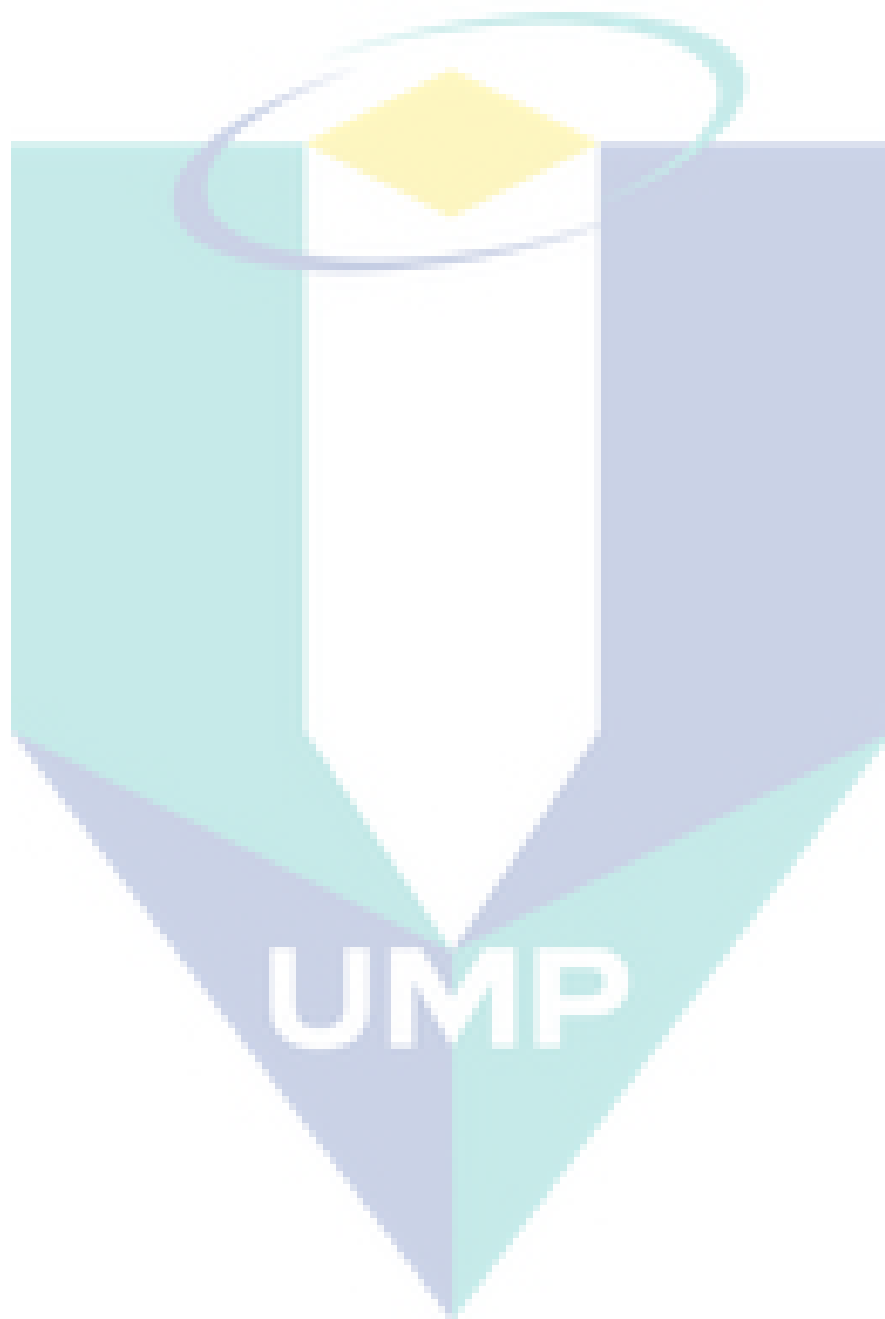


Figure 4.18 PCE volume calculated from image analysis vs. injected PCE volume into the flow chamber for Experiment 12.

After the sixth minute of the PCE migration, the PCE flowed much faster as compared to the behavior during the first five minutes. As it can be seen in Figure 4.19(b), the PCE reached nearly 40 cm of the flow chamber after 10 minutes where some parts of the PCE appeared near to the bottom side of the flow chamber. This phenomenon could be due to some parts of the PCE probably flowed at the back of the flow chamber before it appeared at the front of the flow chamber. This was validated after the end of the experiment where the PCE appears at the back of the flow chamber as expected. The PCE reached the bottom of the flow chamber in 17 minutes and after that, it moved horizontally until it reached both sides of the flow chamber.



When comparing the behavior of PCE in Experiment 12 with the behavior of the PCE in the previous experiments (Experiment 1 and 11), it is clear that the behavior is different where the PCE plumes in Experiment 1 and 11 were fairly symmetric and zigzag. This variation can be explained because of the difference in the combination of the double-porosity medium (i.e the ratio of macro-pores and micro-pores). It is known that the macroscopic behavior of the double-porosity medium is mainly affected by two factors; the local geometry of pores and the contrast in hydraulic conductivity (Lewandowska et al., 2005). As the composition of the double-porosity medium in Experiment 4 contains 60% macro-pores and 40% micro-pores, it is believed that the unsymmetrical PCE behaviour was due to high contrast in the degree of heterogeneity of pores as well as hydraulic conductivity.

The cumulative migration depth of PCE for the three experiments that conducted in double-porosity mediums (i.e Experiment 1, 11 and 12) is shown in Figure 4.20. The migration depth values were obtained for each image based on the image acquisition frequency using the IPP software. From the experiments, it can be observed that the main difference in the three experiments was the volume of macro-pores and micro-pores. It is believed that the dominant type is the macro-pores since the size of macro-pores is many times bigger than the size of micro-pores.

In a previous study, Ngien et al. (2012b) performed some experiments to investigate the LNAPL migration in double-porosity and compared the results with other studies that were conducted in single-porosity media. The authors noted that the LNAPL flow occurred preferentially through the macro-pores. This result is consistent with the results obtained by Peng et al. (2015) and Lewandowska et al. (2008). In their study, they visualized the water flow in double-porosity soil made from the same materials used in this research (i.e sand and clay spheres). They concluded that the water migrated only in the sand matrix (macro-pores). These findings prove that the macro-pores have a big effect on the migration of DNAPL in double-porosity media. The experiment was repeated as the previous experiment and the results are shown in Appendix W.

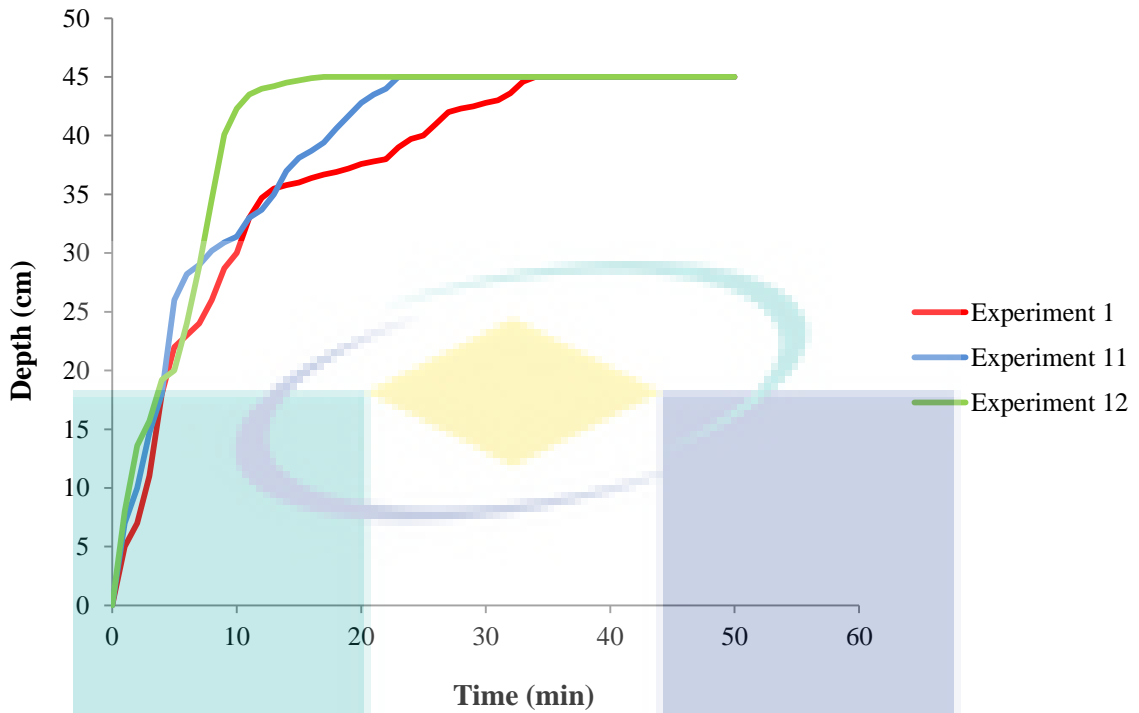


Figure 4.20 Cumulative PCE migration depth for the experiments in double-porosity medium

Statistical analysis was used to validate the accuracy of the method between the three experiments in double-porosity medium through ANOVA (One-way test, $P < 0.05$). The calculated amounts of the PCE from the image analysis were tested. The statistical analysis results show a slight difference between the means of the three experiments (see Appendix Y). Furthermore, the migration velocity of the PCE through the three experiments was calculated where a difference between the average in the velocity was noted where the averages were 2.31 cm/min, 2.68 cm/min and 2.93 cm/min for experiments 1, 11 and 12, respectively as shown in Table 4.9. This difference in velocity is due to the different composition of the double-porosity medium through the three experiments.

A correlation between the composition of the double-porosity medium (the volumetric fractions of the macro-pores and micro-pores) and the average PCE migration within it was plotted as shown in Figure 4.21. It is clear that the PCE migration velocity is

increased with increasing the percentage of the macro-pores. This observation proves that the macro-pores have a significant effect on the PCE migration in double-porosity soil medium. A summary of all experiments results are illustrated in Table 4.9

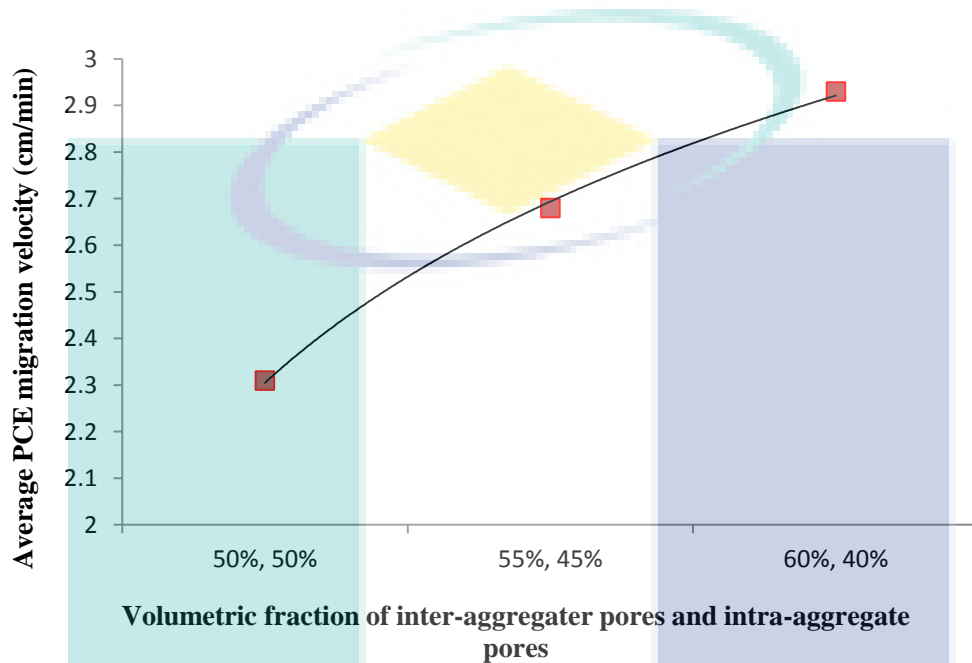


Figure 4.21 A correlation of the PCE migration to the volumetric fraction of the double-porosity

Table 4.10 Injected and calculated volumes of PCE for Experiment 4

Experiment (No.)	Porous Medium	LNAPL/DNAPL	Measured Parameters
1	Double-Porosity	DNAPL	DNAPL saturation in two-fluid phase system
2	Single-Porosity	DNAPL	DNAPL saturation in two-fluid phase system
3	Double-Porosity	DNAPL	DNAPL behavior in three-fluid phase system
4	Single-Porosity	DNAPL	DNAPL behavior in three-fluid phase system
5	Double-Porosity	LNAPL	LNAPL behavior in three-fluid phase system
6	Single-Porosity	LNAPL	LNAPL behavior in three-fluid phase system
7	Double-Porosity	LNAPL	Influence of heavy rainfall event on 50 ml of LNAPL
8	Double-Porosity	LNAPL	Influence of heavy rainfall event on 100 ml of LNAPL
9	Double-Porosity	LNAPL	Influence of light rainfall event on 50 ml of LNAPL
10	Double-Porosity	LNAPL	Influence of light rainfall event on 100 ml of LNAPL
11	Double-Porosity	DNAPL	DNAPL saturation in two-fluid phase system different combination of double-porosity materials
12	Double-Porosity	DNAPL	DNAPL saturation in two-fluid phase system different combination of double-porosity materials

UMP

CHAPTER 5

CONCLUSION & RECOMMENDATIONS

5.1 Introduction

Research through laboratory experiments has been conducted to study and analyze the migration of LNAPL and DNAPL in double-porosity soil media. This chapter presents the main conclusion of the research as well as the recommendations for future work.

5.2 Conclusion

The objectives of the research have been achieved in: (i) proposing a new image analysis method based on LTV to measure the DNAPL saturation in double-porosity soil pixel by pixel (ii) assessment of DNAPL migration in double-porosity soil medium in the case of fully saturated double-porosity in two-fluid phase system (iii) investigation of LNAPL and DNAPL migration in double-porosity soil in three-fluid phase system (v) evaluation the influence of rainfall recharge on the LNAPL migration in double-porosity soil (iv) correlation the movement of the DNAPL to the volumetric fraction of the two distinct scales of porosity (macro-pores pores and micro-pores pores) within the double-porosity soil.

Image analysis was applied to the laboratory experiments using LTV to quantitative and qualitative analyze the migration of DNAPL in double-porosity under different conditions. Quantitative analysis was conducted through applying the equations that

dervied in chanpter 3 in order to calculate the DNAPL saturation in double-porosity soil, pixel by pixel. However, the qualitative analysis was carried out in the other groups of experiments in order to study: the behavior of DNAPL in three-fluid phase system, the behavior of LNAPL in three-fluid phase system and the influence of rainfall recharge on LNAPL migration in double-porosity soil.

The behavior of the LNAPL and DNAPL migration in double-porosity soil was compared to the same behavior in single-porosity to investigate the effect of the double-porosity occurrence on the LNAPL and DNAPL migration in the subsurface. Both LNAPL and DNAPL were found to be migrated much faster in double-porosity as soil compared to single-porosity soil in all experiments with a percentage more than 50% in all experiments . This result was due to the presence of macro-pores in double-porosity soil which contribute in increasing the permeability of the soil.

Qualitative analysis of the laboratory experiments was accomplished through the investigation of LNAPL and DNAPL migration in the double-porosity soil in three-fluid phase system. The observations show that the capillary pressure and fluid wettability that exist in the soil pores have a considerable effect on the NAPL migration. The LNAPL and DNAPL migration were found to be slower in the three-fluid phase zone as compared to the two-fluid phase zone. This observation was due to the existing of air in the three-fluid phase zone. When three fluids are present in a subsurface system, the largest pores are usually filled with air, whereas the smallest pores are occupied by water. NAPLs fill the intermediate pores. LNAPL and DNAPL migration was slower in the three-fluid phase zone because LNAPL and DNAPL migrated through the intermediate pores and took more time to overcome the capillary pressure to enter the smallest and largest pores. In addition, the wettability of the fluids present in the physical model affect the LNAPL and DNAPL migration. In the vadose zone, simulated by the upper zone in this experiment, water is usually a wetting fluid with respect to NAPL whereas NAPL is a wetting fluid with respect to air. At the pore level, the capillary pressure forces the wetting fluid to enter the pore and displace the existing fluid inside the pore while the non-wetting fluid will be repelled. Therefore, when the LNAPL and DNAPL were released into the flow chamber, it would have

migrated and infiltrated initially through the air-filled pores since the LNAPL and DNAPL are the wetting fluids with respect to air.

Moreover, the results show that chemical properties of the LNAPL and DNAPL have a considerable effect on their migration where the LNAPL migration velocity was faster than the velocity of the DNAPL migration in both porous media by 64.8 % and 55.6% in the case of double-porosity and single-porosity soil, respectively. This result is likely because the distribution coefficient of toluene was higher than that of PCE which means in turn that the retardation factor of toluene is lower than the retardation factor of PCE in the same porous media.

In addition, a qualitative observation was carried out to assess the influence of rainfall recharge on the LNAPL migration in double-porosity soil under different conditions. The rainfall recharge was subjected to a gravitational force which in turn flowed towards the groundwater table. From the observation, in all the experiments, the LNAPL was pushed down due to the effect of rainfall recharge. This means that the contaminant can migrate deeper through the saturated capillary zone and pollute the groundwater.

As an overall conclusion for this research, the LNAPL and DNAPL will migrate deeper into the double-porosity soil within less time period compared to single-porosity due to the presence of the macro-pores.

This research proves that the LTV technique provides a non-intrusive and non-destructive tool (that could investigate the fluids migration without disturbing the soil samples) which is viable for studying multiphase flow in double-porosity soil media without disturbing the soil samples where rapid changes in fluid distribution in the entire flow domain are not easy to measure using conventional tools.

5.3 Recommendations

Some recommendations for future work that can be done are listed in this section.

- (i) The results from the laboratory experiments can be used to establish a numerical model to predict the NAPL migration for a long time.
- (ii) For the LTV part, the current equations that developed to calculate the NAPL saturation double-porosity in two-fluid phase system can be developed to calculate the NAPL migration in the double-porosity soil in three-fluid phase system.
- (iii) The LTV method can be used to study the remediation of the NAPL using different methods such as air sparging, surfactant flushing or alcohol flushing.



UMP

REFERENCES

- Abdallah, W., Buckley, J. S., Carnegie, A., Edwards, J., Herold, B., Fordham, E., Graue, A. and Habashy, T. (2007). *Fundamentals of wettability* (Online).
- Agaoglu, B., Coptu, N. K., Scheytt, T. and Hinkelmann, R. (2015). Interphase mass transfer between fluids in subsurface formations: A review. *Advances in Water Resources*, 79, 162-194.
- Al-Gharbi, M. (2004) Dynamic pore-scale modelling of two-phase flow. PhD Thesis, Imperial College London.
- Alaoui, A., Germann, P., Jarvis, N. and Acutis, M. (2003). Dual-porosity and kinematic wave approaches to assess the degree of preferential flow in an unsaturated soil. *Hydrological Sciences Journal*, 48, 455-472.
- Alias, N. (2003) Migration of light nonaqueous phase liquid (LNAPL) in unsaturated media. M.Eng Thesis. Universiti Teknologi Malaysia.
- Andrews, E. B. (1861). Rock oil, its geological relations and distribution. *American Journal of Science*, 94, 85-93.
- Aramide, F. O. (2015). Effects of sintering temperature on the phase developments and mechanical properties of clay. *Leonardo Journal of Sciences*, 26, 67-82.
- ASTM. (2006). *Standard practice for classification of soil for engineers purpose (Unified Soil Classification System)*. ASTM International.
- Bagherieh, A., Khalili, N., Habibagahi, G. and Ghahramani, A. (2009). Drying response and effective stress in a double porosity aggregated soil. *Engineering Geology*, 105, 44-50.
- Bai, M., Roegiers, J.-C. and Inyang, H. I. (1996). Contaminant transport in nonisothermal fractured porous media. *Journal of Environmental Engineering*, 122, 416-423.

- Barenblatt, G., Zheltov, I. P. and Kochina, I. (1960). Basic concepts in the theory of seepage of homogeneous liquids in fissured rocks [strata]. *Journal of Applied Mathematics and Mechanics*, 24, 1286-1303.
- Bear, J. (1972). *Dynamics of fluids in porous media*, Elsevier, New York, 764p.
- Bedient, P. B., Rifai, H. S. and Newell, C. J. (1999). *Ground water contamination - Transport and remediation*. 2nd edn. Prentice Hall, Upper Saddle River.
- Berkowitz, B. (2002). Characterizing flow and transport in fractured geological media: A review. *Advances in Water Resources*, 25, 861-884.
- Black, B. (1998). Oil Creek as Industrial Apparatus: Re-creating the Industrial Process through the Landscape of Pennsylvania's Oil Boom. *Environmental History*, 3, 210-229.
- Bob, M. M., Brooks, M. C., Mravik, S. C. and Wood, A. L. (2008). A modified light transmission visualization method for DNAPL saturation measurements in 2-D models. *Advances in Water Resources*, 31, 727-742.
- British Standard Institution (2012). *BS 933- 1: Tests for geometrical properties of aggregates. Determination of particle size distribution. Sieving method (British Standard)*. American National Standard Institute.
- Carlsoon, C. and Carlsoon, G. (1996). *Basic physics of X-ray imaging*. Linköping university, Sweden.
- Carminati, A., Kaestner, A., Lehmann, P. and Flühler, H. (2008). Unsaturated water flow across soil aggregate contacts. *Advances in Water Resources*, 31, 1221-1232.
- CCOHS (2016). *Ultraviolet Radiation* (Online).
- Charbeneau, R. J. (2006). *Groundwater hydraulics and pollutant transport*. Waveland Press.

- Chen, Z., Huang, G. and Chakma, A. (2000). Risk assessment of a petroleum-contaminated site through a multi-phase and multi-component modeling approach. *Journal of Petroleum Science and Engineering*, 26, 273-281.
- Cheng, Y., Chen, Y., Jiang, Y., Jiang, L., Sun, L., Li, L. and Huang, J. (2016). Migration of BTEX and Biodegradation in Shallow Underground Water through Fuel Leak Simulation. *BioMed Research International*, 2016. doi:10.1155/2016/7040872.
- Chun, H.-C., Gimenez, D., Yoon, S.-W., Park, C.-W., Moon, Y.-H., Sonn, Y.-K. and Hyun, B.-K. (2011). Review of Soil Structure Quantification from Soil Images. *Korean Journal of Soil Science and Fertilizer*, 44, 517-526.
- Conrad, S. H., Glass, R. J. and Peplinski, W. J. (2002). Bench-scale visualization of DNAPL remediation processes in analog heterogeneous aquifers: surfactant floods and in situ oxidation using permanganate. *Journal of Contaminant Hydrology*, 58, 13-49.
- Coppola, A. (2000). Unimodal and bimodal descriptions of hydraulic properties for aggregated soils. *Soil Science Society of America Journal*, 64, 1252-1262.
- Corapcioglu, M. Y., Tuncay, K. and Ceylan, B. K. (1996). Oil mound spreading and migration with ambient groundwater flow in coarse porous media. *Water Resources Research*, 32, 1299-1308.
- Culligan, P. and Soga, K. (2006). Non-aqueous phase liquid behavior in the subsurface: Transportation, source zone characterization and remediation. *Proceedings of the Sixth International Conference on Physical Modelling in Geotechnics, ICPMG '06, Hong Kong*. 29-45.
- Darnault, C., Dicarolo, D., Bauters, T., Jacobson, A., Throop, J., Montemagno, C., Parlange, J. Y. and Steenhuis, T. (2001). Measurement of fluid contents by light transmission in transient three-phase oil-water-air systems in sand. *Water Resources Research*, 37, 1859-1868.
- Darnault, C. J., Throop, J. A., Dicarolo, D. A., Rimmer, A., Steenhuis, T. S. and Parlange, J.-Y. (1998). Visualization by light transmission of oil and water

contents in transient two-phase flow fields. *Journal of Contaminant Hydrology*, 31, 337-348.

- Deng, Y., Shi, X., Xu, H., Sun, Y., Wu, J. and Revil, A. (2017). Quantitative assessment of electrical resistivity tomography for monitoring DNAPLs migration—Comparison with high-resolution light transmission visualization in laboratory sandbox. *Journal of Hydrology*, 544, 254-266.
- Devinny, J. S., Everett, L. G., Lu, J. C. S. and Stollar, R. L. (1990). *Subsurface Migration of Hazardous Wastes*. New York, NY (US), Van Nostrand Reinhold.
- Dicarlo, D., Bauters, T., Steenhuis, T., Parlange, J. Y. and Bierck, B. (1997). High-speed measurements of three-phase flow using synchrotron X rays. *Water Resources Research*, 33, 569-576.
- Diffey, B. L. (2002). Sources and measurement of ultraviolet radiation. *Methods*, 28, 4-13.
- Domenico, P. A. and Schwartz, F. W. (1990) *Physical and Chemical Hydrogeology*. New York: John Wiley & Sons, Inc.
- Dunkerley, D. (2008). Rain event properties in nature and in rainfall simulation experiments: a comparative review with recommendations for increasingly systematic study and reporting. *Hydrological Processes*, 22, 4415-4435.
- Edmund Optics (2016). *Optical filters* (Online). Retrieved from <http://www.edmundoptics.com/> on (12/5/2016).
- Edomwonyi-Otu, L., Aderemi, B. O., Ahmed, A. S., Coville, N. J. and Maaza, M. (2013). Influence of thermal treatment on kankara kaolinite. *Opticon1826*, 5, 1-5.
- El-Zein, A., Carter, J. P. and W Airey, D. (2006). Three-dimensional finite elements for the analysis of soil contamination using a multiple-porosity approach. *International Journal for Numerical and Analytical Methods in Geomechanics*, 30, 577-597.

EPA (2009) *Impacts of DNAPL Source Treatment: Experimental and Modeling Assessment of the Benefits of Partial DNAPL Source Removal*. Oklahoma, USA: National Risk Management Research Laboratory.

Extend Office (2009). How to convert matrix style table to three columns in Excel.

Fabbri, B., Gualtieri, S. and Leonardi, C. (2013). Modifications induced by the thermal treatment of kaolin and determination of reactivity of metakaolin. *Applied Clay Science*, 73, 2-10.

Falode, O. and Manuel, E. (2014). Wettability effects on capillary pressure, relative permeability, and irreducible saturation using porous plate. *Journal of Petroleum Engineering*, 2014, doi:10.1155/2014/465418.

Faroughi, S. and Huber, C. (2016). A theoretical hydrodynamic modification on the soil texture analyses obtained from the hydrometer test. *Géotechnique*, 66, 378-385.

Flores, G., Katsumi, T., Inui, T. and Ramli, H. (2013) Characterization of LNAPL distribution in whole domains subject to precipitation by the simplified image analysis method (ch65) in *Coupled Phenomena in Environmental Geotechnics*. In: Guido Musso. CRC PRESS, L., UK & END, C. C. (eds.). Taylor & Francis.

Flores, G., Katsumi, T. and Kamon, M. (2007). Evaluation of LNAPL migration under fluctuating groundwater by image analysis. *Annual of Disaster Prevention Research. Kyoto University*, 50, 399-405.

Foster, S., Garduno, H., Kemper, K., Tiunhof, A., Nanni, M. and And Dumars, C. (2004). *Groundwater Quality Protection: defining strategy and setting priorities*. Sustainable Groundwater Management: Concepts and Tools. Briefing Note Series Note 8.

Franco, Z. and Nguyen, Q. (2011). Flow properties of vegetable oil–diesel fuel blends. *Fuel*, 90, 838-843.

Geotechdata (2008). *Soil permeability coefficient* (Online). Retrived from <http://geotechdata.info/parameter/permeability.html> on (29/9/2016).

- Gerhard, J. and Kueper, B. (2003). Relative permeability characteristics necessary for simulating DNAPL infiltration, redistribution, and immobilization in saturated porous media. *Water Resources Research*, 39, DOI: 10.1029/2002WR001490.
- Ghanbarian, B., Daigle, H., Hunt, A. G., Ewing, R. P. and Sahimi, M. (2015). Gas and solute diffusion in partially saturated porous media: Percolation theory and effective medium approximation compared with lattice Boltzmann simulations. *Journal of Geophysical Research: Solid Earth*, 120, 182-190.
- Ghezzehei, T. A. and Or, D. (2003). Pore-space dynamics in a soil aggregate bed under a static external load. *Soil Science Society of America Journal*, 67, 12-19.
- Ghosh, S., Warriar, K. and Damodaran, A. (1990). Thermally treated kaolin as an extender pigment. *Journal of Materials Science Letters*, 9, 1046-1048.
- Glass, R. and Nicholl, M. (1996). Physics of gravity fingering of immiscible fluids within porous media: An overview of current understanding and selected complicating factors. *Geoderma*, 70, 133-163.
- Glass, R. J., Conrad, S. H. and Peplinski, W. (2000). Gravity-destabilized nonwetting phase invasion in macroheterogeneous porous media: Experimental observations of invasion dynamics and scale analysis. *Water Resources Research*, 36, 3121-3137.
- Glass, R. J., Steenhuis, T. S. and Parlange, J.-Y. (1989). Mechanism for finger persistence in homogeneous, unsaturated, porous media: theory and verification. *Soil Science*, 148, 60-70.
- Griffiths, D. J. (1989). *Introduction to Electrodynamics*. Prentice-Hall, Inc., Englewood Cliffs, NJ.
- Hedges, R. and Mclellan, M. (1976). On the cation exchange capacity of fired clays and its effect on the chemical and radiometric analysis of pottery. *Archaeometry*, 18, 203-207.

- Henry, E. J. and Smith, J. (2002). The effect of surface-active solutes on water flow and contaminant transport in variably saturated porous media with capillary fringe effects. *Journal of Contaminant Hydrology*, 56, 247-270.
- Hill iii, E. H., Kupper, L. L. and Miller, C. T. (2002). Evaluation of path-length estimators for characterizing multiphase systems using polyenergetic X-ray absorptiometry. *Soil Science*, 167, 703-719.
- Hoa, N. (1981). A new method allowing the measurement of rapid variations of the water content in sandy porous media. *Water Resources Research*, 17, 41-48.
- Høst-Madsen, J. and Jensen, K. H. (1992). Laboratory and numerical investigations of immiscible multiphase flow in soil. *Journal of Hydrology*, 135, 13-52.
- Huling, S. G. and Weaver, J. W. (1991). *Ground water issue: dense nonaqueous phase liquids*. US Environmental Protection Agency.
- Illangasekare, T. and Fripiat, C. C. (2012) Miscible and Immiscible Pollutants in Subsurface Systems. Chapter 19. In: H . J . S . Fernando Harindra Joseph Fernando, C. P. (ed.).
- Jongmans, A., Pulleman, M., Balabane, M., Van Oort, F. and Marinissen, J. (2003). Soil structure and characteristics of organic matter in two orchards differing in earthworm activity. *Applied Soil Ecology*, 24, 219-232.
- Kamaruddin, S. A. (2012) Assessment of the distribution profile of light non-aqueous phase liquid in unsaturated zone under the influence of rainfall recharge. PhD Thesis. Universiti Putra Malaysia.
- Kamaruddin, S. A., Sulaiman, W. N. A., Rahman, N. A., Zakaria, M. P., Mustaffar, M. and And Sa'ari, R. (2011a). A review of laboratory and numerical simulations of hydrocarbons migration in subsurface environments. *Journal of Environmental Science and Technology*, 4, 191-214.
- Kamaruddin, S. A., Sulaiman, W. N. A., Zakaria, M. P., Othman, R. and Rahman, N. A. (2011c). Laboratory simulation of LNAPL spills and remediation in unsaturated

porous media using the image analysis technique: A review. *National Postgraduate Conference (NPC)*, IEEE, 1-7.

- Kamaruddin, S. A., Suliman, W. N. A., Rahman, N. A., Zakaria, M. P. and Muushairry, M. S. A., R. (2011b). Two-Dimensional Laboratory Investigation of Light Non-Aqueous Phase Liquid Migration in Subsurface Environment. In *Contemporary Environmental Quality Management in Malaysia and Selected Countries*. Serdang: Universiti Putra Malaysia Press.
- Kazemi, H., Merrill Jr, L., Porterfield, K. and Zeman, P. (1976). Numerical simulation of water-oil flow in naturally fractured reservoirs. *Society of Petroleum Engineers Journal*, 16, 317-326.
- Kechavarzi, C., Soga, K. and Illangasekare, T. (2005). Two-dimensional laboratory simulation of LNAPL infiltration and redistribution in the vadose zone. *Journal of Contaminant Hydrology*, 76, 211-233.
- Kechavarzi, C., Soga, K. and Wiart, P. (2000). Multispectral image analysis method to determine dynamic fluid saturation distribution in two-dimensional three-fluid phase flow laboratory experiments. *Journal of Contaminant Hydrology*, 46, 265-293.
- Konz, M., Ackerer, P., Meier, E., Huggenberger, P., Zechner, E. and Gechter, D. (2008). On the measurement of solute concentrations in 2-D flow tank experiments. *Hydrology and Earth System Sciences Discussions*, 12, 727-738.
- Kresic, N. (2008). *Groundwater resources: Sustainability, management, and restoration*. McGraw Hill Professional.
- Kueper, B. H., G.P.Wealthall, J.W.N.Smith, S.A.Leharne and D.N.Lerner. (2003). *An illustrated handbook of DNAPL transport and fate in the subsurface*. Environmental Agency.
- Laughlin, G. R. (1959) The effect of thermal treatment on the engineering properties of clays. Commonwealth of Kentucky, Department of Highways.

- Lee, J. Y., Kim, H., Kim, Y. and Han, M. Y. (2011). Characteristics of the event mean concentration (EMC) from rainfall runoff on an urban highway. *Environmental Pollution*, 159, 884-888.
- Lehmann, P., Stauffer, F., Hinz, C., Dury, O. and Flühler, H. (1998). Effect of hysteresis on water flow in a sand column with a fluctuating capillary fringe. *Journal of Contaminant Hydrology*, 33, 81-100.
- Lewandowska, J., Ngoc, T. D. T., Vauclin, M. and Bertin, H. (2008). Water drainage in double-porosity soils: experiments and micro-macro modeling. *Journal of Geotechnical and Geoenvironmental Engineering*.134, 231-243.
- Lewandowska, J., Szymkiewicz, A., Gorczewska, W. and Vauclin, M. (2005). Infiltration in a double-porosity medium: Experiments and comparison with a theoretical model. *Water Resources Research*, 41, doi:10.1029/2004WR003504.
- Li, X., Wu, W. and Cescotto, S. (2000). Contaminant transport with non-equilibrium processes in unsaturated soils and implicit characteristic Galerkin scheme. *International journal for numerical and analytical methods in geomechanics*, 24, 219-243.
- Li, X. and Zhang, L. (2009). Characterization of dual-structure pore-size distribution of soil. *Canadian geotechnical journal*, 46, 129-141.
- Live Science (2017). *What is visible light* (Online). Retrived from <http://www.livescience.com/50678-visible-light.html> on (4/5/2017).
- Luciano, A., Viotti, P. and Papini, M. P. (2010). Laboratory investigation of DNAPL migration in porous media. *Journal of Hazardous Materials*, 176, 1006-1017.
- Malaysia Drainage and Irrigation Department Standard. (2017). *Rainfall online data* (Online). Retrived from <http://www.water.gov.my/home?lang=en> on (12/2/2017).

- Marto, A., Hasan, M., Hyodo, M. and Makhtar, A. M. (2014). Shear strength parameters and consolidation of clay reinforced with single and group bottom ash columns. *Arabian Journal for Science and Engineering*, 39, 2641-2654.
- Mercer, J. W. and Cohen, R. M. (1990). A review of immiscible fluids in the subsurface: properties, models, characterization and remediation. *Journal of Contaminant Hydrology*, 6, 107-163.
- Mitchell, J. K. and Soga, K. (2005). *Fundamentals of soil behavior*. John Wiley & Sons Inc, New Jersey.
- Mohiuddin, E., Isa, Y. M., Mdleleni, M. M., Sincadu, N., Key, D. and Tshabalala, T. (2016). Synthesis of ZSM-5 from impure and beneficiated Grahamstown kaolin: Effect of kaolinite content, crystallisation temperatures and time. *Applied Clay Science*, 119, 213-221.
- Morris, B. L., Lawrence, A. R., Chilton, P., Adams, B., Calow, R. C. and Klinck, B. A. (2003). *Groundwater and its susceptibility to degradation: A global assessment of the problem and options for management*. Early warning and assessment report series , RS. 03-3. United Nations Environment Programme, Nairobi, Kenya.
- Munk, B. A. (2005). *Frequency Selective Surfaces: Theory and Design*. Wiley Online Library.
- Murry, H. H. (1999). *Applied Clay Mineralogy*. 2, Elsevier.
- Nakamura, J. (2016). *Image sensors and signal processing for digital still cameras*. CRC press.
- NASA (2014). *Wavelengths of visible light* (Online). Retrived from <http://missionscience.nasa.gov/ems/09> on (20/9/2016).
- National Research Council. (2013). *Alternatives for Managing the Nation's Complex Contaminated Groundwater Sites*. Washington, D. C., National Research Council Ed.

- Newell, C. J., Acree, S. D., Ross, R. and Huling, S. (1995) *Ground water issue: Light nonaqueous phase liquids*. U.S. Environmental Protection Agency. Groundwater Services, Inc., Houston, TX (United States), EPA/540/S-95/500.
- Ngien, S. K. (2012) Experimental and numerical analysis of non-aqueous phase liquids migration in double-porosity subsurface systems. PhD Thesis, Universiti Teknologi Malaysia.
- Ngien, S. K., Rahman, N. A., Ahmad, K. and Lewis, R. W. (2012a). A review of experimental studies on double-porosity soils. *Scientific Research and Essays*, 7, 3243-3250.
- Ngien, S. K., Rahman, N. A., Bob, M. M., Ahmad, K., Sa'ari, R. and Lewis, R. W. (2012b). Observation of Light Non-Aqueous Phase Liquid Migration in Aggregated Soil Using Image Analysis. *Transport in Porous Media*, 92, 83-100.
- Ngoc, T., Dung, T., Lewandowska, J., Vauclin, M. and Bertin, H. (2011). Two-scale modeling of solute dispersion in unsaturated double-porosity media: Homogenization and experimental validation. *International Journal for Numerical and Analytical Methods in Geomechanics*, 35, 1536-1559.
- Niemet, M. R. and Selker, J. S. (2001). A new method for quantification of liquid saturation in 2D translucent porous media systems using light transmission. *Advances in Water Resources*, 24, 651-666.
- O'carroll, D. M., Bradford, S. A. and Abriola, L. M. (2004). Infiltration of PCE in a system containing spatial wettability variations. *Journal of Contaminant Hydrology*, 73, 39-63.
- Oostrom, M., Dane, J. and Wietsma, T. W. (2007). A review of multidimensional, multifluid, intermediate-scale experiments: Flow behavior, saturation imaging, and tracer detection and quantification. *Vadose Zone Journal*, 6, 610-637.
- Oostrom, M., Hofstee, C., Lenhard, R. J. and Wietsma, T. W. (2003). Flow behavior and residual saturation formation of liquid carbon tetrachloride in unsaturated heterogeneous porous media. *Journal of Contaminant Hydrology*, 64, 93-112.

- Pan, Y., Yang, J., Jia, Y. and Xu, Z. (2016). Experimental study on non-aqueous phase liquid multiphase flow characteristics and controlling factors in heterogeneous porous media. *Environmental Earth Sciences*, 75, 1-13.
- Pankow, J. F. and Cherry, J. A. (1996). *Dense chlorinated solvents and other DNAPLs in groundwater: History, behavior, and remediation*. Oregon, Waterloo press.
- Pansu, M. and Gautheyrou, J. (2007). *Handbook of soil analysis: mineralogical, organic and inorganic methods*. The Netherlands, Springer Science & Business Media.
- Pao, W. K. and Lewis, R. W. (2002). Three-dimensional finite element simulation of three-phase flow in a deforming fissured reservoir. *Computer Methods in Applied Mechanics and Engineering*, 191, 2631-2659.
- Paria, S. (2008). Surfactant-enhanced remediation of organic contaminated soil and water. *Advances in Colloid and Interface Science*, 138, 24-58.
- Parker, B. L., Gillham, R. W. and Cherry, J. A. (1994). Diffusive Disappearance of Immiscible-Phase Organic Liquids in Fractured Geologic Media. *Ground Water*, 32, 805-820.
- Parker, L., Yarwood, R. and Selker, J. (2006). Observations of gas flow in porous media using a light transmission technique. *Water Resources Research*, 42, 1-5.
- Peng, Z., Duwig, C., Delmas, P., Gaudet, J.-P., Strozzi, A. G., Charrier, P. and Denis, H. (2015). Visualization and Characterization of Heterogeneous Water Flow in Double-Porosity Media by Means of X-ray Computed Tomography. *Transport in Porous Media*, 110, 543-564.
- Pennell, K. D., Abriola, L. M. and Weber Jr, W. J. (1993). Surfactant-enhanced solubilization of residual dodecane in soil columns. 1. Experimental investigation. *Environmental Science & Technology*, 27, 2332-2340.
- Pennell, K. D. and Suchomel, E. J. (2006). Reductions in Contaminant Mass Discharge Following Partial Mass Removal from DNAPL Source Zones. *Environmental Science & Technology*, 40, 6110-6116.

- Pokrajac, D. and Deletic, A. (2006). Experimental study of LNAPL migration in the vicinity of a steep groundwater table. *Soils and Foundations*, 46, 271-280.
- Ribeiro, F. R., Egreja Filho, F. B., Fabris, J. D., Mussel, W. D. N. and Novais, R. F. (2007). Potential use of a chemical leaching reject from a kaolin industry as agricultural fertilizer. *Revista Brasileira de Ciência do Solo*, 31, 939-946.
- Rimmer, A., Dicarolo, D. A., Steenhuis, T. S., Bierck, B., Durnford, D. and Parlange, J.-Y. (1998). Rapid fluid content measurement method for fingered flow in an oil-water-sand system using synchrotron X-rays. *Journal of Contaminant Hydrology*, 31, 315-335.
- Rivett, M., Shepherd, K., Keays, L. and Brennan, A. (2005). Chlorinated solvents in the Birmingham aquifer, UK: 1986–2001. *Quarterly Journal of Engineering Geology and Hydrogeology*, 38, 337-350.
- Rivett, M. O., Wealthall, G. P., Dearden, R. A. and Mcalary, T. A. (2011). Review of unsaturated-zone transport and attenuation of volatile organic compound (VOC) plumes leached from shallow source zones. *Journal of Contaminant Hydrology*, 123, 130-156.
- Rosenbrand, E., Haugwitz, C., Jacobsen, P. S. M., Kjøller, C. and Fabricius, I. L. (2014). The effect of hot water injection on sandstone permeability. *Geothermics*, 50, 155-166.
- Rowe, B. L., Toccalino, P. L., Moran, M. J., Zogorski, J. S. and Price, C. V. (2007). Occurrence and potential human-health relevance of volatile organic compounds in drinking water from domestic wells in the United States. *Environmental Health Perspectives*, 115, 1539-1546.
- Ruffino, B. and Zanetti, M. (2009). Adsorption study of several hydrophobic organic contaminants on an aquifer material. *American Journal of Environmental Sciences*, 5, 507-515.
- Russell, A. R. (2010). Water retention characteristics of soils with double porosity. *European Journal of Soil Science*, 61, 412-424.

- Ryer, A. (1998) Light Measurement Handbook. Newburyport, MA: International Light. Inc.
- Sa'ari, R., Rahman, N., Yusof, Z., Ngien, S., Kamaruddin, S., Mustaffar, M. and Hezmi, M. (2015). Application Of Digital Image Processing Technique In Monitoring LNAPL Migration In Double Porosity Soil Column. *Jurnal Teknologi*, 72, 23-29.
- Sarikaya, Y., Önal, M., Baran, B. and Alemdaroğlu, T. (2000). The effect of thermal treatment on some of the physicochemical properties of a bentonite. *Clays and Clay Minerals*, 48, 557-562.
- Schembre, J. and Kovscek, A. (2005). Mechanism of formation damage at elevated temperature. *Journal of Energy Resources Technology*, 127, 171-180.
- Schincariol, R. A. and Schwartz, F. W. (1990). An experimental investigation of variable density flow and mixing in homogeneous and heterogeneous media. *Water Resources Research*, 26, 2317-2329.
- Schlumberger. (2017). *Oilfield Glossary* (Online). Retrived from http://www.glossary.oilfield.slb.com/Terms/i/interfacial_tension.aspx on (7/5/2017).
- Schott (2015). *Optical filters* (Online). Retrived from http://www.schott.com/advanced_optics/english/products/optical-components/optical-filters/optical-filter-glass/ on (14/12/2015).
- Schroth, M. H., Istok, J. D. and Selker, J. S. (1998). Three-phase immiscible fluid movement in the vicinity of textural interfaces. *Journal of Contaminant Hydrology*, 32, 1-23.
- Shamsijazeyi, H. and Kaghazchi, T. (2010). Investigation of nitric acid treatment of activated carbon for enhanced aqueous mercury removal. *Journal of Industrial and Engineering Chemistry*, 16, 852-858.

- Sharma, R. S. and Mohamed, M. H. A. (2003). *Migration of LNAPL in an Unsaturated/Saturated Sand. Geoenvironmental Engineering: Geoenvironmental Impact Management*. MPG Books, UK.
- Sikora, F., Crouse, K., Heckendorn, S., Huluka, G., Mitchell, C., Moore, K. and Oldham, J. (2014) *Cation exchange capacity. Soil Test Methods From the Southeastern United States*. USA: Clemson University.
- Simantiraki, F., Aivalioti, M. and Gidarakos, E. (2009). Implementation of an image analysis technique to determine LNAPL infiltration and distribution in unsaturated porous media. *Desalination*, 248, 705-715.
- Šimůnek, J., Wendroth, O., Wypler, N. and Van Genuchten, M. T. (2001). Non-equilibrium water flow characterized by means of upward infiltration experiments. *European Journal of Soil Science*, 52, 13-24.
- Soga, K., Page, J. and Illangasekare, T. (2004). A review of NAPL source zone remediation efficiency and the mass flux approach. *Journal of Hazardous Materials*, 110, 13-27.
- Somerton, W. H. (1992). *Thermal properties and temperature-related behavior of rock/fluid systems*. Elsevier, USA.
- Sreedharan, V. and Sivapullaiah, P. (2017). Hydraulic Performance of Organo Clay Enhanced Sand Bentonite as Secondary Liner. *Indian Geotechnical Journal*, 1-8. doi:10.1007/s40098-017-0232-z.
- Stasinopoulos, T. C. and Hangarter, R. P. (1990). Preventing photochemistry in culture media by long-pass light filters alters growth of cultured tissues. *Plant Physiology*, 93, 1365-1369.
- Szymkiewicz, A., Lewandowska, J., Angulo-Jaramillo, R. and Butlanska, J. (2008). Two-scale modeling of unsaturated water flow in a double-porosity medium under axisymmetric conditions. *Canadian Geotechnical Journal*, 45, 238-251.

- Tadza, M. Y. M. (2011) Soil-water characteristic curves and shrinkage behaviour of highly plastic clays: An experimental investigation. PhD Thesis, Cardiff University.
- Tenthorey, E., Scholz, C. H., Aharonov, E. and Léger, A. (1998). Precipitation sealing and diagenesis: 1. Experimental results. *Journal of Geophysical Research: Solid Earth*, 103, 23951-23967.
- Testa, S. M. and Winegardner, D. L. (2000). *Restoration of Contaminated Aquifers: Petroleum Hydrocarbons and Organic Compounds. (2nd Edition)*. Boca Raton, Florida, CRC Press.
- The Physics Classroom. (2017). *Light waves and color-Lesson 2-Color and vision* (Online). Retrieved from <http://www.physicsclassroom.com/class/light/Lesson-2/Color-Addition> on (5/5/2017).
- Tidwell, V. C. and Glass, R. J. (1994). X ray and visible light transmission for laboratory measurement of two-dimensional saturation fields in thin-slab systems. *Water Resources Research*, 30, 2873-2882.
- Totsche, K. U., Kögel-Knabner, I., Haas, B., Geisen, S. and Scheibke, R. (2003). Preferential flow and aging of NAPL in the unsaturated soil zone of a hazardous waste site: implications for contaminant transport. *Journal of Plant Nutrition and Soil Science*, 166, 102-110.
- Tran Ngoc, T., Lewandowska, J. and Bertin, H. (2014). Experimental evidence of the double-porosity effects in geomaterials. *Acta Geophysica*, 62, 642-655.
- Trenberth, K. E., Smith, L., Qian, T., Dai, A. and Fasullo, J. (2007). Estimates of the global water budget and its annual cycle using observational and model data. *Journal of Hydrometeorology*, 8, 758-769.
- University of Colorado. (2002). *Online edition for students of organic chemistry lab courses at the University of Colorado, Boulder, Dept. of Chem. and Biochem., Chapter 15, Infrared Spectroscopy: Theory* (Online). Retrieved from www.imsu.edu.ng/repo/index.php/ugr/article/download/2/2 on.

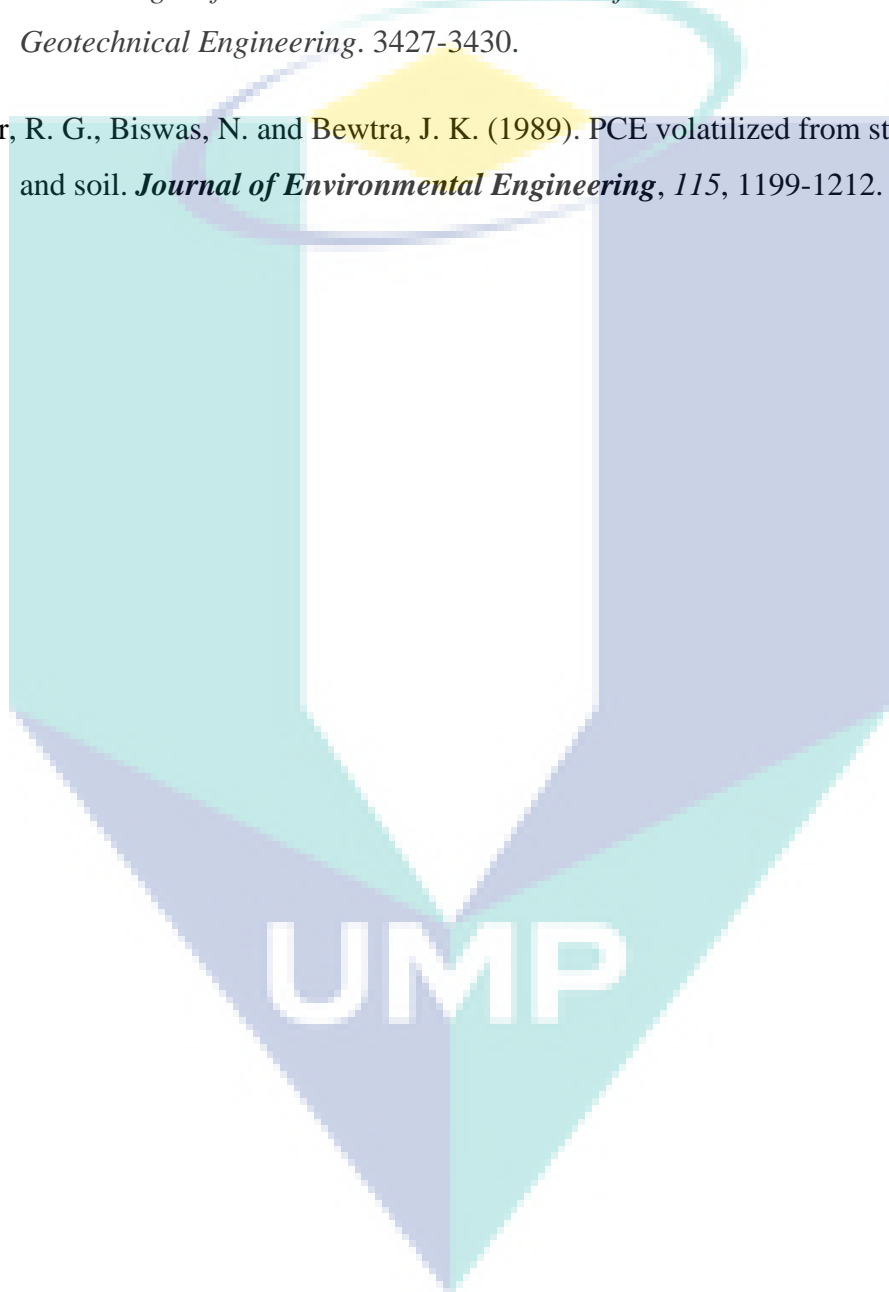
- USGS (2016). *How much water is there on, in, and above the Earth* (Online). Retrieved from <http://water.usgs.gov/edu/earthhowmuch.html> on (28/11/2016).
- Van Geel, P. and Sykes, J. (1994). Laboratory and model simulations of a LNAPL spill in a variably-saturated sand, 1. Laboratory experiment and image analysis techniques. *Journal of Contaminant Hydrology*, 17, 1-25.
- Venturelli, C. and Paganelli, M. (2007). Sintering behaviour of clays for the production of ceramics. *CFI. Ceramic forum international*. Göller.
- Vicaire (2015). *Chapter 2: Porous media- The liquid phase* (Online). Retrieved from http://echo2.epfl.ch/VICAIRE/mod_3/chapt_2/main.htm on (24/6/2015).
- Wade, L. G. (2012). *Organic Chemistry* USA, Pearson.
- Wang, C., Liu, S., Wu, J. and Li, Z. (2014). Effects of temperature-dependent viscosity on fluid flow and heat transfer in a helical rectangular duct with a finite pitch. *Brazilian Journal of Chemical Engineering*, 31, 787-797.
- Wang, G.-C. and Lu, T.-M. (2014). *X-Ray diffraction. RHEED Transmission Mode and Pole Figures*. Springer.
- Wang, H., Chen, X. and Jawitz, J. W. (2008). Locally-calibrated light transmission visualization methods to quantify nonaqueous phase liquid mass in porous media. *Journal of Contaminant Hydrology*, 102, 29-38.
- Warren, J. and Root, P. J. (1963). The behavior of naturally fractured reservoirs. *Society of Petroleum Engineers Journal*, 3, 245-255.
- Weisbrod, N., Niemet, M. R. and Selker, J. S. (2003). Light transmission technique for the evaluation of colloidal transport and dynamics in porous media. *Environmental Science & Technology*, 37, 3694-3700.
- Wildenschild, D. and Sheppard, A. P. (2013). X-ray imaging and analysis techniques for quantifying pore-scale structure and processes in subsurface porous medium systems. *Advances in Water Resources*, 51, 217-246.

- Wipfler, E. and Van Der Zee, S. (2001). A set of constitutive relationships accounting for residual NAPL in the unsaturated zone. *Journal of Contaminant Hydrology*, 50, 53-77.
- Wong, J. (1979). An electrochemical model of the induced-polarization phenomenon in disseminated sulfide ores. *Geophysics*, 44, 1245-1265.
- Yakymenko, I., Sidorik, E., Kyrlyenko, S. and Chekhun, V. (2011). Long-term exposure to microwave radiation provokes cancer growth: evidences from radars and mobile communication systems. *Experimental Oncology*, 33, 62-70.
- Yang, Z., Niemi, A., Fagerlund, F. and Illangasekare, T. (2012). Effects of single-fracture aperture statistics on entrapment, dissolution and source depletion behavior of dense non-aqueous phase liquids. *Journal of Contaminant Hydrology*, 133, 1-16.
- Yarwood, R., Rockhold, M. L., Niemet, M., Selker, J. S. and Bottomley, P. J. (2002). Noninvasive quantitative measurement of bacterial growth in porous media under unsaturated-flow conditions. *Applied and Environmental Microbiology*, 68, 3597-3605.
- Ye, S., Sleep, B. E. and Chien, C. (2009). The impact of methanogenesis on flow and transport in coarse sand. *Journal of Contaminant Hydrology*, 103, 48-57.
- Yilmaz, G. (2011). The effects of temperature on the characteristics of kaolinite and bentonite. *Scientific Research and Essays*, 6, 1928-1939.
- Yuan, Y. and Lee, T. R. (2013). *Contact angle and wetting properties. Surface science techniques*. Springer, Berlin Heidelberg.
- Zhao, Y., Sun, J., Sun, C., Cui, J. and Zhou, R. (2015). Improved light-transmission method for the study of LNAPL migration and distribution rule. *Water Science and Technology*, 71, 1576-1585.
- Zheng, F., Gao, Y., Sun, Y., Shi, X., Xu, H. and Wu, J. (2015). Influence of flow velocity and spatial heterogeneity on DNAPL migration in porous media:

insights from laboratory experiments and numerical modelling. *Hydrogeology Journal*, 23, 1703-1718.

Zihms, S., Switzer, C., Tarantino, A. and Karstunen, M. (2013). Understanding the effects of high temperature processes on the engineering properties of soils. *Proceedings of the 18th International Conference on Soil Mechanics and Geotechnical Engineering*. 3427-3430.

Zytner, R. G., Biswas, N. and Bewtra, J. K. (1989). PCE volatilized from stagnant water and soil. *Journal of Environmental Engineering*, 115, 1199-1212.



APPENDIX A

PROPERTIES OF LIGHT SHAPING DIFFUSER (LSD)

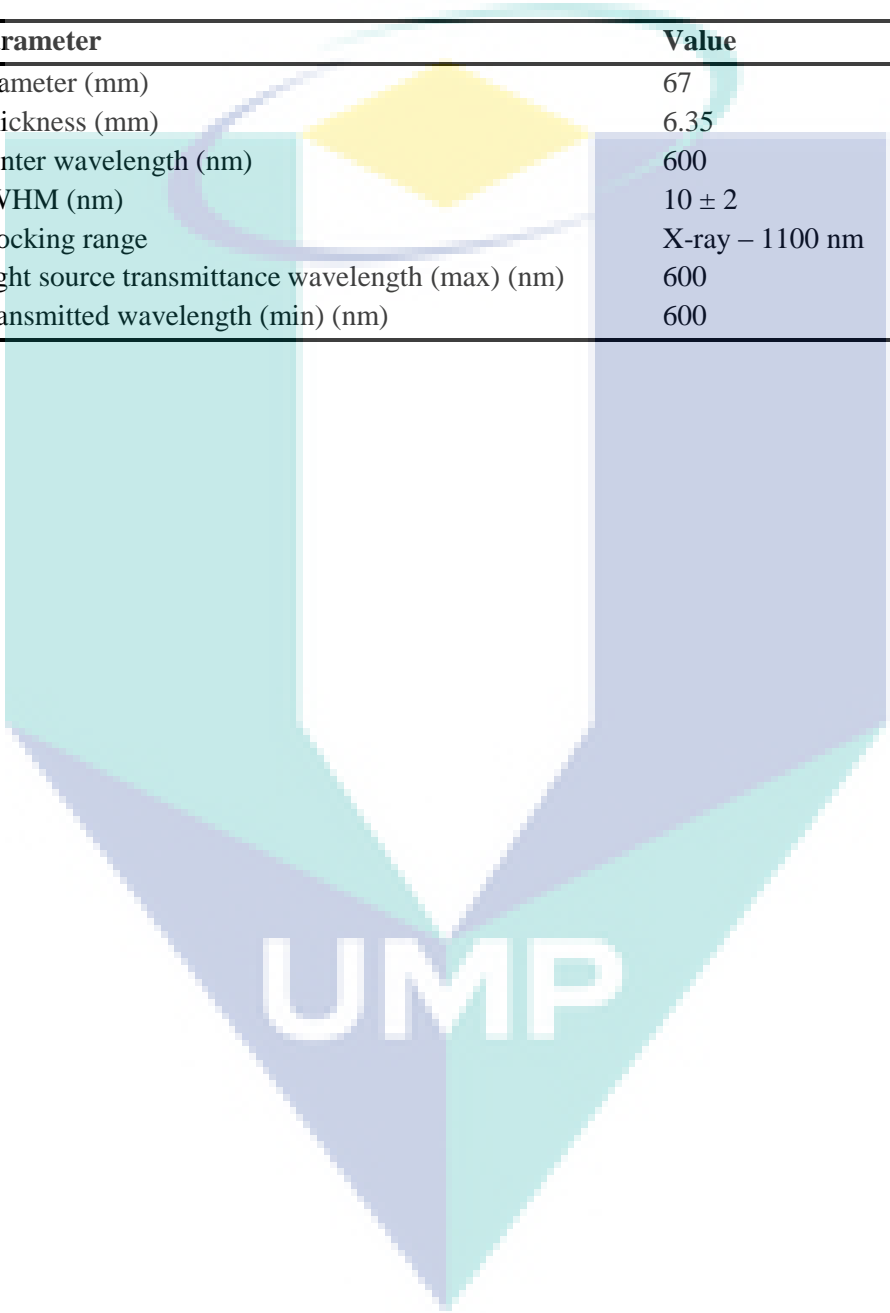
Parameter	Value
Material structure	Polycarbonate
Thickness (in.)	0.010
Size (cm)	24 × 48
Angle	80°
Transmission spectral range (nm)	400 - 1500
Temperature range (°C)	-30 – 80 @ 240 hours
Refractive index	1.586

A large, stylized logo for UWP (University of West Florida) is centered on the page. It features a shield-like shape with a white background and a blue border. The letters 'UWP' are prominently displayed in the center in a bold, white, sans-serif font. The logo is partially overlaid by the table above it.

UWP

APPENDIX B

PROPERTIES OF THE BAND-PASS FILTER



Parameter	Value
Diameter (mm)	67
Thickness (mm)	6.35
Center wavelength (nm)	600
FWHM (nm)	10 ± 2
Blocking range	X-ray – 1100 nm
Light source transmittance wavelength (max) (nm)	600
Transmitted wavelength (min) (nm)	600

APPENDIX C

VBA SCRIPT TO CONVERT MATRIX TO XYZ FORMAT DATA

```
Sub ConvertTable()  
'Update 20150512  
Dim Rng As Range  
Dim cRng As Range  
Dim rRng As Range  
Dim xOutRng As Range  
xTitleId = "KutoolsforExcel"  
Set cRng = Application.InputBox("Select your Column labels", xTitleId, Type:=8)  
Set rRng = Application.InputBox("Select Your Row Labels", xTitleId, Type:=8)  
Set Rng = Application.InputBox("Select your data", xTitleId, Type:=8)  
Set outRng = Application.InputBox("Out put to (single cell):", xTitleId, Type:=8)  
Set xWs = Rng.Worksheet  
k = 1  
xColumns = rRng.Column  
xRow = cRng.Row  
For i = Rng.Rows(1).Row To Rng.Rows(1).Row + Rng.Rows.Count - 1  
    For j = Rng.Columns(1).Column To Rng.Columns(1).Column + Rng.Columns.Count  
    - 1  
        outRng.Cells(k, 1) = xWs.Cells(i, xColumns)  
        outRng.Cells(k, 2) = xWs.Cells(xRow, j)  
        outRng.Cells(k, 3) = xWs.Cells(i, j)  
        k = k + 1  
    Next j  
Next i  
End Sub
```

Adopted from: Extend Office (2009)

APPENDIX D

PARTICLE SIZE DISTRIBUTION RESULTS FOR RAW KAOLIN AND SILICA SAND USED IN EXPERIMENTS

Table D.1 Particle size distribution results for raw kaolin

Sieve Size (mm)	Mass Retained on Sieve (g)	Percent Retained (%)	Percent Passing (%)
5	0	0	100.00
3.35	0	0	100.00
1.18	0	0	100.00
0.6	0.4	0.5	99.50
0.3	1.5	1.88	98.13
0.15	3.65	4.56	95.44
0.063	23.95	29.94	70.06
Pan	50.50	63.13	-

Total mass = 80 g

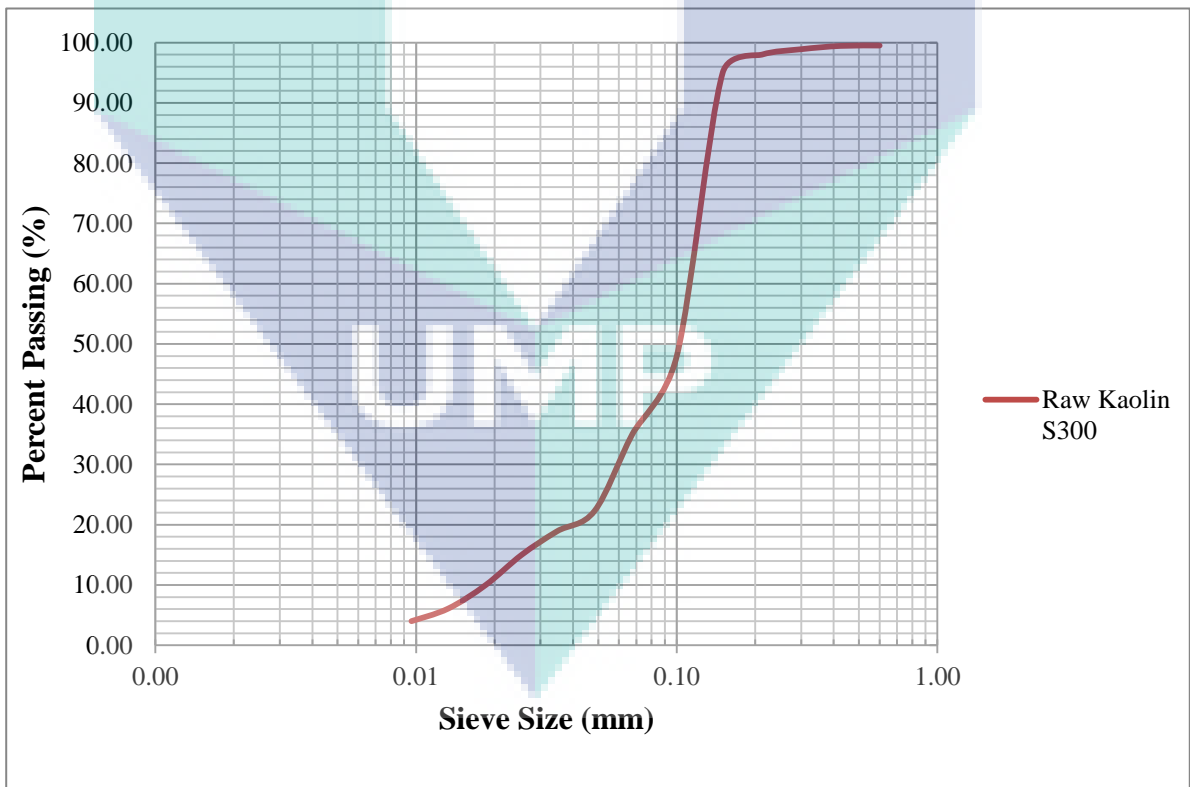


Figure D.1 Particle size analysis for raw kaolin

Table D.2 Particle size distribution results for silica sand

Sieve Size (mm)	Mass retained on Sieve (g)	Percent Retained (%)	Percent Passing (%)
1.18	0.26	0.03	99.97
0.6	17.18	1.72	98.28
0.425	238.00	23.80	76.20
0.3	355.00	35.50	64.50
0.15	300.34	30.03	69.97
0.063	80.84	8.08	91.92
Pan	5.80	0.58	-

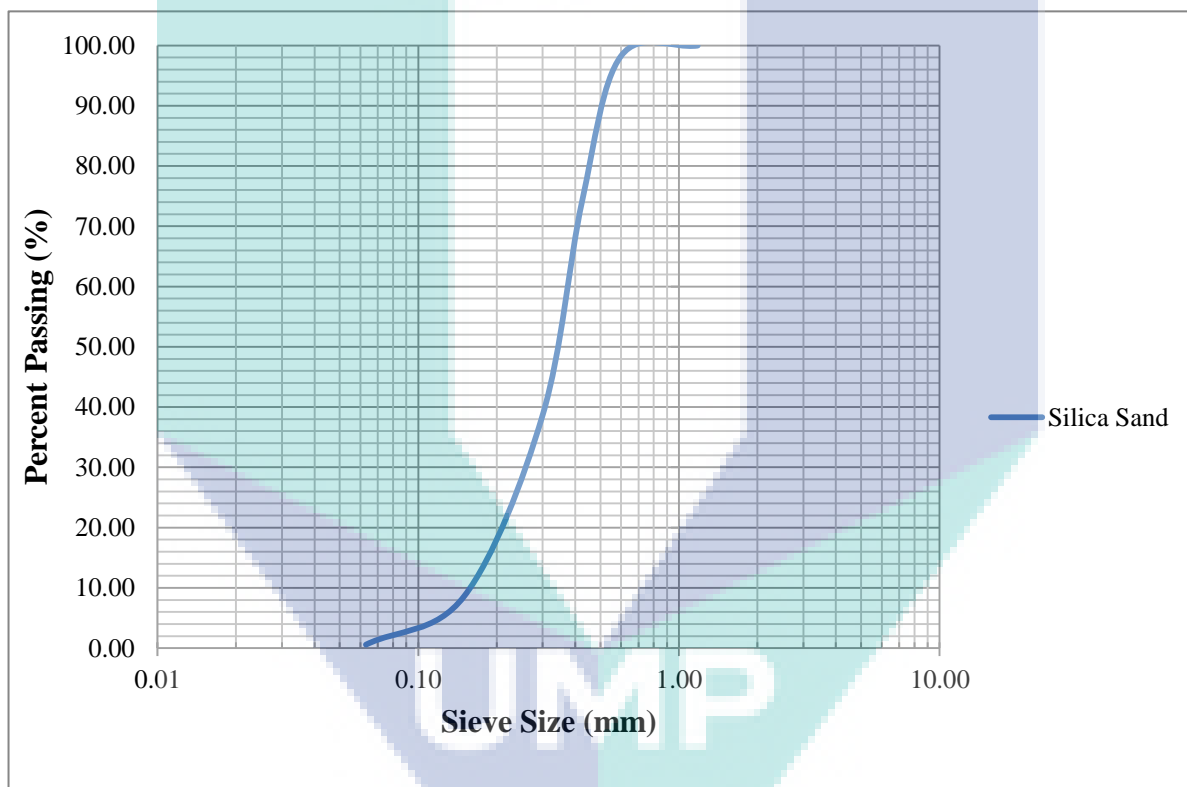


Figure D.2 Particle size analysis for silica sand

$$\text{Percent Retained} = \frac{\text{Mass Retained on sieve}}{\text{Total mass of soil}} \times 100 \%$$

$$\text{Percent Passing} = (100 - \text{Percent Retained}) \times 100 \%$$

APPENDIX E

HYDROMETER TEST RESULTS FOR RAW KAOLIN USED IN EXPERIMENTS

Elapse time, t (minute)	Temperature ($^{\circ}\text{C}$)	Reading (R_h')	$R_h' + C_m$	Viscosity (mPa.S)	Effective depth, H_R (mm)	Particle diameter D(mm)	$R_d = R_h' - R_0'$	% Finer than D (K %)
0.5	25	1.0203	1.0205	0.891	115.0613	0.0617	0.0218	6.9864
1	25.2	1.0198	1.0200	0.88728	117.0720	0.0439	0.0212	6.8258
2	25.1	1.0180	1.0183	0.88914	124.1094	0.0320	0.0195	6.2636
4	25	1.0160	1.0163	0.891	132.1522	0.0234	0.0175	5.6212
8	25	1.0128	1.0131	0.891	145.0207	0.0173	0.0143	4.5933
16	25	1.0098	1.0101	0.891	157.0849	0.0127	0.0113	3.6297
32	25	1.0065	1.0068	0.891	170.3555	0.0094	0.0080	2.5697
60	25	1.0045	1.0048	0.891	178.3983	0.0070	0.0060	1.9273
120	25	1.0034	1.0037	0.891	182.8219	0.0050	0.0049	1.5739
240	25	1.0025	1.0028	0.891	186.4411	0.0036	0.0040	1.2848
1440	25	1.0008	1.0010	0.891	193.4786	0.0015	0.0022	0.7227
2880	25	1.0005	1.0008	0.891	194.4839	0.0011	0.0020	0.6424
4320	25	1.0005	1.0008	0.891	194.4839	0.0009	0.0020	0.6424
9840	26.4	1.0000	1.0003	0.8649	196.4946	0.0006	0.0015	0.4818
10080	25.4	1.0000	1.0003	0.87955	196.4946	0.0006	0.0015	0.4818
11520	25	1.0003	1.0005	0.891	195.4893	0.0005	0.0018	0.5621
12960	23.4	1.0005	1.0008	0.92652	194.4839	0.0005	0.0020	0.6424
21720	26	1.0000	1.0003	0.8724	196.4946	0.0004	0.0015	0.4818

Meniscus correction C_m	0.0005
Reading in dispersant R_0'	0.9985
Dry mass of soil (passing 0.063mm) (g)	50
Particle density (measured) ρ_s (Mg/m^3)	2.65
Length of the bulb, h (mm)	164
N (mm)	10
Distance between 100ml and 1000ml,L (mm)	317
Volume of hydrometer, V_h (ml)	78.83

APPENDIX F

SPECIFIC GRAVITY TEST RESULTS FOR MATERIALS USED IN EXPERIMENTS

Table F.1 Specific gravity result for raw kaolin

Test No.	1	2	3	4	5
Weight of density bottle (g)	31.35	31.50	30.31	31.88	30.33
Weight of bottle + Stopper (W_1) (g)	35.77	35.32	35.98	36.06	36.29
Weight of bottle + Stopper + Dry Soil (W_2) (g)	41.94	41.47	41.06	41.21	40.55
Weight of bottle + Stopper + Soil + Water (W_3) (g)	143.00	142.58	142.50	142.70	142.85
Weight of bottle + Stopper + Water (W_4) (g)	139.35	138.87	139.39	139.28	140.21
Weight of Dry Soil ($W_2 - W_1$) (g)	6.17	6.15	5.08	5.15	4.26
Weight of Water ($W_4 - W_1$) (g)	103.58	103.55	103.41	103.22	103.92
Weight of Water Used ($W_3 - W_2$) (g)	101.06	101.11	101.44	101.49	102.30
Specific gravity	2.45	2.52	2.58	2.98	2.63

Average value of specific gravity = 2.63

UMP

Table F.2 Specific gravity result for burned kaolin

Test No.	1	2	3	4	5
Weight of density bottle (g)	31.71	32.59	31.88	33.15	31.90
Weight of bottle + Stopper (W_1) (g)	36.30	36.99	36.07	37.27	36.35
Weight of bottle + Stopper + Dry Soil(W_2) (g)	41.31	41.97	41.74	42.28	41.31
Weight of bottle + Stopper + Soil + Water (W_3) (g)	139.20	139.94	138.82	140.72	138.86
Weight of bottle + Stopper + Water (W_4) (g)	136.08	136.85	135.29	137.60	135.77
Weight of Dry Soil ($W_2 - W_1$) (g)	5.01	4.98	5.67	5.01	4.96
Weight of Water ($W_4 - W_1$) (g)	99.78	99.86	99.22	100.33	99.42
Weight of Water Used ($W_3 - W_2$) (g)	97.89	97.97	97.08	98.44	97.55
Specific gravity	2.65	2.63	2.65	2.65	2.65

Average value of specific gravity = 2.65

UMP

Table F.3 Specific gravity result for silica sand

Test No.	1	2	3	4	5
Weight of density bottle (g)	29.83	31.48	31.34	32.61	29.83
Weight of bottle+Stopper (W1) (g)	34.34	35.89	35.94	36.7	34.34
Weight of bottle+Stopper+Dry Soil(W2) (g)	39.35	41.02	40.99	41.86	39.35
Weight of bottle + Stopper+ Soil + Water (W3) (g)	138.36	139.73	139.22	139.79	138.36
Weight of bottle + Stopper+ Water (W4) (g)	135.21	136.5	136.04	136.56	135.21
Weight of Dry Soil (W2-W1) (g)	5.01	5.13	5.05	5.16	5.01
Weight of Water (W4-W1) (g)	100.87	100.61	100.1	99.86	100.87
Weight of Water Used (W3-W2) (g)	99.01	98.71	98.23	97.93	99.01
Specific gravity	2.69	2.7	2.7	2.67	2.69

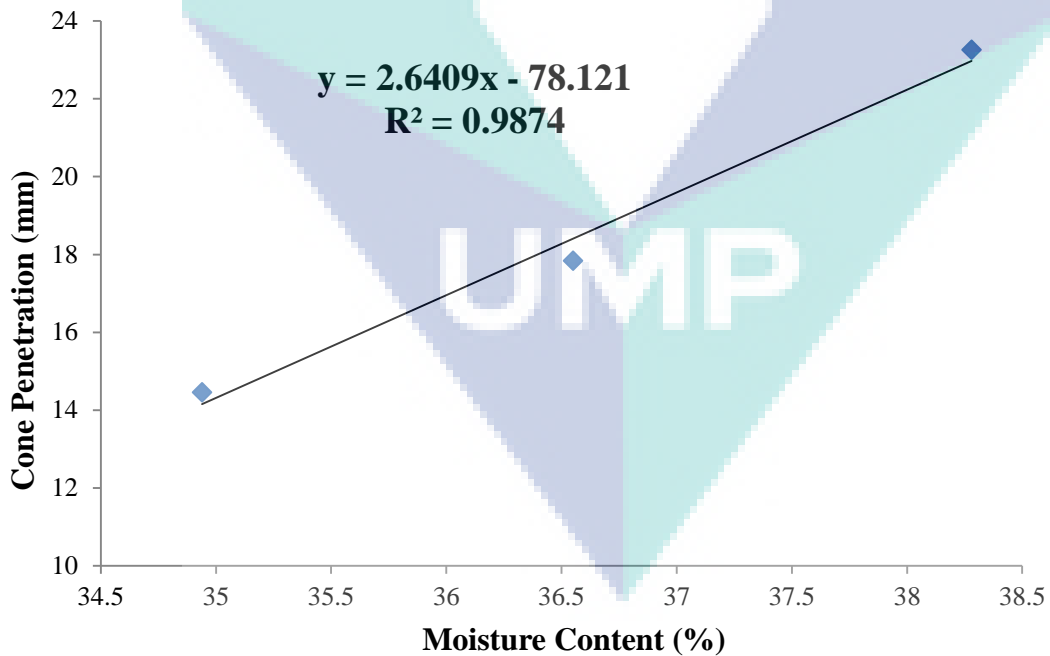
Average value of specific gravity = 2.69

UMP

APPENDIX G

LIQUID LIMIT TEST RESULTS FOR RAW KAOLIN USED IN EXPERIMENTS

Test Number	1		2		3	
Cone penetration (mm)	14.50	14.40	17.90	17.75	23.40	23.10
Average penetration (mm)	14.45		17.83		23.25	
Container Weight (g)	9.79	9.96	10.34	9.93	10.83	10.54
Wet soil + container (g)	15.62	18.71	14.15	16.94	22.61	24.00
wet soil, W_w (g)	5.83	8.75	3.81	7.01	11.78	13.46
Dry soil + container (g)	14.12	16.43	13.09	15.14	19.47	20.14
Dry soil, W_d (g)	4.33	6.47	2.75	5.21	8.64	9.60
Moisture loss, $W_w - W_d$ (g)	1.50	2.28	1.06	1.80	3.14	3.86
Moisture content (%)	34.64	35.24	38.55	34.55	36.34	40.21
Average Moisture content (%)	34.94		36.55		38.28	



At 20 mm of cone penetration, moisture content is 37.20 % according to the plotted results.

APPENDIX H

PLASTIC LIMIT TEST RESULTS FOR RAW KAOLIN USED IN EXPERIMENTS

Test No.	1	2	3
Container weight (g)	10.47	10.16	10.36
Wet soil + container (g)	19.70	19.11	19.58
Wet soil, W_w (g)	9.23	8.95	9.22
Dry soil + container (g)	17.83	17.18	17.8
Dry soil, W_d (g)	7.36	7.02	7.44
Moisture loss, $W_w - W_d$ (g)	1.87	1.93	1.78
Moisture content (%)	25.41	27.49	23.92

By averaging the moisture contents obtained, the plastic limit value for the raw kaolin is 25.61 %.

UMP

APPENDIX I

PERMEABILITY TEST RESULTS FOR RAW KAOLIN USED IN EXPERIMENTS

FALLING HEAD TEST

Sample weight = 2000 g

Specimen diameter = 0.1007 m

Specimen height = 0.131 m

Area = 0.0796 m²

Manometer tube	Diameter (m)	Start level h ₁ (m)	End level h ₂ (m)	Time, t (Sec)
T ₁	0.01617	1	0.894	900
T ₂	0.00733	1	0.563	900
T ₃	0.00815	1	0.494	900

h ₁ /h ₂	Log h ₁ /h ₂	Time, t (sec)	Radius of manometer tube, r (m)	Area of manometer tube, a (m ²)	Area of permeator A	A x t (m ² /s)	Permeability Coefficient, K _t (m/s)
1.1185	0.04866	900	0.00809	0.00021	0.00786	7.074	7.106 × 10 ⁻¹²
1.7762	0.24949	900	0.00367	0.00004	0.00786	7.074	7.486 × 10 ⁻¹²
2.0242	0.30627	900	0.00408	0.00005	0.00786	7.074	1.136 × 10 ⁻¹²

$$K = \frac{3.84 \times a \times L \times \log \frac{h_1}{h_2} \times 0.00001}{A \times t}$$

The average permeability value from the table above is 8.54 × 10⁻¹² m/s. (Very low permeability)

**PERMEABILITY TEST RESULTS FOR BURNED KAOLIN USED IN
EXPERIMENTS**

Manometer tube	Diameter(m)	Start level h1 (m)	End level h2 (m)	Time, t (Sec)
T1	0.01617	1.00	0.889	900
T2	0.00733	1.00	0.742	900
T3	0.00815	1.00	0.554	900

Manometer tube	h1/h2	Log h1/h2	Time, t (sec)	Radius of manometer tube, r (m)	Area of manometer tube, a (m²)	Area of permeter, A	A x t (m²/s)	Permeability Coefficient, K_t (m/s)
T1	1.1248	0.05110	900	0.00809	0.00021	0.00796	7.164	7.368×10^{-12}
T2	1.3477	0.12960	900	0.00367	0.00004	0.00796	7.164	3.840×10^{-12}
T3	1.8050	0.25649	900	0.00408	0.00005	0.00796	7.164	9.395×10^{-12}

The average permeability value from the table above is 6.8679×10^{-12} m/s. (Very low permeability)

PERMEABILITY TEST RESULTS FOR SILICA SAND USED IN EXPERIMENTS
CONSTANT HEAD PERMEABILITY

Sample Description	Value
Sample diameter (m)	0.8
Sample length (m)	0.23
Area (m ²)	0.5024
Volume (m ³)	0.115552
Density	2.69
Head difference (m)	0.38
Distance difference (m)	0.9
Hydraulic gradient (i)	0.42

Time (min)	Time interval	Discharge (Q) ml	Flow rate, q = Q/t (ml/min)	Flow rate, q = Q/t (m/s)	Permeability, k (m/s) = (q/A*i)
10:30 AM	1	340	340	5.66667×10^{-6}	2.68552×10^{-5}
10:31 AM	1	340	340	5.66667×10^{-6}	2.68552×10^{-5}
10:32 AM	1	340	340	5.66667×10^{-6}	2.68552×10^{-5}
10:33 AM	1	340	340	5.66667×10^{-6}	2.68552×10^{-5}
10:34 AM	2	710	355	5.91667×10^{-6}	2.804×10^{-5}
10:36 AM	2	710	355	5.91667×10^{-6}	2.804×10^{-5}
10:38 AM	2	710	355	5.91667×10^{-6}	2.804×10^{-5}
10:40 AM	2	710	355	5.91667×10^{-6}	2.804×10^{-5}
10:42 AM	2	710	355	5.91667×10^{-6}	2.804×10^{-5}
10:45 AM	3	1050	350	5.83333×10^{-6}	2.76451×10^{-5}
10:48 AM	3	1050	350	5.83333×10^{-6}	2.76451×10^{-5}
10:51 AM	3	1050	350	5.83333×10^{-6}	2.76451×10^{-5}
10:54 AM	3	1050	350	5.83333×10^{-6}	2.76451×10^{-5}
10:59 AM	5	1820	364	6.06667×10^{-6}	2.87509×10^{-5}
11:04 AM	5	1820	364	6.06667×10^{-6}	2.87509×10^{-5}
11:09 AM	5	1820	364	6.06667×10^{-6}	2.87509×10^{-5}
Sum					0.000444454
Average					2.77784×10^{-5}

The average permeability is 2.78×10^{-5} m/s (Low permeability)

APPENDIX J

EXAMPLE OF CALCULATION THE CEC VALUE

Steps of calculation CEC for Na⁺ as an example:

The value of Na⁺ in (ppm) obtained from the ICP-OES for the case of raw kaolin was 0.83 ppm

The molar mass of Na⁺ = 23 g/mol.

1. Convert the value from g/mol to g/L as follow:
 $0.83 \text{ mg/L} \times 1\text{g}/1000 \text{ mg} = 0.83 \times 10^{-3} \text{ g/L}.$
2. Convert from g/L to mol/L as follow:
 $0.83 \times 10^{-3} \text{ g/L} \times (1 \text{ mol}/23 \text{ g}) = 3.609 \times 10^{-5} \text{ mol/L}.$
3. Convert from mol/L to Cmol/L as follow:
 $3.609 \times 10^{-5} \text{ mol/L} \times (100 \text{ Cmol}/1\text{mol}) = 3.609 \times 10^{-3} \text{ Cmol/L}.$
4. Convert from Cmol/L to Cmol/g as follow:
 $3.609 \times 10^{-3} \text{ Cmol/L} \times (0.16 \text{ L}/5\text{g}) = 1.154 \times 10^{-4} \text{ Cmol/g}.$

Where the 0.16 L represents the amounts of the ammonium acetate solution and the 5g is the weight of soil sample.
5. Convert from Cmol/g to Cmol/kg as follow:
 $1.154 \times 10^{-4} \text{ Cmol/g} \times (1000\text{g}/1\text{kg}) = 0.1154 \text{ Cmol/kg} = \text{meq}/100\text{g}.$

APPENDIX K

CALCULATION STEPS TO DETERMINE THE DOUBLE-POROSITY VALUE FROM MODEL COMPACTION

The double- porosity in all the experiments was calculated from compacting the flow chamber with materials.

- **Density of sand (ρ_s) = 2.69 g/cm³.**

Weight of sand after compaction (W) = 2433 g.

Volume of compacted sand (V) = $W / \rho_s = 904.46 \text{ cm}^3$.

Volume of flow chamber (V_t) = $45 \text{ cm} \times 30 \text{ cm} \times 1 \text{ cm} = 1350 \text{ cm}^3$.

Volume of voids (V_v) = $1350 - 904.46 = 445.54 \text{ cm}^3$.

Porosity = $V_v / V_t = 445.54 / 1350 = 0.33$.

- **Density of kaolin (ρ_s) = 2.65 g/cm³.**

Weight of kaolin spheres (W) = 1912 g.

Volume of compacted sand (V) = $W / \rho_s = 721.51 \text{ cm}^3$.

Volume of flow chamber (V_t) = $45 \text{ cm} \times 30 \text{ cm} \times 1 \text{ cm} = 1350 \text{ cm}^3$.

Volume of voids (V_v) = $1350 - 721.51 = 628.49 \text{ cm}^3$.

$$\text{Porosity} = V_v/V_t = 628.49/1350 = 0.46.$$

Following (Tran Ngoc et al., 2014), the double-porosity was calculated by knowing the porosity of each material and its volumetric fraction in creating the double-porosity. The volumetric fraction used to build the double-porosity in Experiment 1 was approximately 50 % of each material. Therefore, the double porosity was calculated as follow:

$$\begin{aligned} \text{The double-porosity value} &= (P_s \times F_s) + (P_c \times F_c) \\ &= (0.33 \times 0.5) + (0.46 \times 0.5) = 0.395 \end{aligned}$$

Where P_s is the porosity of sand, F_s the volume fraction of sand, P_c is the porosity of kaolin clay and the F_c the volume fraction of kaolin clay.

The logo of UIMP (University of Management and Information Technology) is a large, stylized shield shape. It is divided into four quadrants by a white vertical line and a white horizontal line. The top-left and bottom-right quadrants are light blue, while the top-right and bottom-left quadrants are light purple. The letters 'UIMP' are written in white, bold, sans-serif font across the bottom of the shield.

UIMP

APPENDIX L

CALCULATION STEPS TO DETERMINE THE NUMBER OF PORES (N_p)

The number of pores (N_p) across the thickness of the flow chamber which was compacted with double-porosity can be calculated using equation 3.20 and 3.21 as follow:

After extracting the light intensity values for the dry case (I_d) and for the case of fully saturated with water (I_s), calculate $\ln(I_s/I_d)$ pixel by pixel. The next step is to calculate the τ_{sw} , τ_{sa} , τ_{cw} , τ_{ca} using equation 3.23 and using the refractive index value is 1 for air, 1.6 for sand, 1.33 for water (Tidwell and Glass, 1994; Niemet and Selker, 2001) and 1.56 for kaolin (Ghosh et al., 1990) as follow:

$$\tau = \frac{4n_1n_2}{(n_1 + n_2)^2}$$

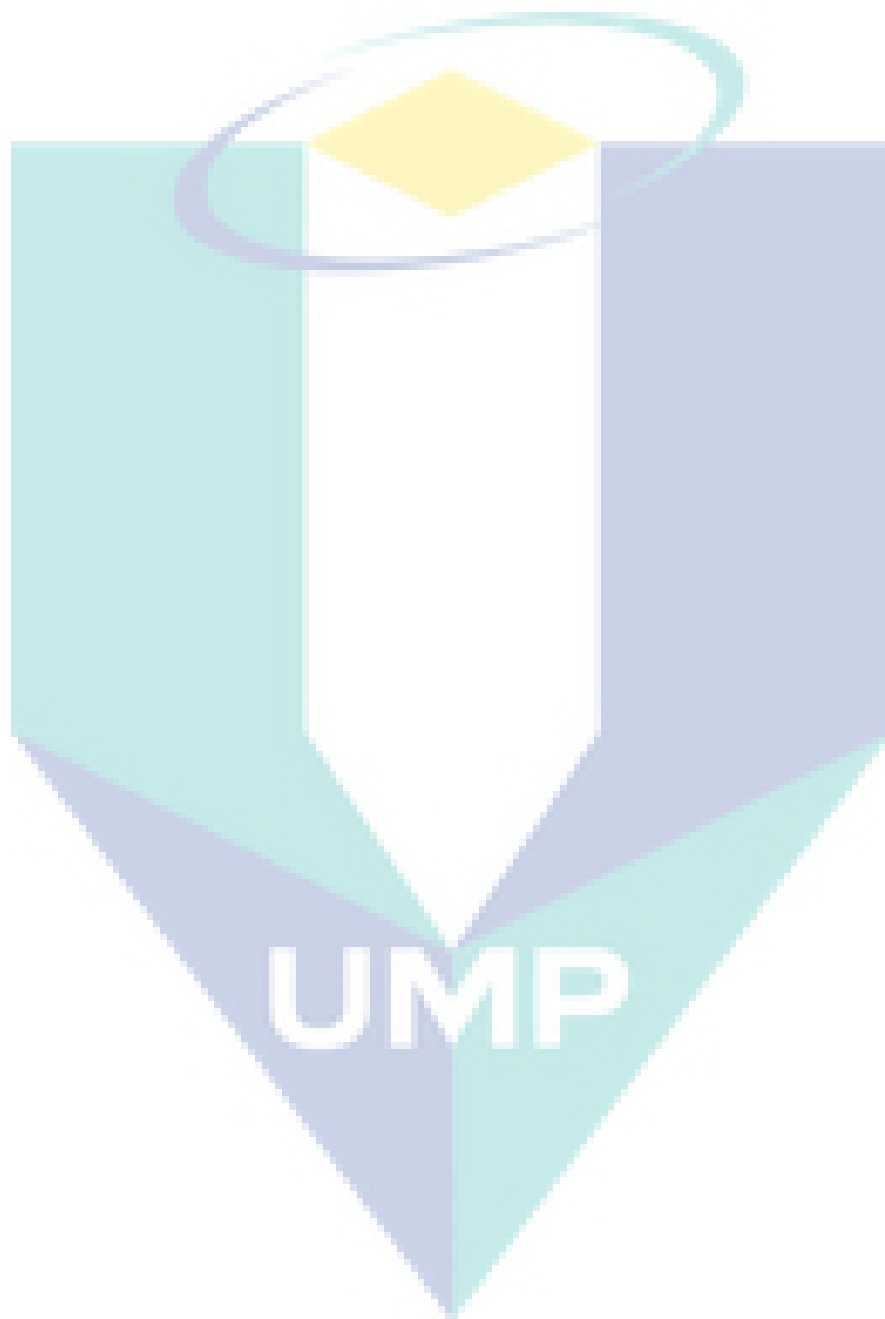
$$\tau_{sw} = 0.9915$$

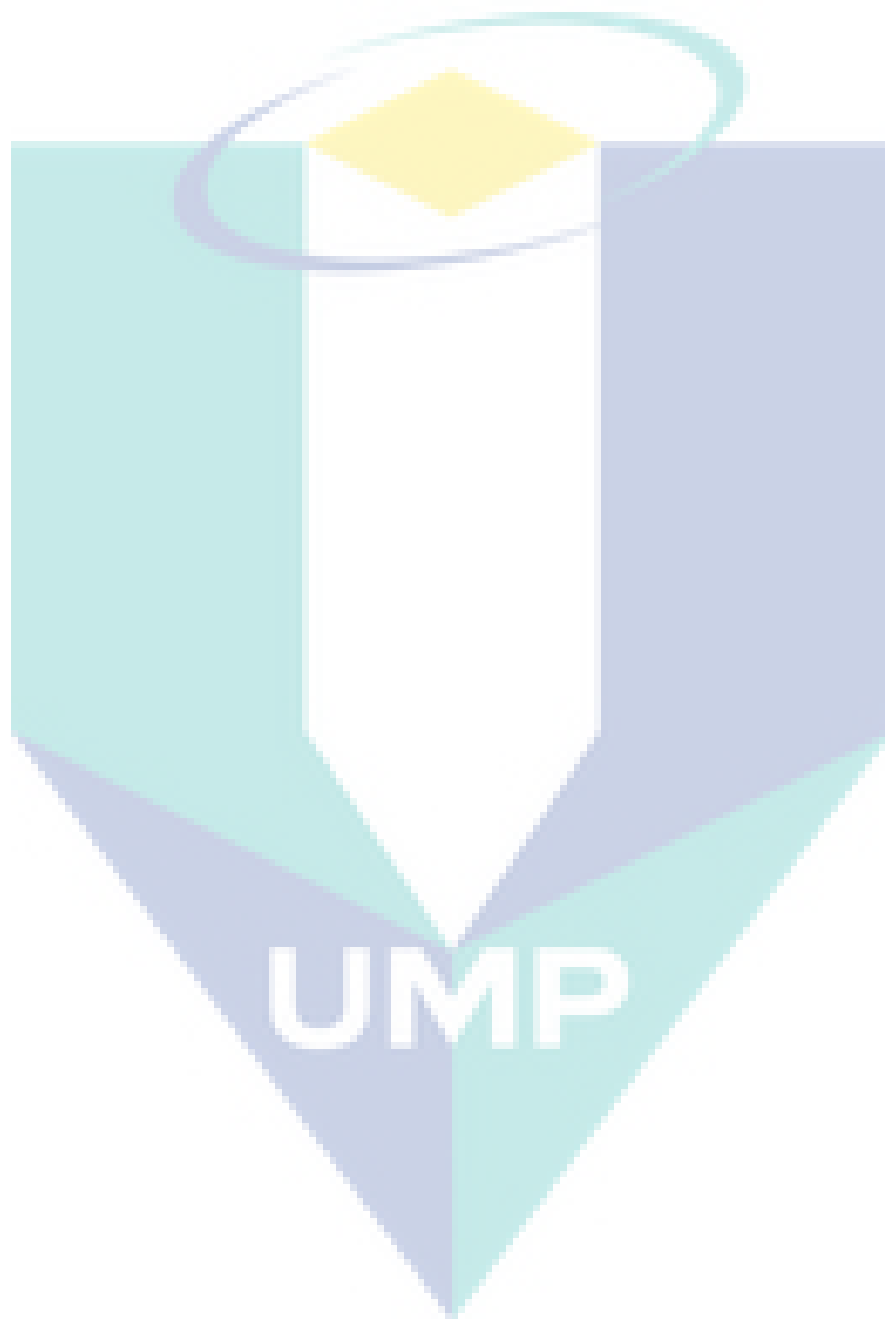
$$\tau_{sa} = 0.9467$$

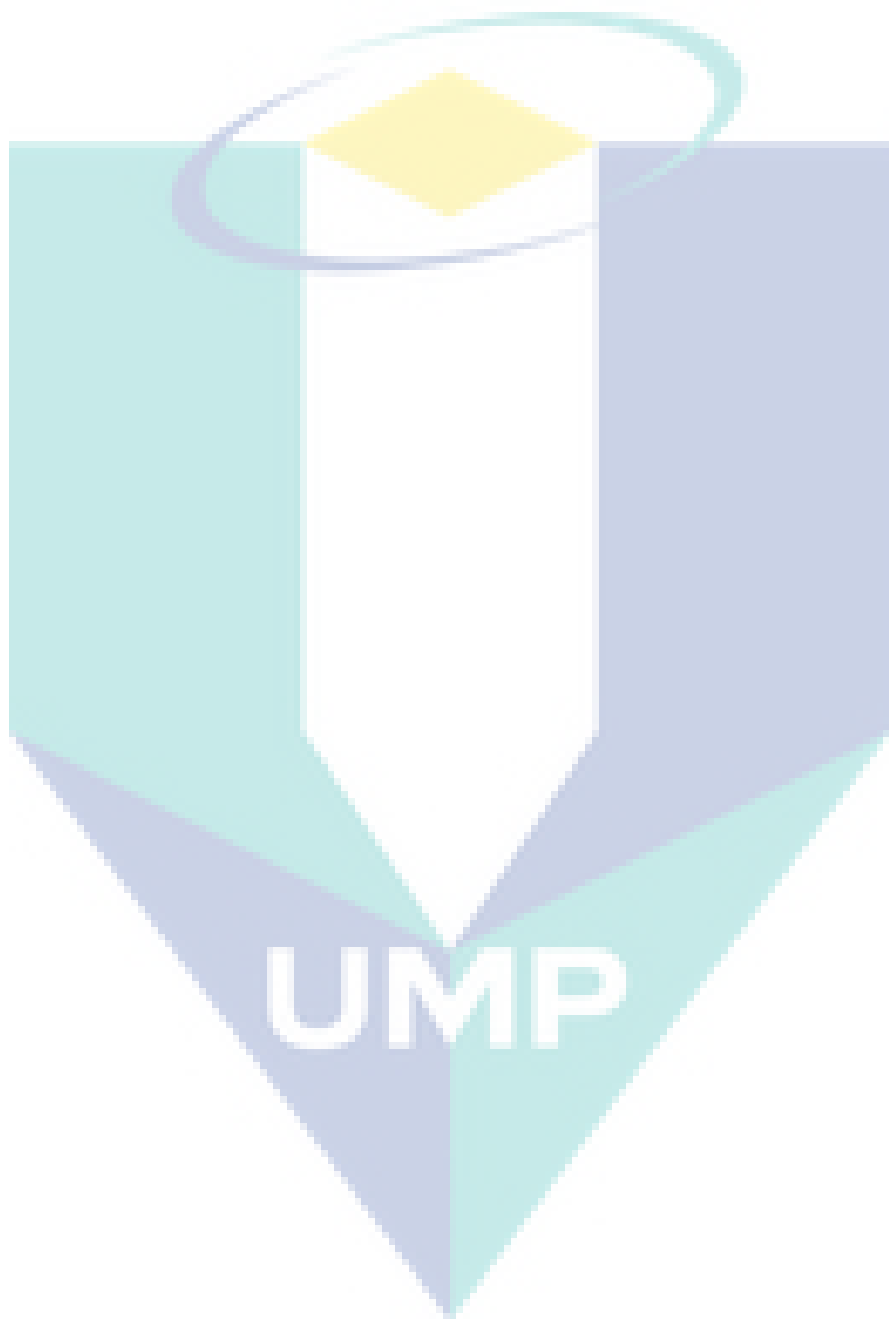
$$\tau_{cw} = 0.9885$$

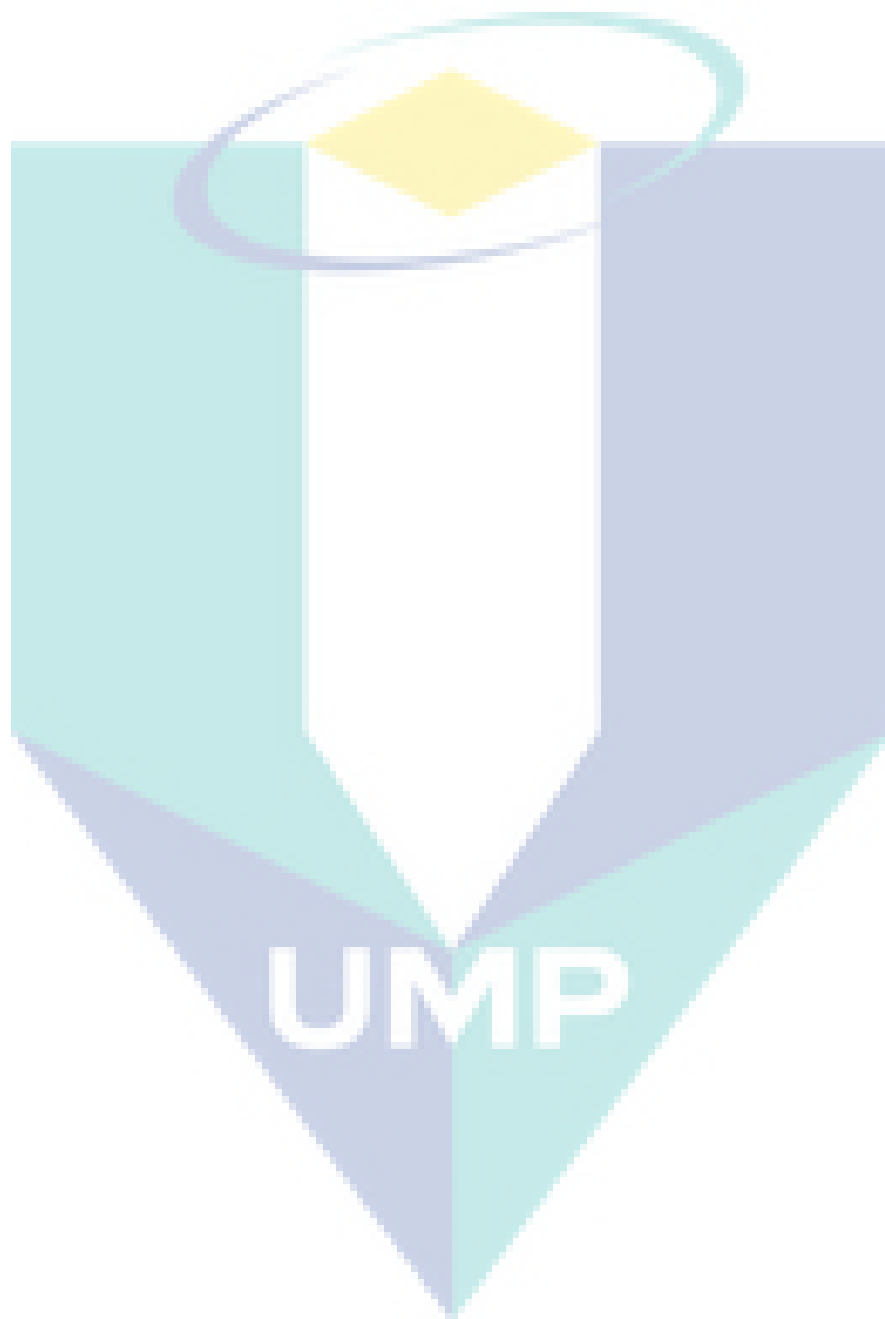
$$\tau_{ca} = 0.9398$$

By substituting these values in equation 3.20 and 3.21, N_{ps} and N_{pc} were calculated.









For the flow chamber used in the experiments, the V_{pixel} was calculated as follow:

From the (IPP), it was found the height of the flow chamber is equal to 1660 pixels where the length is equal 1098 pixels.

By dividing the dimensions in cm by the dimensions in pixels, to get the V_{pixel}

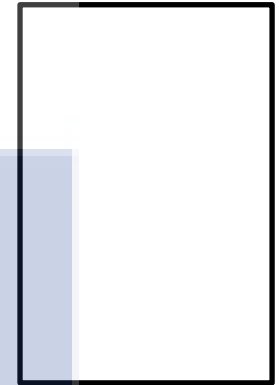
$$45/1600 = 0.027.$$

$$30/1098 = 0.027$$

Then, the $V_{\text{pixel}} = 0.027 \times 0.027 \times 1.$

30 cm, 1098 pixels

45 cm, 1660 pixels



APPENDIX O

EXAMPLE OF THE DETAILED CALCULATION OF PCE VOLUMES IN DOUBLE-POROSITY SAMPLES

Since the actual calculation sheets were very huge (i.e. every image contains approximately 10,000 cell), these calculation sheets are just example to show how the calculations have been carried out which are present part from the actual sheets.

Table O.1 The values of light intensity of the dry image (I_d) extracted from Image Pro. Primere

X/Y	1	2	3	4	5	6	7	8	9	10	11	12	13	14
1	640.576	672.146	562.159	458.282	492.907	493.926	395.141	365.607	400.233	350.331	381.901	482.723	565.214	338.110
2	628.355	448.097	402.269	362.552	354.404	361.533	286.171	281.079	296.355	267.840	235.251	279.043	252.564	253.582
3	592.711	426.711	367.644	329.963	297.374	263.766	237.288	268.858	232.196	181.276	236.27	203.681	219.975	219.975
4	591.692	426.711	328.944	248.490	252.564	198.589	231.178	202.662	214.883	202.662	213.865	164.981	198.589	166.000
5	510.220	396.159	350.331	268.858	235.251	202.662	218.957	214.883	185.349	216.92	206.736	170.073	202.662	186.368
6	583.545	431.803	296.355	267.84	236.270	235.251	202.662	140.540	152.761	163.963	131.374	120.172	121.19	137.484
7	655.852	382.920	288.208	214.883	235.251	183.313	236.270	136.466	152.761	163.963	147.668	120.172	153.779	135.448
8	478.650	427.729	334.036	269.877	215.902	263.766	218.957	200.625	169.055	169.055	180.257	180.257	121.190	168.037
9	591.692	349.312	351.349	252.564	204.699	188.405	170.073	180.257	180.257	213.865	168.037	120.172	152.761	170.073
10	510.220	382.92	285.153	255.619	249.509	213.865	183.313	196.552	131.374	168.037	118.135	139.521	155.816	82.491
11	564.195	550.956	351.349	267.840	230.159	235.251	230.159	202.662	184.331	131.374	184.331	131.374	118.135	117.116
12	524.478	542.809	297.374	296.355	236.270	172.101	202.662	163.963	200.625	184.331	135.448	118.135	155.816	123.227
13	550.956	469.484	285.153	280.061	196.552	188.405	170.073	152.761	120.172	168.037	147.668	190.441	125.264	106.932
14	542.809	410.417	314.687	214.883	188.405	169.055	169.055	152.761	163.963	139.521	102.859	168.037	151.742	123.227
15	512.257	394.122	346.257	285.153	251.546	202.662	136.466	169.055	122.208	134.429	134.429	140.54	135.448	151.742
16	612.060	415.509	313.668	282.098	231.178	218.957	188.405	134.429	134.429	163.963	118.135	138.503	118.135	122.208
17	540.772	501.054	327.926	251.546	251.546	186.368	205.717	152.761	131.374	147.668	168.037	122.208	133.411	150.724

Table O.2 The values of light intensity of the fully saturated image with water (I_s) extracted from Image Pro. Primere

X/Y	1	2	3	4	5	6	7	8	9	10	11	12	13	14
1	3312.152	3081.783	2936.019	2834.085	2736.229	2686.282	2656.721	2593.523	2539.498	2410.043	2438.584	2471.203	2742.345	2723.997
2	3062.416	2954.366	2676.089	2607.793	2590.465	2399.849	2328.496	2330.535	2265.297	2162.345	2232.679	2234.717	2197.002	2148.074
3	2982.908	2801.467	2652.644	2456.932	2263.259	2307.09	2233.698	2132.784	2131.765	2111.378	2085.895	2064.489	1954.401	1914.647
4	3043.048	2781.080	2660.799	2476.299	2267.336	2197.002	2128.707	2020.658	1980.904	2028.812	1938.092	1899.357	1780.095	1886.106
5	3079.744	2793.312	2592.503	2447.758	2297.916	2164.384	2078.760	1981.923	1918.724	1902.415	1733.206	1769.902	1819.849	1751.554
6	3096.054	2883.013	2719.920	2447.758	2277.529	2167.442	2116.475	2097.108	1951.343	1803.540	1852.468	1733.206	1721.993	1607.828
7	3178.620	3037.952	2586.387	2356.018	2167.442	2101.185	2162.345	2017.600	1952.362	1716.896	1799.462	1765.824	1718.935	1734.225
8	3098.092	2748.461	2621.045	2324.419	2193.944	2068.566	2066.528	2014.542	2016.58	1983.962	1831.062	1721.993	1738.302	1639.427
9	3087.899	2786.177	2539.498	2356.018	2210.253	2035.948	1944.208	1866.738	1850.429	1751.554	1782.134	1685.297	1592.538	1606.808
10	3103.189	2802.486	2523.189	2326.457	2215.350	2066.528	1886.106	1753.592	1738.302	1686.316	1690.394	1603.75	1488.566	1619.04
11	3147.020	2856.511	2881.994	2443.681	2280.587	2114.436	2032.890	1903.434	1783.153	1690.394	1706.703	1602.731	1552.784	1503.856
12	3263.224	2815.737	2823.892	2473.241	2380.482	2081.818	1890.183	1865.719	1674.084	1739.322	1684.278	1552.784	1526.281	1508.952
13	3132.750	2836.124	2675.069	2376.405	2200.060	2000.271	1802.520	1869.796	1832.081	1716.896	1651.659	1575.209	1476.334	1393.768
14	3068.532	2783.119	2650.605	2408.004	2212.292	2027.793	1919.744	1883.048	1787.230	1721.993	1592.538	1569.093	1459.005	1411.096
15	3191.871	2867.723	2619.006	2379.463	2264.278	2048.180	1955.420	1866.738	1820.868	1750.534	1684.278	1524.242	1554.822	1414.154
16	3211.238	2915.632	2625.122	2395.772	2362.134	2050.218	1890.183	2001.29	1705.684	1602.731	1586.422	1536.474	1443.715	1446.773
17	3021.642	2858.549	2691.379	2421.255	2295.877	2046.141	1947.266	2001.29	1766.844	1659.814	1770.921	1657.775	1552.784	1507.933

Table O.3 The values of light intensity of the image after the first PCE increment (*I*) extracted from Image Pro. Primere.

X/Y	1	2	3	4	5	6	7	8	9	10	11	12	13	14
1	3216.630	3033.074	2951.148	2864.037	2933.519	2896.185	2880.630	2902.407	2914.852	2900.333	2914.852	2881.667	3061.074	2963.593
2	3131.593	2969.815	2810.111	2897.222	2844.333	2802.852	2833.963	2819.444	2860.926	2832.926	2815.296	2818.407	2799.741	2793.519
3	3077.667	2914.852	2786.259	2833.963	2833.963	2828.778	2828.778	2817.370	2815.296	2762.407	2759.296	2746.852	2644.185	2613.074
4	3134.704	2930.407	2866.111	2912.778	2860.926	2777.963	2729.222	2749.963	2799.741	2761.370	2644.185	2601.667	2535.296	2565.370
5	3109.815	2929.370	2833.963	2902.407	2704.333	2669.074	2740.630	2826.704	2734.407	2729.222	2594.407	2643.148	2618.259	2597.519
6	3168.926	3052.778	2929.307	2781.074	2782.111	2794.556	2893.074	2879.593	2782.111	2785.222	2735.444	2765.519	2837.074	2803.889
7	3296.481	3266.407	2817.370	2744.778	2733.370	2865.074	2945.963	2957.370	2920.037	2864.037	2782.111	2734.407	2733.370	2746.852
8	3228.037	2933.519	2893.074	2893.074	2863.000	2793.519	2828.778	2876.481	2830.852	2930.407	2845.370	2712.630	2729.222	2613.074
9	3147.148	2960.481	2786.259	2831.889	2815.296	2744.778	2734.407	2619.296	2664.926	2686.704	2793.519	2663.889	2576.778	2494.852
10	3196.926	2969.815	2813.222	2817.370	2817.370	2682.556	2579.889	2532.185	2449.222	2503.148	2628.630	2579.889	2513.519	2548.778
11	3200.037	3028.926	3165.815	2885.815	2836.037	2727.148	2710.556	2668.037	2680.481	2600.630	2644.185	2644.185	2548.778	2581.963
12	3330.704	3017.519	3176.185	2916.926	2942.852	2680.481	2633.815	2676.333	2684.630	2748.926	2709.519	2698.111	2626.556	2610.000
13	3252.926	3080.778	2999.889	2829.815	2731.296	2647.296	2584.037	2717.815	2785.222	2734.407	2675.296	2732.333	2658.704	2644.185
14	3210.407	2998.852	2871.296	2794.556	2680.481	2613.074	2617.222	2664.926	2814.259	2633.815	2609.963	2647.296	2531.148	2627.593
15	3336.926	3096.333	2937.667	2798.704	2865.074	2665.963	2660.778	2650.407	2749.963	2697.074	2682.556	2644.185	2682.556	2808.037
16	3316.185	3147.148	2912.778	2777.963	2851.593	2751.000	2695.000	2977.074	2693.963	2625.519	2577.815	2528.037	2583.000	2682.556
17	3136.778	3046.556	2883.741	2802.852	2763.444	2698.111	2732.333	2843.296	2668.037	2627.593	2801.815	2726.111	2579.889	2565.370

Table O.4 The values of light intensity of the first correction zone at the reference image (The saturated image with water) [A1]

2847.337	2637.354	2373.347	2292.819	2263.259	2149.094	2050.218	1887.125	1897.318	1851.448	1885.086
2702.591	2594.542	2379.463	2217.389	2149.094	2062.45	1984.981	1912.608	1947.266	1865.719	1802.520
2866.704	2626.141	2525.227	2245.930	2143.997	2027.793	1930.956	1864.700	1754.612	1737.283	1749.515
2840.201	2751.519	2424.313	2257.143	2077.740	2017.600	1869.796	1847.371	1835.139	1704.664	1765.824
2815.737	2721.959	2444.700	2262.239	2145.016	2094.050	1963.575	1819.849	1737.283	1688.355	1606.808
2920.729	2723.997	2428.391	2324.419	2131.765	2065.508	1952.362	1947.266	1997.213	1882.028	1733.206
2904.419	2733.171	2525.227	2241.853	2176.615	2044.102	1951.343	1849.410	1939.111	1951.343	1814.752
2965.579	2741.326	2474.261	2392.714	2160.306	2093.030	2000.271	1897.318	1851.448	1769.902	1716.896
2964.560	2659.779	2506.879	2376.405	2190.886	2050.218	1984.981	1881.009	1901.396	1789.269	1672.046
2998.198	2757.635	2505.860	2276.510	2190.886	2065.508	1967.652	1865.719	1871.835	1773.979	1692.432
2953.347	2798.409	2522.169	2340.728	2226.563	2147.055	1930.956	1935.034	1716.896	1751.554	1651.659
2937.038	2786.177	2537.459	2340.728	2180.693	2103.224	2069.586	1983.962	1914.647	1753.592	1716.896
2948.250	2703.611	2455.913	2296.897	2192.925	2098.127	2013.522	1864.700	1815.772	1897.318	1765.824
2929.903	2704.630	2488.531	2276.510	2094.005	2016.580	1936.053	1864.700	1831.062	1783.153	1750.534
2879.955	2738.268	2474.261	2308.109	2109.340	2028.812	1962.556	1831.062	1788.25	1705.684	1673.065
2884.033	2659.779	2506.879	2330.535	2164.384	1952.362	1929.937	1852.468	1749.515	1700.587	1690.394
2867.723	2707.688	2361.115	2259.181	2093.030	2109.340	1978.865	1814.752	1769.902	1700.587	1674.084
2807.583	2621.045	2488.531	2246.949	2181.712	2015.561	1918.724	1847.371	1818.83	1782.134	1684.278
2791.273	2619.006	2394.753	2232.679	2093.030	1978.865	1804.559	1738.302	1770.921	1684.278	1623.118

Table O.5 The light intensity of the second correction zone for at the reference image [B1]

2799.428	2624.103	2408.004	2213.311	2114.436	1984.981	1887.125	1852.468	1782.134	1667.968	1802.520
2807.583	2626.141	2413.101	2259.181	2093.03	2045.122	1930.956	1704.664	1765.824	1684.278	1700.587
2854.472	2684.243	2462.029	2248.988	2098.127	2020.658	1865.719	1788.25	1704.664	1769.902	1667.968
2855.491	2643.47	2448.777	2216.369	2111.378	2012.503	1832.081	1766.844	1690.394	1676.123	1586.422
2904.419	2643.47	2480.377	2279.568	2148.074	2065.508	1912.608	1765.824	1720.974	1651.659	1606.808
2988.004	2658.76	2455.913	2346.844	2078.760	2050.218	1879.99	1782.134	1716.896	1684.278	1569.093
3180.658	2771.906	2852.433	2525.227	2246.949	1951.343	1966.633	1788.250	1685.297	1619.040	1673.065
2852.433	2694.437	2562.943	2464.067	2378.443	2131.765	2000.271	1733.206	1657.775	1651.659	1590.499
2907.477	2654.683	2458.971	2258.162	2127.688	2011.484	2017.600	2039.006	1954.401	1721.993	1655.736
2735.210	2675.069	2465.087	2281.607	2213.311	2001.290	1983.962	1734.225	1819.849	1857.564	1982.942
2886.071	2701.572	2528.285	2359.076	2153.171	2032.890	1898.338	1832.081	1706.703	1634.303	1573.170
2946.212	2640.412	2487.512	2408.004	2193.944	2016.580	1886.106	1788.250	1734.225	1673.065	1651.659
2919.709	2689.340	2426.352	2311.167	2151.132	1978.865	1831.062	1847.371	1701.606	1689.374	1552.784
3162.310	2922.767	2706.669	2588.426	2425.333	2163.364	2111.378	1739.322	1765.824	1625.156	1619.040
3168.426	2938.057	2756.616	2580.271	2442.661	2346.844	2136.862	1820.868	1951.343	1619.040	1590.499
2936.019	2446.739	2653.663	2606.774	2490.570	2346.844	2181.712	2110.359	2039.006	1832.081	1542.590
2797.389	2561.923	2415.139	2297.916	2183.751	2179.673	2194.963	2083.856	2010.464	1957.459	1770.921
2802.486	2578.233	2343.786	2193.944	2177.635	2052.257	1820.868	1790.288	1788.250	1912.608	1772.960
2736.229	2559.885	2324.419	2177.635	2032.890	1930.956	1852.468	1720.974	1684.278	1652.678	1537.494
2771.906	2561.923	2357.037	2180.693	2080.798	1903.434	1857.564	1673.065	1586.422	1641.466	1540.552
2766.809	2510.957	2445.719	2177.635	2020.658	1952.362	1734.225	1690.394	1641.466	1602.731	1586.422
2741.326	2619.006	2342.767	2183.751	2045.122	1915.666	1865.719	1607.828	1574.190	1556.861	1471.237
2805.544	2605.755	2365.192	2267.336	1999.252	1922.802	1788.250	1733.206	1641.466	1552.784	1472.256
3029.797	2825.931	2426.352	2193.944	2031.870	1901.396	1771.94	1652.678	1690.394	1508.952	1324.453

Table O.6 The light intensity for the first correction zone at the image after the first PCE increment (The image to be corrected) [A2]

3104.630	2931.444	2781.074	2729.222	2733.370	2846.407	2794.556	2696.037	2696.037	2825.667	2746.852
3080.778	2899.296	2797.667	2672.185	2702.259	2635.889	2697.074	2672.185	2752.037	2826.704	2718.852
3048.630	2968.778	3025.815	2766.556	2763.444	2664.926	2702.259	2704.333	2712.630	2744.778	2826.704
3083.889	2996.778	2817.370	2795.593	2717.815	2713.667	2601.667	2662.852	2708.481	2697.074	2712.630
3102.556	2983.296	2866.111	2732.333	2736.481	2676.333	2718.852	2659.741	2633.815	2614.111	2632.778
3166.852	2999.889	2837.074	2817.370	2650.407	2703.296	2685.667	2783.148	2896.185	2867.148	2685.667
3166.852	3034.111	2943.889	2761.370	2713.667	2619.296	2663.889	2652.481	2679.444	2892.037	2879.593
3131.593	3029.963	2895.148	2867.148	2743.741	2734.407	2744.778	2748.926	2611.000	2648.333	2668.037
3220.778	3028.926	2955.296	2898.259	2764.481	2693.963	2699.148	2650.407	2621.370	2629.667	2696.037
3230.111	3036.185	2835.000	2826.704	2763.444	2635.889	2580.926	2614.111	2551.889	2534.259	2576.778
3182.407	3031.000	2900.333	2769.667	2744.778	2697.074	2629.667	2693.963	2530.111	2511.444	2563.296
3196.926	3049.667	2915.889	2832.926	2728.185	2714.704	2730.259	2664.926	2670.111	2586.111	2613.074
3183.444	2968.778	2801.815	2766.556	2728.185	2702.259	2602.704	2569.519	2601.667	2677.370	2631.741
3162.704	3003.000	2851.593	2712.630	2697.074	2551.889	2615.148	2676.333	2601.667	2602.704	2684.630
3127.444	3013.370	2858.852	2798.704	2648.333	2580.926	2614.111	2613.074	2600.630	2602.704	2531.148
3146.111	2994.704	2863.000	2784.185	2668.037	2614.111	2567.444	2646.259	2517.667	2596.481	2517.667
3130.556	3017.519	2819.444	2733.370	2652.481	2702.259	2663.889	2601.667	2613.074	2579.889	2546.704
3077.667	2947.000	2836.037	2732.333	2730.259	2619.296	2629.667	2660.778	2619.296	2579.889	2562.259
3085.963	2962.556	2846.407	2719.889	2681.519	2568.481	2569.519	2561.222	2615.148	2534.259	2617.222

Table O.7 The values of light intensity of the second correction zone at the image after the first PCE increment (The image to be corrected) [B2]

3112.926	2902.407	2847.444	2782.111	2659.741	2643.148	2552.926	2553.963	2597.519	2583.000	2910.704
3118.111	2965.667	2896.185	2743.741	2681.519	2684.63	2614.111	2519.741	2532.185	2581.963	2581.963
3195.889	3025.815	2897.222	2780.037	2768.63	2626.556	2576.778	2601.667	2515.593	2581.963	2564.333
3097.370	2980.185	2811.148	2760.333	2745.815	2679.444	2627.593	2561.222	2519.741	2518.704	2499.000
3134.704	3011.296	2866.111	2781.074	2715.741	2763.444	2596.481	2597.519	2512.481	2499.000	2563.296
3358.704	3013.370	2901.370	2835.000	2719.889	2697.074	2662.852	2596.481	2531.148	2537.37	2534.259
3499.741	3201.074	3353.519	3028.926	2894.111	2634.852	2732.333	2568.481	2501.074	2480.333	2532.185
3096.333	3065.222	2999.889	2978.111	3001.963	2829.815	2743.741	2515.593	2518.704	2519.741	2580.926
3191.741	2937.667	2846.407	2753.074	2715.741	2714.704	2933.519	2930.407	2881.667	2586.111	2515.593
3227.000	3066.259	2963.593	2851.593	2828.778	2741.667	2574.704	2565.370	2634.852	2662.852	2909.667
3212.481	3096.333	2934.556	2865.074	2831.889	2795.593	2630.704	2635.889	2615.148	2651.444	2550.852
3224.926	3068.333	2930.407	2929.370	2852.63	2650.407	2626.556	2702.259	2745.815	2704.333	2647.296
3265.370	3049.667	2913.815	2901.370	2874.407	2730.259	2812.185	2667.000	2662.852	2618.259	2614.111
3546.407	3398.111	3267.444	3183.444	3182.407	2997.815	2979.148	2669.074	2631.741	2596.481	2613.074
3517.370	3395.000	3335.889	3280.926	3191.741	3118.111	2982.259	2846.407	2980.185	2616.185	2678.407
3320.333	3315.148	3196.926	3261.222	3235.296	3119.148	3100.481	3052.778	3101.519	2910.704	2613.074
3197.963	3080.778	3017.519	2867.148	2903.444	3017.519	3062.111	3050.704	3083.889	3064.185	2963.593
3213.519	3131.593	2935.593	2848.481	2800.778	2812.185	2714.704	2714.704	2749.963	2980.185	2879.593
3202.111	3063.148	2942.852	2833.963	2761.37	2820.481	2758.259	2764.481	2679.444	2679.444	2652.481
3245.667	3115.000	3095.296	2943.889	2817.37	2762.407	2799.741	2729.222	2648.333	2629.667	2696.037
3269.519	3181.37	3160.630	3011.296	2933.519	2900.333	2800.778	2744.778	2728.185	2682.556	2696.037
3146.111	3064.185	3046.556	3017.519	2878.556	2794.556	2827.741	2711.593	2764.481	2752.037	2632.778
3118.111	3027.889	2978.111	2952.185	2877.519	2848.481	2826.704	2732.333	2744.778	2678.407	2684.63
3474.852	3401.222	3177.222	2935.593	2949.074	2881.667	2767.593	2741.667	2747.889	2744.778	2662.852

The correction coefficient can be calculated as follow:

$$\frac{\left(\text{Average} \frac{A1}{B1}\right)}{\left(\text{Average} \frac{A2}{B2}\right)} = \frac{\left(\frac{2155.92}{2111.40}\right)}{\left(\frac{2766.37}{2857.63}\right)} = 1.05$$

After that, for the light intensity of the image after injecting the first PCE increment, all pixels have to be multiplied by 1.05 to be corrected. This procedure has to be repeated for all images for correction of the investable errors as discussed in Chapter 3.

The logo for UMP (Universitas Muhammadiyah Palembang) is a shield-shaped emblem. It features a central white shield with a yellow sunburst at the top. The shield is flanked by two vertical bars, one light blue on the left and one light purple on the right. The bottom of the shield is a downward-pointing triangle, also divided into light blue and light purple sections. The letters 'UMP' are written in white, bold, sans-serif font across the bottom of the shield.

UMP

Table O.8 The values of K_s pixel by pixel which was calculated in Excel using the following formula:

$((LN(I_s/I_d)/(2*LN(1.05))),$ where 1.05 is the value of (τ_{sw} / τ_{sa}) as calculated in Appendix M.

X/Y	1	2	3	4	5	6	7	8	9	10	11	12	13	14
1	14.44998	16.09849	15.10893	16.57803	18.31159	17.37638	17.24182	19.28186	19.86223	18.39872	19.88407	19.13602	17.80201	16.11648
2	14.72060	15.86318	18.31416	19.15487	20.15186	19.60153	19.08811	21.49269	21.38572	20.36671	21.73151	23.0704	21.14651	21.93744
3	15.41200	15.91706	18.72514	19.46656	19.73329	20.99554	21.89326	22.50360	21.21864	22.62253	25.03509	22.21414	23.17356	22.17429
4	14.52739	15.85984	18.75660	20.68688	22.65783	22.16824	24.30851	22.21750	23.36300	23.00783	23.13909	22.3808	24.37573	23.06851
5	15.08392	17.42299	19.25146	19.92255	21.98778	22.74268	23.85714	22.57573	22.43610	23.86381	21.29732	22.00481	24.29056	22.10199
6	15.12330	16.37082	18.86024	21.63725	21.93533	22.71285	22.51329	23.94719	26.96016	25.29846	24.84756	26.43648	27.2833	26.49386
7	14.04118	15.71017	19.57558	21.53145	23.68520	22.43899	25.28946	21.97870	27.26697	24.79392	24.55005	25.42937	27.26509	24.82877
8	15.05658	17.91167	18.57791	19.88082	21.47451	23.15822	21.09608	22.74302	23.64945	25.23692	24.41504	23.12817	23.22477	26.69332
9	15.86139	15.87860	20.32947	19.50135	22.22987	23.54139	23.91892	24.55126	23.86535	23.30260	21.72796	23.62682	26.48239	24.11480
10	14.89923	17.45659	19.32206	21.51126	22.13026	21.66554	22.30905	23.14223	22.33787	26.15541	23.65777	26.72948	24.26056	23.98960
11	14.36090	16.62175	16.95611	19.87574	21.94908	22.72767	22.10036	21.65031	22.28522	22.70933	26.27856	22.16360	25.30998	26.07042
12	13.52696	17.22249	16.90006	21.70821	21.35164	22.29980	24.55715	22.74908	23.80993	22.13369	22.67218	24.99701	26.22210	23.26796
13	15.18523	16.79169	17.83245	21.72895	21.12344	23.77642	23.14347	24.56803	25.45936	27.25292	23.42021	24.25875	20.98758	24.69086
14	14.47228	16.75102	19.11625	20.85436	23.89509	24.35029	24.89972	24.70193	25.20536	24.09909	24.95246	27.92462	22.14920	22.85235
15	14.09675	17.65158	19.40852	19.75243	21.23364	21.49082	23.23030	26.80737	24.35782	27.27959	25.90744	24.88428	24.63226	24.03865
16	14.73081	15.99702	18.89088	20.83541	21.77761	22.36633	22.09004	24.21547	26.03686	25.39885	23.25874	26.29031	24.02209	25.67385
17	14.88873	17.06360	17.22781	20.48828	22.66076	21.48061	24.04643	23.31459	25.08780	25.99307	25.45891	23.45808	26.05115	24.85194

Table O.9 The values of K_c pixel by pixel which was calculated in Excel using the following formula:

$((LN(I_s/I_d)/(2*LN(1.04))),$ where 1.04 is the value of (τ_{cw} / τ_{ca}) as calculated in Appendix M.

X/Y	1	2	3	4	5	6	7	8	9	10	11	12	13	14
1	17.97563	20.02635	18.79535	20.62290	22.77943	21.61604	21.44864	23.98643	24.70841	22.88782	24.73558	23.80501	22.14551	20.04873
2	18.31228	19.73363	22.78263	23.82846	25.06870	24.38410	23.74542	26.73668	26.60361	25.33598	27.03377	28.69934	26.30604	27.28995
3	19.17236	19.80065	23.29388	24.21620	24.54801	26.11824	27.23499	27.99425	26.39577	28.14220	31.14340	27.63416	28.82768	27.58459
4	18.07192	19.72948	23.33301	25.73427	28.18610	27.57706	30.23954	27.63834	29.06333	28.62151	28.78479	27.84148	30.32316	28.69698
5	18.76424	21.67402	23.94861	24.78345	27.35257	28.29166	29.67803	28.08398	27.91028	29.68634	26.49365	27.37376	30.21721	27.49464
6	18.81323	20.36513	23.46194	26.91651	27.28732	28.25456	28.00630	29.79006	33.53816	31.47102	30.91011	32.88607	33.94015	32.95809
7	17.46708	19.54329	24.35182	26.78490	29.46414	27.91387	31.45982	27.34128	33.91983	30.84338	30.54001	31.63387	33.91749	30.88673
8	18.73023	22.28193	23.11073	24.73153	26.71407	28.80858	26.24331	28.29209	29.41967	31.39447	30.37205	28.77120	28.89137	33.20621
9	19.73141	19.75282	25.28965	24.25948	27.65372	29.28524	29.75489	30.54152	29.68826	28.98819	27.02936	29.39152	32.94382	29.99857
10	18.53449	21.71582	24.03644	26.75979	27.52981	26.95171	27.75223	28.78870	27.78809	32.53706	29.43002	33.25102	30.17989	29.84281
11	17.86482	20.67729	21.09323	24.72521	27.30443	28.27298	27.49262	26.93277	27.72258	28.25017	32.69026	27.57129	31.48536	32.43133
12	16.82739	21.42460	21.02351	27.00479	26.56122	27.74072	30.54885	28.29962	29.61931	27.53409	28.20396	31.09603	32.62003	28.94510
13	18.89027	20.88869	22.18338	27.03059	26.27735	29.57762	28.79023	30.56238	31.67119	33.90236	29.13449	30.17763	26.10833	30.71518
14	18.00336	20.83810	23.78041	25.94261	29.72525	30.29151	30.97500	30.72895	31.35521	29.97902	31.0406	34.73794	27.55337	28.42809
15	17.53621	21.95839	24.1440	24.57182	26.41443	26.73436	28.89826	33.34810	30.30088	33.93553	32.22858	30.95579	30.64228	29.90383
16	18.32497	19.90035	23.50006	25.91903	27.09112	27.82348	27.47979	30.12379	32.38959	31.59591	28.93364	32.70488	29.88323	31.93801
17	18.52143	21.22694	21.43122	25.48721	28.18975	26.72166	29.91351	29.00312	31.20896	32.33512	31.67062	29.18161	32.40737	30.91556

Table O.10 The values of total K pixel by pixel which was calculated in Excel. From this sheet, the average K can be measured

X/Y	1	2	3	4	5	6	7	8	9	10	11	12	13	14
1	32.42562	36.12484	33.90428	37.20093	41.09103	38.99242	38.69046	43.26829	44.57064	41.28654	44.61966	42.94103	39.94752	36.16521
2	33.03288	35.59681	41.09679	42.98333	45.22056	43.98563	42.83353	48.22937	47.98933	45.70269	48.76528	51.76973	47.45254	49.22738
3	34.58436	35.71771	42.01902	43.68277	44.28129	47.11378	49.12825	50.49785	47.61442	50.76473	56.17849	49.84830	52.00124	49.75888
4	32.59931	35.58932	42.08961	46.42115	50.84393	49.74531	54.54805	49.85583	52.42633	51.62934	51.92387	50.22228	54.69889	51.76549
5	33.84816	39.09701	43.20007	44.70601	49.34035	51.03434	53.53517	50.65971	50.34638	53.55016	47.79097	49.37857	54.50777	49.59663
6	33.93652	36.73594	42.32218	48.55376	49.22265	50.96741	50.51959	53.73726	60.49832	56.76949	55.75767	59.32318	61.22345	59.45196
7	31.50826	35.25346	43.92739	48.31635	53.14934	50.35286	56.74928	49.31998	61.18680	55.63730	55.09007	57.06324	61.18258	55.71550
8	33.78681	40.19361	41.68864	44.61235	48.18858	51.96680	47.33940	51.03511	53.06912	56.63139	54.78709	51.89937	52.11614	59.89953
9	35.59281	35.63143	45.61912	43.76083	49.88359	52.82663	53.67381	55.09278	53.55361	52.29079	48.75733	53.01834	59.42621	54.11337
10	33.43372	39.17242	43.35850	48.27105	49.66007	48.61724	50.06129	51.93093	50.12596	58.69247	53.08779	59.98069	54.44045	53.83241
11	32.22572	37.29905	38.04934	44.60095	49.25351	51.00065	49.59299	48.58308	50.00780	50.95950	58.96882	49.73489	56.79534	58.50174
12	30.35435	38.64708	37.92357	48.71300	47.91286	50.04052	55.10600	51.04869	53.42923	49.66778	50.87615	56.09304	58.84213	52.21306
13	34.07550	37.68038	40.01583	48.75954	47.40079	53.35404	51.9337	55.13042	57.13055	61.15528	52.55470	54.43638	47.09591	55.40605
14	32.47564	37.58912	42.89666	46.79696	53.62034	54.64180	55.87472	55.43089	56.56058	54.07810	55.99306	62.66257	49.70257	51.28045
15	31.63297	39.60997	43.55252	44.32426	47.64806	48.22517	52.12856	60.15547	54.65871	61.21513	58.13602	55.84007	55.27454	53.94247
16	33.05578	35.89754	42.39094	46.75444	48.86873	50.18981	49.56983	54.33926	58.42645	56.99476	52.19238	58.99519	53.90531	57.61186
17	33.41017	38.29054	38.65902	45.97549	50.85051	48.20227	53.95994	52.31771	56.29676	58.32819	57.12953	52.63970	58.45852	55.76750

Table O.11 The values of average pore diameter (d_o) calculated pixel by pixel calculated as follow

$$d_o = \frac{1 \times 0.395}{K(\text{total})}$$

X/Y	1	2	3	4	5	6	7	8	9	10	11	12	13	14
1	0.012182	0.010934	0.011650	0.010618	0.009613	0.010130	0.010209	0.009129	0.008862	0.009567	0.008853	0.009199	0.009888	0.010922
2	0.011958	0.011097	0.009611	0.009190	0.008735	0.008980	0.009222	0.008190	0.008231	0.008643	0.008100	0.007630	0.008324	0.008024
3	0.011421	0.011059	0.009401	0.009042	0.008920	0.008384	0.008040	0.007822	0.008296	0.007781	0.007031	0.007924	0.007596	0.007938
4	0.012117	0.011099	0.009385	0.008509	0.007769	0.007940	0.007241	0.007923	0.007534	0.007651	0.007607	0.007865	0.007221	0.007631
5	0.01167	0.010103	0.009144	0.008836	0.008006	0.007740	0.007378	0.007797	0.007846	0.007376	0.008265	0.007999	0.007247	0.007964
6	0.011639	0.010752	0.009333	0.008135	0.008025	0.007750	0.007819	0.007351	0.006529	0.006958	0.007084	0.006658	0.006452	0.006644
7	0.012536	0.011205	0.008992	0.008175	0.007432	0.007845	0.006960	0.008009	0.006456	0.007100	0.007170	0.006922	0.006456	0.007090
8	0.011691	0.009827	0.009475	0.008854	0.008197	0.007601	0.008344	0.007740	0.007443	0.006975	0.007210	0.007611	0.007579	0.006594
9	0.011098	0.011086	0.008659	0.009026	0.007918	0.007477	0.007359	0.007170	0.007376	0.007554	0.008101	0.007450	0.006647	0.007299
10	0.011814	0.010084	0.009110	0.008183	0.007954	0.008125	0.007890	0.007606	0.00788	0.00673	0.007441	0.006585	0.007256	0.007338
11	0.012257	0.01059	0.010381	0.008856	0.008020	0.007745	0.007965	0.008130	0.007899	0.007751	0.006698	0.007942	0.006955	0.006752
12	0.013013	0.010221	0.010416	0.008109	0.008244	0.007894	0.007168	0.007738	0.007393	0.007953	0.007764	0.007042	0.006713	0.007565
13	0.011592	0.010483	0.009871	0.008101	0.008333	0.007403	0.007606	0.007165	0.006914	0.006459	0.007516	0.007256	0.008387	0.007129
14	0.012163	0.010508	0.009208	0.008441	0.007367	0.007229	0.007069	0.007126	0.006984	0.007304	0.007054	0.006304	0.007947	0.007703
15	0.012487	0.009972	0.009070	0.008912	0.008290	0.008191	0.007577	0.006566	0.007227	0.006453	0.006794	0.007074	0.007146	0.007323
16	0.011949	0.011004	0.009318	0.008448	0.008083	0.00787	0.007969	0.007269	0.006761	0.00693	0.007568	0.006695	0.007328	0.006856
17	0.011823	0.010316	0.010218	0.008592	0.007768	0.008195	0.007320	0.007550	0.007016	0.006772	0.006914	0.007504	0.006757	0.007083

Table O.12 The values of transmission factor of NAPL-water interface τ_{Nw} , which was calculated pixel by pixel in Excel using the following formula

POWER(0.993,2*K total). The calibration step was done in this stage where the 0.993 is the value of τ_{Nw} which resulted in the exact PCE volume for the first increment (i.e 1 ml).

X/Y	1	2	3	4	5	6	7	8	9	10	11	12	13	14
1	0.634096	0.601983	0.621059	0.592950	0.561414	0.578213	0.580671	0.544501	0.534629	0.559874	0.53426	0.547010	0.570506	0.601642
2	0.628709	0.606465	0.561368	0.546685	0.529769	0.539041	0.547837	0.507842	0.509557	0.526193	0.504032	0.483200	0.513415	0.500771
3	0.615153	0.605436	0.554142	0.541339	0.536806	0.515864	0.501469	0.491912	0.512248	0.490071	0.454179	0.496421	0.481631	0.497045
4	0.632550	0.606529	0.553592	0.520908	0.489526	0.497140	0.464702	0.496369	0.478763	0.484154	0.482155	0.493820	0.463719	0.483229
5	0.621549	0.577364	0.545023	0.533613	0.499977	0.488218	0.471362	0.490794	0.492960	0.471263	0.510979	0.499708	0.464965	0.498180
6	0.620778	0.596837	0.551787	0.505532	0.500804	0.488677	0.491762	0.470026	0.427434	0.450423	0.456872	0.434550	0.423102	0.433764
7	0.642321	0.609398	0.539482	0.507222	0.473924	0.492915	0.450551	0.500120	0.423320	0.457645	0.461177	0.448568	0.423345	0.457143
8	0.622085	0.568537	0.556702	0.534315	0.508133	0.481864	0.514231	0.488213	0.474459	0.451298	0.463144	0.482321	0.480854	0.431045
9	0.606499	0.60617	0.526811	0.540746	0.496175	0.476078	0.470445	0.461160	0.471240	0.479676	0.504089	0.474798	0.433921	0.467549
10	0.625179	0.576752	0.543811	0.507544	0.497736	0.505082	0.494938	0.482107	0.494489	0.438417	0.474334	0.430554	0.465405	0.469398
11	0.635879	0.592134	0.585925	0.534401	0.500587	0.488449	0.498205	0.505324	0.495310	0.488732	0.436718	0.497213	0.450260	0.439594
12	0.652819	0.581025	0.586961	0.504403	0.510105	0.495083	0.461074	0.488120	0.472065	0.497682	0.489304	0.454724	0.437497	0.480200
13	0.619567	0.588970	0.569959	0.504073	0.513788	0.472563	0.482088	0.460916	0.448144	0.423507	0.477900	0.465432	0.515993	0.459134
14	0.633650	0.589725	0.547351	0.518165	0.470799	0.464091	0.456121	0.458974	0.451747	0.467781	0.455363	0.414633	0.497439	0.486533
15	0.641197	0.573218	0.542331	0.536482	0.512006	0.507872	0.480770	0.429498	0.463981	0.423151	0.441858	0.456343	0.459983	0.468673
16	0.628507	0.603908	0.551254	0.518475	0.503300	0.494045	0.498367	0.466068	0.440059	0.44900	0.480339	0.436557	0.468918	0.445124
17	0.625385	0.583943	0.580927	0.524180	0.489481	0.508035	0.468558	0.479494	0.453425	0.440667	0.448151	0.477330	0.439861	0.456809

Table O.13 The values of the light intensity of (I_N) pixel by pixel calculated using Equation 3.7 in section 3.3.

2120.708	2020.105	1947.864	1836.023	1784.461	1723.480	1560.55	1646.596	1699.617	1512.099	1516.305	1625.975	1605.031	1492.824
1933.039	1707.503	1678.29	1546.702	1413.874	1429.600	1419.879	1299.762	1249.612	1241.91	1199.129	1244.168	1439.983	1508.411
1772.104	1649.095	1382.686	1312.156	1263.106	1190.641	1174.091	1089.329	1062.413	1047.237	1035.762	993.8587	1038.183	990.0645
1688.879	1561.094	1352.929	1224.159	1118.22	1095.406	1030.964	965.6269	1005.067	952.3577	871.9558	943.275	866.3696	875.9111
1771.655	1552.532	1355.743	1187.243	1021.567	1005.274	910.4709	923.1507	872.8896	904.0667	860.0743	863.2776	759.7541	838.8689
1761.835	1484.377	1300.496	1202.181	1057.448	972.5757	901.8506	895.2857	870.5610	825.1713	815.1335	814.0311	778.8096	803.1281
1768.968	1583.716	1381.346	1138.919	1049.801	974.8661	957.9503	907.2313	767.6765	747.6905	778.9693	693.2101	670.5815	641.9018
1879.170	1703.951	1284.238	1099.896	945.4355	953.2602	896.6942	928.7191	760.6839	723.1829	763.8107	729.0396	669.7752	729.6800
1773.860	1438.214	1343.032	1143.108	1026.072	917.4219	978.0816	905.2337	880.6217	824.0850	780.5392	764.4384	769.3319	650.4145
1723.728	1554.457	1231.34	1172.592	1009.375	892.1135	841.8352	792.3369	802.5834	773.2971	826.8422	736.4786	636.0275	691.4589
1785.614	1487.675	1262.912	1086.787	1014.884	960.6790	859.1961	778.1210	791.1463	680.4590	737.9857	635.5352	637.6389	699.4783
1841.830	1556.793	1554.212	1201.952	1050.755	950.5812	932.1749	885.2854	812.9075	760.3852	686.0169	733.4632	643.5012	608.4613
1960.717	1505.782	1525.572	1148.204	1117.634	948.6274	802.1391	838.2002	727.3675	796.7226	758.5218	649.8819	614.5884	666.9182
1786.443	1537.424	1403.310	1102.527	1040.384	870.0000	799.8006	793.2153	755.6796	669.2373	726.4956	674.7916	701.1389	588.9869
1789.599	1510.626	1335.323	1148.420	958.6346	866.1673	805.9328	795.4721	743.1067	741.3938	667.4569	598.8087	667.9927	631.8937
1883.701	1512.976	1307.302	1174.924	1067.039	957.4087	865.2722	737.938	777.5950	681.7757	684.9706	640.2076	658.2611	610.0168
1857.624	1620.612	1331.914	1143.269	1094.226	932.2708	867.0191	858.4878	690.8515	662.3419	701.3617	617.3638	623.0936	592.7298
1739.266	1536.353	1439.037	1168.143	1034.331	956.7634	839.7767	883.2195	737.3584	673.2015	730.4634	728.3156	628.6392	634.0036

The values of S_N pixel by pixel calculated using Equation 3.19 in section 3.3.

Table O.14 NAPL saturation values

0.514185	0.505190	0.457681	0.330270	0.336807	0.330022	0.253546	0.211285	0.154603	0.153955	0.195294	0.27590	0.344103	0.174182	0.190254
0.484457	0.361660	0.265616	0.270361	0.188968	0.133233	0.127858	0.071639	0.024227	0.072672	0.068649	0.060362	0.032214	0.050038	0.042227
0.424119	0.354292	0.208021	0.089086	0.112537	0.066604	0.011745	0.012721	0.023765	0.009063	0.002693	0.017940	0.029810	0.014226	0.086748
0.403772	0.316417	0.170500	0.069164	0.067863	0.046132	0.026146	0.071131	0.025479	0.028281	0.034184	0.077472	0.024569	0.008863	0.072183
0.379801	0.287920	0.164991	0.160833	0.097615	0.013491	0.084766	0.084239	0.087647	0.153376	0.145960	0.089631	0.136418	0.136052	0.150157
0.384712	0.315104	0.209148	0.113059	0.041998	0.031393	0.035096	0.071829	0.166827	0.117849	0.195956	0.224378	0.292354	0.290214	0.230519
0.372125	0.288732	0.177162	0.067129	0.028355	0.024494	0.122071	0.121873	0.259113	0.172758	0.169125	0.186891	0.198927	0.209365	0.145636
0.343587	0.282566	0.096986	0.028308	0.015700	0.035149	0.085622	0.062149	0.116510	0.179572	0.205338	0.200488	0.193077	0.265638	0.290072
0.389004	0.269317	0.148635	0.058335	0.013400	0.063771	0.059549	0.092270	0.171392	0.210701	0.205557	0.210852	0.180619	0.318572	0.255130
0.362691	0.258452	0.126425	0.060577	0.034964	0.032495	0.09813	0.070098	0.118255	0.185594	0.202802	0.278591	0.197912	0.278896	0.39172
0.377406	0.313765	0.171064	0.089954	0.041545	1.7E-05	0.065318	0.152677	0.179136	0.164708	0.272452	0.235994	0.279421	0.282700	0.377717
0.349045	0.276278	0.159881	0.099996	0.044438	0.051424	0.091382	0.221446	0.217783	0.235361	0.304037	0.280505	0.319210	0.273237	0.386121
0.334686	0.268285	0.147216	0.095328	0.008920	0.089204	0.100662	0.148142	0.188630	0.236938	0.310338	0.403693	0.409433	0.344436	0.469362
0.348622	0.302949	0.187473	0.114454	0.040091	0.025623	0.069168	0.189555	0.162891	0.237262	0.244323	0.33695	0.415757	0.357986	0.510531
0.329948	0.248782	0.177704	0.069572	0.031649	0.024937	0.067708	0.146430	0.153307	0.197563	0.303396	0.299852	0.473682	0.411214	0.381560
0.359745	0.270743	0.18879	0.129132	0.008040	0.086022	0.129336	0.187393	0.232988	0.242313	0.230614	0.349943	0.369532	0.365237	0.438153
0.360740	0.349233	0.193904	0.128322	0.014584	0.060695	0.077619	0.142430	0.190245	0.193191	0.254977	0.243313	0.281244	0.400992	0.394154
0.368284	0.311811	0.226138	0.118144	0.081083	0.018325	0.026398	0.144830	0.139529	0.221835	0.242313	0.229644	0.281536	0.298631	0.341905
0.401597	0.317668	0.209125	0.111155	0.083680	0.053696	0.029018	0.119159	0.189674	0.211160	0.318083	0.235034	0.250229	0.253588	0.284921

The last step is calculating the volume of the PCE increment as discussed in Appendix N. This sheet shows the PCE volume pixel by pixel where after that the summation of total pixels resulted in the PCE increment.

Table O.15 Calculation of PCE volumes



0.000148	0.000145	0.000132	0.000095	0.000097	0.000095	0.000073	0.000061	0.000045	0.000044	0.000056	0.000079	0.000099	0.000050	0.000055
0.000140	0.000104	0.000076	0.000078	0.000054	0.000038	0.000037	0.000021	0.000007	0.000021	0.000020	0.000017	0.000009	0.000014	0.000012
0.000122	0.000102	0.000060	0.000026	0.000032	0.000019	0.000003	0.000004	0.000007	0.000003	0.000001	0.000005	0.000009	0.000004	0.000025
0.000116	0.000091	0.000049	0.000020	0.000020	0.000013	0.000008	0.000020	0.000007	0.000008	0.000010	0.000022	0.000007	0.000003	0.000021
0.000109	0.000083	0.000048	0.000046	0.000028	0.000004	0.000024	0.000024	0.000025	0.000044	0.000042	0.000026	0.000039	0.000039	0.000043
0.000111	0.000091	0.000060	0.000033	0.000012	0.000009	0.000010	0.000021	0.000048	0.000034	0.000056	0.000065	0.000084	0.000084	0.000066
0.000107	0.000083	0.000051	0.000019	0.000008	0.000007	0.000035	0.000035	0.000075	0.000050	0.000049	0.000054	0.000057	0.000060	0.000042
0.000099	0.000081	0.000028	0.000008	0.000005	0.000010	0.000025	0.000018	0.000034	0.000052	0.000059	0.000058	0.000056	0.000076	0.000084
0.000112	0.000078	0.000043	0.000017	0.000004	0.000018	0.000017	0.000027	0.000049	0.000061	0.000059	0.000061	0.000052	0.000092	0.000073
0.000104	0.000074	0.000036	0.000017	0.000010	0.000009	0.000028	0.000020	0.000034	0.000053	0.000058	0.000080	0.000057	0.000080	0.000113
0.000109	0.000090	0.000049	0.000026	0.000012	0.000000	0.000019	0.000044	0.000052	0.000047	0.000078	0.000068	0.000080	0.000081	0.000109
0.000101	0.000080	0.000046	0.000029	0.000013	0.000015	0.000026	0.000064	0.000063	0.000068	0.000088	0.000081	0.000092	0.000079	0.000111
0.000096	0.000077	0.000042	0.000027	0.000003	0.000026	0.000029	0.000043	0.000054	0.000068	0.000089	0.000116	0.000118	0.000099	0.000135
0.000100	0.000087	0.000054	0.000033	0.000012	0.000007	0.000020	0.000055	0.000047	0.000068	0.000070	0.000097	0.000120	0.000103	0.000147
0.000095	0.000072	0.000051	0.000020	0.000009	0.000007	0.000019	0.000042	0.000044	0.000057	0.000087	0.000086	0.000136	0.000118	0.000110
0.000104	0.000078	0.000054	0.000037	0.000002	0.000025	0.000037	0.000054	0.000067	0.000070	0.000066	0.000101	0.000106	0.000105	0.000126
0.000104	0.000101	0.000056	0.000037	0.000004	0.000017	0.000022	0.000041	0.000055	0.000056	0.000073	0.000070	0.000081	0.000115	0.000113
0.000106	0.000090	0.000065	0.000034	0.000023	0.000005	0.000008	0.000042	0.000040	0.000064	0.000070	0.000066	0.000081	0.000086	0.000098
0.000116	0.000091	0.000060	0.000032	0.000024	0.000015	0.000008	0.000034	0.000055	0.000061	0.000092	0.000068	0.000072	0.000073	0.000082

APPENDIX P

REPETATION OF EXPERIMENT (1)

Injected volume of PCE (ml)	Calculated volume of PCE (ml) (Test 1)	Calculated volume of PCE (ml) (Test 2)	Calculated volume of PCE (ml) (Test 3)
2.00	1.80	1.77	1.82
4.00	3.80	3.92	3.78
6.00	5.60	5.82	5.76
8.00	7.45	7.90	7.85
10.00	8.90	9.20	9.45
12.00	11.60	11.94	11.77

ANOVA-One way

Increment volume (ml)	Average	Variance
2	1.8475	0.010758
4	3.8750	0.010767
6	5.7950	0.027300
8	7.8000	0.058333
10	9.3870	0.217292
12	11.827	0.032492

Source of Variation	SS	df	MS	F	P-value	F crit
Between Groups	268.2076	5	53.64151	901.6854	<0.05	2.772853
Within Groups	1.070825	18	0.05949			
Total	269.2784	23				

SS: sum of squares; df: degree of freedom; MS: mean square.

APPENDIX Q

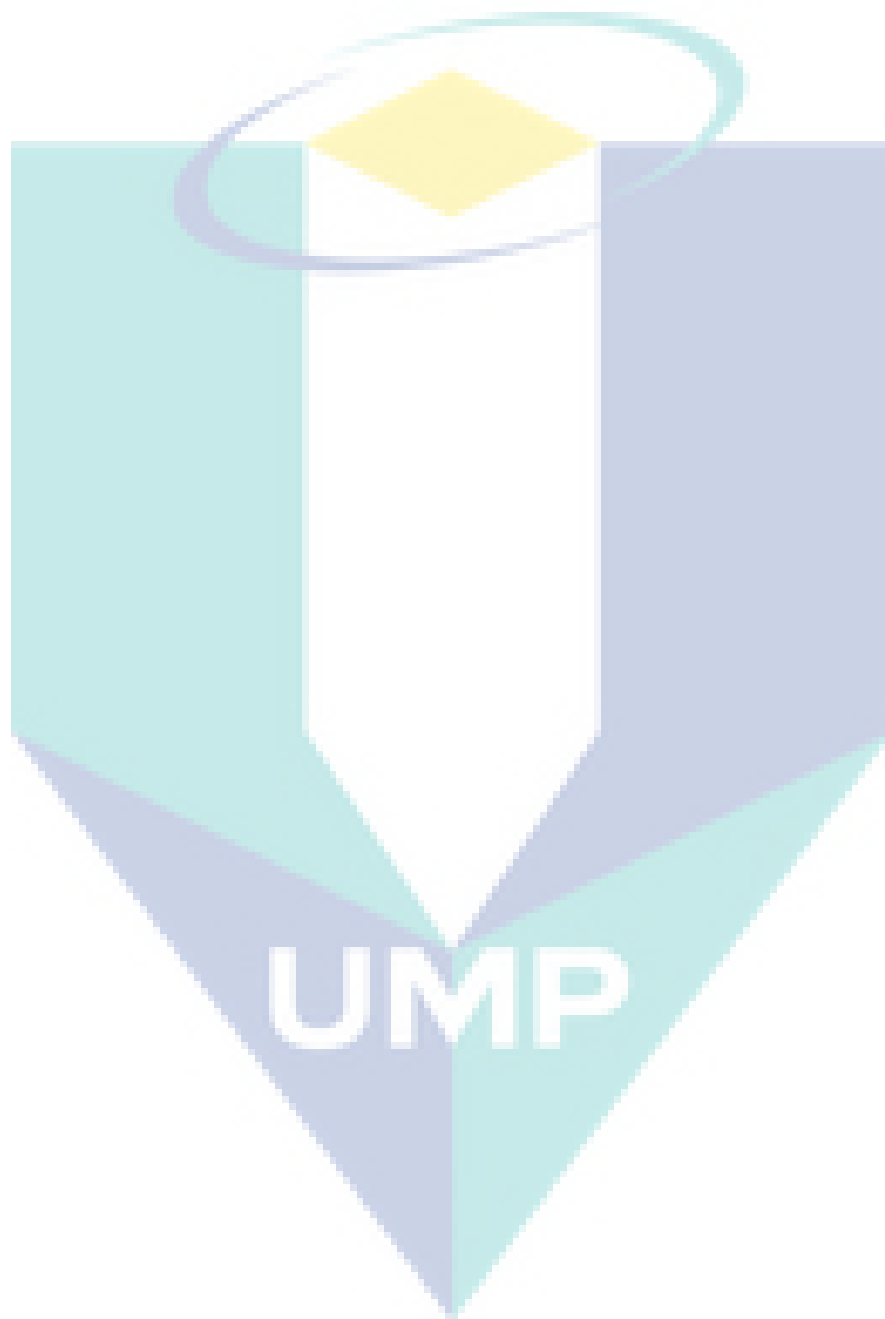
REPETATION OF EXPERIMENT (2)

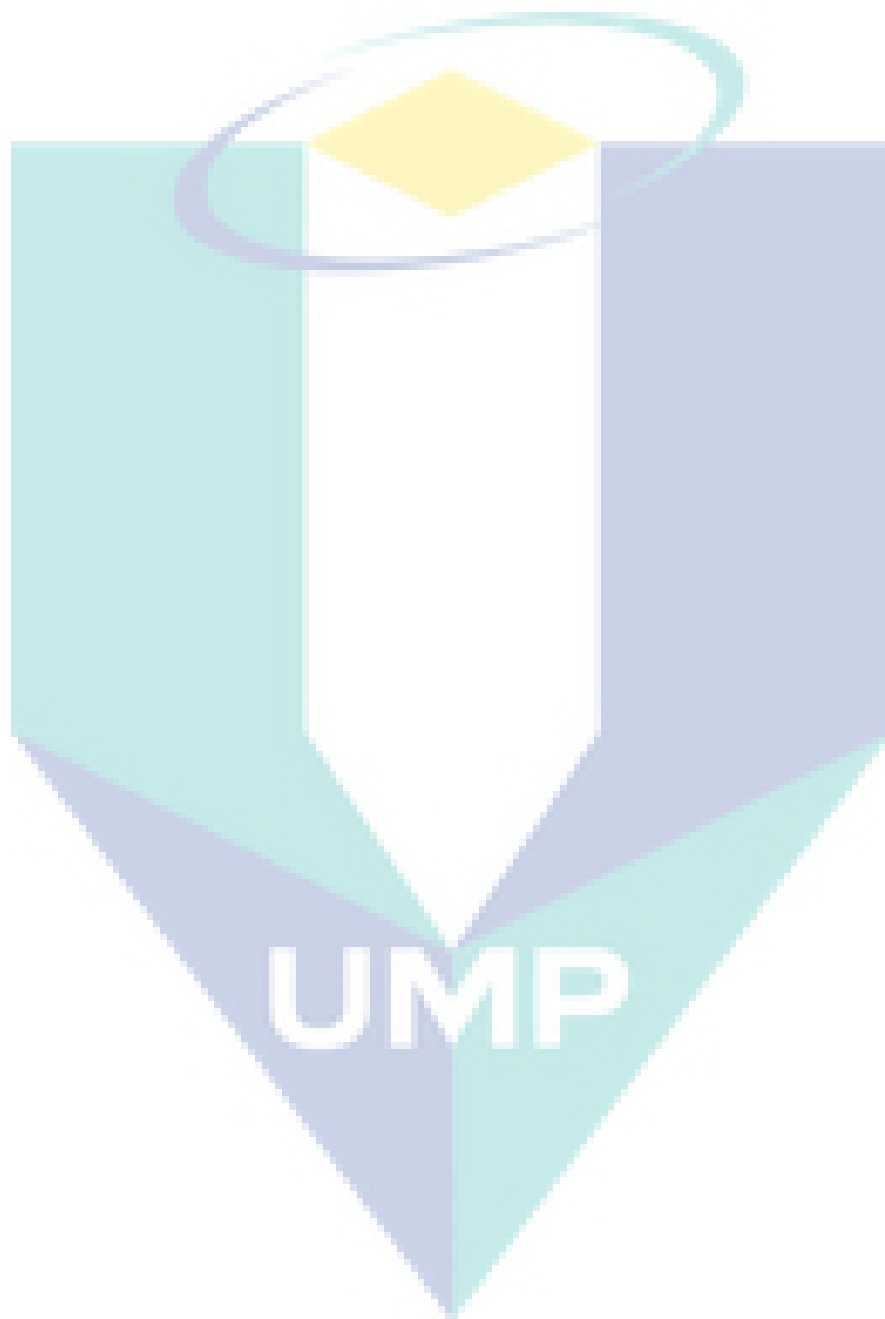
Injected volume of PCE (ml)	Calculated volume of PCE (ml) (Test 1)	Calculated volume of PCE (ml) (Test 2)	Calculated volume of PCE (ml) (Test 3)
2.00	1.75	1.84	1.87
4.00	3.65	3.75	3.91
6.00	5.35	5.56	5.83
8.00	7.55	7.78	7.84
10.00	8.9	9.65	9.44
12.00	11.8	11.91	11.76

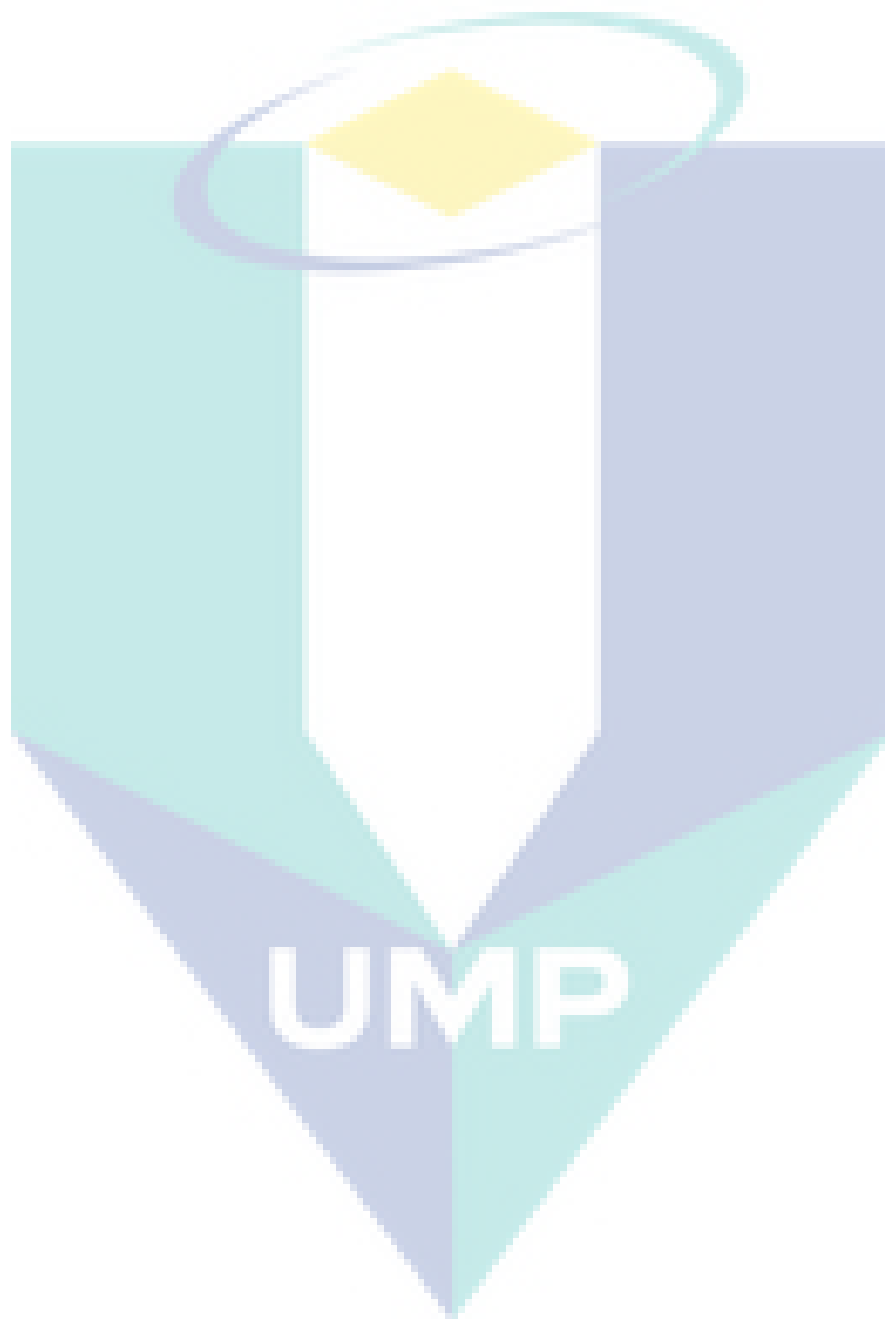
ANOVA-One way

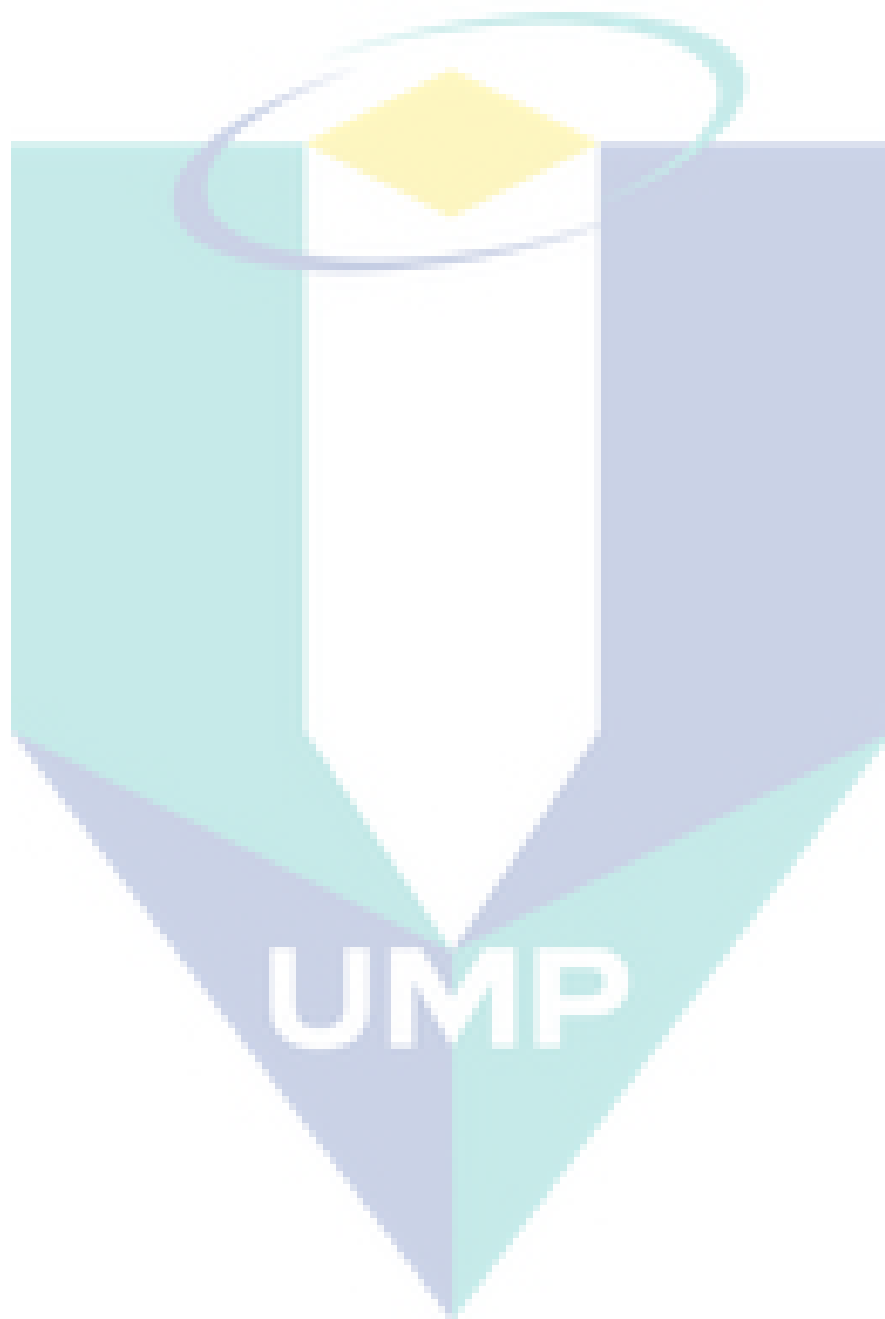
Increment volume (ml)	Average	Variance
2	1.8600	0.01070
4	3.8275	0.024692
6	5.9300	0.429367
8	7.7925	0.034758
10	9.49750	0.212025
12	11.8670	0.011825

Source of Variation	SS	df	MS	F	P-value	F crit
Between Groups	271.5172	5	54.30343	450.4224	<0.05	2.772853
Within Groups	2.1701	18	0.120561			
Total	273.6873	23				









APPENDIX V

REPETATION OF EXPERIMENT (11)

Injected volume of PCE (ml)	Calculated volume of PCE (ml) (Test 1)	Calculated volume of PCE (ml) (Test 2)	Calculated volume of PCE (ml) (Test 3)
2.00	1.967	2.40	1.82
4.00	3.85	4.45	3.70
6.00	5.40	5.85	4.81
8.00	7.652	8.03	6.8
10.00	9.475	10.00	8.87
12.00	11.377	11.33	11.36

ANOVA-One way

Increment volume (ml)	Average	Variance
2	1.92925	0.006122
4	3.905	0.004433
6	5.645	0.064633
8	7.768	0.025736
10	9.66125	0.059706
12	11.58175	0.130299

Source of Variation	SS	df	MS	F	P-value	F crit
Between Groups	261.6487	5	52.32974	1079.223	<0.05	2.772853
Within Groups	0.87279	18	0.048488			
Total	262.5215	23				

APPENDIX W

REPETATION OF EXPERIMENT (4)

Injected volume of PCE (ml)	Calculated volume of PCE (ml) (Test 1)	Calculated volume of PCE (ml) (Test 2)	Calculated volume of PCE (ml) (Test 3)
2.00	1.75	1.77	1.80
4.00	3.60	3.65	3.57
6.00	5.72	5.70	5.78
8.00	7.30	7.80	7.67
10.00	9.10	9.57	9.20
12.00	11.76	11.86	11.77

ANOVA-One way

Increment volume (ml)	Average	Variance
2	1.83	0.013267
4	3.705	0.039767
6	5.8	0.018933
8	7.6925	0.086892
10	9.4675	0.166892
12	11.8325	0.016758

Source of Variation	SS	df	MS	F	P-value	F crit
Between Groups	273.9235	5	54.78471	959.7088	< 0.05	2.772853
Within Groups	1.027525	18	0.057085			
Total	274.9511	23				

APPENDIX X

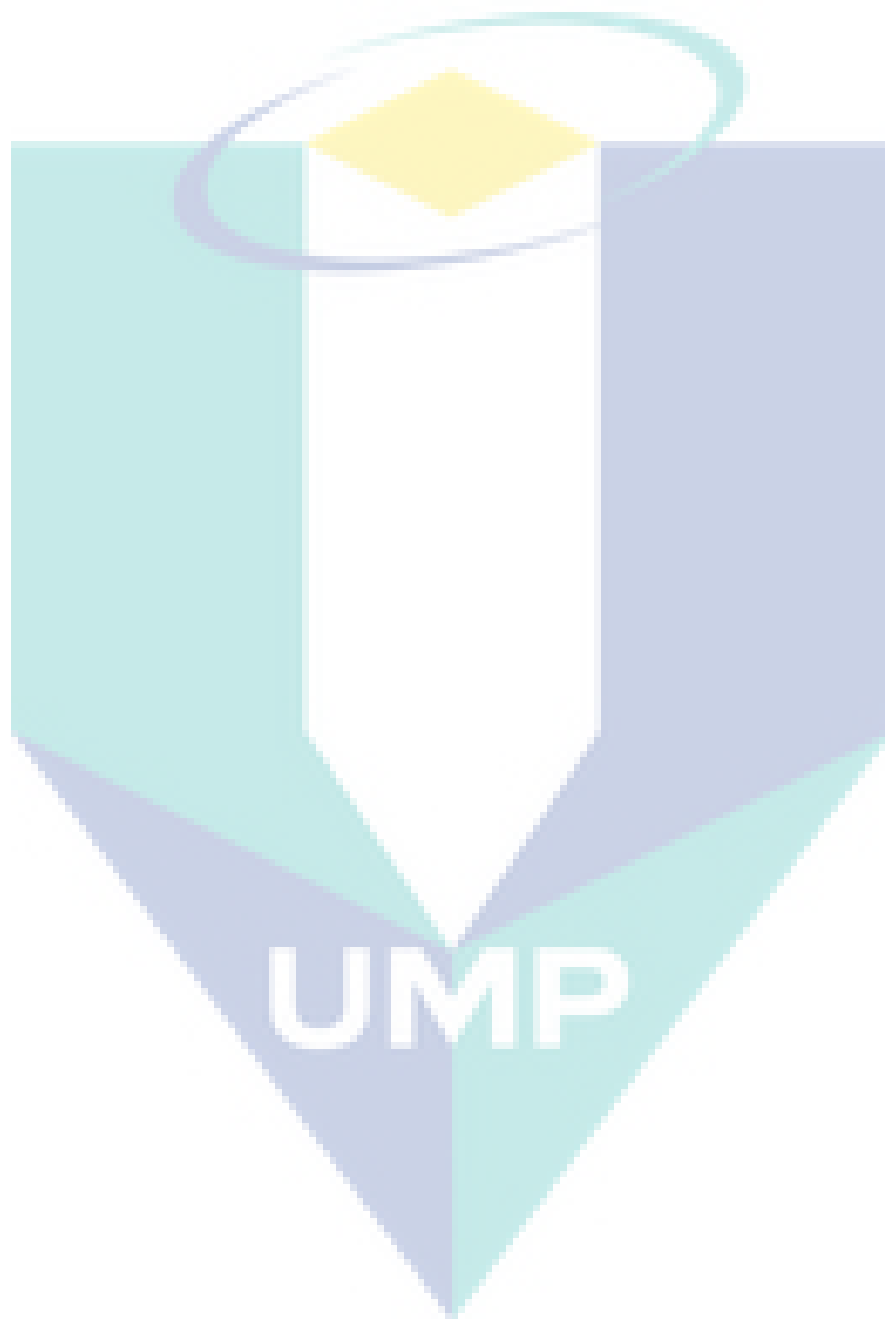
COMPARISON BETWEEN EXPERIMENTS 1, 11 AND 12

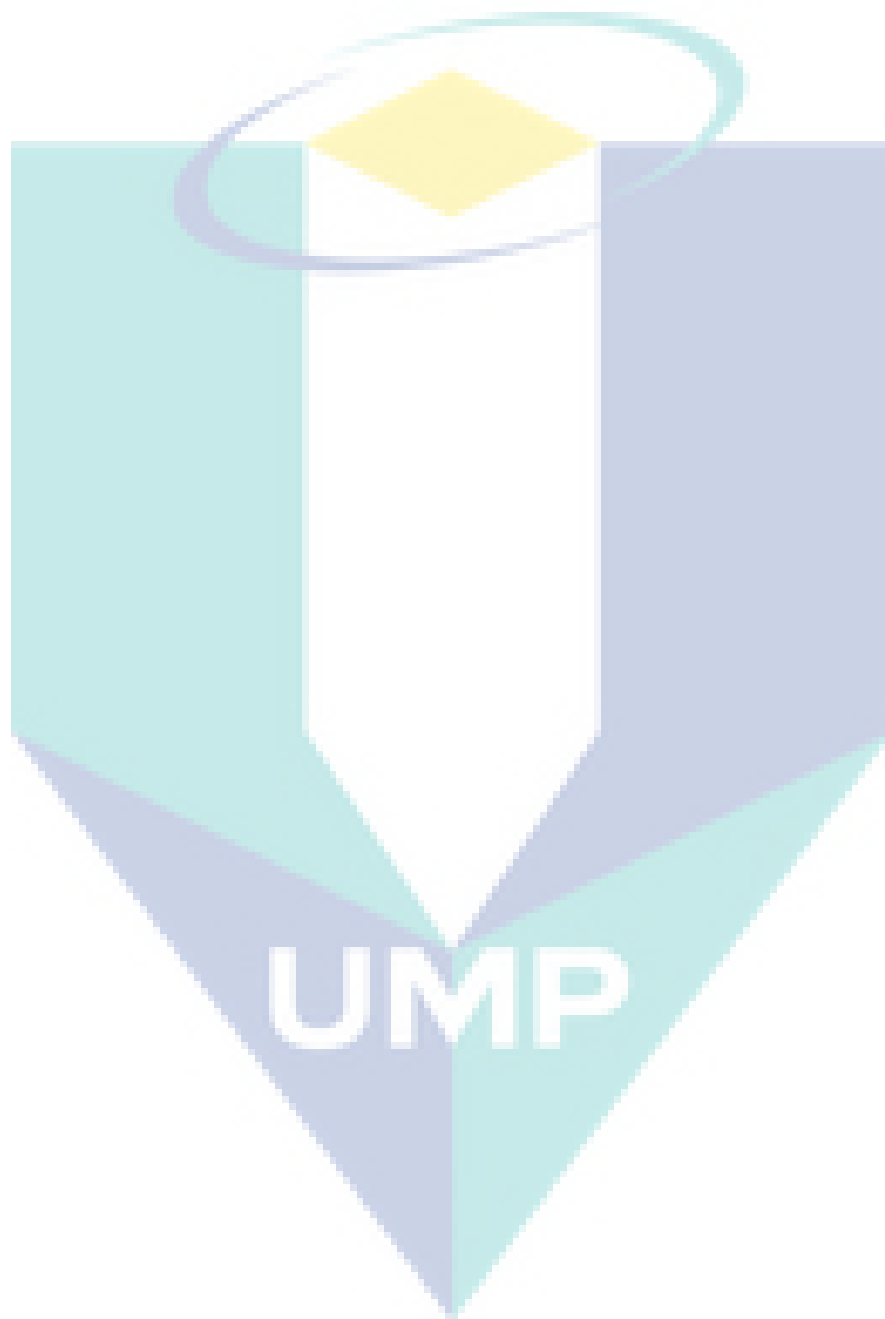
Injected volume of PCE (ml)	Calculated volume of PCE (ml) (Exp. 1)	Calculated volume of PCE (ml) (Exp. 3)	Calculated volume of PCE (ml) (Exp. 4)
2.00	1.80	1.967	1.75
4.00	3.80	3.85	3.60
6.00	5.60	5.40	5.72
8.00	7.45	7.652	7.30
10.00	8.90	9.475	9.10
12.00	11.60	11.377	11.70

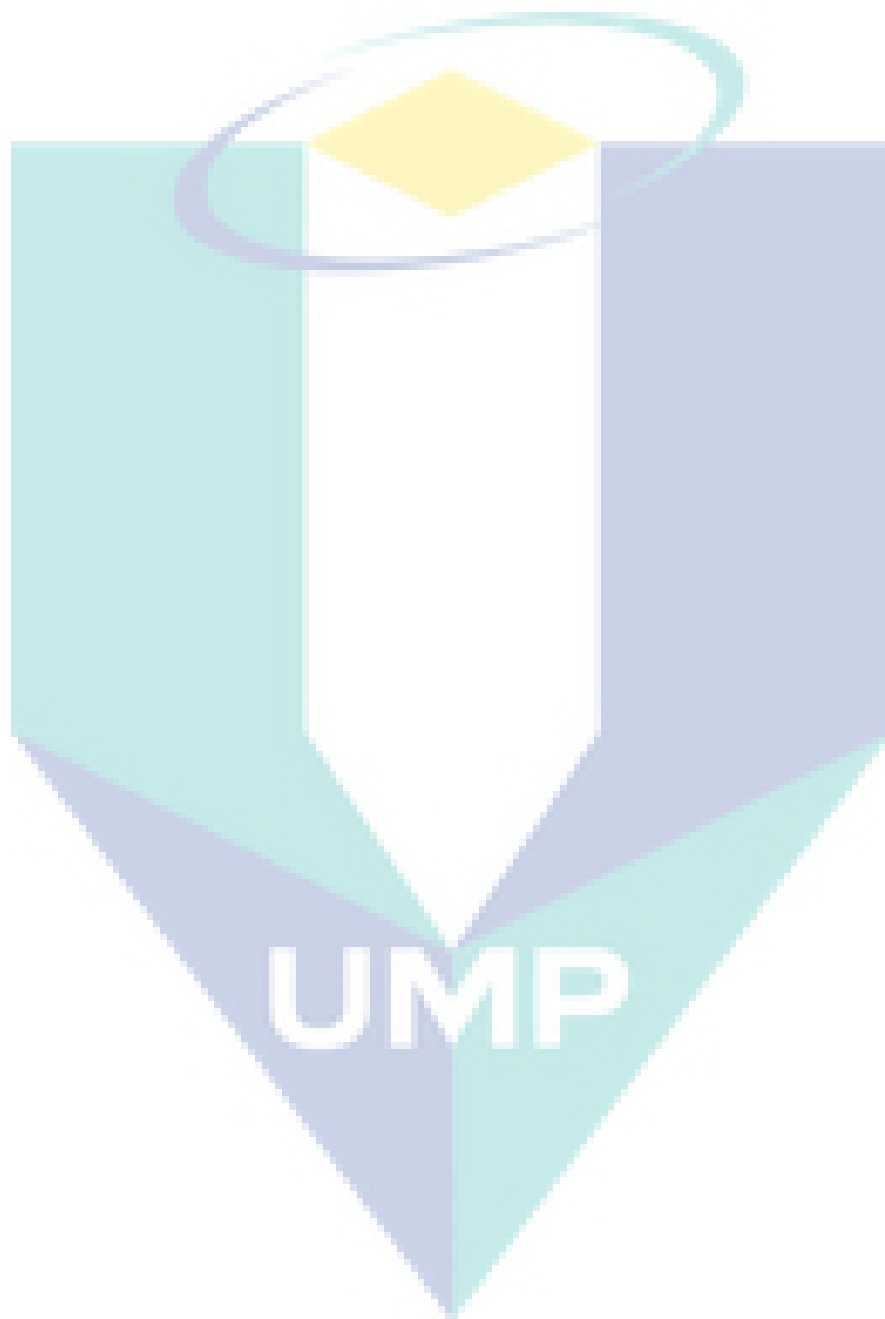
ANOVA-One way

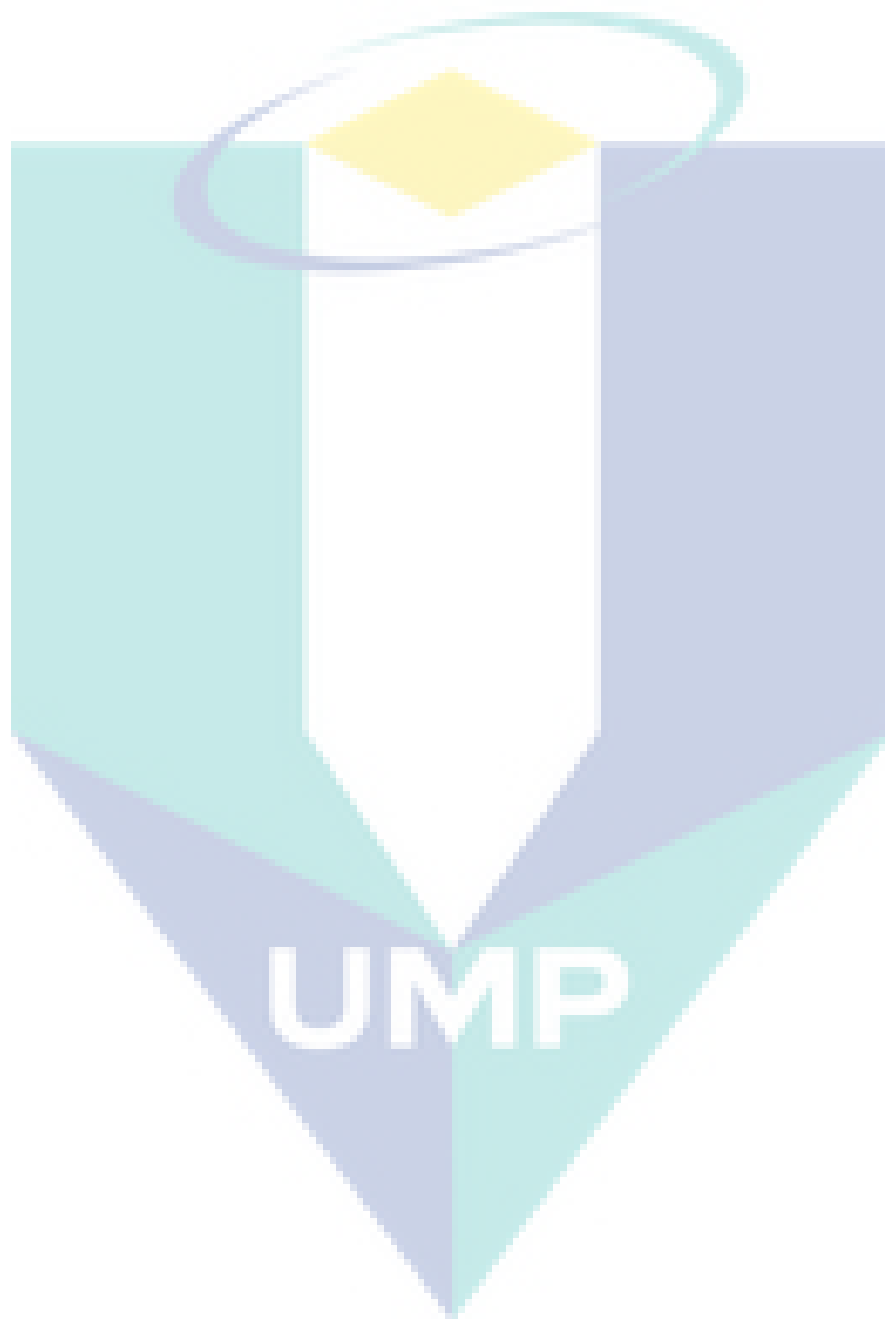
Increment volume (ml)	Average	Variance
2	1.87925	0.015089
4	3.8125	0.027292
6	5.68	0.062933
8	7.6005	0.091734
10	9.36875	0.233906
12	11.66925	0.066849

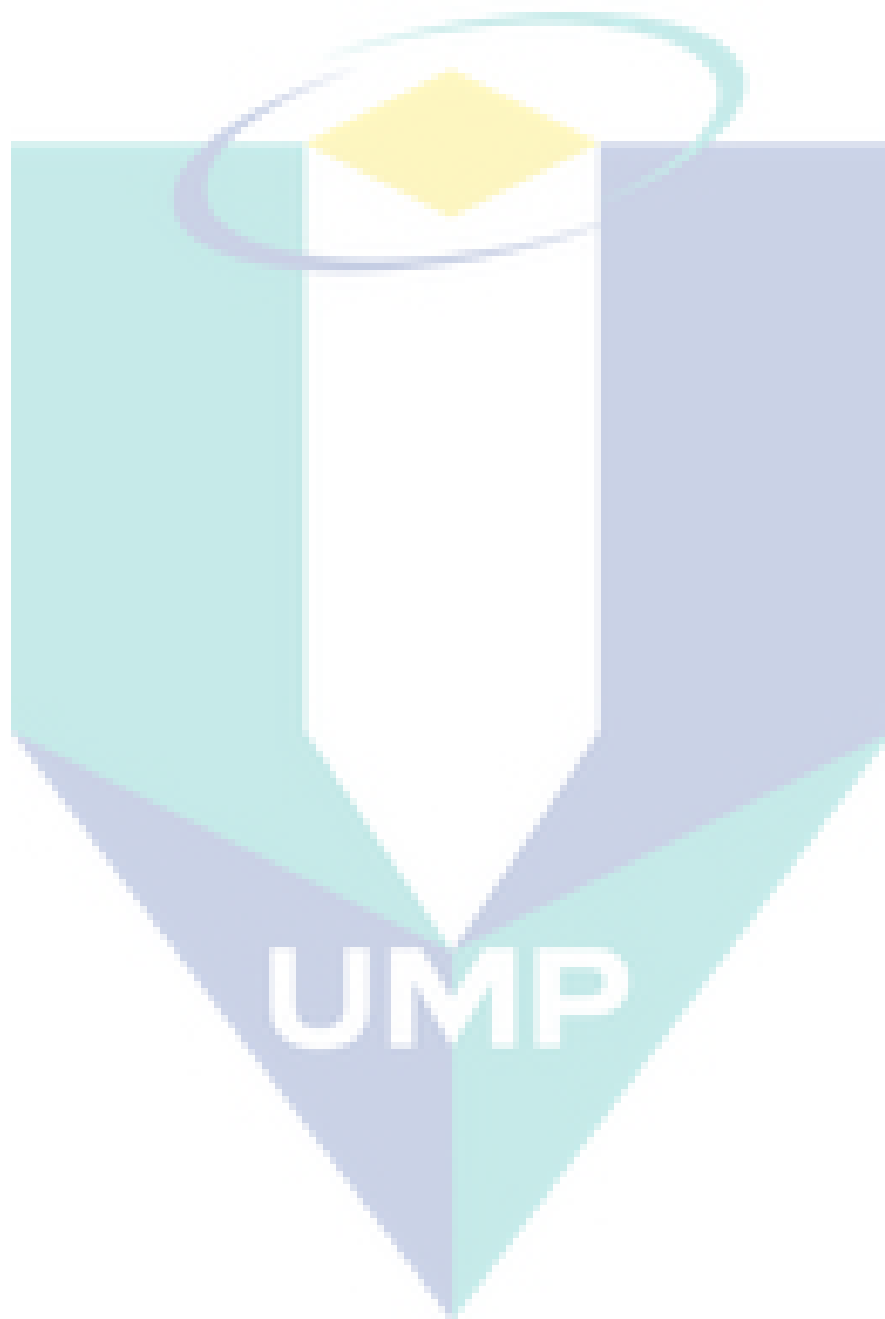
Source of Variation	SS	df	MS	F	P-value	F crit
Between Groups	260.953	5	52.19061	629.0508	< 0.05	2.772853
Within Groups	1.49341	18	0.082967			
Total	262.4464	23				

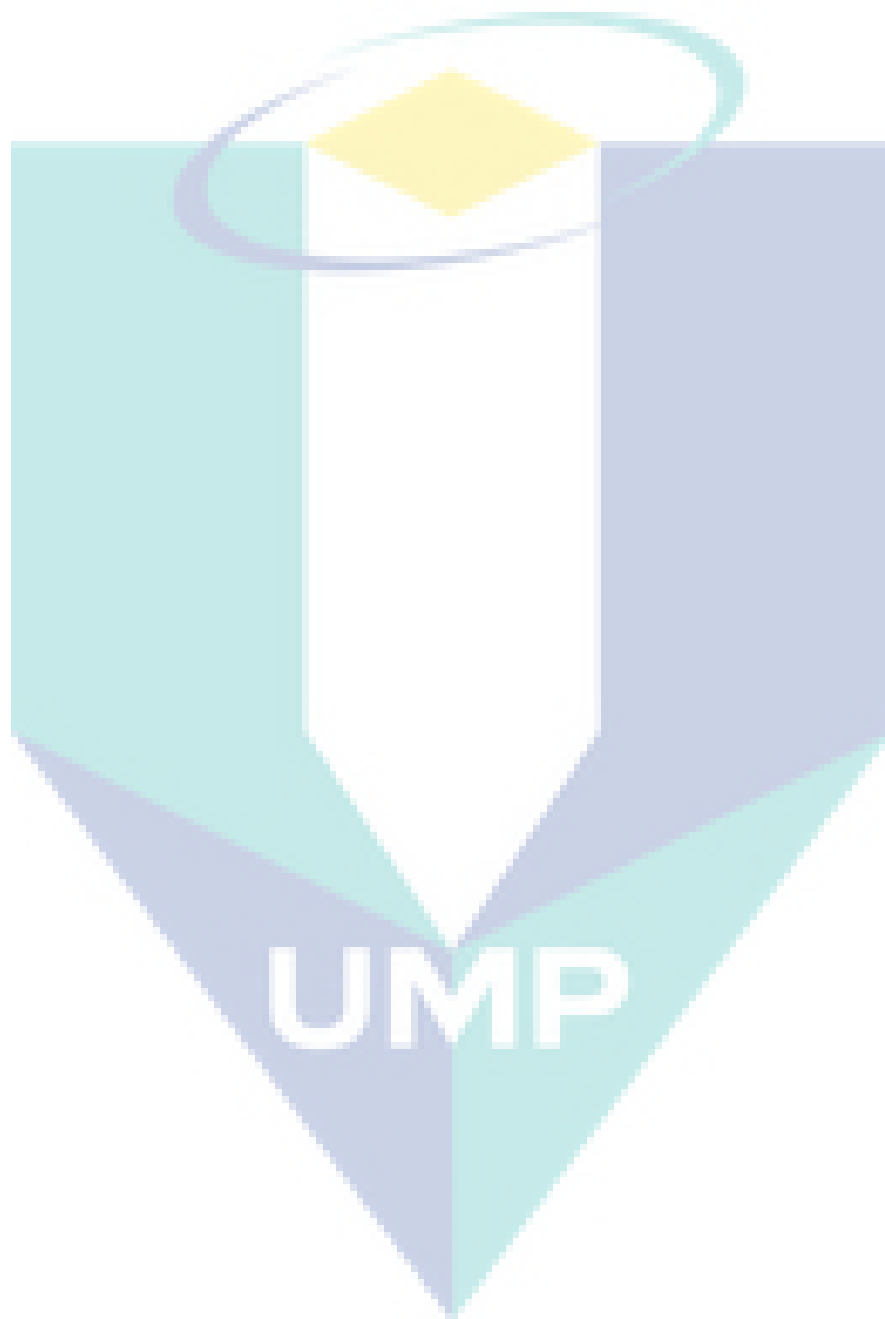


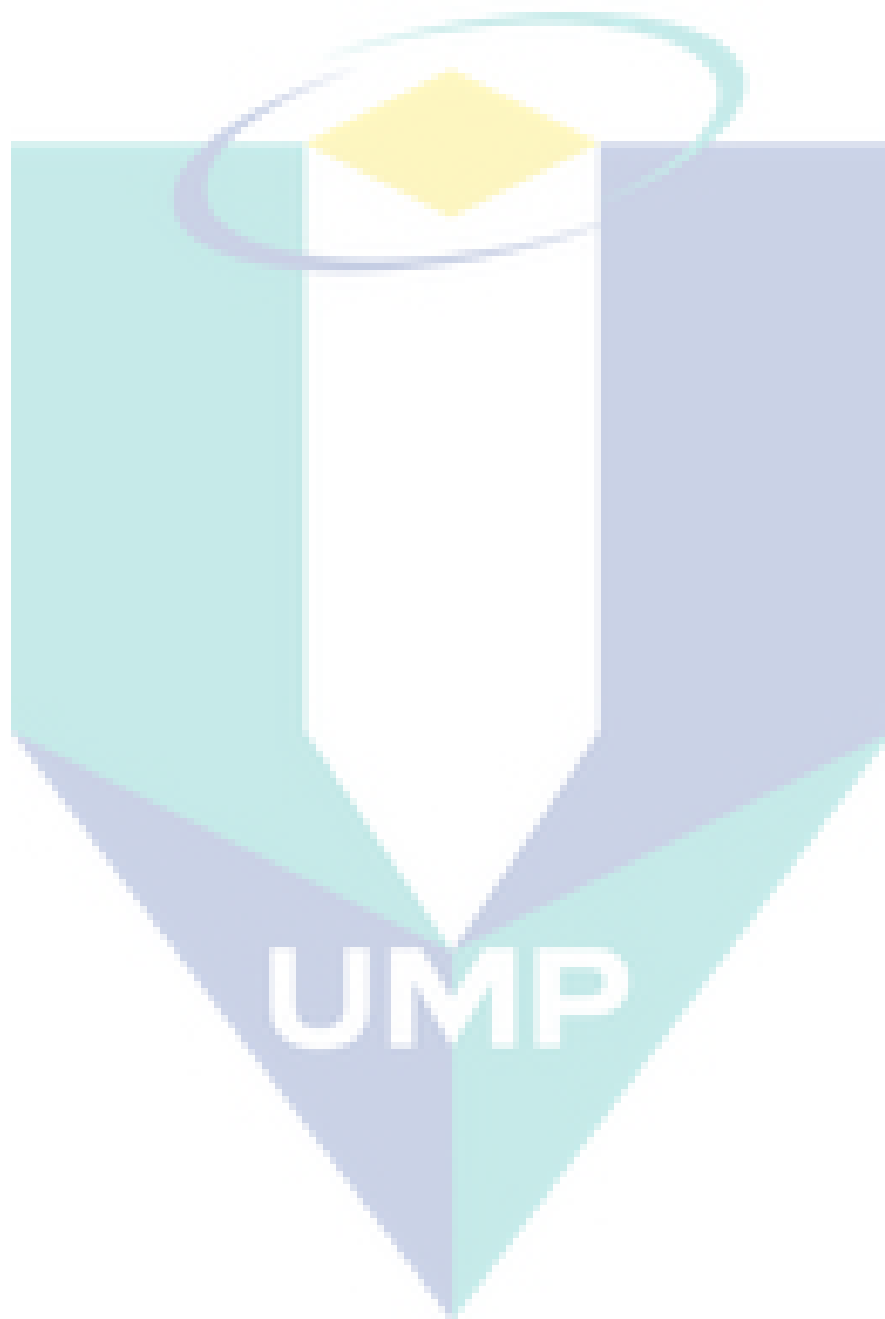


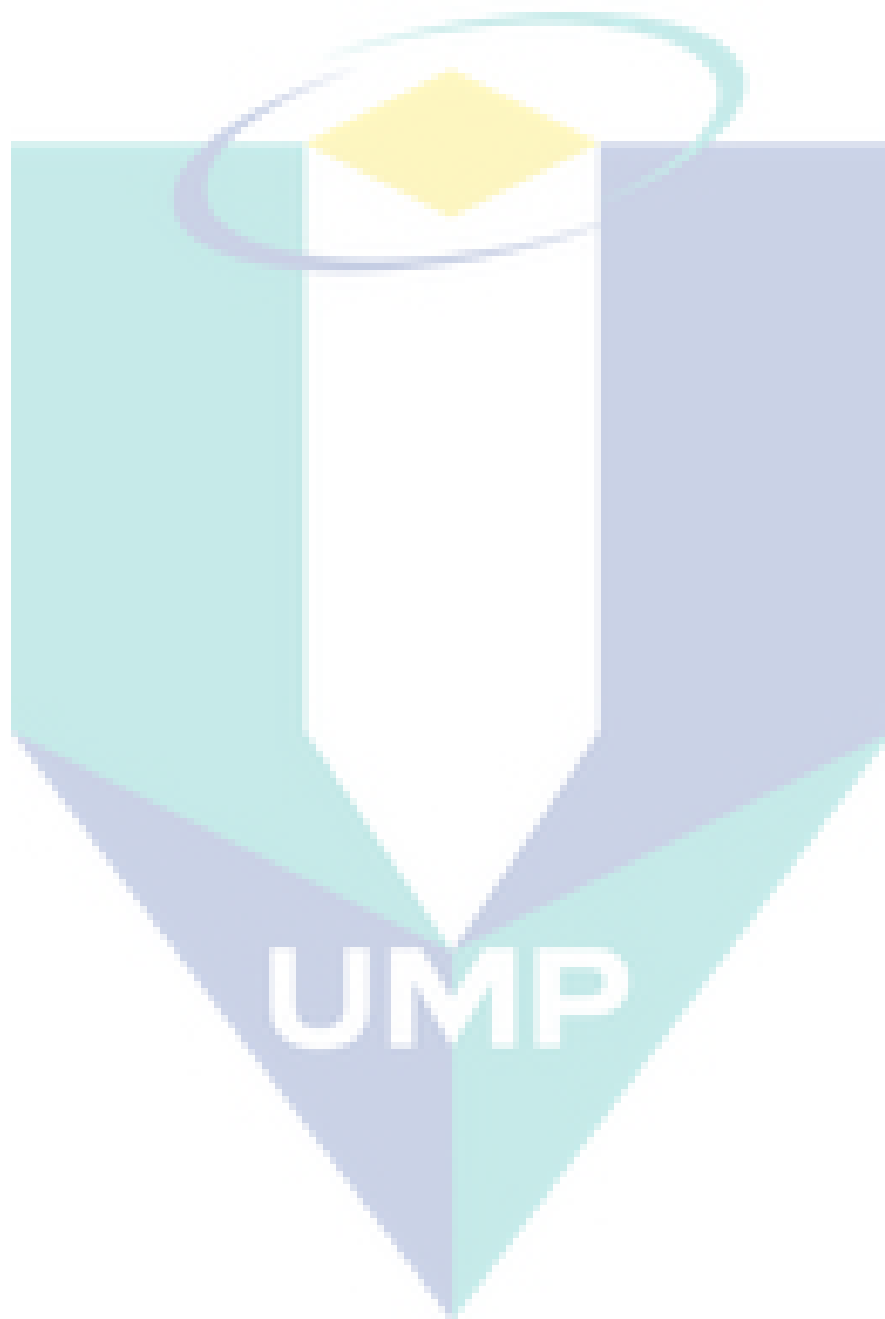


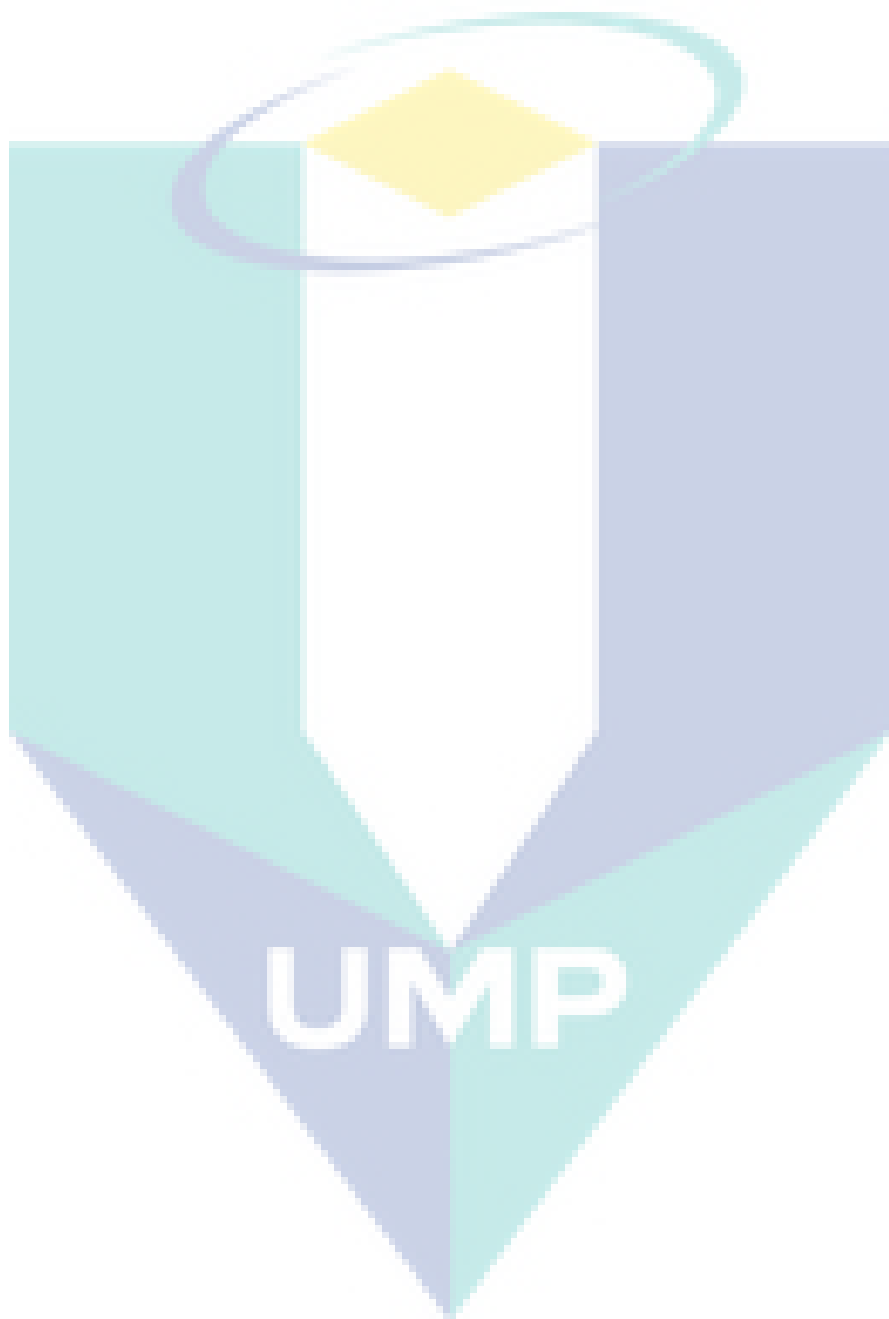


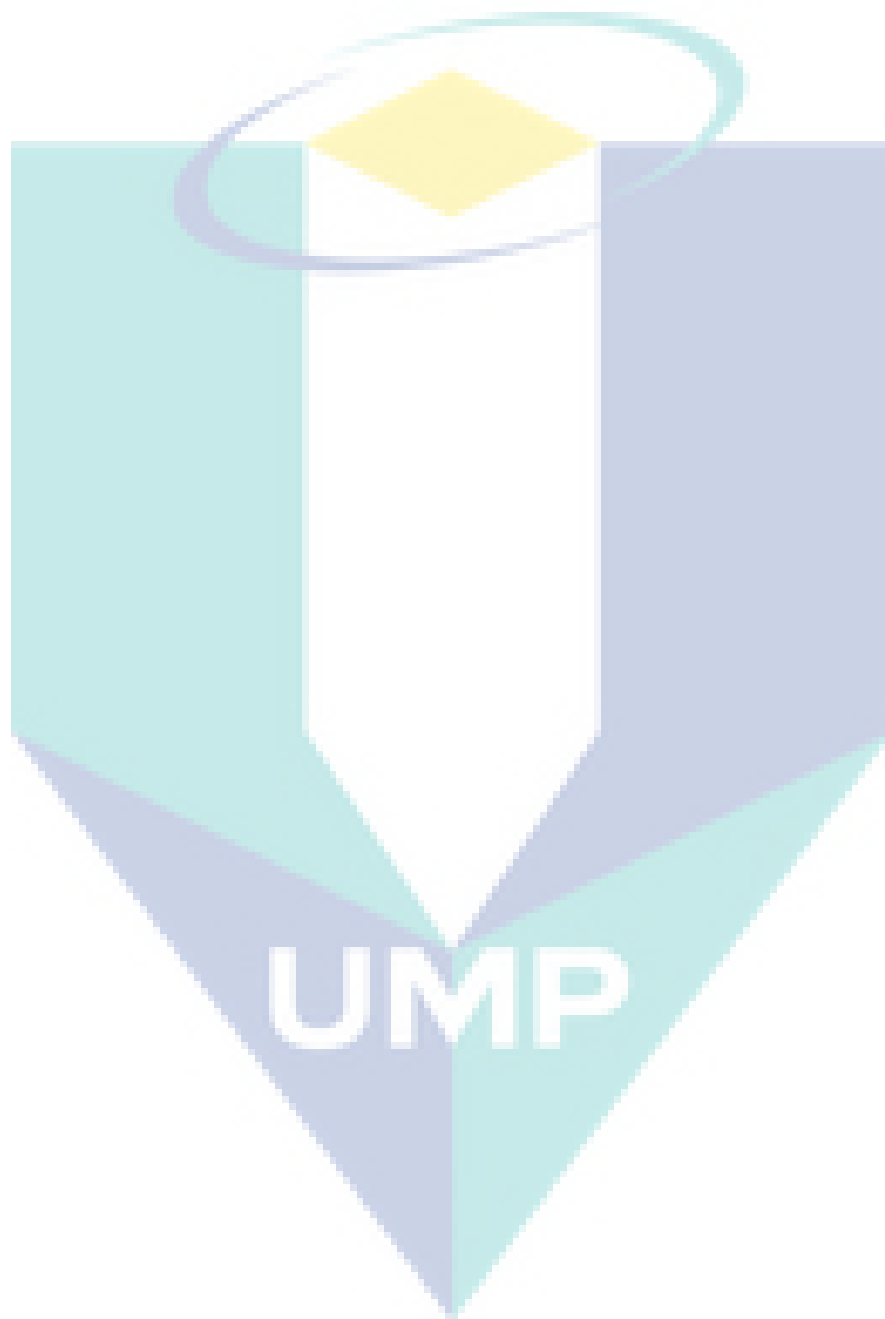


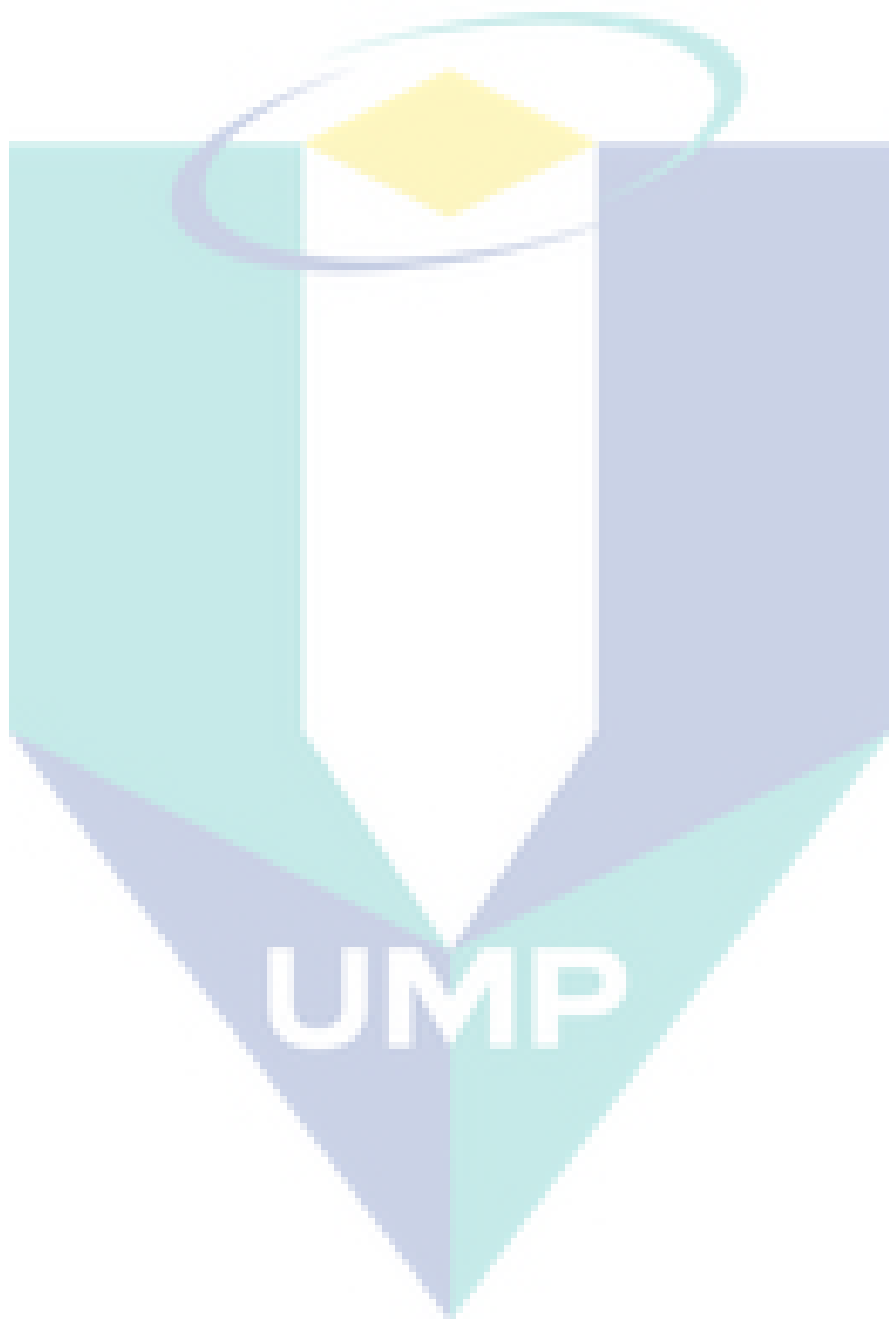


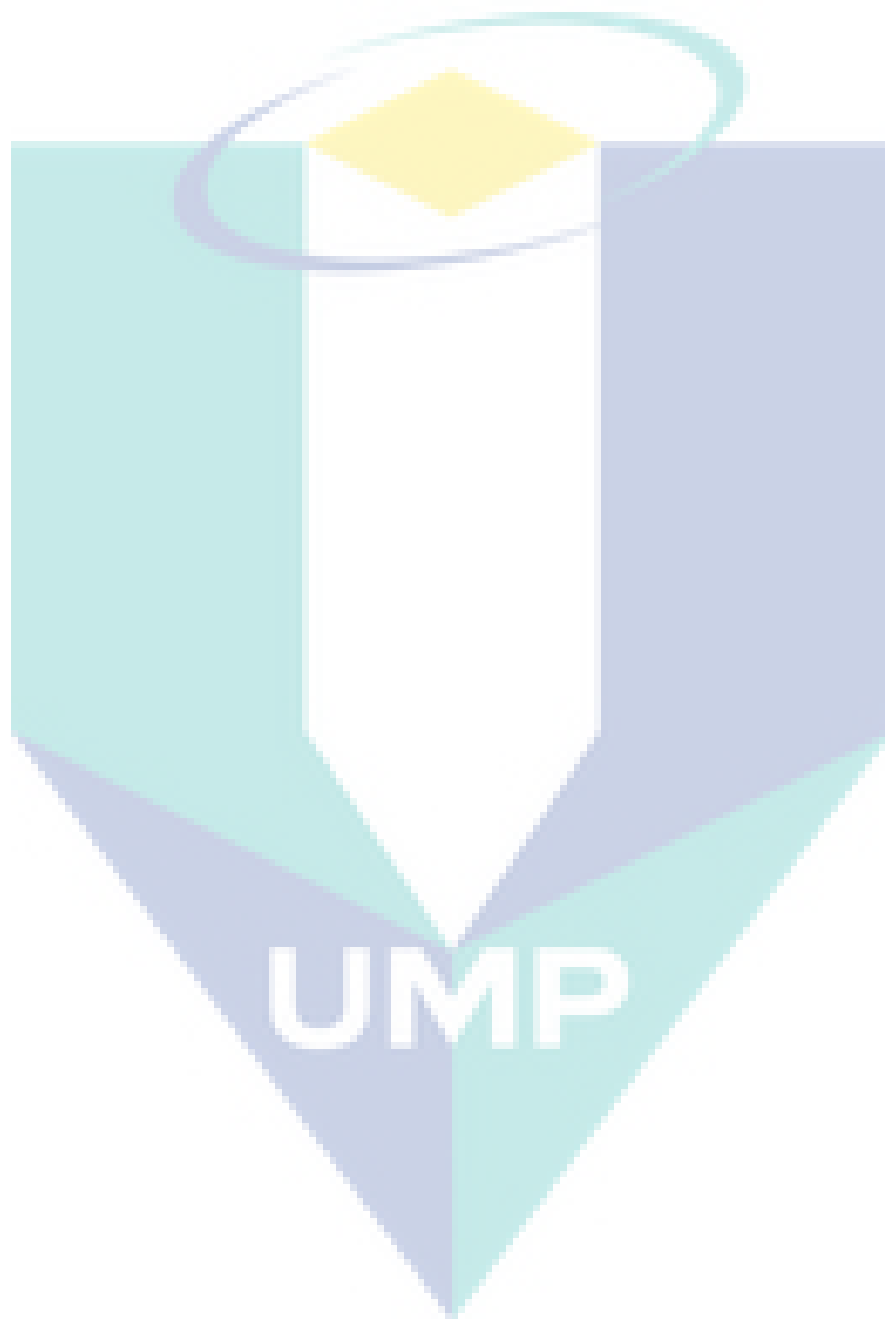


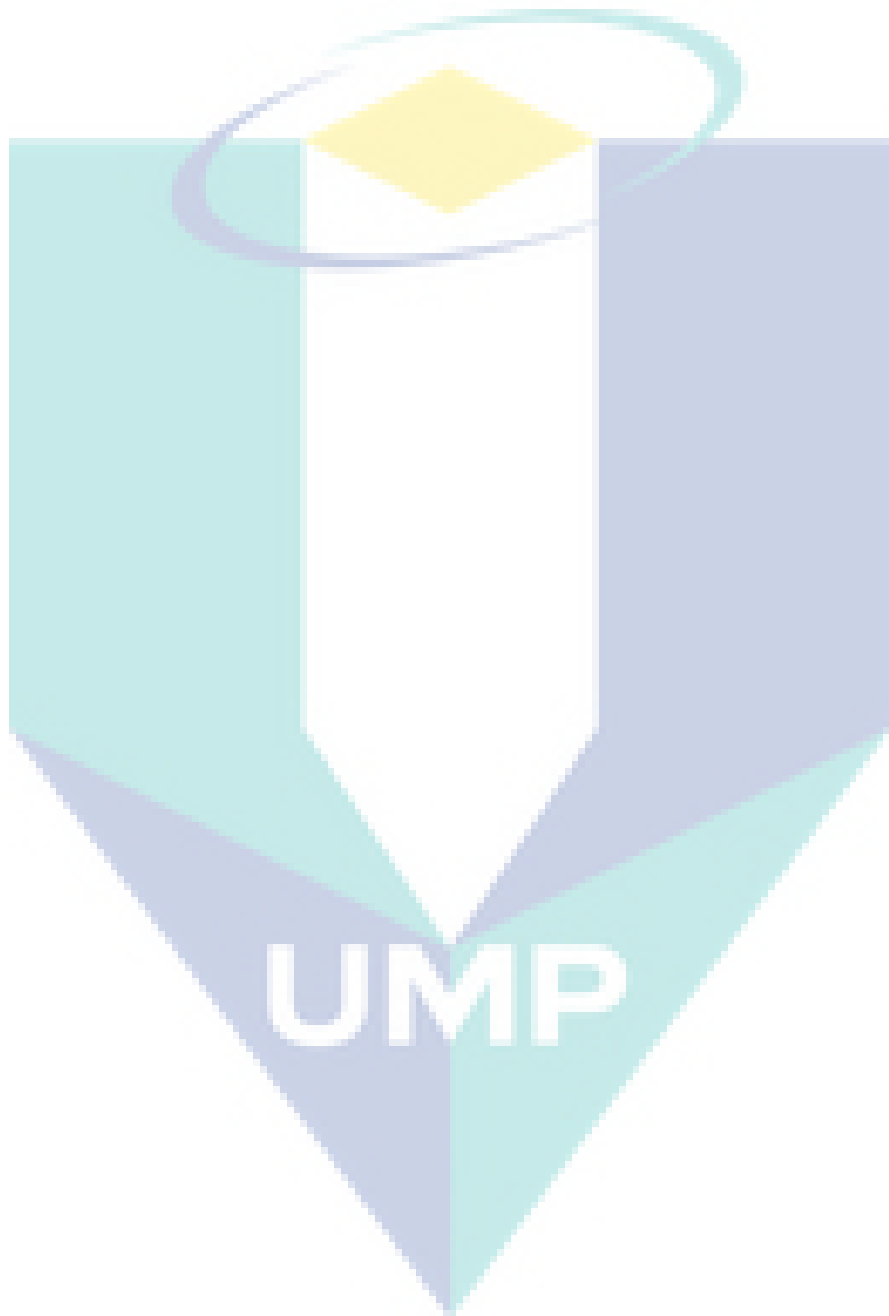


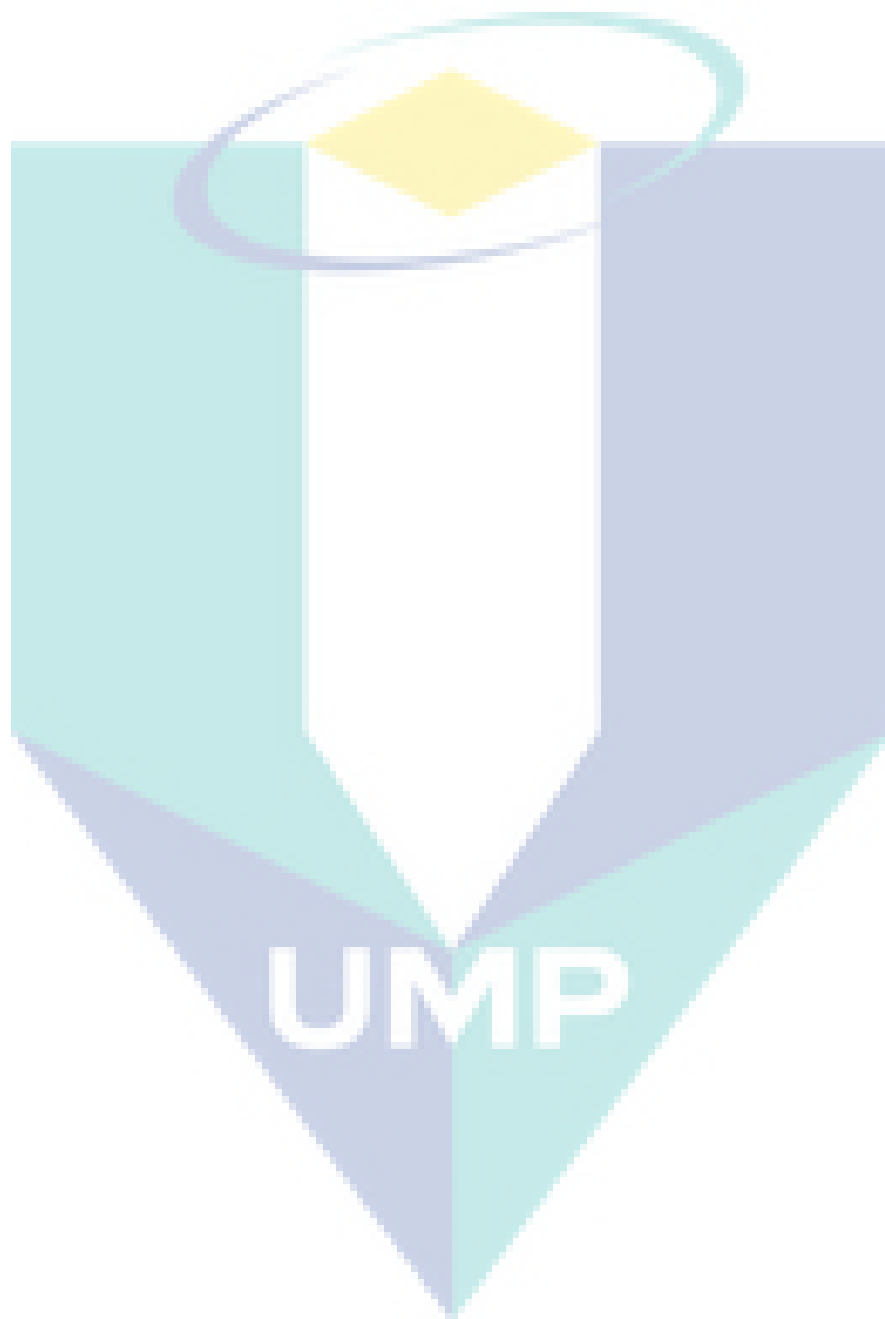


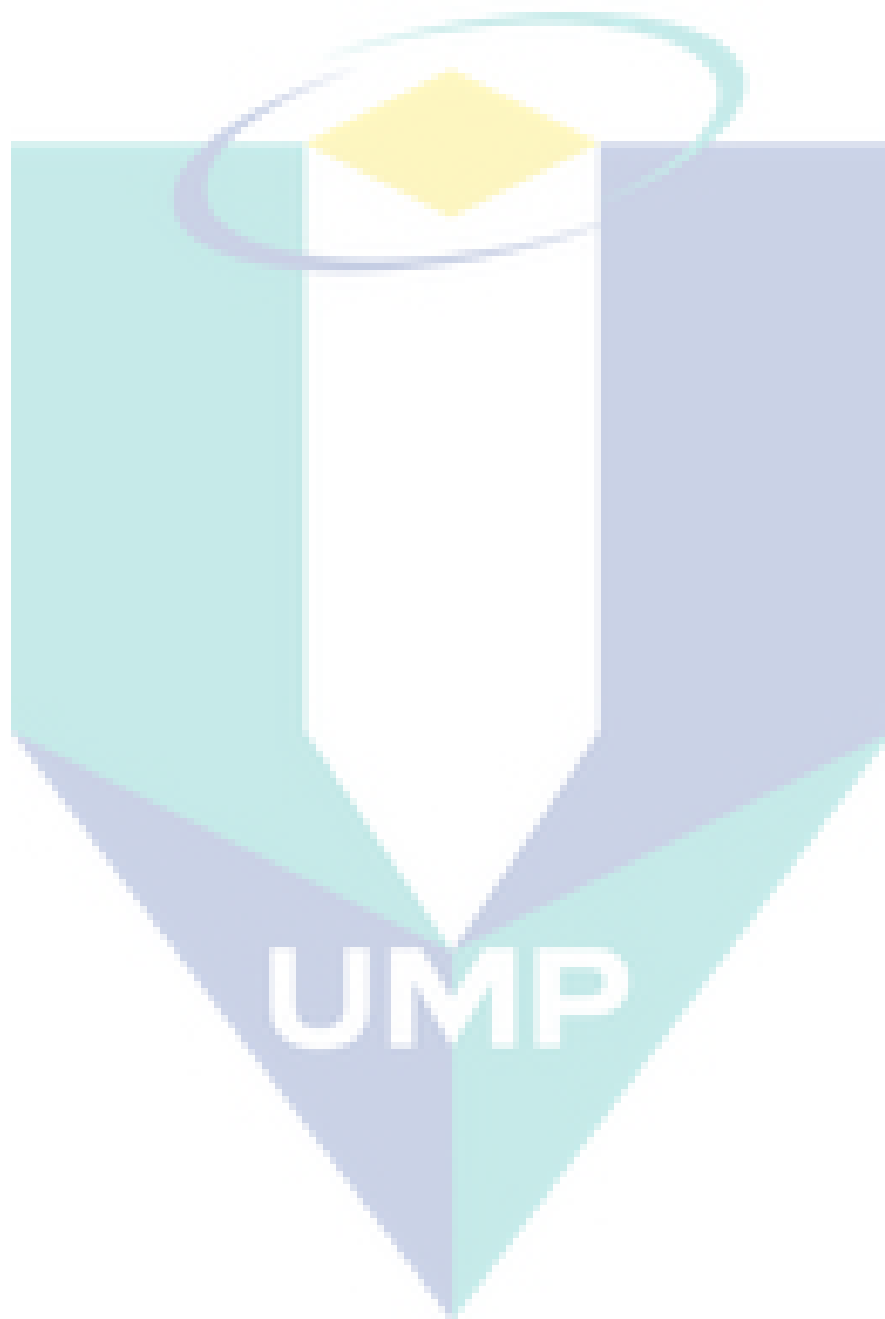


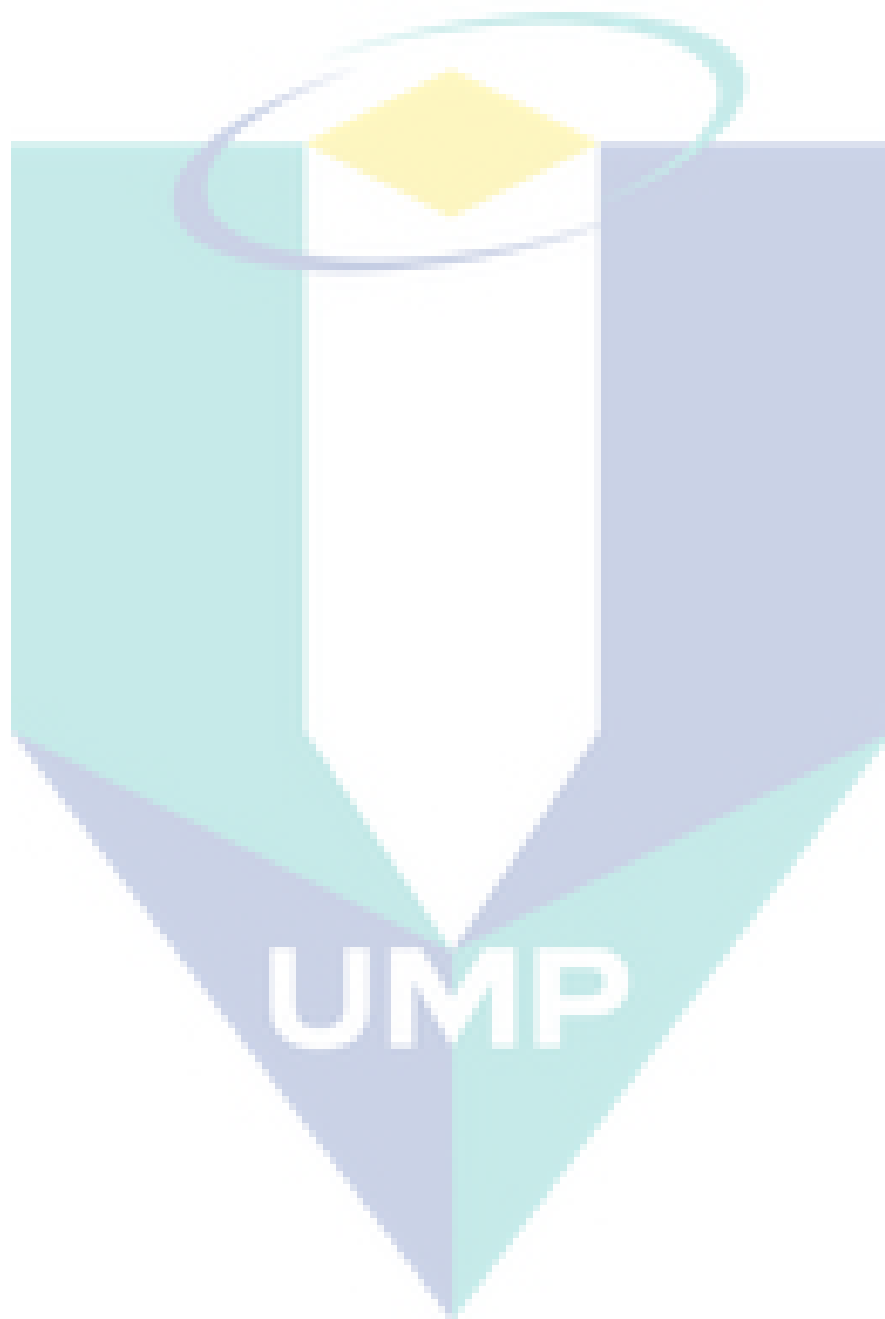












LIST OF PUBLICATIONS

Journal papers:

- Alazaiza, M.Y.D**, Ngien, S.K, Bob, M.M, Kamaruddin, S.A, Ishak, W.M.F. (2017) .
Influence of macro-pores on DNAPL migration in double-porosity soil using light transmission visualization method. *Transport in Porous Media*. DOI: 10.1007/s11242-017-0822-3. (IF = 2.204).
- Alazaiza, M.Y.D**, Ngien, S.K, Bob, M.M, Kamaruddin, S.A, Ishak, W.M.F. (2017).
Quantification of dense non-aqueous phase liquid saturation in double-porosity soil media using light transmission visualization technique. *Journal of Porous Media*. (IF= 1.143, Accepted).
- Alazaiza, M.Y.D**, Ngien, S.K, Bob, M.M, Kamaruddin, S.A, Ishak, W.M.F. (2017).
Qualitative assessment of non-aqueous phase liquids distribution in three-fluid phase systems in double-porosity soil media. *Groundwater for sustainable development*. (Under review).
- Alazaiza, M.Y.D**, Ngien, S.K, Bob, M.M, Kamaruddin, S.A, Ishak, W.M.F. (2017).
Light transimission visualization of rainfall recharge influence on light non-aqueous phase liquid migration in double-porosity soil media. *Environmental Monitoring and Assessment*. (IF = 1.633, Under review).
- Alazaiza, M.Y.D**, Ngien, S.K, Bob, M.M, Kamaruddin, S.A, Ishak, W.M.F. (2016).
Assessment of the behaviour of soil structure in double-porosity kaolin media using light transmission visualization (LTV) method. *International Journal of Geotechnical Engineering*. DOI: 10.1080/19386362.2016.1211370. (SCOPUS).
- Alazaiza, M.Y.D**, Ngien, S.k, Bob, M.M, Ishak, W.M.F, Kamaruddin, S.A,. (2015). An overview of photographic methods in monitoring non-aqueous phase liquid migration in porous media. *Special Topics and Reviews in Porous Media - An International Journal*. 6(4), 367-381. (SCOPUS).
- Alazaiza, M.Y.D**, Ngien, S.K, Bob, M.M, Kamaruddin, S.A, Ishak, W.M.F. (2016). A review of light reflection and transmission methods in monitoring non-aqueous

phase liquid migration in porous media. *ARPN Journal of Engineering and Applied Sciences*. 11(4), 2319-2326. (SCOPUS).

Proceeding:

Alazaiza, M.Y.D, Ngien, S.K, Bob, M.M, Kamaruddin, S.A, Ishak, W.M.F. (2015). Investigation of light non-aqueous phase liquid migration in single and double-porosity soil using light transmission visualization method (LTV). *Proceeding of the 3rd International Conference on Civil and Environmental Engineering and Sustainability, Melaka, Malaysia, 1-2 December 2015.*

Alazaiza, M.Y.D, Ngien, S.K, Bob, M.M, Kamaruddin, S.A, Ishak, W.M.F. (2016). Viability assessment of soil structure in double-porosity kaolin media using light transmission visualization (LTV) method. *Proceeding of the 10th International Conference on Geotechnical and Transportation Engineering, Kuala Lumpur, Malaysia, 17-18 February 2016.*

Alazaiza, M.Y.D, Ngien, S.K, Bob, M.M, Kamaruddin, S.A. (2016). Investigation of the influence of particle size on the migration of DNAPL in unsaturated sand. *Proceeding of the World Engineering, Science and Technology Congress, Kuala Lumpur, Malaysia, 15-17 August 2016.*

Alazaiza, M.Y.D, Ngien, S.K, Bob, M.M, Kamaruddin, S.A, Ishak, W.M.F. (2016). Application of light reflection method to observe DNAPL movement in different soil media. *Proceeding of the 3rd National Conference for Post Graduate, Pekan, 24-25 September 2016.*

Awards:

- 1. Gold Medal:** Light transmission visualization for NAPL measurements in double-porosity soil. *Creation, Innovation, Technology and Research Exposition (CITREx) 2016.*

2. **Gold Medal:** Image analysis for organic contaminant saturation in double-porosity soil. *International Festival Innovation on Green Technology (i-FINOG 2016)*.
3. **Silver Medal:** CONTALISIS – Innovative system for DNAPL saturation measurements in double-porosity. *27th International Invention and Innovation Exhibition (ITEX 2016)*.

